Improvement of the muon spectrometer and precision W-boson physics in ATLAS

Zhibo Wu

THESE DE DOCTORAT

NNT : 2023UPASP110

Improvement of the muon spectrometer and precision W-boson physics in ATLAS

Amélioration du spectromètre à muons et physique de précision du boson W dans ATLAS

Thèse de doctorat de l'Université Paris-Saclay et de l'University of Science and Technology of China

École doctorale n°576, Particules, hadrons, énergie et noyau : instrumentation, imagerie, cosmos et simulation (PHENIICS)
Spécialité de doctorat : Physique des particules
Graduate School : Physique. Référent : Faculté des sciences d'Orsay

Thèse préparée dans le **Département d'Electronique des Détecteurs et d'Informatique pour la Physique** (Université Paris-Saclay, CEA), sous la direction d'**Esther FERRER RIBAS**, Directrice de recherche, la co-direction de **Zhengguo ZHAO**, Professeur, et le co-encadrement de **Fabrice BALLI**, Ingénieur

Thèse soutenue à Paris-Saclay, le 25 septembre 2023, par

Zhibo WU

Composition du jury

Membres du jury avec voix délibérative

Laurent SERIN Directeur de recherche, Université Paris-Saclay	Président
Theodoros GERALIS Directeur de recherche, National Technical University of Athens	Rapporteur & Examinateur
Monica DUNFORD Professeure, Heidelberg University	Rapporteure & Examinatrice
Mario ANTONELLI Directeur de recherche, Sapienza Università di Roma	Examinateur
Mika VESTERINEN Docteur, Warwick University	Examinateur
Yusheng WU Professeur, University of Science and Technology of China	Examinateur

université PARIS-SACLAY
ÉCOLE DOCTORALE
Particules, hadrons, énergie et noyau : instrumentation, imagerie, cosmos et simulation (PHENIICS)

Title: Improvement of the muon spectrometer and precision W-boson physics in ATLAS
Key words: *MPGD, Micromegas, ATLAS, NSW, Cosmic bench, Electroweak interactions, Standard Model, Large Hadron Collider, W-boson, Statistics*
Abstract: This thesis presents the work on the production and the qualification of the ATLAS NSW Micromegas Large Modules 1 (LM1), as well as the measurements of the W-boson transverse momentum and the W-boson mass using low pile-up data recorded by ATLAS at center-of-mass energies of $\sqrt{s}$ =5.02 and 13 TeV. Detailed protocols and results of the cosmic bench characterization for the LM1 Micromegas modules are documented, including the preliminary tests of the improved working gas mixture which was in the end adopted for the Run 3 data taking. The physics modelling and detector calibration for the W-boson analyses using the low pile-up data are described. The data-driven estimation of the multijet background is presented, emphasizing the improvements with respect to the procedures used in the previous analyses. The measurement of the W-boson transverse momentum achieves a remarkably high precision and will become a valuable input to the W mass analysis. Based on a profile likelihood fit, the framework of statistical analysis for the low pile-up W mass measurement has been studied and optimized. Benefiting from the detector calibration derived from the measurement of the W-boson transverse momentum, the low pile-up W mass analysis is expected to become a proof-of-concept measurement for the precise determination of the W-boson mass using future low pile-up datasets in ATLAS. Also, a coherent approach of uncertainty decomposition for profile likelihood fits is developed and illustrated for the first time.

Titre : Amélioration du spectromètre à muons et physique de précision du boson W dans ATLAS
Mots clés : *MPGD, Micromegas, ATLAS, NSW, Banc cosmique, Interactions électrofaibles, Modèle standard, Grand collisionneur de hadrons, boson W, Statistiques*
Résumé : Cette thèse présente les travaux sur la production et la qualification des modules NSW Micromegas "Large Modules 1" (LM1) de l'expérience ATLAS, ainsi que les mesures de l'impulsion transverse du boson W et de la masse du boson W à l'aide de données à faible empilement enregistrées par ATLAS à des énergies dans le centre de masse de $\sqrt{s}$ =5.02 et 13 TeV. Les protocoles et les résultats détaillés de la caractérisation du banc cosmique pour les modules Micromegas LM1 sont documentés, y compris les tests préliminaires avec un mélange gazeux qui aboutit à des performances améliorées et qui a finalement été adopté pour la prise de données du Run 3. La modélisation physique et l'étalonnage du détecteur pour les analyses du boson W à l'aide des données à faible empilement sont décrits. L'estimation basée sur les données du fond multijet est présentée, en soulignant les améliorations par rapport aux procédures utilisées dans les analyses précédentes. La mesure de l'impulsion transverse du boson W atteint une précision remarquablement élevée et deviendra une donnée précieuse pour l'analyse de la masse du boson W. Sur la base de l'ajustement par maximum de vraisemblance profilé, le cadre d'analyse statistique pour la mesure de la masse du boson W à faible empilement a été étudié et optimisé. Bénéficiant de l'étalonnage du détecteur obtenu pour la mesure de l'impulsion transverse du boson W, l'analyse de masse du boson W à faible empilement devrait devenir une preuve de concept pour la détermination précise de la masse du boson W à l'aide de futures données à faible empilement dans ATLAS. En outre, une approche cohérente de la décomposition de l'incertitude pour l'ajustement par maximum de vraisemblance profilé est développée et illustrée pour la première fois.

Synthèse en français

La physique des particules a pour sujet d'études les particules élémentaires et les interactions de l'univers. La compréhension la plus récente et la plus complète de cette discipline est résumée dans le Modèle Standard de la physique des particules, qui est de loin l'une des théories les plus réussies de la physique moderne. Le Modèle Standard est une théorie quantique des champs comprenant trois générations de fermions et les forces fondamentales qui agissent entre eux : l'interaction électromagnétique, l'interaction faible et l'interaction forte, chaque interaction étant médiée par les bosons correspondants. De plus, le mécanisme de Brout-Englert-Higgs (BEH) et la théorie de la brisure spontanée de symétrie expliquent comment les particules acquièrent leurs masses et prédisent l'existence du boson de Higgs, qui a été découvert lors d'expériences en 2012. Dans le secteur électrofaible du Modèle Standard, le boson W est le boson vecteur qui transporte l'interaction faible de courant chargé. La masse du boson W est un paramètre crucial du Modèle Standard. Elle peut être déterminée théoriquement à partir de la masse du boson Z, de la constante de structure fine et de la constante de Fermi à l'ordre le plus bas, tout en recevant des corrections d'ordre supérieur des autres particules du Modèle Standard, en particulier du quark top et du boson de Higgs. Bien que la masse du W puisse être mesurée expérimentalement, sa précision est néanmoins inférieure à celle de l'ajustement électrofaible global, la prédiction théorique. De plus, il existe une tension d'environ un écart type entre la moyenne mondiale des mesures directes et la détermination indirecte fournie par l'ajustement électrofaible global. Il est donc très important d'améliorer davantage la mesure directe de la masse du W, car toute divergence entre la mesure directe et la prédiction théorique constituerait une indication claire de nouvelle physique. De plus, dans le contexte de l'ajustement électrofaible global, le pouvoir d'exclusion d'une nouvelle physique au-delà du Modèle Standard est actuellement limité par la précision des mesures directes de la masse du W. Pour les deux raisons mentionnées ci-dessus, il est nécessaire de réaliser davantage et de meilleures mesures de la masse du W afin de faciliter le test de la cohérence globale du Modèle Standard.

La masse du boson W a été mesurée depuis sa découverte. Aux collisionneurs proton-proton, le boson W peut être produit par l'annihilation d'un quark et d'un autre quark de saveur différente à l'ordre le plus bas. L'extraction de la masse du boson W est basée sur les mesures des produits de la désintégration leptonique du boson W. Cependant, le neutrino produit par la désintégration ne peut être mesuré par le détecteur, ce qui induit une difficulté sur la modélisation théorique pour la mesure de la masse du boson W. En particulier, la modélisation de l'impulsion transverse du boson W (p_{T}^{W}), un spectre non nul induit par les radiations dans l'état initial (ISR) de la QCD, a été signalée comme une source majeure d'incertitude systématique dans les mesures précédentes de la masse du boson W. Une nouvelle stratégie de mesure a été conçue, dont les détails sont couverts dans la thèse, impliquant une mesure

directe du spectre p_{T}^{W} afin de contraindre les sources d'incertitudes systématiques correspondantes.

Les travaux documentés dans cette thèse bénéficient des données obtenues à partir du détecteur ATLAS du Grand Collisionneur de Hadrons (LHC). Le LHC est jusqu'à présent l'outil le plus puissant de la recherche en physique des particules. Le LHC est conçu pour faire entrer en collision des faisceaux de protons avec une énergie de centre de masse pouvant atteindre 14 TeV et peut atteindre une luminosité instantanée sans précédent de $10^{3}4\mathrm{cm}^{-2}\mathrm{s}^{-1}$. Il s'agit d'un accélérateur de hadrons supraconducteur à deux anneaux installés dans un tunnel d'une circonférence de 26,7 km. ATLAS, l'une des quatre principales expériences du LHC, est un détecteur de particules cylindrique polyvalent avec une symétrie avant-arrière. Les sous-systèmes du détecteur comprennent le détecteur de traces interne (ID), les calorimètres électromagnétiques et hadroniques, ainsi que le spectromètre à muons. Le point de collision est entouré par l'ID, puis enveloppé par un solénoïde supraconducteur générant un champ magnétique axial de 2 T. L'ID est capable de fournir des mesures précises des traces de particules chargées dans la plage de pseudorapidité inférieure à 2,5. Le système ID est composé d'un détecteur de pixels en silicium, d'un détecteur à microbandes en silicium et d'un détecteur de traces à rayonnement de transition. Ces trois sous-détecteurs sont disposés selon une géométrie coaxiale autour de l'axe du faisceau. Le calorimètre électromagnétique couvre la région de pseudorapidité inférieure à 3,2 et est basé sur une technologie d'échantillonnage plomb/argon liquide à haute granularité. Le calorimètre hadronique adopte la technologie en acier/scintillateur-tuile dans la région de pseudorapidité inférieure à 1,7 et la technologie cuivre/argon liquide dans la région de pseudorapidité entre 1,5 et 3,2. De plus, le calorimètre avant couvre la plage de pseudorapidité entre 3,2 et 4,9, avec l'argon liquide comme matériau actif et des absorbeurs en cuivre ou en tungstène pour les parties électromagnétiques et hadroniques, respectivement. Le système de détecteur le plus externe de l'ATLAS est le spectromètre à muons (MS), composé de chambres de déclenchement séparées et de chambres de suivi de haute précision pour mesurer la déviation des muons dans un champ magnétique fourni par trois grands toroïdes supraconducteurs. Ces toroïdes sont disposés avec une symétrie de bobine azimutale à huit voies autour des calorimètres. Les chambres de suivi permettent de suivre les muons dans la plage de pseudorapidité inférieure à 2,7, tandis que le système de déclenchement des muons couvre la région de pseudorapidité inférieure à 2,4. La sélection des événements dans ATLAS est effectuée en temps réel par un système de déclenchement à deux niveaux. Le déclenchement de premier niveau basé sur le matériel recherche des signatures spécifiques des détecteurs. Le déclenchement de haut niveau basé sur les logiciels utilise des algorithmes pour améliorer la sélection du déclenchement et réduire la fréquence des déclenchements.

Pour aider aux mesures de précision électrofaibles, ATLAS a pris des ensembles de données spécifiques lors du Run 2 avec un empilement moyen d'environ 2, à des énergies de centre de masse de 5,02 et 13 TeV. Les mesures de précision électrofaibles, telles que la mesure du spectre p_{T}^{W} et la masse du W, bénéficient de l'amélioration en résolution du détecteur et de la réduction du bruit de fond QCD apportées par les conditions de faible empilement. Malgré la faible luminosité intégrée des ensembles de données à faible empilement, les grandes sections efficaces de production des particules W et Z offrent suffisamment de statistiques pour les analyses de physique pertinentes.

Une campagne de simulation dédiée a été lancée pour correspondre aux conditions

de faible empilement dans les données pour le processus de signal, le bruit de fond lié au quark top et le bruit de fond électrofaible. Le processus de signal est considéré dans huit canaux pour les analyses du boson W, répartis par énergie de centre de masse, charge du boson et saveur du lepton. Les activités d'empilement sont simulées par des échantillons d'événements à biais minimal. Dans la sélection des candidats boson W, exactement un électron ou un muon doit être reconstruit, identifié et isolé, tout en correspondant au lepton du système de déclenchement. Le moment transverse du lepton doit être supérieur à 25 GeV. Des coupures cinématiques supplémentaires sont appliquées à la masse transverse du W et à l'énergie transverse manquante du neutrino, dans le but d'améliorer le rejet du bruit de fond QCD. Le bruit de fond QCD, également connu sous le nom de bruit multijet, est estimé par une méthode basée sur les données, comprenant l'estimation du nombre d'événements et l'extrapolation de la forme des distributions cinématiques. Pour l'estimation du nombre d'événements, une région d'ajustement est construite en relâchant la coupure cinématique de la sélection nominale (région de signal), de sorte que le pic cinématique du bruit de fond multijet soit récupéré, ce qui facilite une détermination précise de la fraction multijet à l'aide d'une méthode d'ajustement par modèle. L'impact de la relaxation des coupes cinématiques peut être évalué par le rapport d'événements multijets dans deux régions de contrôle enrichies en multijets, dont chacune correspond aux coupes cinématiques de la région de signal et de la région d'ajustement, mais avec une exigence d'isolation du lepton inversée. Une extrapolation du rendement vers la région de signal est réalisée avec quatre intervalles anti-isolés consécutifs dans les régions de contrôle pour prendre en compte la dépendance vis-à-vis de l'isolation du lepton. La cible de l'extrapolation du nombre d'événements multijets dans la région de signal est estimée à partir des échantillons MC de désintégration des quarks de saveur lourde dans les canaux muoniques, puis prise comme référence pour les canaux muoniques et électroniques. La forme du bruit de fond multijet dans la région de signal est extrapolée à partir de la région de contrôle en supposant une dépendance linéaire vis-à-vis de l'isolation du lepton. Par rapport aux analyses précédentes, l'estimation du bruit de fond multijet a été améliorée en introduisant une correction d'isolation au recul hadronique pour tenir compte du biais causé par la procédure standard de reconstruction. Une deuxième amélioration a été introduite, des corrections de forme sont appliquées aux modèles de la région de contrôle pour l'ajustement de fraction afin de tenir compte de la dépendance de la forme du modèle vis-à-vis de l'isolation du lepton. La convergence de l'estimation du nombre d'événements multijet basée sur différentes observables est améliorée après la mise en œuvre de la correction d'isolation du recul hadronique et de la correction de forme du modèle. L'incertitude statistique due à la taille finie de l'échantillon utilisé dans l'extrapolation de la forme multijet, ainsi que l'incertitude systématique associée à la méthodologie d'estimation du nombre d'événements et d'extrapolation de la forme, sont prises en compte et propagées à la chaîne d'analyse.

La section efficace différentielle de production et de désintégration du boson W peut être factorisée en 5 termes : le pic de résonance du boson qui peut être décrit par une distribution de Breit-Wigner, la rapidité du boson, l'impulsion transverse (p_{T}) du boson à rapidité donnée, et les distributions angulaires des produits de désintégration qui sont influencées par les états de polarisation du boson. Les corrections physiques pour les analyses du boson W comprennent la correction de l'efficacité de sélection du vertex simulé, la radiation dans l'état final (FSR) de la QED, la polarisation du

boson et une correction de modélisation du p_{T} du boson basée sur les données, selon laquelle les distributions sous-jacentes du p_{T} du boson prises à partir du générateur d'événements sont réajustées par des fonctions de p_{T} pour optimiser l'accord entre les données et le MC au niveau reconstruit.

Les principaux objets physiques utilisés dans les analyses du boson W à bas empilement sont les électrons, les muons et le recul hadronique. Pour la reconstruction des vertex primaires, au moins deux traces de particules chargées associées sont requises. Le vertex primaire ayant la somme quadratique des p_{T} de toutes les traces associées la plus élevée est considéré comme le vertex de diffusion dure. Un électron est défini comme un objet provenant du vertex primaire et comprenant un amas construit à partir des dépôts d'énergie dans le calorimètre et une trace correspondante ou plusieurs traces dans le détecteur interne (ID). La sélection des électrons comprend la reconstruction, l'identification, l'isolation et le système de déclenchement. Les différences entre les données et la simulation pour ces efficacités de sélection sont corrigées par des facteurs d'échelle avec les incertitudes correspondantes. L'extraction de l'échelle et de la résolution de l'énergie des électrons utilise les techniques standard d'ATLAS. Un objet muon est combiné à partir des reconstructions du muon effectuées indépendamment dans l'ID et dans le spectromètre à muons (MS). Les muons doivent satisfaire aux critères de reconstruction, d'association trace-vertex, d'isolation et de déclenchement. Les efficacités de sélection sont également corrigées par des facteurs d'échelle avec des incertitudes. La calibration du muon implique les corrections de l'échelle et de la résolution du moment, ainsi que du biais de flèche. La stratégie générale de calibration des leptons pour les analyses du boson W à bas empilement consiste à extrapoler les résultats à haut empilement aux conditions de faible empilement chaque fois que cela est applicable. Sinon, les calibrations in situ sont réalisées en utilisant les techniques standard d'ATLAS. Le recul hadronique mesure les sommes vectorielles et scalaires de toutes les particules issues de la radiation des gluons et des quarks de l'état initial. Il est calculé à l'aide d'un algorithme basé sur les Particle Flow Objects (PFOs). La calibration du recul hadronique est réalisée à l'aide d'événements Z in situ, ce qui permet de corriger les erreurs de modélisation de l'événement sous-jacent, de la direction, de la réponse et de la résolution.

La mesure du p_{T}^{W} à bas empilement est principalement motivée par les besoins de la mesure de la masse du boson W. Dans la région de faible p_{T} où les bosons W sont principalement produits, le spectre en p_{T}^{W} ne peut pas être calculé de manière fiable en utilisant uniquement la QCD perturbative. Soit une resommation analytique, soit une cascade de partons est utilisée pour faire converger le calcul de la section efficace différentielle. Dans le passé, la modélisation de p_{T}^{W} dans la simulation était effectuée par une cascade de partons, dont les paramètres étaient ajustés à partir du spectre bien mesuré de l'impulsion transverse du boson Z (p_{T}^{Z}). Cependant, en raison des échelles d'énergie légèrement différentes impliquées dans la production des bosons W et Z, ainsi que de la participation différente des quarks de saveur lourde dans l'état initial, l'extrapolation souffre d'une grande incertitude systématique. Grâce aux conditions de faible empilement, la distribution de p_{T}^{W} peut être mesurée avec une granularité de 7 GeV dans la région de bas p_{T}, avec une incertitude totale de l'ordre de 1.5 à 2 pour cent, ce qui permettra de contraindre efficacement la modélisation du p_{T} du boson dans la simulation de la production du boson W. Dans la désintégration leptonique du boson W, en raison de la non-détection du neutrino, le spectre en p_{T}^{W} est déduit de la mesure de la distribution du recul hadronique en appliquant la déconvolution

bayésienne itérative, qui corrige les effets d'acceptance et de résolution du détecteur. Afin d'éviter de grandes incertitudes de déconvolution, l'estimation initiale de la distribution sous-jacente de p_{T}^{W} dans la simulation est pondérée par une fonction de p_{T}^{W}, afin d'obtenir un accord optimisé entre les données et la simulation au niveau reconstruit. Des incertitudes de biais sont attribuées à cette pondération de p_{T}^{W}, en tenant compte des incertitudes de l'ajustement des paramètres de la fonction de pondération, de l'arbitraire du choix de la forme de la fonction et de la possible mauvaise modélisation de la corrélation entre le p_{T} et la rapidité du boson dans le générateur MC par défaut. Les variations des deux dernières composantes d'incertitude sont également nécessaires pour obtenir un bon accord entre les données et la simulation au niveau reconstruit. Après l'évaluation de l'incertitude de biais, l'optimisation de la déconvolution est réalisée pour la largeur des bins au niveau déconvolué, et le nombre d'itérations de déconvolution. La ligne directrice de l'optimisation est de conserver une résolution raisonnable du spectre obtenu, tout en maintenant l'incertitude totale et l'incertitude de biais aussi faibles que possible. En fin de compte, une largeur de bin de 7 GeV est choisie pour la déconvolution de la distribution de p_{T}^{W} à la fois à 5,02 TeV et à 13 TeV. Le nombre optimal d'itérations de déconvolution est déterminé à 9 pour 5,02 TeV et à 25 pour 13 TeV. Les distributions mesurées de p_{T}^{W} sont combinées dans les canaux électroniques et muoniques, en tenant compte des incertitudes systématiques corrélées. Les mesures des sections efficaces différentielles, des sections efficaces intégrées et des rapports de sections efficaces sont présentées et comparées à différentes prédictions théoriques.

La mesure de la masse du boson W à bas empilement bénéficie de l'étalonnage du détecteur de la mesure du p_{T}^{W} à bas empilement. Traditionnellement, les mesures de la masse du boson W aux collisionneurs hadroniques sont basées sur une méthode de χ^2, dans laquelle des modèles de distributions cinématiques avec différentes valeurs hypothétiques de la masse du boson W sont générés et comparés aux données. Le modèle qui est le plus proche des données indique la valeur la plus probable de la masse du boson W. L'incertitude statistique est dérivée de la courbure de la valeur du χ^2 entre les données et les modèles. Les incertitudes systématiques sont estimées via une procédure similaire en remplaçant les données par des pseudo-données obtenues à partir des variations systématiques et en calculant la différence en masse ajustée du boson W causée par les variations. L'incertitude statistique et les incertitudes systématiques sont ajoutées en quadrature pour donner l'incertitude totale de la mesure. En tant que méthode améliorée d'inférence statistique, l'ajustement profilé du maximum de vraisemblance décrit la distribution de l'observable en paramétrant l'effet du changement de la masse du boson W et des variations systématiques dans un modèle de probabilité unique, de sorte que le petit biais causé par les variations systématiques puisse être corrigé dans les données et que les incertitudes systématiques puissent être contraintes par la puissance des statistiques des données. Par conséquent, on s'attend à ce que l'ajustement profilé du maximum de vraisemblance donne un résultat plus précis que la simple méthode du χ^2 non profilé. Les modèles pour la mesure de la masse du boson W sont généralement générés pour les distributions au niveau reconstruit de la masse transverse W (m_{T}), du p_{T} du lepton et des distributions d'énergie transverse manquante du neutrino. La mesure de la masse du boson W à bas empilement utilise principalement m_{T} comme observable, car c'est l'observable la plus sensible à la masse du boson W parmi les trois choix précédents dans les conditions de faible empilement. Une catégorisation basée sur le

recul hadronique et la pseudorapidité du lepton est introduite dans la mesure, afin de contraindre les incertitudes de modélisation, telles que la distribution de p_{T}^{W} et la fonction de distribution de partons (PDF). Un changement de PDF dans la simulation est obtenu au niveau reconstruit en pondérant les distributions cinématiques de la PDF de référence par défaut CT10 vers une nouvelle PDF de référence plus moderne : CT18ANNLO. Des efforts ont été faits pour améliorer l'ajustement profilé du maximum de vraisemblance pour la masse du boson W, en particulier en ce qui concerne la simplification du modèle de probabilité. Le nombre de paramètres de nuisance dans le modèle de probabilité est réduit en suivant une analyse en composantes principales standard, tandis que l'incertitude statistique du MC est prise en compte en utilisant la prescription conventionnelle de Barlow-Beeston-Lite. Les performances de l'ajustement profilé du maximum de vraisemblance en termes de consommation de temps CPU sont largement améliorées après la simplification du modèle de probabilité sans affecter la précision du résultat de l'ajustement. Des études préliminaires sont menées pour comprendre la faisabilité de la combinaison d'observables statistiquement corrélés dans le contexte de l'ajustement profilé du maximum de vraisemblance. En particulier, une nouvelle observable, combinaison linéaire de m_{T} et du p_{T} du lepton est proposée, dont le coefficient de combinaison doit être optimisé à l'aide de simulations. Malgré l'introduction de complications supplémentaires dans l'analyse statistique, il est constaté que la nouvelle observable est plus sensible à la masse du boson W que m_{T} ou le p_{T} du lepton seul. Le fond multi-jets pour l'analyse de la masse du boson W à bas empilement est obtenu en utilisant une méthode similaire à l'analyse du p_{T}^{W} à bas empilement. L'extrapolation de la forme du fond multi-jets est ajustée pour devenir plus stable pour les statistiques plus faibles par bin d'analyse dans la mesure de la masse du boson W en raison de la catégorisation. Les incertitudes du p_{T}^{W} issues de la mesure directe sont propagées à l'ajustement préliminaire de la masse du boson W. Les variations du p_{T}^{W} sont d'abord déduites de la diagonalisation de la matrice de covariance au niveau déconvolué. Ensuite, les spectres sous-jacents de p_{T}^{W} dans la simulation sont pondérés par ces variations, ce qui permet de propager les incertitudes du p_{T}^{W} de la mesure aux distributions cinématiques au niveau reconstruit utilisées pour l'ajustement de la masse du boson W. Bien que la propagation des incertitudes effectuée de cette manière soit inclusive en termes de rapidité du boson et ne tienne pas compte de la corrélation entre les deux analyses, on s'attend à ce qu'elle offre une estimation approximativement correcte du niveau d'incertitude du p_{T}^{W} dans la mesure de la masse du W. Avec toutes les incertitudes disponibles incluses dans le modèle de probabilité de l'ajustement préliminaire de la masse du boson W, l'ajustement profilé du maximum de vraisemblance a été réalisé dans les canaux individuels et dans un ajustement conjoint de tous les canaux. Une décomposition dédiée des incertitudes est appliquée aux résultats de l'ajustement. L'incertitude sur la PDF et l'incertitude sur la modélisation du p_{T}^{W} sont estimées être réduites par rapport à la mesure précédente de la masse du boson W réalisée par ATLAS. Si une longue période de prise de données à bas empilement peut être réalisée pendant la période du Run 3, une mesure de la masse du boson W par ATLAS avec une précision au niveau de 10 MeV est possible.

Une approche cohérente de décomposition des incertitudes pour l'ajustement profilé du maximum de vraisemblance est développée et illustrée dans la thèse. Le fondement de cette méthode repose sur le fait que le résultat de l'ajustement profilé du maximum de vraisemblance dépend uniquement des données d'entrée et des observ-

ables globaux, ces derniers étant fournis par les mesures auxiliaires. Par conséquent, la valeur post-ajustement du paramètre d'intérêt (POI) dans le modèle de probabilité peut être exprimée comme une fonction des données et des observables globaux. Par conséquent, l'incertitude sur le POI suit la formule standard de propagation des erreurs. En fluctuant les données à l'aide de la méthode de bootstrap tout en laissant tout le reste inchangé dans le modèle de probabilité, l'écart des résultats de l'ajustement correspond à l'incertitude statistique de l'ajustement profilé du maximum de vraisemblance. De même, en fluctuant chaque observable global selon la forme de la mesure auxiliaire correspondante, l'écart des résultats de l'ajustement donne la contribution de la source systématique. De manière équivalente, il est également possible de modifier l'observable global d'un écart type dans le modèle et d'estimer ainsi l'incertitude systématique correspondante comme étant la différence dans le résultat de l'ajustement. Il peut être vérifié que la somme quadratique des sources d'incertitude décomposées via la procédure décrite ci-dessus reproduit l'incertitude totale renvoyée par l'ajustement profilé du maximum de vraisemblance. Des exemples numériques sont fournis pour l'illustration et la validation de cette approche de décomposition des incertitudes. L'ajustement de la masse du boson W à bas empilement utilise cette méthode de décomposition des incertitudes pour la présentation des résultats.

La luminosité croissante du LHC exige le remplacement des extrémités du spectromètre à muons d'ATLAS par les "New Small Wheel" (NSW) équipées de détecteurs utilisant des technologies améliorées, en particulier les sTGC et Micromegas. Micromegas est un type populaire de détecteurs gazeux à micro-patterns (MPGD). Le volume de gaz du Micromegas est divisé de manière asymétrique par une grille métallique en deux espaces. Lorsqu'une particule chargée traverse l'espace de conversion, des électrons libres sont ionisés à partir du gaz de travail et dérivent vers l'espace d'amplification guidés par le champ électrique. Une fois les électrons libres passés à travers la grille, le champ électrique devient beaucoup plus fort. Par conséquent, une multiplication des électrons libres se produit, induisant des signaux sur les bandes de lecture. Le Micromegas NSW est conçu pour supporter un taux de déclenchement élevé de 15 kHz/cm^2 tout en maintenant une précision spatiale élevée, avec une résolution de 100 microns par couche de détection. Sur NSW, les modules Micromegas fonctionnent principalement comme des détecteurs de traces et sont complémentaires aux modules sTGC. Les deux types de détecteurs forment une structure en sandwich sTGC-Micromegas-Micromegas-sTGC pour chaque secteur. Parmi les quatre types de modules Micromegas installés sur NSW, tous les modules larges de bas rayon (LM1) ont été produits et qualifiés à Saclay. Chaque module Micromegas LM1 comprend quatre couches de détection. La direction des bandes de lecture est perpendiculaire à la pseudorapidité sur deux couches de détection. Sur les deux autres couches, les bandes de lecture sont approximativement alignées parallèlement aux deux premières couches, mais avec un angle incliné de $\pm$1,5 degré, de sorte que les quatre couches de détection puissent fonctionner ensemble et reconstruire entièrement la trajectoire de la particule chargée incidente. Il y a 5 panneaux PCB par couche de détecteur dans un module Micromegas LM1, chaque panneau étant séparé en deux moitiés pour l'alimentation en haute tension. Le gaz de travail par défaut du Micromegas NSW a initialement été décidé comme étant composé de 93% d'argon et de 7% de CO2. Après la production de chaque module LM1, il a été testé sur un banc cosmique à Saclay pour sa caractérisation. Le banc cosmique à Saclay est équipée de 3 couches de détecteurs bidimensionnels en tant que détecteurs de traces externes, capables de

fournir une reconstruction indépendante de la trajectoire du muon cosmique en tant que référence pour le module LM1. Les détecteurs de traces externes fonctionnent avec un mélange gazeux de 95% d'argon et de 5% d'isobutane fourni par un système de gaz indépendant. L'électronique de lecture sur le banc cosmique est l'électronique DREAM. Le principal défi de la caractérisation du banc cosmique réside dans le grand nombre de bandes de lecture (environ 20 000) à tester par module LM1. Afin d'accélérer la prise de données, un canal électronique est connecté à deux bandes de lecture à l'aide d'un adaptateur de multiplexage spécialement conçu, de sorte que la granularité du module LM1 soit conservée pendant la prise de données. Aucune dégradation significative due à la lecture multiplexée n'est observée dans les conditions de fonctionnement nominal du module LM1 lors des tests sur banc cosmique. L'analyse des données des rayons cosmiques commence par la soustraction des bruits de fond des signaux numériques. Ces signaux sont ensuite corrigés pour former une carte de réponse de tous les canaux électroniques, qui est ensuite traduite en positions reconstruites des amas d'électrons par couche de détection grâce à un algorithme de démultiplexage. Ensuite, les amas reconstruits sont comparés à la trajectoire des muons prédite par les détecteurs de traces externes pour révéler l'efficacité du module LM1 avec une granularité fine. La principale sortie de la caractérisation du banc cosmique est la carte d'efficacité et de charge sur chaque couche de détection. La carte de charge peut être utilisée pour calculer le gain global du détecteur, estimé à environ 8000. Les cartes d'efficacité et de charge ont été surveillées pendant toute la période de production de tous les modules LM1. De plus, la perte d'efficacité causée par les interconnexions mécaniques dans les modules LM1 a également été étudiée par l'analyse des données cosmiques, qui s'est avérée plusieurs fois plus importante que l'effet géométrique. La résolution spatiale intrinsèque du module Micromegas LM1 a été mesurée sur le banc cosmique après l'alignement amélioré des détecteurs de traces externes et la mise en œuvre de la correction de l'angle du muon cosmique. Le résultat final de la mesure est de 110 microns par couche de détection, ce qui est conforme aux spécifications du rapport de conception technique de NSW. Un mélange gazeux de travail amélioré pour le Micromegas NSW a été proposé par Saclay, remplaçant le mélange gazeux par défaut par 93% d'Ar, 5% de CO2 et 2% d'iso-C4H10. Les performances des modules LM1 utilisant le mélange gazeux amélioré ont été mesurées lors du test sur banc cosmique, ce qui montre que les secteurs faibles susceptibles de voir apparaitre des étincelles peuvent être en grande partie récupérés tandis que l'efficacité des autres secteurs n'est pas affectée. Aucun effet de vieillissement significatif dû à la présence d'iso-C4H10 dans le mélange gazeux n'a été observé jusqu'à présent. En fin de compte, le mélange gazeux amélioré a été adopté par la collaboration ATLAS et choisi comme gaz de travail pour le Micromegas NSW pour la prise de données du Run 3. Les NSW ont été installés, mis en service et sont opérationnels lors de la prise de données du Run 3.

Pour conclure, cette thèse présente les travaux sur la production et la qualification des modules NSW Micromegas LM1 de l'expérience ATLAS, ainsi que les mesures de l'impulsion transverse du boson W et de la masse du boson W à l'aide de données à faible empilement enregistrées par ATLAS à des énergies dans le centre de masse de 5.02 et 13 TeV. Les protocoles et les résultats détaillés de la caractérisation du banc cosmique pour les modules Micromegas LM1 sont documentés, y compris les tests préliminaires avec un mélange gazeux qui aboutit à des performances améliorées et qui a finalement été adopté pour la prise de données du Run 3. La modélisation

physique et l'étalonnage du détecteur pour les analyses du boson W à l'aide des données à faible empilement sont décrits. L'estimation basée sur les données du fond multijet est présentée, en soulignant les améliorations par rapport aux procédures utilisées dans les analyses précédentes. La mesure de l'impulsion transverse du boson W atteint une précision remarquablement élevée et deviendra une donnée précieuse pour l'analyse de la masse du boson W. Sur la base de l'ajustement par maximum de vraisemblance profilé, le cadre de l'analyse statistique pour la mesure de la masse du boson W à faible empilement a été étudié et optimisé. Bénéficiant de l'étalonnage du détecteur obtenu pour la mesure de l'impulsion transverse du boson W, l'analyse de masse du boson W à faible empilement devrait devenir une preuve de concept pour la détermination précise de la masse du boson W à l'aide de futures données à faible empilement dans ATLAS. En outre, une approche cohérente de la décomposition de l'incertitude pour l'ajustement par maximum de vraisemblance profilé est développée et illustrée pour la première fois.

Contents

Introduction

Particle physics, as the center of our understanding of the fundamental laws of nature, studies the basic constituents and interactions of our universe, which concern the elementary particles and the forces between them. As a discipline of experimental science, the development of particle physics relies on the progress on both the theoretical side and the experimental side. While efforts have been constantly made to explore the possibility of extending our current understanding of particle physics, the experimental research of particle physics are also carried out based on various foundations, including the measurement of neutrino properties [1], the detection of cosmic ray [2] and the experiments at colliders [3], [4].

Ever since the discovery of the Higgs boson [5], [6] in 2012 declaring the completion of the Standard Model of particle physics (SM), no smoking gun proof has yet been found regarding the possible existence of new elementary particles and interactions beyond the SM. However, the lack of new discovery hardly marks the end of the particle physics, but on the contrary, as eminent physicist Albert Abraham Michelson, Nobel Prize laureate known for his work on the measurement of the speed of light and especially for the famous Michelson-Morley experiment, once remarked:

"The future truths of physical science are to be looked for in the sixth place of decimals."

The future of particle physics counts on precision measurement, indeed. One important parameter in the SM that needs to be precisely measured at the moment is the mass of the W-boson (m_W), since any discrepancy between the precisely calculable SM prediction and the results of the experimental measurements will be a strong indication of new physics. The W-boson is an elementary particle in the SM as the mediator of the electrically-charged weak interaction. The measurement of m_W started from the discovery of the W-boson in 1983 [7], and has been performed in various experimental conditions. However, considering that the most up-to-date world average result of direct m_W measurements is still less precise than the state-of-the-art SM prediction and that there is a discrepancy of around one standard deviation between the two quantities, more efforts have to be continually spent on the determination of m_W from the experimental side. Furthermore, the recently released CDF II result has achieved the best precision so far as a single measurement, but revealed a significant tension with the SM prediction [8], which calls for urgent needs for more and better m_W measurements at other experiments as crucial validations. As one frontier of experimental particle physics, the ATLAS experiment [9] located at the Large Hadron Collider (LHC) [10] benefits from the stably controlled collisions of the proton beams happening at high energies and high rates, as well as its advanced particle detection system and full coverage of the azimuthal angle, making it a highly competitive platform for carrying out precision measurements of m_W and other W-boson properties. With the increasing luminosity at LHC, the ATLAS detector has to be upgraded accordingly so as to better exploit its physics potential for both precision measurement and searches of new physics. During the last long shut-down of LHC, the inner end-cap of the ATLAS muon system has been upgraded to the New Small Wheels (NSWs) [11]. The ATLAS NSWs are equipped with detectors made of improved technologies, specifically sTGC [12] and Micromegas [13]. In ATLAS, the muons not only carry important kinematic information that helps reveal the interactions happening during the proton-proton collisions, but also provides clean signature

for event triggering. The NSW upgrade is expected to enhance the background rejection for the triggering of the muon system and keep the precision tracking of the muons.

The work of this thesis is dedicated to the detector upgrade of the ATLAS experiment and the precision measurement of the W-boson physics at ATLAS using specialized datasets. The thesis is structured in the following way: The basic theoretical background is reviewed in Chapter 1, followed by an introduction to the LHC and ATLAS experiment in Chapter 2. Chapter 3 documents the cosmic bench qualification of the LM1 Micromegas modules for the ATLAS NSW upgrade. The discussions about precision W-boson physics start from an overview of m_W measurements in Chapter 4, then covered by Chapters 5, 6, 7 and 8 with more details. In Chapter 9, the work related to the development of the statistical method is presented, which benefits to the precision measurements at high energy physics experiments. Finally, Chapter 10 concludes the thesis.

References

[1] K. Abe *et al.*, "The t2k experiment", *Nuclear Instruments and Methods in Physics Research Section A: Accelerators, Spectrometers, Detectors and Associated Equipment*, vol. 659, no. 1, pp. 106–135, 2011, ISSN: 0168-9002. DOI: https://doi.org/10.1016/j.nima.2011.06.067. [Online]. Available: https://www.sciencedirect.com/science/article/pii/S0168900211011910 (cit. on p. 2).

[2] S. Ting, "The alpha magnetic spectrometer on the international space station", *Nuclear Physics B - Proceedings Supplements*, vol. 243-244, pp. 12–24, 2013, Proceedings of the IV International Conference on Particle and Fundamental Physics in Space, ISSN: 0920-5632. DOI: https://doi.org/10.1016/j.nuclphysbps.2013.09.028. [Online]. Available: https://www.sciencedirect.com/science/article/pii/S0920563213005525 (cit. on p. 2).

[3] R. Bailey, C. Benvenuti, S. Myers, and D. Treille, "The lep collider", *Comptes Rendus Physique*, vol. 3, no. 9, pp. 1107–1120, 2002, ISSN: 1631-0705. DOI: https://doi.org/10.1016/S1631-0705(02)01402-0. [Online]. Available: https://www.sciencedirect.com/science/article/pii/S1631070502014020 (cit. on p. 2).

[4] S. Holmes, R. S. Moore, and V. Shiltsev, "Overview of the tevatron collider complex: goals, operations and performance", *Journal of Instrumentation*, vol. 6, no. 08, T08001, Aug. 2011. DOI: 10.1088/1748-0221/6/08/T08001. [Online]. Available: https://dx.doi.org/10.1088/1748-0221/6/08/T08001 (cit. on p. 2).

[5] G. Aad *et al.*, "Observation of a new particle in the search for the standard model higgs boson with the atlas detector at the lhc", *Physics Letters B*, vol. 716, no. 1, pp. 1–29, 2012, ISSN: 0370-2693. DOI: https://doi.org/10.1016/j.physletb.2012.08.020. [Online]. Available: https://www.sciencedirect.com/science/article/pii/S037026931200857X (cit. on p. 2).

[6] S. Chatrchyan *et al.*, "Observation of a new boson at a mass of 125 gev with the cms experiment at the lhc", *Physics Letters B*, vol. 716, no. 1, pp. 30–61, 2012, ISSN: 0370-2693. DOI: https://doi.org/10.1016/j.physletb.2012.08.021. [Online]. Available: https://www.sciencedirect.com/science/article/pii/S0370269312008581 (cit. on p. 2).

[7] G. Arnison *et al.*, "Experimental observation of isolated large transverse energy electrons with associated missing energy at s=540 gev", *Physics Letters B*, vol. 122, no. 1, pp. 103–116, 1983, ISSN: 0370-2693. DOI: https://doi.org/10.1016/0370-2693(83)91177-2. [Online]. Available: https://www.sciencedirect.com/science/article/pii/0370269383911772 (cit. on p. 2).

[8] CDF collaboration *et al.*, "High-precision measurement of the w boson mass with the cdf ii detector", *Science*, vol. 376, no. 6589, pp. 170–176, 2022. DOI: 10.1126/science.abk1781. eprint: https://www.science.org/doi/pdf/10.1126/science.abk1781. [Online]. Available: https://www.science.org/doi/abs/10.1126/science.abk1781 (cit. on p. 2).

[9] The ATLAS Collaboration, "The ATLAS experiment at the CERN large hadron collider", *Journal of Instrumentation*, vol. 3, no. 08, S08003–S08003, Aug. 2008. DOI: 10.1088/1748-0221/3/08/s08003. [Online]. Available: https://doi.org/10.1088/1748-0221/3/08/s08003 (cit. on p. 2).

[10] L. Evans and P. Bryant, "LHC machine", *Journal of Instrumentation*, vol. 3, no. 08, S08001–S08001, Aug. 2008. DOI: 10.1088/1748-0221/3/08/s08001. [Online]. Available: https://doi.org/10.1088/1748-0221/3/08/s08001 (cit. on p. 2).

[11] T. Kawamoto, S. Vlachos, L. Pontecorvo, *et al.*, "New Small Wheel Technical Design Report", Tech. Rep. CERN-LHCC-2013-006. ATLAS-TDR-020, Jun. 2013, ATLAS New Small Wheel Technical Design Report. [Online]. Available: https://cds.cern.ch/record/1552862 (cit. on p. 2).

[12] Y. Benhammou, "Precision tracking with small-strip Thin Gap Chamber (sTGC): from Test Beam to ATLAS NSW Upgrade", *PoS*, vol. EPS-HEP2013, p. 486, 2013. DOI: 10.22323/1.180.0486 (cit. on p. 2).

[13] I. Giomataris, R. De Oliveira, S. Andriamonje, *et al.*, "Micromegas in a bulk", *Nucl. Instrum. Meth.*, vol. A560, pp. 405–408, 2006. DOI: 10.1016/j.nima.2005.12.222. arXiv: physics/0501003 [physics] (cit. on p. 2).

Chapter 1

Theoretical background

Contents

This chapter briefly illustrates the main aspects of the theoretical background of the work related to the thesis. Particularly, the theory prediction of the W-boson mass and the production mechanism of W-bosons in proton-proton colliders will be discussed.

1.1 The Standard model of particle physics

The state-of-the-art of the understanding of particle physics is condensed in the Standard Model of particle physics (SM), which is a quantum field theory that comprises three generations of quarks and leptons as well as three fundamental forces between them: the electromagnetic interaction, the weak interaction and the strong interaction. The SM follows the gauge symmetries of the unitary product group $SU(3) \times SU(2)_L \times U(1)$, while the gravity is neglected in the SM because of its tiny magnitude on the microscopic scale and consequently its negligible effect on the predictions of the SM.

An overview of the elementary particles in the SM is summarized in Fig. 1.1, where the fermions of spin 1/2 contain six quarks: up, down, charm, strange, top and bottom, while the six leptons are the electron, muon, tau, electron neutrino, muon neutrino and tau neutrino. Each of the above fermions comes with its anti-particle that are also included in the SM. The gauge bosons carry a spin of 1 and mediate interactions via the bosonic fields. The photon is the mediator of the electromagnetic interaction, the $W^{\pm}$ and Z bosons mediate the weak interaction, and the eight gluons are the mediators of the strong interaction. One scalar particle in the SM, the Higgs boson, is introduced by the mechanism of spontaneous symmetry breaking (Section 1.1.3) to explain the origin of the masses of the $W^{\pm}$ and Z bosons.

Assuming neutrinos are normal Dirac fermions, the SM has 25 free parameters that have to be set by hand [2]. They are:

— The masses of the twelve fermions.
— The three coupling constants corresponding to the strengths of the gauge interactions: α, G_F and α_S.
— The vacuum expectation value of the Higgs potential v, and the mass of the Higgs m_H.
— The eight mixing angles of the PMNS and CKM matrices.

In addition, if Charge Parity (CP) violation is allowed in the strong interaction, the strong phase θ_{CP} can be counted as the 26th free parameter of the SM, even though its value is experimentally known to be extremely small and is usually considered to be zero.

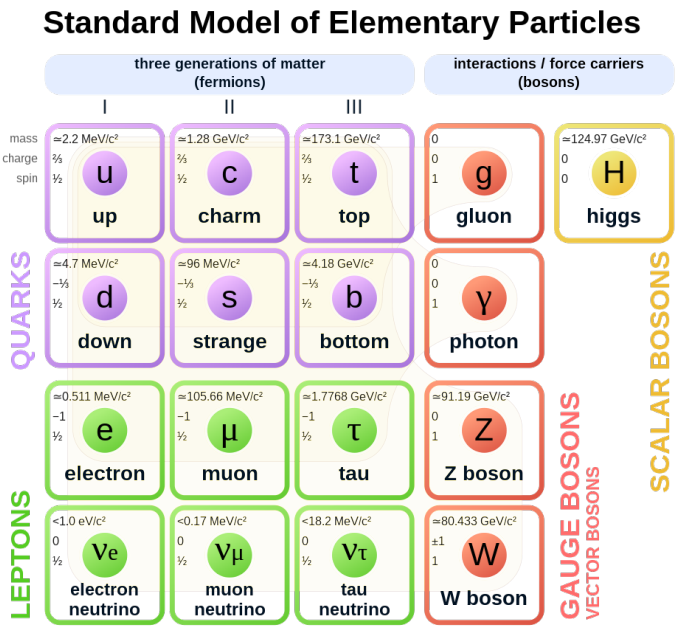

Figure 1.1 – Elementary particles of the Standard Model. (Figure from [1].)

The SM is by far the most successful theory in the domain of particle physics and represents one the triumphs of modern physics, achieving good descriptions of almost all the experimental data and the relevant phenomena. The SM has been tested by a variety of different experiments for decades. At TeV scale, the tests have been performed to a precision of typically 1 %, as shown in the example of Figure 1.2, where the SM total and fiducial production cross section measurements at ATLAS are found to be in good agreement with the theoretical calculations [3]. At lower energies, the SM has been tested to the precision of even better than 1 ppb for certain processes, such as the muon magnetic anomaly [4]. As an overview of the theoretical foundation of the work covered in this thesis, the electroweak sector of the SM (Section 1.1.1), the strong interaction sector (Section 1.1.2) of the SM and the BEH mechanism (Section 1.1.3) will be briefly summarized in the sections below, followed by an introduction to the global EW fit (Section 1.1.4).

1.1.1 The electroweak sector

Quantum field theory (QFT) is a set of ideas and tools that comprise three major themes of modern physics: quantum theory, concept of field and relativity [5]. QFT underlies particle physics and is the bridge between physics and mathematics.

Each of the fundamental forces covered in the SM can be described by QFT. In the case of electromagnetism, the theory of Quantum Electrodynamics (QED), from which QFT is established, dictates that the interactions between charged particles are mediated by the exchange of virtual photons. A virtual particle is a mathematical construct that represents the effect of summing over all possible time-ordered diagrams, and summing over the possible polarization states of the exchanged particle where it applies. The long range interaction of electromagnetic force can be described in terms of a photon exchange. Similar to the exchange of photon in QED, the weak charged-current interaction is mediated by the charged W^+ and W^- bosons, while

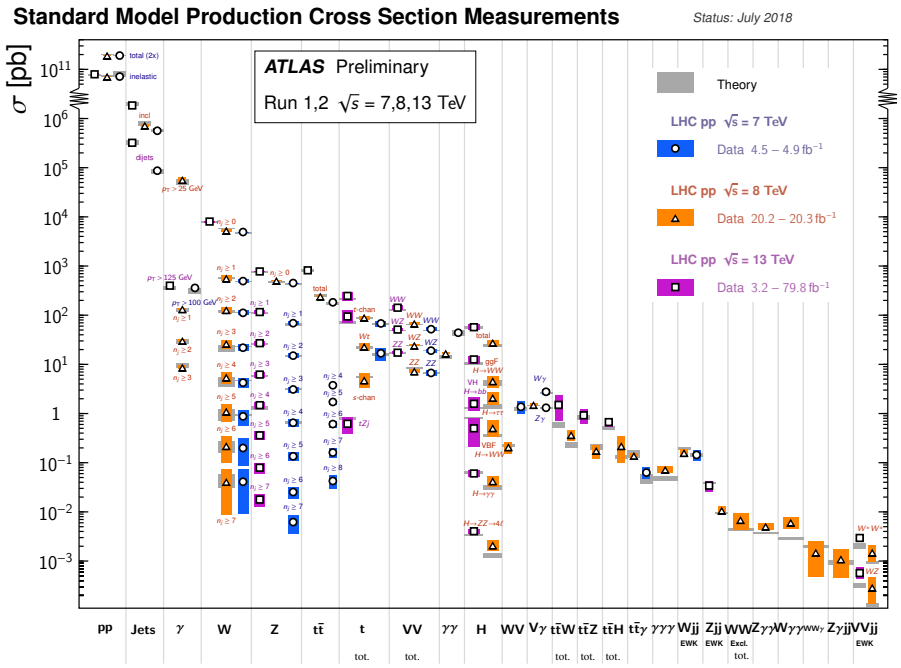

Figure 1.2 – Summary of several Standard Model total and fiducial production cross section measurements at ATLAS compared with the corresponding theoretical expectations. (Figure from [3].)

the weak neutral-current interaction is mediated by the electrically neutral Z boson.

QED is considered to be one of the most precise physical theories, of which the theoretical predictions match the experimental results up to $\mathcal{O}(10^{-11})$. QED follows the U(1) Abelian gauge symmetry and describes the electromagnetic interactions. The electromagnetic interaction is unified with the weak interaction by the electroweak (EW) theory [6]–[8], where a $SU(2)_L \times U(1)$ gauge symmetry is established, coming with four spin-1 vector bosons as the mediators: photon, W^+, W^- and Z. The generator of the U(1) group is denoted as the weak hypercharge Y, while the $SU(2)_L$ group raises three generators τ^a (a=1,2,3) built upon the Pauli matrices. The two sets of generators are linked by the relation $Y = 2(Q - \tau_3)$, where Q is the electrical charge. The Lagrangian of the EW theory can be written down as following, using the two sets of generators mentioned above:

$$\mathcal{L}_{EW} = -\frac{1}{4}W^a_{\mu\nu}W^{\mu\nu}_a - \frac{1}{4}B_{\mu\nu}B^{\mu\nu} + \sum \overline{\psi}_i\gamma^\mu(i\partial_\mu - \frac{1}{2}g'YB_\mu - \frac{1}{2}g\tau^a_L W^a_\mu)\psi \qquad (1.1)$$

Here g and g' represent the weak and electromagnetic couplings, respectively. B_μ and W^a_μ are the U(1) and SU(2) gauge fields. $B_{\mu\nu} = \partial_\mu B_\nu - \partial_\nu B_\mu$ and $W^a_{\mu\nu} = \partial_\mu W^a_\nu - \partial_\nu W^a_\mu + g\epsilon^{abc}W_{b\mu}W_{c\nu}$ are the field strength tensors. The gauge boson for the electromagnetic interaction (photon) and those three for weak interactions are formulated as the linear combinations of the gauge fields B_μ and W^a_μ:

$$A_\mu = B_\mu \cos\theta_W + W^3_\mu \sin\theta_W \qquad (1.2)$$

$$Z_\mu = -B_\mu \sin\theta_W + W^3_\mu \cos\theta_W \qquad (1.3)$$

$$W^\pm_\mu = \frac{1}{\sqrt{2}}(W^1_\mu \mp W^2_\mu) \qquad (1.4)$$

θ_W is known as the weak mixing angle, which is associated to the masses of weak gauge bosons via $\cos\theta_W = m_W/m_Z$. The U(1) symmetry dictates the photon (A_μ) to be exactly massless, leading to the equation of $e = g\sin\theta_W = g'\cos\theta_W$. e is the unit charge.

1.1.2 Strong interaction

In the SM, the strong interaction is described by the Quantum Chromodynamics (QCD) theory. The SU(3) gauge symmetry of QCD leads to the eight generators, corresponding to the eight massless gluons carrying a quantum number of color charge. The three types of color charges, denoted as red (r), green (g) and blue (b) also apply to each flavor of the quarks, such that the strong interaction is interpreted to be the exchange of gluon between quarks. The Lagrangian of QCD is written as:

$$\mathcal{L}_{QCD} = -\frac{1}{4}F^a_{\mu\nu}F^{\mu\nu}_a + \sum_{flavor}\overline{\psi}_i(i\gamma^\mu(\partial_\mu\delta_{ij} - ig_sF^a_\mu T^a_{ij}) - m_\psi\delta_{ij})\psi_j \tag{1.5}$$

ψ_i are the Dirac spinors of a quark with a color index and mass m. The F^a_μ are the eight gluon fields, T^a_{ij} are the generators of SU(3) group. Using the Gell-Mann matrices, $F^a_{\mu\nu} = \partial_\mu F^a_\nu - \partial_\nu F^a_\mu + g_s f^{abc}F^b_\mu F^c_\nu$ are the gluon field strength tensors, where the coefficients f^{abc} are the structure constants of the SU(3) group. g_s is the strong coupling constant and is universally shared by all the eight gluons. The first term of the Lagrangian describes the gluon self-interaction, due to the presence of which the strong interaction cannot become a long range interaction. The second term describes the quark-gluon interaction. The coupling constant of QCD is expressed in the form of running coupling constant $\alpha_S = g_S^2/4\pi$:

$$\alpha_S(Q^2) = \frac{12\pi}{(11n_c - 2n_f)\ln(Q^2/\Lambda^2_{QCD})} \tag{1.6}$$

Q indicates the energy scale, or in another word, the energy transferred in the interaction. n_c=3 corresponds to the number of colors involved in the interaction. n_f is the number of flavors of quarks involved in the interaction, which varies between 3 to 6 depending on the energy scale. $\Lambda_{QCD} \approx 200\,\text{MeV}$ is the QCD energy scale, below which the perturbative calculation of the QCD is no longer valid, bringing a transition from the regime of perturbative QCD to quark confinement. Based on this equation, two important features of the QCD can be derived [2]:

- Color confinement: $\alpha_S(Q^2) \to \infty$ when $Q^2 \to 0$. For $|Q| \approx 1\,\text{GeV}$, the interaction between quarks increases rapidly when they are separated in space, such that the quarks are limited to a bound state or the latter stages in the hadronization process instead of being free. Consequently, quarks can only be found in hadrons or quark-gluon-plasma (QGP). Free quarks have never been observed.
- Asymptotic freedom: $\alpha_S(Q^2) \to 0$ when $Q^2 \to \infty$. This property suggests that as long as the energy scale is high enough, i.e. $|Q| > 100\,\text{GeV}$ is the typical scale for modern high-energy colliders, the strong coupling constant drops to a sufficiently small value $\alpha_S \approx 0.1$, allowing the application of the perturbation theory. Quarks turn to quasi-free states rather than being bound in the proton. Even though the perturbative expansion of QCD (pQCD) becomes a valid

approach for the calculation of the strong interaction with asymptotic freedom, the contributions beyond the lowest order cannot be neglected, since $\alpha_S \approx 0.1$ is still not so small as the coupling constant of QED.

1.1.3 BEH mechanism and spontaneous symmetry breaking

In order to preserve the $SU(2)_L \times U(1)$ gauge symmetry in the Lagrangian of the EW interaction, all fermions and bosons are supposed to remain massless, which is contradicted by experimental facts. For this reason, the spontaneous symmetry breaking hypothesis of the BEH mechanism is introduced to help explain how the particles in EW processes gain their masses [9]–[12]. In brief, the BEH mechanism combines the EW theory with an additional Higgs field that interacts with all particles, leading to a spontaneous symmetry breaking. Therefore, one extra degree of freedom is given to each gauge boson as a finite mass. The Higgs field ϕ_H itself, is a four-component scalar field that forms a complex doublet of the weak isospin SU(2) symmetry. The Lagrangian of the Higgs part is:

$$\mathcal{L}_H = |(\partial_\mu - igW_\mu^a \tau^a - \frac{1}{2} ig' B_\mu)\phi|^2 - \mu^2 \phi^\dagger \phi - \lambda(\phi^\dagger \phi)^2 \tag{1.7}$$

τ^a are the three generators of the SU(2) symmetry. Once assuming $\lambda > 0$ and $\mu^2 < 0$, the ground state of the Higgs potential becomes non-zero but $|\phi| = \sqrt{-\mu^2/2\lambda}$. Defined by $v^2 = \frac{-\mu^2}{\lambda}$. The vacuum expectation value v sets the scales for the masses of the Higgs boson and the weak guage bosons. The mass of the Higgs boson is given by:

$$m_H = \sqrt{2\lambda} v \tag{1.8}$$

The coupling terms of ϕ to quadratic W_μ and B_μ give masses to the W and Z bosons:

$$m_W = \frac{1}{2} g v \tag{1.9}$$

$$m_Z = \frac{v}{2}\sqrt{g^2 + g'^2} = \frac{m_W}{\cos\theta_W} \tag{1.10}$$

The masses of the W and Z bosons are linked to the parameters of the Higgs field and the weak mixing angle $\cos\theta_W$, while the fermions gain their masses from the Yukawa couplings between fermion fields and Higgs field according to the following Lagrangian:

$$\mathcal{L}_Y = -g\overline{\psi}\psi\phi = -g\overline{\psi}\psi\frac{v}{\sqrt{2}} \tag{1.11}$$

According to the calculation, v is approximately 246 GeV, which gives the predictions of W-boson mass and Z-boson mass within the SM. However, the mass of the Higgs boson has to be measured experimentally due to unknown value of the free parameter λ. Since the discovery of the Higgs boson in 2012 by ATLAS [13] and CMS [14] experiments, efforts have been made to the measurement of the Higgs boson mass. The current world average of Higgs boson mass, measured by ATLAS and CMS at center-of-mass energies of 7, 8 and 13 TeV, is 125.25 ± 0.17 GeV [15].

1.1.4 Global electroweak fit and m_W

While the SM describes physics phenomena up to high energies at TeV scale and demonstrates impressively the predictive power of the electroweak unification as well as the quantum loop corrections, its overall consistency is also examined by the global electroweak fit. In particular, the mass of the W-boson is a very sensitive quantity for the consistency check of the SM, since its value is tightly constrained by the SM. Therefore, it is possible to obtain a predicted value of m_W from the global electroweak fit as an indirect measurement, which can be compared with the result of direct measurements, providing not only the probe of the SM, but also the excluding power of physics beyond the SM. A precise comparison relies on high precision of both the experiments and the theory predictions. For the latter, the global electroweak fit can nowadays be handled by the gFitter software package [16]–[18] that features the minimisation of a test statistics and its interpretation using frequentist statistics.

The gFitter package adopts a least-square-like notation. The corresponding test statistics is defined to be:

$$\chi^2(y_{mod}) = -2\ln\mathcal{L}(y_{mod}) \tag{1.12}$$

Where the y_{mod} are the theoretical expressions as functions of model parameters. The y_{mod} consists of three subsets: One corresponds to the unconstrained parameters of the theory. The second subset are theoretical parameters for which the fit uses the prior knowledge from direct measurements or from available calculations. The last subset includes those hard-to-quantify theoretical uncertainties, such as higher-order QCD corrections to a truncated perturbative series.

The likelihood function $\mathcal{L}(y_{mod})$ is essentially the product of two contributions

$$\mathcal{L}(y_{mod}) = \mathcal{L}(x_{theo}(y_{mod}) - x_{exp}) \cdot \mathcal{L}_{theo}(y_{mod}) = \prod_{i,j=1}^{N_{exp}} \mathcal{L}_{exp}(i,j) \cdot \prod_{k=1}^{N_{mod}} \mathcal{L}_{theo}(k) \tag{1.13}$$

x_{exp} are the involved measurements considered in the analysis, while x_{theo} are the theoretical expressions used to describe those x_{exp}. The first term on the right-hand side of Equation 1.13 shows the experimental likelihood, which measures the agreement between the theoretical calculation and the measurements. N_{exp} individual likelihood components for observables are accounted for, of which the model predictions depend on a subset of y_{mod} parameters that come with the constraint power from the prior knowledge. The correlations between measurements as well as the experimental and systematical uncertainties are also taken into account. The second term indicates the theoretical likelihood, containing the prior knowledge of certain y_{mod} parameters. The $\mathcal{L}_{theo}(k)$ terms may be constant if there is no prior information, be bound, or may express a probability function whenever the information is reliable.

The SM tree-level relations and radiative corrections related to W and Z bosons are accounted for in the formalism adopted by gFitter. In particular, the electroweak unification leads to a tree-level relation between the Fermi constant G_F (precisely determined by the measurements of muon lifetime) and the electromagnetic coupling (α):

$$G_F = \frac{\pi\alpha}{\sqrt{2}\left(m_W^{(0)}\right)^2\left(1 - \frac{\left(m_W^{(0)}\right)^2}{m_Z^2}\right)} \tag{1.14}$$

The superscript "(0)" indicates tree-level quantities. The radiative corrections can be parameterized by multiplying a form factor $(1-\Delta r)^{-1}$ to the right-hand side of Equation 1.14. Therefore, the m_W is resolved to be

$$m_W^2 = \frac{m_Z^2}{2}\left(1+\sqrt{1-\frac{\sqrt{8}\pi\alpha}{G_F m_Z^2(1-\Delta r)}}\right) \tag{1.15}$$

In the SM, the form factor Δr depends nearly quadratically on top-quark mass m_t and logarithmically on m_H due to the virtual quantum loop corrections illustrated in Figure 1.3. Consequently, the physical mass of the W-boson is different from the tree level calculation in Equation 1.14 according to

$$m_W = m_W^{(0)} + a\, m_t^2 + b \ln\left(\frac{m_H}{m_W}\right) + \cdots \tag{1.16}$$

Where a and b are constants determined by calculation, m_t and m_H for the masses of the top quark and Higgs boson [2]. In gFitter, besides the one-loop corrections from m_t and m_H, the effect of Δr also takes into account the full two-loop results [19] and the four-loop QCD calculation. Therefore, according to the SM, the prediction of m_W is parameterized as a function of Higgs mass, top-quark mass, Z-boson mass and the running QED coupling strength at m_Z^2 [20].

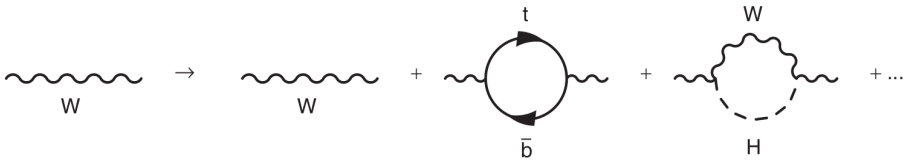

Figure 1.3 – Two largest loop corrections to m_W. (Figure from [2].)

Five classes of observables are used in the global EW fit:

— Z resonance parameters: Z mass and width , total $e^+e^- \to Z \to$ hadron production cross-sections.

— Partial Z cross sections: Ratios of leptonic to hadronic cross-sections, and heavy-flavour hadronic to total hadronic cross-sections.

— Neutral current couplings: Effective weak mixing angle, as well as the left-right and the forward-backward asymmetries for universal leptons and heavy quarks.

— W-boson parameters: mass and width of the W-boson.

— Higgs boson parameter: Higgs mass.

— Additional input parameters: Heavy-flavour quark masses (m_c, m_b and m_t. The masses of lighter quarks along with leptons are fixed to the world average values), QED and QCD coupling strengths at the Z-mass scale.

The most up-to-date global EW fit with gFitter uses the data of electroweak precision measurements at the Z pole by the LEP and SLD collaborations [21], the world averages of running quark masses, of m_W (80379 $\pm$ 13 MeV) and the width of the W-boson, as well as the latest determination of the five quark hadronic vacuum polarisation contribution to $\alpha(m_Z^2)$, known as $\Delta\alpha_{had}^{(5)}(m_Z^2)$. The mass of the top quark m_t = 172.47$\pm$ 0.46 GeV, is taken from the average of direct measurements by the ATLAS and CMS experiments based on 7 and 8 TeV data, assigned with an additional theoretical uncertainty of 0.5 GeV due to the ambiguity in the kinematic top-mass

definition, the colour structure of the fragmentation process and the finite perturbative order of the relation between the pole and the $\bar{M}S$ mass currently known. The experimental input of the LHC Run 1 Higgs mass $m_H = 125.09 \pm 0.21 \pm 0.11\,\text{GeV}$, is the weighted average of ATLAS and CMS results.

On the theoretical side, in addition to the aforementioned parameterized prediction of m_W, the width of the W-boson is known up to one electroweak loop order. Dominant contributions from final-state QED and QCD radiations are also included in the calculations [20].

The indirect determination of m_W by the fit is $m_W = 80.354 \pm 0.007\,\text{GeV}$, receiving uncertainty contributions from the measurements and the theoretical uncertainty of top-quark mass, the uncertainties of Z-boson mass, strong coupling constant, Higgs mass, and theoretical uncertainty of the unknown higher-order corrections to the mass of the W-boson $\delta_{th} m_W \approx 4\,\text{MeV}$.

One crucial consistency check of the SM is the simultaneous indirect determination of m_W and m_t, with direct measurements of m_H included or excluded. The corresponding plot is shown in Figure 1.4, in which it can be appreciated that the indirect determination of m_W outperforms the world average of direct measurements. The additional symmetries and fields in the extensions to the SM, such as the Minimal Supersymmetric Standard Model (MSSM) [22], the Two-Higgs-Doublet Model (2HDM) [23] and the dark photons [24], would possibly modify m_W with respect to the SM prediction. However, no significant deviation from the SM has so far been fully confirmed from the determination of m_W.

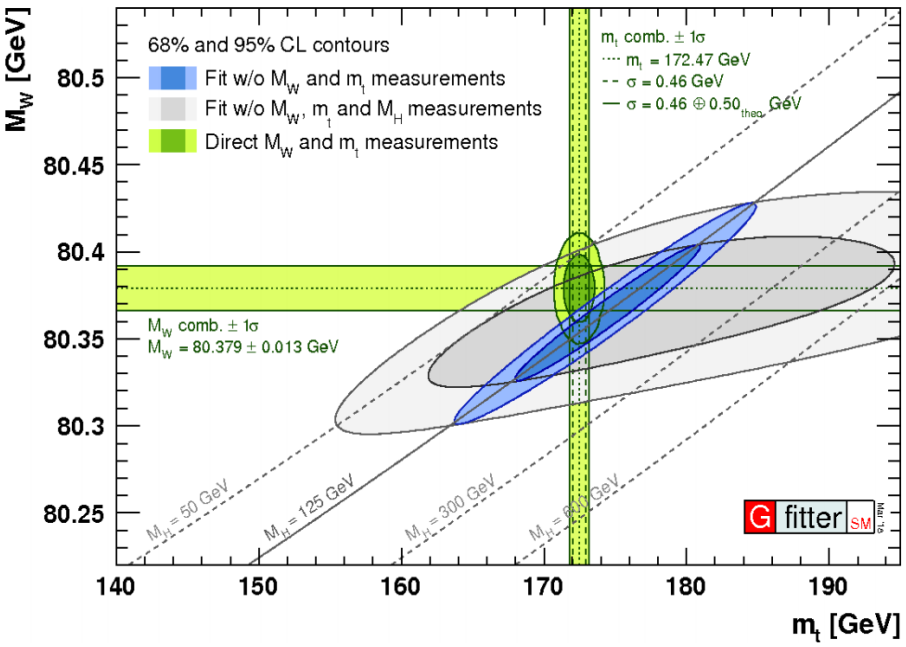

Figure 1.4 – The consistency of the SM is probed by the scanning m_W versus m_t for the global EW fit including or excluding m_H measurement, while excluding m_W and m_t from the fits. 68% and 95% CL contours are shown. (Figure from [20].)

1.2 Weak boson production in proton-proton colliders

Weak bosons can be produced from high-energy proton-proton collisions. By studying the quantum numbers, it appears as if each proton is made of two up quarks (u) and one down quark (d). This composition of "uud" forms the valence quarks in a proton. However, in the scope of inelastic scattering of the collision, the proton turns into a complicated dynamic structure, where the gluons that link the valence quarks through strong interaction can also split into virtual quark-antiquark pairs, known as sea quarks, or produce more gluons via gluon self-interaction. The quarks and gluons in this dynamic structure of the proton are considered to be point-like constituents. The high-energy proton-proton collisions are essentially the interactions between partons from the two protons colliding against each other.

The scattering processes can be divided into soft processes and hard processes by the amount of transferred transverse momentum following the QCD. In the soft processes with low values of Q^2 (i.e. $Q^2 < \Lambda^2_{QCD}$), such as single diffraction, double diffraction, multi-partonic interactions, soft initial state radiation (ISR) and final state radiation (FSR), and beam remnants at a hadron collider. In contrast, the productions of vector bosons are the typical hard processes, where the annihilation of a quark and an anti-quark is involved, coming with a high value of Q^2. The hard processes can be computed perturbatively in the context of QCD, while the prediction of soft processes has to take into account the non-perturbative effects. In a collision event at hadron collider, a hard process is accompanied by soft processes. The collection of all these soft processes in that event is noted as the underlying event (UE).

The production of vector boson cross-section in a proton-proton collision can be calculated according to the QCD factorization theorem. As constructed by Drell and Yan [25], the process is factorized into the hard scattering of the partons multiplied by the momentum distribution of partons inside the proton $f_i(x, Q^2)$ (a.k.a. Parton Distribution Functions or PDFs, functions of the fraction of the momentum of the proton carried by the struck quark x at a given energy scale Q^2). The PDFs describe the non-perturbative QCD of the soft interactions and have to be extracted by experiments. Once evolved to a large enough energy scale, denoted as $Q^2 = \mu^2$, the cross-section of the $q\overline{q} \to V$ is expressed as:

$$\sigma_{pp\to V} = \sum_{a,b} \int dx_a dx_b f_{a/A}(x_a, \mu_F^2) f_{b/B}(x_b, \mu_F^2) \times \sigma_{ab\to V}(x_a p_1, x_b p_2, \mu_F^2) \tag{1.17}$$

where a and b denote the quark and the anti-quark involved in the scattering, A and B stand for the two colliding protons. The spurious factorization scale μ_F helps separate the non-perturbative factors from the total cross-section, curing the infrared divergences caused by a particle reaching zero momentum or a massless particle radiating another massless particle. At high energy scale, the strong coupling constant $\alpha_S \ll 1$, which allows the expansion of the hard QCD process, for instance:

$$\sigma_{ab\to V} = \sigma_0 + \alpha_S(\mu_R^2)\sigma + \alpha_S^2(\mu_R^2)\sigma^2 + \mathcal{O}(\alpha_S^3) \tag{1.18}$$

where the μ_R is the renormalization scale of the running QCD coupling, another spurious parameter introduced to resolve the ultraviolet divergence caused by large

momentum in the loops of the Feynman diagrams representing the amplitude. The first term σ_0 stands for the cross-section calculated at Leading Order (LO). The $\alpha_S(\mu_R^2)\sigma$ term and the $\alpha_S^2(\mu_R^2)\sigma^2$ term are the Next-to-Leading Order (NLO) and Next-to-Next-to-Leading Order (NNLO) calculations. In the perturbative theory, as long as the calculation of the cross-section is expanded to all orders of α_S, the result will no longer depend on the scale parameters μ_F and μ_R. However, with a finite computing power in reality, the calculation of the cross-section can only be carried out up to a certain level of accuracy, such as NLO or NNLO. Therefore, the choice of μ_F and μ_R has an impact on the outcome of the perturbative QCD calculation. The typical choice of the scale parameters for a Drell-Yan process is $\mu_F = \mu_R = m_V$, where m_V is the mass of the vector boson of interest, either W or Z.

In the center-of-mass frame for the hard scattering, neglecting the mass of the partons, the four-momenta of the two incoming partons can be written as:

$$p_1 = \frac{\sqrt{s}}{2}(x_1, 0, 0, x_1), p_2 = \frac{\sqrt{s}}{2}(x_2, 0, 0, x_2) \tag{1.19}$$

x_1 and x_2 are related to $\hat{s}$ by $\hat{s} = (p_1 + p_2)^2 = x_1 x_2 s$. The rapidity of the produced vector boson is $y = 1/2(\ln(x_1/x_2))$, which leads to:

$$x_1 = \frac{m_V}{\sqrt{s}} e^y, x_2 = \frac{m_V}{\sqrt{s}} e^{-y} \tag{1.20}$$

Such that the cross-section at leading order is:

$$\frac{\mathrm{d}\sigma}{\mathrm{d}y} = \frac{1}{s} \sum \sigma_0(m_V) f_1(x_1, m_V^2) f_2(x_2, m_V^2) \tag{1.21}$$

The partonic cross-section of W and Z production can be derived from:

$$\begin{aligned} \sigma^{q\bar{q}' \to W} &= \frac{\sqrt{2}\pi G_F m_W^2}{3} |V_{q\bar{q}'}|^2 \delta(\hat{s} - m_W^2), \\ \sigma^{q\bar{q}' \to Z} &= \frac{\sqrt{2}\pi G_F m_Z^2}{3} (v_q^2 + a_q^2) \delta(\hat{s} - m_Z^2) \end{aligned} \tag{1.22}$$

Here $\hat{s}$ is the square of the parton center-of-mass energy, $V_{q\bar{q}'}$ is the appropriate CKM matrix element, corresponding to the strength of the flavour-changing weak interaction. v_q and a_q are the vector coupling and axial vector coupling of the Z-boson to the quarks.

At leading order, the transverse momentum of the produced vector boson is zero. At higher orders, additional quarks and gluons come into play in the production of vector bosons, specifically the soft processes between partons that lead to the gluon radiations and the emissions or virtual loops of gluons and quarks in the hard process. The involvement of additional quarks and gluons brings a non-zero transverse momentum distribution to the produced vector boson. The hard process part of the higher order effect can be predicted by pQCD calculations. For instance, the NLO approximation of the differential cross-section at high p_{T}^W is:

$$\left(\frac{\mathrm{d}\sigma}{\mathrm{d}(p_{\mathrm{T}}^W)^2} \right)_{\mathcal{O}(\alpha_S)} = \frac{4\alpha_S \sigma^0}{3\pi^2} \frac{1}{(p_{\mathrm{T}}^W)^2} \ln \left(\frac{m_W^2}{(p_{\mathrm{T}}^W)^2} \right) \tag{1.23}$$

However, it is obvious that this formulation of cross-section does not apply to the low p_{T}^{W} region. i.e. the logarithmic term expands rapidly for $p_{\mathrm{T}}^{W} < m_W$ and compensates for the small α_S, causing the divergence of the higher-order terms. Particularly, at order N, there is a series of terms proportional to $\alpha_S^N \ln^M(m_W^2/(p_{\mathrm{T}}^{W})^2)$ in the differential cross-section, where $M \leq 2N-1$. As for $p_{\mathrm{T}}^{W} \ll m_W$, the logarithmic term becomes the leading contribution to the calculation, which makes the perturbative calculation become inapplicable. The contribution from soft process can be accounted for by modelling the gluon radiations (parton shower, or PS) based on the knowledge of soft QCD effects accumulated from the fixed target proton-neutron collisions. In an analytic approach, following the argument that the cross-section integrated over all $(p_{\mathrm{T}}^{W})^2$ should be finite [26], the divergence can be resolved by resumming all the logarithms to the leading logarithm by the following form:

$$\left(\frac{\mathrm{d}\sigma}{\mathrm{d}(p_{\mathrm{T}}^{W})^2}\right)_{\mathcal{O}(\alpha_S)} = \frac{\mathrm{d}}{\mathrm{d}(p_{\mathrm{T}}^{W})^2}\left\{\sigma^0 \exp\left[-\frac{2\alpha_S}{3\pi}\ln^2\left(\frac{m_W^2}{(p_{\mathrm{T}}^{W})^2}\right)\right]\right\} \tag{1.24}$$

Such that the full expression of the differential cross-section becomes:

$$\frac{\mathrm{d}\sigma}{\mathrm{d}(p_{\mathrm{T}}^{W})^2} = \left(\frac{\mathrm{d}\sigma}{\mathrm{d}(p_{\mathrm{T}}^{W})^2}\right)_{pQCD} + \left(\frac{\mathrm{d}\sigma}{\mathrm{d}(p_{\mathrm{T}}^{W})^2}\right)_{resumm} \tag{1.25}$$

In the low p_{T}^{W} region, the contribution from soft effects are corrected by the resummation techniques. Moving to the high p_{T}^{W} region, the hard emissions can be predicted by pQCD at a given fixed order.

References

[1] `https://en.wikipedia.org/wiki/Standard_Model` (cit. on p. 7).

[2] M. Thomson, *Modern particle physics*. New York: Cambridge University Press, 2013, ISBN: 978-1-107-03426-6 (cit. on pp. 6, 9, 12).

[3] `https://atlas.web.cern.ch/Atlas/GROUPS/PHYSICS/CombinedSummaryPlots/SM/ATLAS_b_SMSummary_FiducialXsect/ATLAS_b_SMSummary_FiducialXsect.pdf` (cit. on pp. 7, 8).

[4] A. Keshavarzi, K. S. Khaw, and T. Yoshioka, "Muon g-2: a review", *Nuclear Physics B*, vol. 975, p. 115 675, 2022, ISSN: 0550-3213. DOI: `https://doi.org/10.1016/j.nuclphysb.2022.115675`. [Online]. Available: `https://www.sciencedirect.com/science/article/pii/S0550321322000268` (cit. on p. 7).

[5] M. E. Peskin and D. V. Schroeder, *An Introduction to Quantum Field Theory*. Westview Press, 1995, Reading, USA: Addison-Wesley (1995) 842 p (cit. on p. 7).

[6] S. Weinberg, "A model of leptons", *Phys. Rev. Lett.*, vol. 19, pp. 1264–1266, 21 Nov. 1967. DOI: `10.1103/PhysRevLett.19.1264`. [Online]. Available: `https://link.aps.org/doi/10.1103/PhysRevLett.19.1264` (cit. on p. 8).

[7] A. Salam, "Weak and Electromagnetic Interactions", *Conf. Proc. C*, vol. 680519, pp. 367–377, 1968. DOI: `10.1142/9789812795915_0034` (cit. on p. 8).

[8] S. L. Glashow, "Partial-symmetries of weak interactions", *Nuclear Physics*, vol. 22, no. 4, pp. 579–588, 1961, ISSN: 0029-5582. DOI: https://doi.org/10.1016/0029-5582(61)90469-2. [Online]. Available: https://www.sciencedirect.com/science/article/pii/0029558261904692 (cit. on p. 8).

[9] P. W. Higgs, "Broken symmetries and the masses of gauge bosons", *Phys. Rev. Lett.*, vol. 13, pp. 508–509, 16 Oct. 1964. DOI: 10.1103/PhysRevLett.13.508. [Online]. Available: https://link.aps.org/doi/10.1103/PhysRevLett.13.508 (cit. on p. 10).

[10] P. Higgs, "Broken symmetries, massless particles and gauge fields", *Physics Letters*, vol. 12, no. 2, pp. 132–133, 1964, ISSN: 0031-9163. DOI: https://doi.org/10.1016/0031-9163(64)91136-9. [Online]. Available: https://www.sciencedirect.com/science/article/pii/0031916364911369 (cit. on p. 10).

[11] G. S. Guralnik, C. R. Hagen, and T. W. B. Kibble, "Global conservation laws and massless particles", *Phys. Rev. Lett.*, vol. 13, pp. 585–587, 20 Nov. 1964. DOI: 10.1103/PhysRevLett.13.585. [Online]. Available: https://link.aps.org/doi/10.1103/PhysRevLett.13.585 (cit. on p. 10).

[12] F. Englert and R. Brout, "Broken symmetry and the mass of gauge vector mesons", *Phys. Rev. Lett.*, vol. 13, pp. 321–323, 9 Aug. 1964. DOI: 10.1103/PhysRevLett.13.321. [Online]. Available: https://link.aps.org/doi/10.1103/PhysRevLett.13.321 (cit. on p. 10).

[13] G. Aad *et al.*, "Observation of a new particle in the search for the standard model higgs boson with the atlas detector at the lhc", *Physics Letters B*, vol. 716, no. 1, pp. 1–29, 2012, ISSN: 0370-2693. DOI: https://doi.org/10.1016/j.physletb.2012.08.020. [Online]. Available: https://www.sciencedirect.com/science/article/pii/S037026931200857X (cit. on p. 10).

[14] S. Chatrchyan *et al.*, "Observation of a new boson at a mass of 125 gev with the cms experiment at the lhc", *Physics Letters B*, vol. 716, no. 1, pp. 30–61, 2012, ISSN: 0370-2693. DOI: https://doi.org/10.1016/j.physletb.2012.08.021. [Online]. Available: https://www.sciencedirect.com/science/article/pii/S0370269312008581 (cit. on p. 10).

[15] P. Zyla *et al.*, "Review of Particle Physics", *PTEP*, vol. 2020, no. 8, p. 083C01, 2020, and 2021 update. DOI: 10.1093/ptep/ptaa104 (cit. on p. 10).

[16] H. Flächer *et al.*, "Revisiting the global electroweak fit of the Standard Model and beyond with Gfitter", *The European Physical Journal C*, vol. 60, pp. 543–583, 2009. DOI: 10.1140/epjc/s10052-009-0966-6 (cit. on p. 11).

[17] M. Baak *et al.*, "Updated status of the global electroweak fit and constraints on new physics", *The European Physical Journal C*, vol. 72, p. 2003, 2012. DOI: 10.1140/epjc/s10052-012-2003-4 (cit. on p. 11).

[18] M. Baak *et al.*, "The electroweak fit of the standard model after the discovery of a new boson at the LHC", *The European Physical Journal C*, vol. 72, p. 2205, 2012. DOI: 10.1140/epjc/s10052-012-2205-9 (cit. on p. 11).

[19] M. Awramik, M. Czakon, A. Freitas, and G. Weiglein, "Precise prediction for the w-boson mass in the standard model", *Phys. Rev. D*, vol. 69, p. 053 006, 5 Mar. 2004. DOI: 10.1103/PhysRevD.69.053006. [Online]. Available: https://link.aps.org/doi/10.1103/PhysRevD.69.053006 (cit. on p. 12).

[20] J. Haller *et al.*, "Update of the global electroweak fit and constraints on two-Higgs-doublet models", *The European Physical Journal C*, vol. 78, p. 675, 2018. DOI: 10.1140/epjc/s10052-018-6131-3 (cit. on pp. 12, 13).

[21] M. Baak *et al.*, "The global electroweak fit at NNLO and prospects for the LHC and ILC", *The European Physical Journal C*, vol. 74, p. 3046, 2014. DOI: 10.1140/epjc/s10052-014-3046-5 (cit. on p. 12).

[22] S. Heinemeyer, W. Hollik, G. Weiglein, and L. Zeune, "Implications of lhc search results on the w boson mass prediction in the mssm", *Journal of High Energy Physics*, vol. 2013, p. 84, 12 Dec. 2013. DOI: 10.1007/JHEP12(2013)084. [Online]. Available: https://doi.org/10.1007/JHEP12(2013)084 (cit. on p. 13).

[23] D. López-Val and J. Solà, "ΔR in the two-higgs-doublet model at full one loop level—and beyond", *The European Physical Journal C*, vol. 73, p. 2393, 4 Apr. 2013. DOI: 10.1140/epjc/s10052-013-2393-y. [Online]. Available: https://doi.org/10.1140/epjc/s10052-013-2393-y (cit. on p. 13).

[24] D. Curtin, R. Essig, S. Gori, and J. Shelton, "Illuminating dark photons with high-energy colliders", *Journal of High Energy Physics*, vol. 2015, p. 157, 2 Feb. 2015. DOI: 10.1007/JHEP02(2015)157. [Online]. Available: https://doi.org/10.1007/JHEP02(2015)157 (cit. on p. 13).

[25] S. D. Drell and T.-M. Yan, "Massive lepton-pair production in hadron-hadron collisions at high energies", *Phys. Rev. Lett.*, vol. 25, pp. 316–320, 5 Aug. 1970. DOI: 10.1103/PhysRevLett.25.316. [Online]. Available: https://link.aps.org/doi/10.1103/PhysRevLett.25.316 (cit. on p. 14).

[26] G. Parisi and R. Petronzio, "Small Transverse Momentum Distributions in Hard Processes", *Nucl. Phys. B*, vol. 154, pp. 427–440, 1979. DOI: 10.1016/0550-3213(79)90040-3 (cit. on p. 16).

Chapter 2

The LHC and the ATLAS experiment

Contents

2.1 The Large Hardron Collider

The Large Hadron Collider (LHC) at CERN is by far the most powerful tool for particle physics research [1]. Mainly designed to collide proton beams with a centre-of-mass energy of 14 TeV at maximum, it can reach an unprecedented luminosity of $10^{34}\,\mathrm{cm}^{-2}\,\mathrm{s}^{-1}$. The LHC is a two-ring-superconducting-hadron accelerator and collider installed in the tunnel of its predecessor: Large Electron Positron Collider (LEP), of which the circumference is 26.7 km (Fig 2.1). The existing LEP tunnel is composed of 8 straight sections and 8 arcs buried between 45 m and 170 m underground. Linked by two transfer tunnels, the tunnel of LHC is connected to the CERN accelerator complex that functions as an injector.

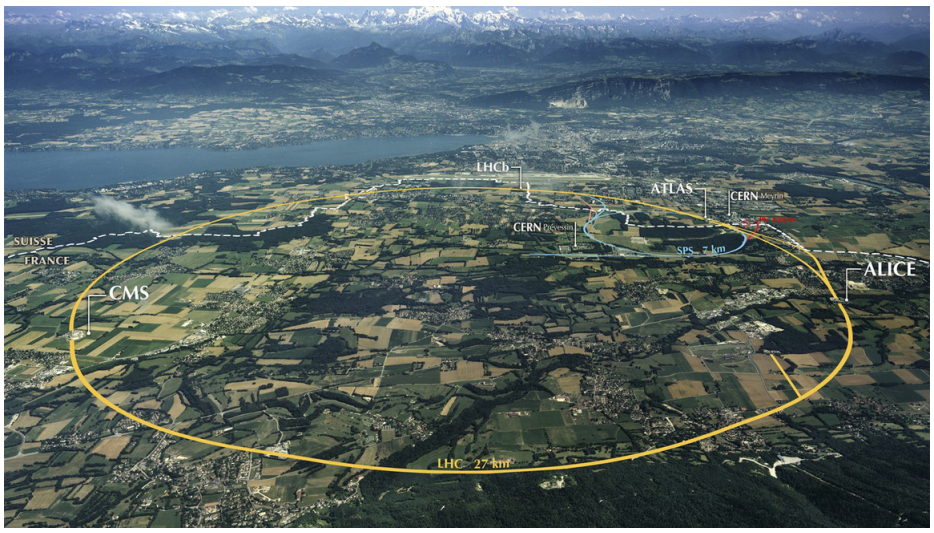

Figure 2.1 – A photo illustrating the LHC main tunnel and four major experiments.

The so-called "lattice magnets" on the LHC bend and tighten the trajectory of particles and are responsible for keeping the beams stable and precisely aligned. The LHC is equipped with 1232 main dipoles, each 15 m long and as heavy as 35 t, for

handling tighter turns of the beam. The dipoles make use of superconducting magnet technology and generate a peak dipole field of 8.33 T at the maximum proton beam energy of 7 TeV. These dipoles cooperate with multipoles correctors such as sextupole, octupole and decapole magnets, so that the small imperfections in the magnetic field at the extremities of the dipoles can be corrected. In addition, the quadrupoles made of four magnetic poles around the beam pipe squeeze the beam either vertically or horizontally, keeping the particles in a tight beam as a net effect, such that the RMS of the beam size in the arcs is kept at the level of 0.3 mm during collisions. The "insertion magnets" take over the beam in front of the LHC detectors. These insertion magnets are deployed in the form of inner triplet, which is a system based on three quadrupoles. There are eight inner triplets at LHC in total, every two of which are located at each of the four large LHC detectors: ALICE, ATLAS, CMS and LHCb. Thanks to the inner triplets, particles are squeezed closer together before they reach a detector, which increases the chance of colliding with particles coming from the opposite direction.

All the work of this thesis, covering both the Quality Assurance and Quality Control (QAQC) of particle detectors and the study of W-boson properties, is based on the ATLAS experiment. A Toroidal LHC ApparatuS (ATLAS), is a multi-purpose particle detector of the Large Hadron Collider designed to collect data from high-energy proton-proton or heavy ion collisions. This chapter will first give a brief introduction to the principle of particle acceleration at LHC, as well as the key parameters to describe the particle beams at collisions. The second part of the chapter will review all the sub-systems of ATLAS, followed by a detailed description of the specific datasets used for W-boson physics analysis.

2.1.1 The acceleration system of LHC

The injected protons supplied to the LHC come from the CERN accelerator complex. The protons are initially accelerated by the Linac2 to reach 50 MeV, then transferred to the Proton Synchrotron Booster (PSB) where their energy increases to 1.4 GeV. As the last part of the pre-injector chain, the Proton Synchrotron (PS) receives beams from the PSB and further accelerate them to 25 GeV. After that, the Super Proton Synchrotron (SPS) takes over the acceleration and injects the proton beam to LHC at 450 GeV. Following the injection of the beam, the protons are accelerated at LHC up to an energy of 7 TeV via the Radio Frequency (RF) systems.

Inside a proton beam of the LHC, instead of spreading uniformly along the circumference, the particles are grouped in structures called bunches. The acceleration system operates coordinately, meeting the requirement of holding more than 2800 proton bunches per LHC ring with a nominal bunch spacing of 25 ns while achieving small transverse and well defined longitudinal emittances. The high center-of-mass energy in the collisions increases the cross-sections of hard-scattering processes in general and opens a wider kinematic window for rare physics processes.

2.1.2 Proton beam and luminosity

Two proton beams circulate in opposite clock-wise directions in the tunnel of the LHC, manipulated by separate magnet dipole fields and vacuum chambers in the main arcs. The two equally charged particles beams enter common sections only at

the insertions regions reserved for detectors. The number of events per unit of time generated in proton-proton collisions at LHC is described by the following relation [2]:

$$N_{event} = L\sigma_{event} \tag{2.1}$$

Here σ_{event} is the cross section of the process of interest, and L is the machine luminosity determined by the beam parameters. Assuming a Gaussian beam distribution, we have:

$$L = \frac{N_b^2 n_b f_{rev} \gamma_r}{4\pi\epsilon_n \beta_*} F \tag{2.2}$$

where N_b stands for the number of protons per bunch, n_b is the number of bunches per beam, f_{rev} for the revolution frequency, γ_r for the relativistic factor, ϵ_n for the normalized transverse beam emittance and β_* is the beta function at the interaction point (IP). The beta function describes the envelope of the single particle trajectory, which has to be squeezed to a minimum at the IP. The emittance is an invariant determined by the optics of the machine. It describes the space occupied by the particle in the transverse two-dimensional phase space. Due to the non-zero crossing angle of the two colliding beams at the IP, the luminosity is reduced according to the factor

$$F = \frac{1}{\sqrt{1 + \left(\frac{\theta_c \sigma_z}{2\sigma^*}\right)^2}} \tag{2.3}$$

in which θ_c, σ_z and σ^* are the full crossing angle at IP, the RMS bunch length and the transverse RMS beam size at IP, respectively.

As high luminosity experiments, ATLAS and CMS require a peak luminosity of $L = 10^{34}\,\mathrm{cm}^{-2}\,\mathrm{s}^{-1}$. The limit of the LHC machine performance depends on multiple factors, such as the beam-beam interactions, the aperture of the focusing magnets on the two sides of the IP, the maximum dipole field as well as the magnet quench limits, the capability of the beam dumping system and so on.

Continuous data taking at high instantaneous luminosity leads to a high integrated luminosity, therefore helping accumulate more statistics of interactions at a given center-of-mass energy. Together with the high beam energy, the high beam intensity also facilitates the exploration of rare processes.

A precise measurement of the integrated luminosity is a key part of the physics measurements at LHC. In particular, the uncertainty on the luminosity is an important concern in precision measurements.

2.2 The ATLAS detector

ATLAS [3] is a cylindrical multi-purpose particle detector designed to be forward-backward symmetry. The detector sub-systems are comprised of the inner tracking detector, the electromagnetic and hadronic calorimeters and the muon spectrometer, as shown in Fig 2.2. In addition to the detectors, there is a thin superconducting solenoid surrounding the inner detector, as well as three large superconducting toroid magnets (one for the barrel and two for the end-caps) distributed in an eight-fold azimuthal symmetric pattern around the calorimeters.

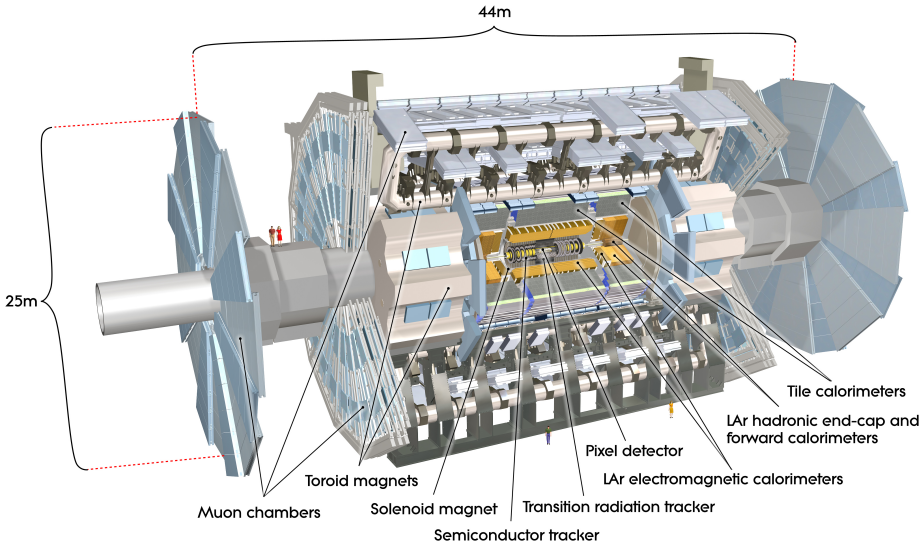

Figure 2.2 – An overview of the ATLAS magnet and detector sub-systems. (Figure from [3].)

2.2.1 The coordinate system in ATLAS

Based on its cylindrical geometry, ATLAS uses a right-handed coordinate system centering at the Interaction Point (IP). The z-axis is parallel to the beam pipe while the x-y plane is perpendicular to the beam. The positive direction of the x-axis points towards the center of LHC. The positive direction of the y-axis is defined to be pointing upwards. The cylindrical coordinates are introduced to the x-y plane to simplify the description of particle kinematics, with ϕ denoted to be the azimuthal angle and θ as the polar angle.

Benefiting from the cylindrical coordinate system of ATLAS, the rapidity of the particle is frequently used to study the kinematics, since the calculation of rapidity is additive under Lorentz transformations. For a particle with energy E and momentum p_z along the z-axis, the definition of rapidity is as following:

$$y = \frac{1}{2} \ln \frac{E + p_z}{E - p_z} \tag{2.4}$$

When the mass of the particle is negligible to its momentum, pseudorapidity is used for approximation:

$$\eta = -\ln \left[\tan(\theta/2) \right] \tag{2.5}$$

The pseudorapidity-azimuthal angular distance between two particles is defined as:

$$\Delta R = \sqrt{\Delta\eta^2 + \Delta\phi^2} \tag{2.6}$$

2.2.2 Magnet system

The magnet system of ATLAS is a hybrid of four superconducting magnets, stretching 22 m in diameter and 26 m in length. The ATLAS magnet system consists of one solenoid, one barrel toroid and two end-cap toroids. A volume of about 12 000 m^3 is covered by the magnetic field provided by the magnet system.

The central solenoid is aligned on the beam axis, producing a 2 T axial magnetic field for the inner detector. In order to minimise the impact on the calorimeters outside, the material budget of the solenoid is kept as low as possible: the inner and outer diameters are 2.46 m and 2.56 m, respectively. The axial length of the solenoid is 5.8 m.

The barrel toroids comprises eight coils enclosed by individual vacuum-vessels. They generate a magnetic field that fills the cylindrical volume surrounding the calorimeters and two end-cap toroids. The total size of the barrel toroid system after installation is 25.3 m in length, 9.4 m and 20.1 m in inner and outer diameters.

Each of the two end-cap toroid, with 5 m in axial length and 10.7 m in outer diameter, contains eight flat, squared coil units in a rigid structure. The end-cap toroid coil system is rotated by an offset of 22.5° with respect to the barrel toroid coil system so as to provide radial overlap and to optimize the bending power at the interface between the two coil systems.

The toroid system provides the muon detectors a toroidal magnetic field, of which the magnitude is around 0.5 T in the central region and approximately 1 T in the end-cap regions.

2.2.3 Inner detectors

As the innermost detector sub-system of ATLAS, the Inner Detector (ID) is capable of providing pattern recognition, measuring momentum, determining both primary and secondary vertex for charged tracks within $|\eta| < 2.5$. Additional electron identification is also provided by ID within $|\eta| < 2$. The ID is located within a cylindrical coverage with 1150 mm in radius and 3512 mm in length (Fig 2.3). Thanks to the enclosing thin solenoid, there is an axial magnetic field of 2 T throughout the entire ID. As illustrated in Fig 2.4, the ID is made of three different types of sub-detectors: the silicon-pixels and the silicon micro-strip sensors (SCT) at inner radii, as well as the transition radiation tracker modules (TRT) at larger radii. The three sub-detectors operate independently but are complementary to each other (Fig 2.5).

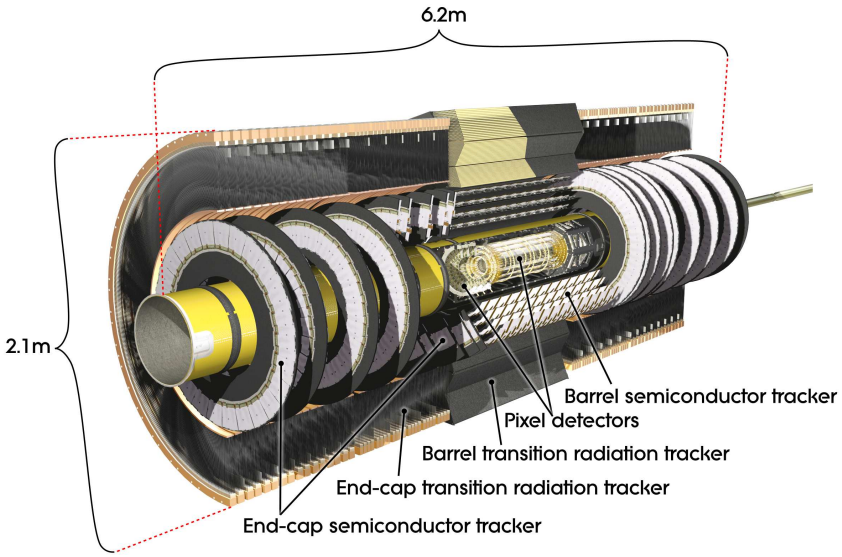

Figure 2.3 – Cut-away view of ATLAS Inner Detector. (Figure from [3].)

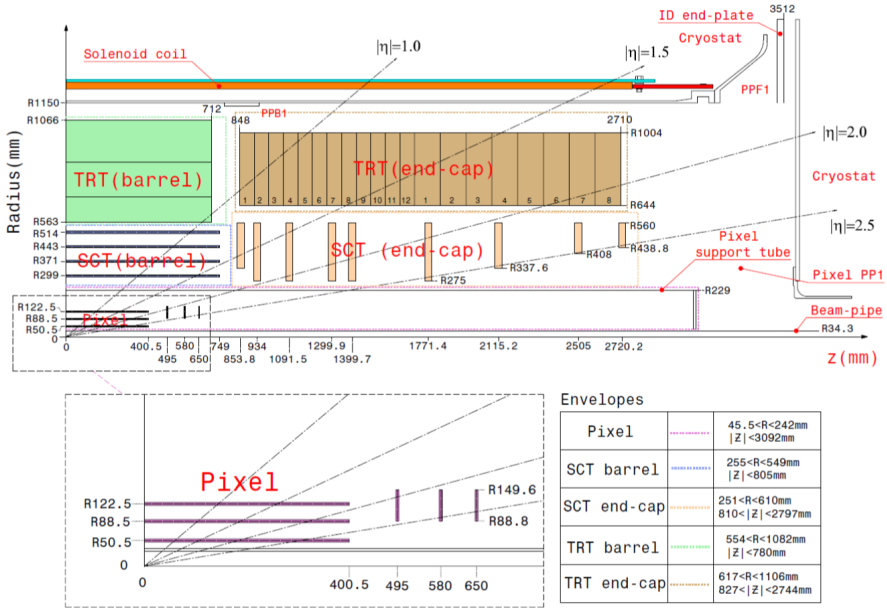

Figure 2.4 – Sectional view of ATLAS ID. (Figure from [3].)

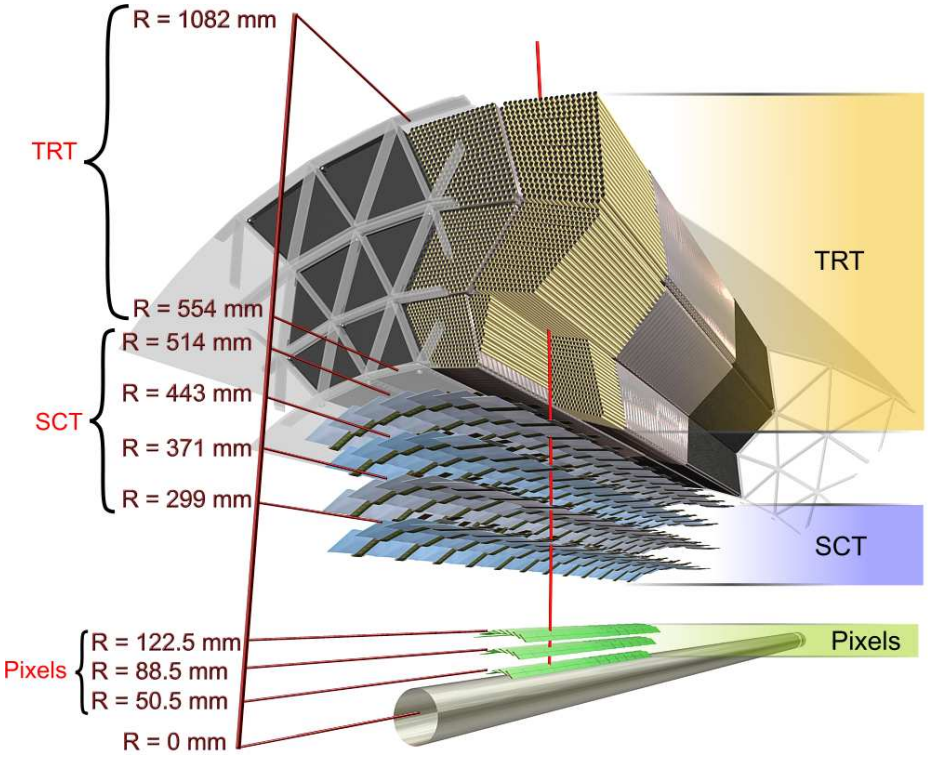

Figure 2.5 – ATLAS ID transversed by a charged particle. (Figure from [3].)

The working principle of silicon detectors is that when the charged particles pass through the depleted region in a PN-junction, the ionized free electrons and holes will quickly drift towards the electrodes under the external electric field, inducing signals at the same time [4]. The silicon pixel layers and the SCT layers closer to the beam pipe are designed to realise high-resolution pattern recognition abilities. The 1744 modules of pixel detectors are arranged in three barrel layers at R=50.5 mm, 88.5 mm, 122.5 mm and in three disk layers on each of the two end-caps at |z|=495 mm, 580 mm,

650 mm. The intrinsic accuracy of pixel detectors is 10 µm in $R - \phi$ direction and 115 µm in z (R) direction for barrel layers (disks). An extra pixel layer, called the Insertable B-Layer (IBL) [5], was inserted between the original pixel detectors and a new beam pipe during the shutdown of LHC in 2013-2014, aiming at improving the track reconstruction performance of the ATLAS ID system at a higher luminosity.

Covering a range of radius from 275 mm to 560 mm, the 4088 SCT modules are placed on four tilting coaxial cylindrical layers in the barrel regions and on nine disk layers in the end-cap regions. The SCTs provide an intrinsic tracking accuracy of 17 µm in $R - \phi$ and 580 µm in z (R) for barrel layers (disks).

The TRT is installed in the outermost regions of the ID. The basic TRT detector elements are polyimide drift tubes (straw tubes) with 4 mm in diameter. The low energy transition radiation photons can be absorbed by the Xe-based working gas of straw tubes, inducing a much larger signal than what is caused by the ionization of charged particle. As a result, the identification of electron is enhanced by distinguishing transition radiation from tracking signals. 73 layers of straw tubes are axially arranged in the barrel region while 160 straw tube planes are installed radially in each of the end-cap regions. Fibres or foils are inserted among the straw tubes in the barrel or end-caps, rendering the emissions of transition radiation from traversing electrons. The inner radius and the outer radius of the TRT are 563 mm and 1066 mm, respectively. The intrinsic accuracy of the TRT is 130 µm.

2.2.4 Calorimetry

In order to measure the energies of particles that pass through the ID, the electromagnetic calorimeter and the hadronic calorimeters of ATLAS are designed to absorb most high-energy particles through electromagnetic showering and hadronic showering. The layout of ATLAS calorimeters are shown in Fig 2.6.

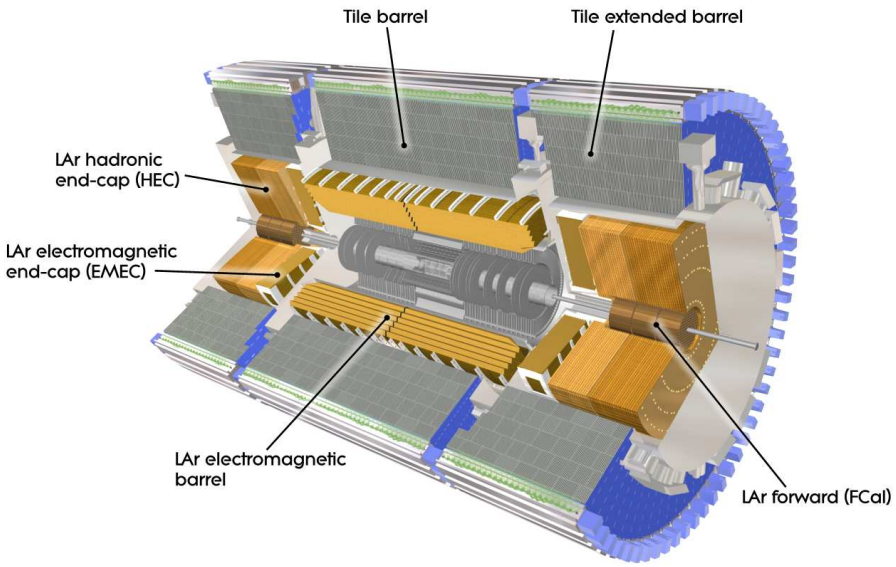

Figure 2.6 – The layout of ATLAS calorimeter systems. The LAr electromagnetic calorimeter in the barrel and on the end-caps measure the energy of electrons and photons through electromagnetic showering. The tile calorimeter, LAr hadronic end-caps and LAr forward calorimeters are designed to measure the energies of hadrons. (Figure from [3].)

Typically, electromagnetic showers happen when a high-energy electron, positron or photon enters a material and interacts with its atomic nucleus. The high-energy electron emits a photon due to bremsstrahlung while the high-energy photon produces a pair of electron-positron in the Coulomb field of the atomic nucleus. Then the electron and positron produced in the pair production further annihilate into a pair of photons. These processes develop a cascade of electron and photons, resulting in an electromagnetic shower. The electromagnetic showers come to an end if the energy of the photons is insufficient for pair production and the bremsstrahlung of secondary electrons is not strong anymore. After that, electrons lose energy via ionization while photons give up energy through Compton scattering and photoelectric effect until finally being absorbed by the material. The radiation length X_0, depending on the material, is commonly used to describe the longitudinal development of electromagnetic showers. It is defined to be the average thickness of the material that reduces the average energy of high-energy electrons to 1/e of its initial value because of bremsstrahlung.

The hadronic showers begin when high-energy hadrons interact with atomic nuclei in the material through strong interaction and produce multiple secondary hadrons. The secondary hadrons, still with high-energy, will carry on the interaction with atomic nuclei and produce even more secondary particles. Even though most secondary particles are pions and nuclear fragments in hadronic showers, protons, neutrons, electrons, photons, muons and neutrinos can also be produced as secondary particles, which leads to the complexity of hadronic showers. The characteristic of longitudinal development of a hadronic shower is the nuclear interaction length:

$$\lambda = \frac{A}{N_A \rho \sigma} \tag{2.7}$$

where A is the atomic number, N_A is the Avogadro constant, ρ is the matter density and σ is the cross-section of inelastic scattering.

2.2.5 LAr electromagnetic calorimeter (EM)

The EM calorimeter of ATLAS is a sampling calorimeter made of lead-Liquid Argon (LAr) detectors with accordion-shaped kapton electrodes and lead absorber plates [6]. The lead absorbers are glued to two stainless-steel sheets with resin-impregnated glass-fibre fabric to improve the mechanical strength. The gaps between absorbers plates are filled by flowing liquid argon. The readout electrodes are also situated in the gaps between the absorbers and are made of three conductive copper layers insulated and separated by polyimide sheets. The two copper layers on the outside provide high voltage potential while the layer in the middle reads out signal through capacitive coupling.

As high energy particles pass through the EM calorimeter, electromagnetic showers take place in the lead absorber. Between the absorbers plates, the shower particles ionize liquid argon, creating ions and free electrons. Since an external electric field is applied to the gap filled by LAr, the ions and the electrons will drift towards the absorber and the electrode, therefore inducing a current signal to the readout electrodes. After converting the signals to energy deposit in individual cells, the energies and positions of the electromagnetic showers are recorded, which determines the interaction point and allows electron/photon identification as well as lepton isolation.

The accordion geometry of the calorimeter guarantees a fast extraction of the signal as well as a full coverage in ϕ without azimuthal cracks. Supported by independent cryostats, the EM calorimeter includes a barrel part covering $|\eta| < 1.475$ and two end-cap parts covering $1.375 < |\eta| < 3.2$. The LAr calorimeter shares the vacuum vessel with the adjacent central solenoid.

The barrel calorimeter is composed of two half-barrels, each of length 3.2 m and with inner and outer diameter of 2.8 m and 4 m, respectively. Between the two half-barrels there is only a small gap at $z = 0$. A half-barrel is divided into 16 modules of which the coverage of azimuthal angle is 22.5° per module. The thickness of a module is $22X_0$ at minimum, then increased from $22X_0$ to $30X_0$ between $0 < |\eta| < 0.8$ and from $24X_0$ to $33X_0$ between $0.8 < |\eta| < 1.3$. One barrel region module has three layers in depth, and contains 3424 readout cells in total including the presampler cells. The first calorimeter sampling is based on the strip cells that have fine granularity in η to measure the pointing of the photon and to facilitate the π_0 rejection. The main sampling for energy measurement comes from the square towers in the second layer of the calorimeter with corresponding sampling size of $\Delta\eta \times \Delta\phi = 0.025 \times 0.025$. The third sampling collects the tail of the electromagnetic shower and has a granularity of $\Delta\eta \times \Delta\phi = 0.05 \times 0.025$. The trigger tower of the barrel module is of the size $\Delta\eta \times \Delta\phi = 0.1 \times 0.1$. The 3-layer sampling structure of a module in the barrel calorimeter as well as the granularity of trigger tower is shown in Fig 2.7.

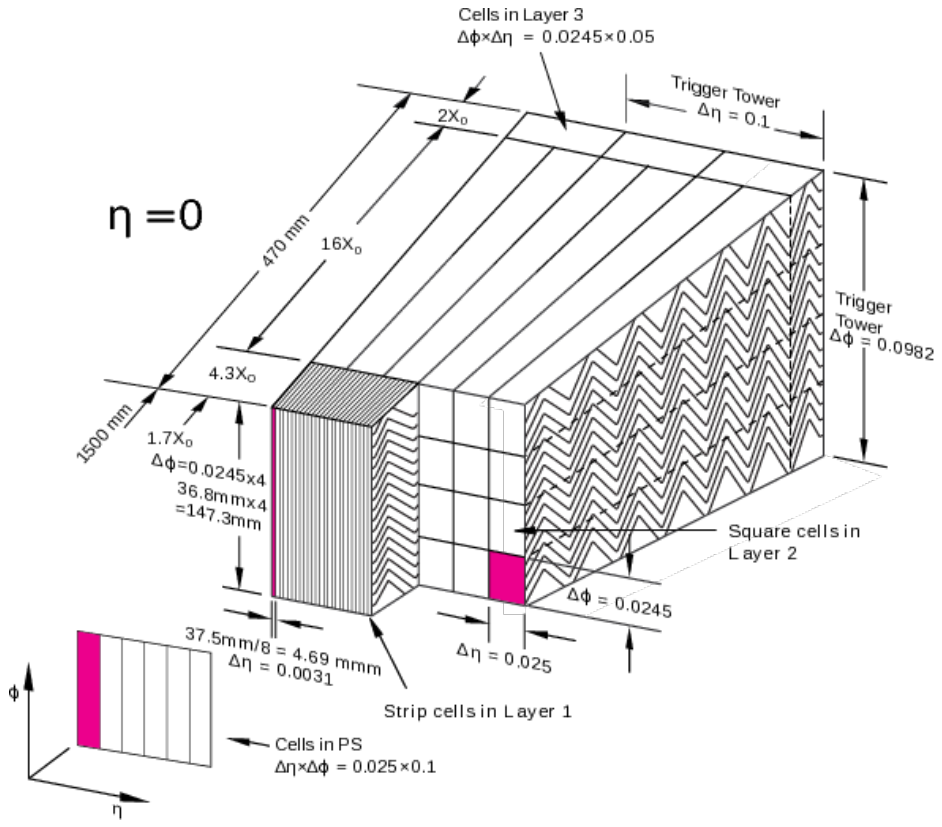

Figure 2.7 – Sketch of a module installed in the barrel EM calorimeter of ATLAS. (Figure from [3].)

The end-cap calorimeter on each side is divided into an outer wheel covering $1.375 < |\eta| < 2.5$ and an inner wheel covering $2.5 < |\eta| < 3.2$. Each end-cap wheel is 63 cm thick and stretches from 330 mm to 2098 mm along its radius. A LAr

presampler is installed in front of the end-cap wheel ranging $1.5 < |\eta| < 1.8$ in order to improve the energy measurement. Above $|\eta| > 1.475$, the total active thickness of the end-cap is more than $24X_0$. Specifically, the thickness increases from 24 to 38 X_0 for η going from 1.475 to 2.5 and increases from 26 to 36 X_0 for η going from 2.5 to 3.2. Similar to the barrel electromagnetic calorimeter, the precision region in the end-cap calorimeter is also divided into 3 layers in depth. The front layer with 4.4 X_0 in thickness is built of strips in η direction. The transverse size of the projective cell in the middle layer matches the precision of its barrel electromagnetic calorimeter counterpart. The $|\eta| < 1.5$ region of the outer wheel as well as the inner wheel is segmented into 2 longitudinal layers, which brings a coarser transverse granularity.

2.2.6 Hadronic calorimeters

The hadronic calorimeters locate beyond the EM calorimeters and consist of three components: the tile calorimeter, the liquid-argon hadronic end-cap calorimeter (HEC) and liquid-argon forward calorimeter (FCal).

The tile calorimeter functions as a sampling calorimeter of which the absorber is steel and the active material is scintillator. The scintillator tiles equipped with wavelength-shifting fibre readout on the edge are aligned radially and normal to the beam line, which achieves an almost full azimuthal coverage. The scintillation light is converted to current and multiplied by photomultiplier tubes (PMTs). The tile calorimeter is placed in $|\eta| < 1.7$ and divided into a 5.8 m long central barrel for $|\eta| < 1.0$ along with two 2.6 m long extended barrels for $0.8 < |\eta| < 1.7$. Each subdivision has an inner radius of 2.28 m and an outer radius of 4.25 m, contributing to a radial length of approximately 7.4 λ. The segmentation is 1.5, 4.1 and 1.8 λ for the barrel region and 1.5, 2.6, 3.3 λ for the extended barrel region. The dimensions of the sampling cells are $\Delta\eta \times \Delta\phi = 0.1 \times 0.1$ in the first two layers, followed by $\Delta\eta \times \Delta\phi = 0.2 \times 0.1$ in the last layer.

The HEC is made of two separate wheels on each end-cap behind the electromagnetic calorimeter. The HEC extends out to $|\eta| = 3.2$ and overlaps the forward calorimeter to compensate for the drop in material density in the transitional region (between the end-cap and forward calorimeter, around $|\eta| = 3.1$). Inwards, the HEC overlaps the η range of the tile calorimeter by extending to $|\eta| = 1.5$. One HEC wheel is divided into 2 segments along the depth, which makes 4 layers in total on each end-cap. The outer radius of the HEC wheels is 203 mm. The inner radius is 47.5 mm in general but reduced to 37.2 mm in the overlap region with the forward calorimeter. The first segment of the wheel closer to the interaction point are built of 25 mm copper plates while the second segment uses 50 mm copper plates. Between the copper plates, a 8.5 mm gap is filled with LAr as the active medium for the sampling calorimeter. The readout cells correspond to the pads etched on the central foil in these gaps. Below $|\eta| < 2.5$ the size of the readout cells is $\Delta\eta \times \Delta\phi = 0.1 \times 0.1$, while in the region of higher η the granularity of the readout is $\Delta\eta \times \Delta\phi = 0.2 \times 0.2$.

Installed in the same cryostats as the end-cap calorimeters and providing a coverage over $3.1 < |\eta| < 4.9$, the FCal is about 10 λ in depth comprised of three layers of modules in each end-cap. The first layer is made of copper and optimized for EM measurements. Meanwhile, the other two layers are built with tungsten, since they mainly focus on the measurement of the energy of hadronic interactions. Every single FCal module contains a metal matrix, where the regularly spaced channels are filled

with electrode structure made of concentric rods and tubes parallel to the beam. Between the rod and the tube, liquid argon functions as the active medium in the gap. Given that the FCal modules are all located at high η only around 4.7 m away from the IP, the LAr gaps are designed to be very small not only to avoid ion build-up issues when exposed to high particle fluxes, but also to maintain the highest possible density at the same time.

2.2.7 Muon spectrometer

The muon spectrometer makes up the outermost part of the ATLAS detector (Fig 2.8). It is dedicated to the detection of charged particles that penetrate the barrel and end-cap calorimeters. The momenta of the particles can be measured in the range $|\eta| < 2.7$, while the trigger on these particles covers the region $|\eta| < 2.4$. The most important performance goal is to achieve a stand-alone transverse momentum resolution of about 10 % for 1 TeV tracks, or equivalently a sagitta along the beam axis of around 500 µm to be measured within a resolution of 50 µm.

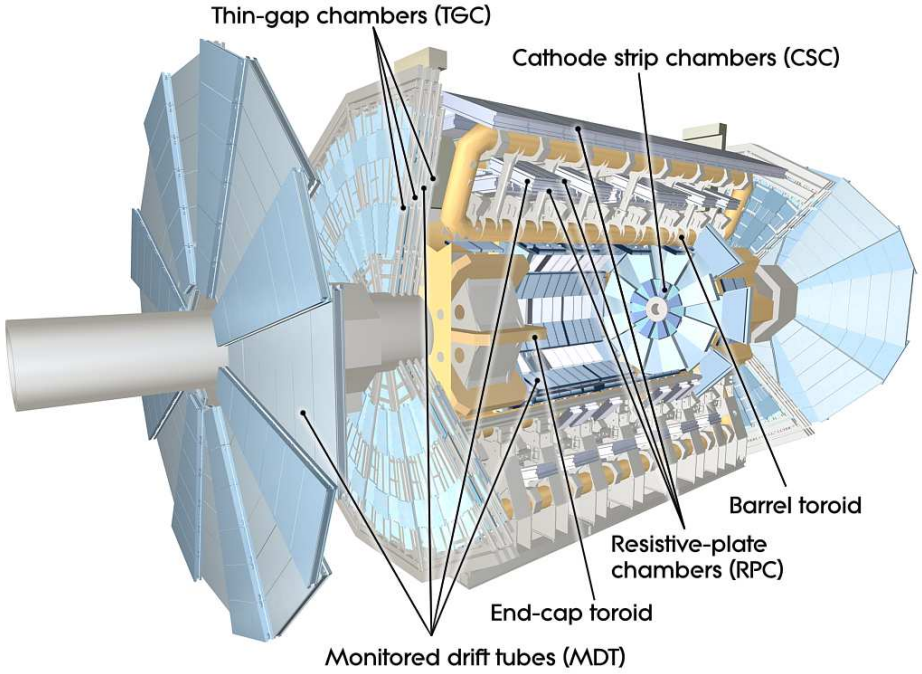

Figure 2.8 – Cut-away view of ATLAS muon system. The toroids are also drawn in the schematics (Figure from [3]).

The operation of the muon spectrometer is based on the magnetic deflection of muon tracks and high-precision tracking chambers combined with separate trigger chambers. Below $|\eta| < 1.4$, the magnetic bending is brought by the large barrel toroid, while between $1.6 < |\eta| < 2.7$ the muon tracks are bent by the end-cap toroids. In the transitional region $1.4 < |\eta| < 1.6$, both the barrel field and the end-cap fields contribute to the magnetic deflection. As for particle detection, in the barrel region, the tracks are measured by three concentric cylindrical shells of chamber around the beam at radii of approximately 5 m, 7.5 m and 10 m. In the transitional and end-cap regions, the muon chambers are also installed in three layers, but in planes perpendicular to the beam axis. The Muon chambers form large wheels in the

end-cap region, located at $|z| \approx$7.4 m, 10.8 m, 14 m and 21.5 m with respect to the IP. In the central region of the detector around $|\eta| = 0$, a gap is left open to accommodate the services to the solenoid magnet, the calorimeters and the inner detectors.

The purpose of the precision-tracking chamber is to determine the coordinate of the track in the bending (η) plane. The precision momentum measurement relies on the Monitored Drift Tube chambers (MDT's). The MDTs cover the pseudorapidity range of $|\eta| < 2.7$ except for the innermost end-cap layer where its coverage is limited to $|\eta| < 2.0$. Each MDT chamber consists of three to eight layers of drift tubes with a diameter of 29.970 mm. The working gas of drift tube is $93\,\%Ar + 7\,\%CO_2$ under an absolute pressure of 3 bar, allowing to achieve an average spatial resolution of 80 µm per tube. A high-precision optical alignment system is also installed to monitor the positions and internal deformations of the MDT chambers, which is accompanied by track-based alignment algorithms.

Because of requirements of high rate capability and time resolution, Cathode-Strip Chambers are used in the innermost tracking layer in the forward region $2 < |\eta| < 2.7$. The CSC detectors are multiwire proportional chambers in which the cathode planes are segmented into strips in orthogonal directions, such that both coordinates can be measured from the induced-charge distributions. The spatial resolution of a CSC chamber of 40 µm in the bending plane and about 5 mm in the transverse plane.

The capability to trigger on muon tracks is a crucial design criterion for the muon system, according to which the precision tracking chambers have to cooperate with a system of fast trigger chambers that delivers track information in tens of nanoseconds after the passage of the muon. In the barrel region $|\eta| < 1.05$, Resistive Plate Chambers (RPC) is chosen as the fast trigger, while for the end-cap region $1.05 < |\eta| < 2.4$ the choice is Thin Gap Chambers (TGC). Both types of trigger chambers can deliver signals with a spread of 15-25 ns, enabling the tagging of the beam-crossing. Besides the fast triggering, the trigger chambers also measure both η (bending) and ϕ (non-bending) coordinates of the track. Once the matching of the MDT and trigger chamber is complete, the trigger chamber's coordinate in the ϕ plane is used as the second coordinate of the MDT measurement.

In Run 3, the inner end-cap of the muon spectrometer, the previous Small Wheels, are replaced by the New Small Wheels (NSW) that are equipped with sTGC and Micromegas detectors. The upgrade of the inner end-cap ensures a high tracking resolution in the high luminosity environment of LHC. More details about the NSW upgrade is covered in Section 3.1.

2.2.8 The Data Aquisition (DAQ) and trigger system

The bunch-crossing interval as short as 25 ns at LHC makes the trigger a challenging task for ATLAS. It is essentially impossible to fully record all of the data for every proton-proton collision. In addition, the majority of the interactions are the soft processes and therefore not concerned by the physics interest in most analysis. For this reason, the Level 1 hardware trigger (L1) and the High Level Trigger (HLT) make up for the trigger system of ATLAS during Run 2 data taking, which aims at eventually reducing the event rate down to around 1.5 kHz [7]. The ATLAS DAQ system delivered high performance and availability during the Run 2 data taking. A detailed work-flow of ATLAS Run 2 trigger and data acquisition system is presented in Fig 2.9.

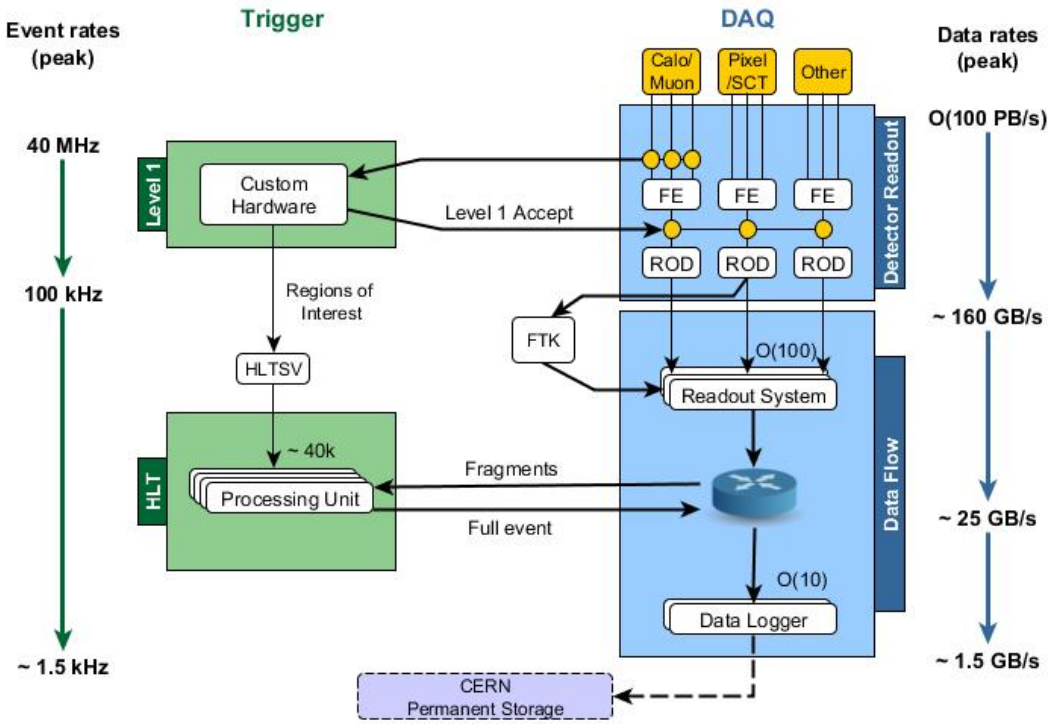

Figure 2.9 – Block diagram showing the work-flow of ATLAS trigger and data acquisition system in Run 2. (Figure from [7].)

The L1 trigger looks for specific signatures from high-p_{T} muons, electrons/photons, jets as well as τ decaying into hadrons. Events with large missing transverse energy ($E_{\mathrm{T}}^{\mathrm{miss}}$) and large total transverse energy are also selected by L1. The L1 trigger makes use of the reduced-granularity information from a subset of detectors, such as the RPC and TGC for high-p_{T} muons, the calorimeter sub-systems for electromagnetic clusters, jets, τ-leptons, large $E_{\mathrm{T}}^{\mathrm{miss}}$ as well as large total transverse energy. The detector Regions of Interest (RoI) are flagged by the L1 trigger for further event processing performed by the HLT.

The possible trigger objects within an event identified by the L1 trigger is passed down to the HLT, which is seeded by RoI defined by these objects. The HLT will first exploit the information on the coordinates, energy and the type of signatures to limit the amount of data transferred from the detector readout. After that, the HLT continues to select the events based on the offline analysis on fully-built events, therefore reducing the rate to a level that can be recorded for the offline analysis. Full granularity and precision of the calorimeters and the muon chamber data is used by the HLT algorithms to further improve the trigger selections.

The event data from the detector front-end electronics systems are sent to the Readout System (ROS) in response to a L1 trigger acceptance signal. The ROS buffers the event data passing L1 selection. The HLT requests data from the ROS during its processing of each event, then decides either to accept this event and send it to the Data Logger for permanent storage, or to request the deletion of the event from the ROS buffers. The ROS in Run 2 is capable of buffering an input data rate

of 100 kHz while sending 50 % of the data to the HLT without loss of performance, which comfortably satisfies the ATLAS requirement for Run 2.

References

[1] L. Evans and P. Bryant, "LHC machine", *Journal of Instrumentation*, vol. 3, no. 08, S08001–S08001, Aug. 2008. DOI: 10.1088/1748-0221/3/08/s08001. [Online]. Available: https://doi.org/10.1088/1748-0221/3/08/s08001 (cit. on p. 20).

[2] O. S. Brüning, P. Collier, P. Lebrun, *et al.*, *LHC Design Report* (CERN Yellow Reports: Monographs). Geneva: CERN, 2004. DOI: 10.5170/CERN-2004-003-V-1. [Online]. Available: http://cds.cern.ch/record/782076 (cit. on p. 22).

[3] The ATLAS Collaboration, "The ATLAS experiment at the CERN large hadron collider", *Journal of Instrumentation*, vol. 3, no. 08, S08003–S08003, Aug. 2008. DOI: 10.1088/1748-0221/3/08/s08003. [Online]. Available: https://doi.org/10.1088/1748-0221/3/08/s08003 (cit. on pp. 22–26, 28, 30).

[4] C. Grupen and B. Shwartz, *Particle Detectors* (Cambridge Monographs on Particle Physics, Nuclear Physics and Cosmology). Cambridge University Press, 2008, ISBN: 9781139469531. [Online]. Available: https://books.google.fr/books?id=XCPlJTu3GQkC (cit. on p. 25).

[5] The ATLAS Collaboration, "Production and integration of the ATLAS insertable b-layer", *Journal of Instrumentation*, vol. 13, no. 05, T05008–T05008, May 2018. DOI: 10.1088/1748-0221/13/05/t05008. [Online]. Available: https://doi.org/10.1088/1748-0221/13/05/t05008 (cit. on p. 26).

[6] S. Morgenstern, "ATLAS LAr calorimeter performance in LHC Run-2", *Nucl. Instrum. Meth. A*, vol. 936, G. Batignani, M. Grassi, R. Paoletti, *et al.*, Eds., pp. 86–89, 2019. DOI: 10.1016/j.nima.2018.11.027 (cit. on p. 27).

[7] W. P. Vazquez and on behalf of the ATLAS Collaboration, "The atlas data acquisition system in lhc run 2", *Journal of Physics: Conference Series*, vol. 898, no. 3, p. 032 017, Oct. 2017. DOI: 10.1088/1742-6596/898/3/032017. [Online]. Available: https://dx.doi.org/10.1088/1742-6596/898/3/032017 (cit. on pp. 31, 32).

Chapter 3

Cosmic Bench Characterization of ATLAS NSW LM1 Micromegas quadruplets

Contents

3.1 NSW upgrade of ATLAS experiment

The steadily increasing luminosity of LHC requires an upgrade to high rate and high-resolution capable detector technology for the inner end cap of the muon spectrometer of the ATLAS experiment. To fulfill this goal, the original two Small Wheels were replaced with New Small Wheels that are more powerful in terms of triggering and precision tracking [1]. In the high background of the upgraded LHC, the maximum hit rate predicted for the inner end-caps of the muon spectrometer will be approximately 15 kHz cm^{-2} [2]. In order to maintain the high precision of muon momentum resolution (ranges from 1.7 % to 4 % depending on transverse momentum as well as rapidity [3]), the spatial resolution of around 100 µm for track reconstruction is required.

The NSW sub-detector system is composed of two wheel-like structures of 10 m in diameter, as shown in Figure 3.1. Each wheel includes 8 small sectors and 8 large sectors. While the small sectors are settled towards the ATLAS Interaction Point (IP), the large sectors are installed beyond the small sectors, further away from the IP. The coverage area in radius is from 90 to 445 cm for small sectors and from 92 to 465 cm for large sectors [4]. Besides being compatible with the existing tracking detectors and the end-cap alignment system of ATLAS as well as having high-precision trigger and tracking capability, the layout of NSW also requires a certain degree of redundancy for tracking and triggering. The small and large sectors on a wheel are installed in the projective geometry of EM and EO Monitored Drift Tube (MDT) chambers [5]. The redundancy is achieved by placing 8 detection layers of small-strip Thin Gap

Chambers (sTGC) [6] and 8 detection layers of Micromegas (MM) [7] in each sector. The lever arm between primary trigger chambers are maximized by covering two Micromegas quadruplets with a sTGC quadruplet on each side, in a sTGC - MM - spacer frame - MM - sTGC pattern. With the overlap area between adjacent small and large sectors, the NSW is competent to obtain a full coverage of $|\eta|$ from 1.3 to 2.7 for precision tracking and from 1.3 to 2.5 for trigger acceptance.

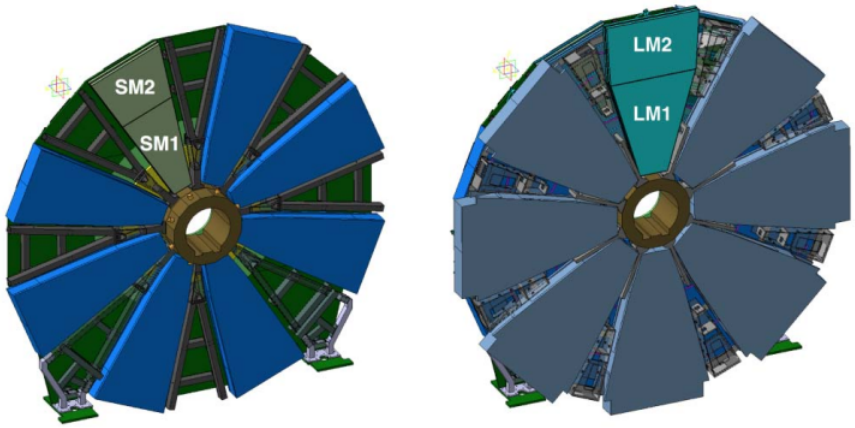

Figure 3.1 – View of the ALTAS NSW with 8 small sectors (left) covered by 8 large sectors(right). Each sector has a trapezoidal shape. (The mechanical structure is also presented. Figure from [4].)

Four different shapes of planar detectors are produced to fill the small and sectors for both sTGC and Micromegas, noted as LM1, LM2, SM1 and SM2. Since one large or small double-wedge sector consists of two quadruplets, there are 16 quadruplets of each planar detector on a wheel and 32 quadruplets in total.

3.2 Micromegas for NSW upgrade

3.2.1 The Micromegas technology

Micromegas [8] is one type of Micro-Pattern Gaseous Detectors (MPGD). The name Micromegas stands for MICRO-MEsh GAseous Structure, which indicates the main characterization of the detector: the gas volume is asymmetrically divided by metallic mesh into two gaps. The primary ionization occurs in the thicker conversion gap by design, where the electric field supports a uniform drift of free electrons. After passing the mesh, the strength of electric field is higher so that the multiplication of electrons can be concentrated within the thinner amplification gap. This ratio between the electric field in the amplification gap and the one in the conversion gap needs to be tuned to a properly large value in order to achieve an optimal performance of the detector. A schematic view of the electric field in a Micromegas detector is shown in Fig 3.2 (Image taken from [9]).The high electric field field in the amplification gap also provides an advantage of collecting the ion cloud quickly, such that only a small part of the ions pass through the micromesh and escape to the conversion gap [10]. The amount of escaping ions is in fact inversely proportional to the electric field ratio described above. The electron multiplication process is restricted locally to the holes

on the mesh, providing a great potential for high rate capability as well as high spatial resolution.

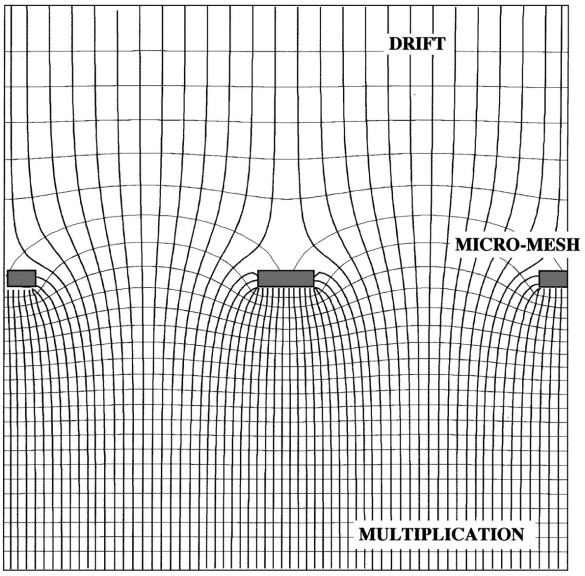

Figure 3.2 – The electric field map in Micromegas detector. (Figure from [9].)

A typical Micromegas detector is composed of the following components:

(1) Anode electrode. Anode strips can be directly placed at the end of gas gap for signal collection in non-resistive Micromegas. For Micromegas with resistive readout design, such as NSW Micromegas modules, the readout strips have to be separated and isolated from the resistive anode. The resistive readout scheme suppresses the global drop of voltage due to sparks at high rate, preventing the occurrence of a long dead time.

(2) Supporting pillars. Pillars are glued on the anode to support the micro-mesh structure during the operation. When high voltage is applied to the detector, the micro-mesh tends to be pressed towards the anode due to the electric force. Hence, the thickness of the amplification gap is determined by the height of supporting pillars, which is in the order of 100 µm. A photo of a supporting pillar used in NSW Micromegas is shown in Fig 3.3.

(3) The micro-mesh. The micro mesh tunes the electric field in the gas volume. Following the non-uniform local electric field, free electrons are induced to drift through the holes on the mesh. Although the mesh is usually fabricated in a dense pattern and shows a low optical transparency, the electric transparency is mainly influenced by the electric field ratio between two gaps and can easily become higher than 95 % for most designs.

(4) The cathode. The cathode, together with the micro mesh, defines the volume of conversion gap.

(5) The working gas. Working gas is filled in the gas volume to facilitate the primary ionization, drift as well as multiplication of electrons with quenching capabilities.

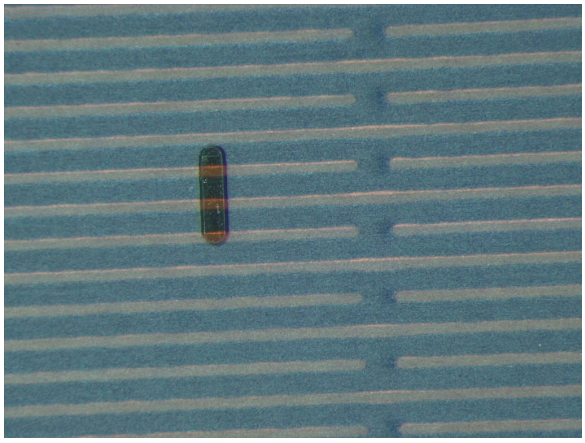

Figure 3.3 – Photo of a pillar on top of the readout panel of NSW Micromegas. The surface of this supporting pillar is about $1.2\,mm \times 200\,\mu m$. The strips in shallow color are the resistive strips.

3.2.2 An overview on NSW Micromegas

The Micromegas detectors used for NSW upgrade are constructed in parallel plate structures and working in proportional mode. While a negative voltage is applied to the cathode at the beginning of the 5 mm-thick drift gap, the mesh is connected to the ground. The positive voltage on the other side of amplification gap ensures a sufficient amount of electron multiplication. The NSW Micromegas adopted the resistive readout scheme, according to which the positive voltage is applied to a layer of resistive material above the readout PCB panel. Although the resistive strips have the same shape of readout strips and are aligned in the same position and direction to the readout strip, the two types of strips are separated by a glued Kapton foil as insulator to prevent any direct contact. The "ladders" between resistive strips are designed to realise a uniform resistivity on the anode surface. Figure 3.4 shows the appearance of a PCB readout panel, along with a zoomed view of the details on the PCB. The sensitive area of each detecting layer is surrounded by metal frame that defines the thickness of the drift gap. Above the PCB panel, an O-ring is inserted in the groove of the metal frame to ensure the gas tightness in the peripheral region, while in the central region of the panel far away from the O-ring, additional interconnections provide mechanical support of the structure. These interconnections are hollow cylinders appearing in all the gas gaps of the module. During the assembly in the clean room, a long screw is perpendicularly penetrated through the 4 layers of the detector, tightening the detector and fixing the position of each interconnection. The internal components of the Micromegas are shown in Figure 3.5.

At the start of the project, the working gas of NSW Micromegas was chosen to be the mixture of 93 % Ar and 7 % CO_2 at atmospheric pressure. While argon can be easily ionized by the high energy muons, the CO_2 plays the role of a quencher to maintain a stable operation.

The NSW Micromegas quadruplets are produced by different institutes (SM1: INFN, Italy, SM2: Germany, LM1: Saclay, France, LM2: Dubna, Russia - Thessaloniki, Greece - CERN) and then transported to CERN for construction of double-wedge sector as well as final installation. The structure of double-wedge sectors is shown in Figure 3.6.

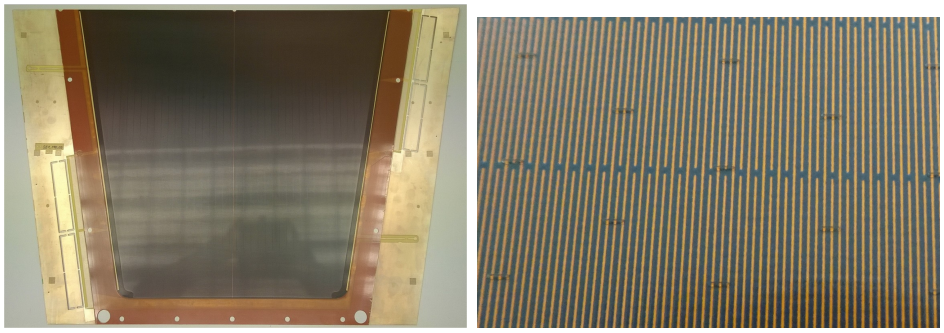

Figure 3.4 – Left: Picture of a trapezoidal PCB1 readout panel. Right: The resistive strips and pillars on the readout PCB. (Figures from [4].)

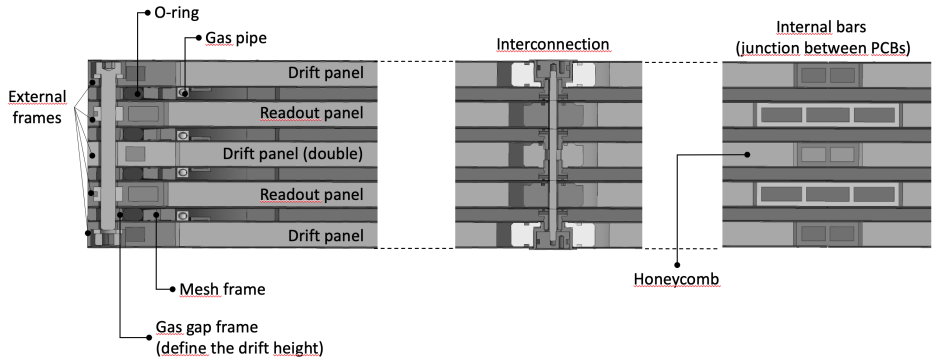

Figure 3.5 – Sectional view of a NSW Micromegas quadruplet, showing the internal components such as O-ring, the interconnections and so on. (Figure from [4].)

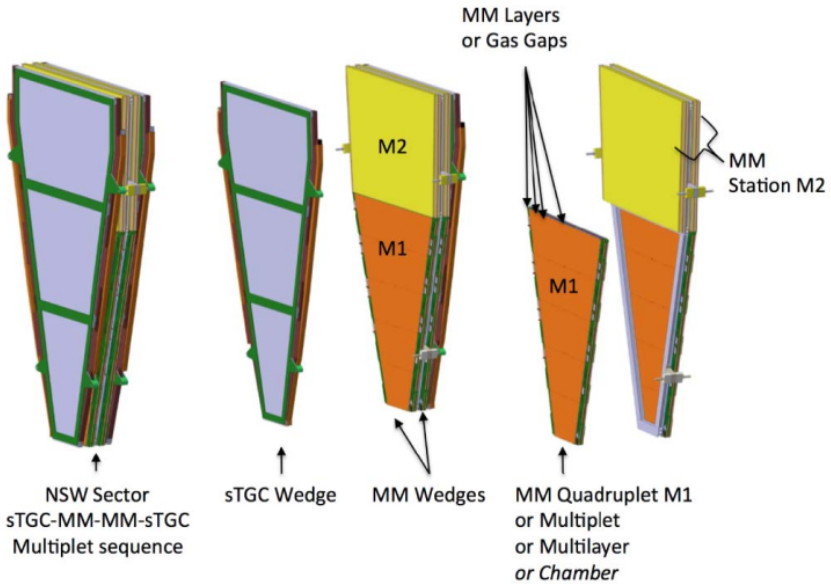

Figure 3.6 – A NSW double-wedge sector. (Figure from [4].)

3.2.3 NSW LM1 Micromegas quadruplets

The 32 LM1 Micromegas quadruplets are all produced at CEA Saclay. The production of the quadruplets comprises of the construction of readout and drift panels,

the resistivity measurement and passivation, planarity scan of the panels, as well as the assembling of the quadruplets [11]. After the production, the LM1 modules are validated both at Saclay and at CERN but via different sets of test procedures to ensure the detectors meet the requirement of NSW. Geometrically, the NSW LM1 Micromegas quadruplet is made of 4 trapezoidal detection layers with each layer containing 5 PCBs: starting from PCB1, the index increases from the small base to the large base. (Figure 3.7, Figure 3.8)(A picture to show the dimensions of LM1 modules, emphasis that LM1 is the largest type of Micromegas in NSW upgrade) The detection layers are arranged in a sandwich pattern. The readout strips on the first two readout panels (noted as Layer 1 and Layer 2) are perpendicular to the height of the panels and are also called eta panels since the measurement of position from those strips can offer the eta information of muon in the ATLAS experiment. Meanwhile, the other two panels (Layer 3 and Layer 4) are composed of readout strips carrying ± 1.5 degrees inclinations to reconstruct the second coordinate while allowing the measurement of the eta coordinates (Figure 3.9). With the $93\,\%Ar + 7\,\%CO_2$ gas mixtrue, the drift voltage of NSW LM1 Micromegas quadruplets is $-300\,\mathrm{V}$, while the nominal high voltage on the resistive layer is $570\,\mathrm{V}$. One PCB panel is divided into left and right sectors with separate high voltage supply. For each gas gap, the mesh is supported by $128\,\mu\mathrm{m}$-high Pyralux pillars above the resistive layer [12], as the structure presented in Figure 3.10. To compensate for the insufficient surface resistance of the resistive layer, a technique called "passivation" is applied to the areas that are prone to sparks, including the borders of PCBs and the vicinity of mechanical interconnections. Passivation involves applying glue above the vulnerable sensitive areas of the readout panel to prevent the amplification of electrons from ever happening. Despite the loss of acceptance, this technique is proved to be an indispensable step in the production to ensure a good HV performance of the module.

In order to achieve the $100\,\mu\mathrm{m}$ spatial resolution required by NSW, nominally one PCB panel on a single layer of LM1 Micromegas should have 1024 readout strips, each $300\,\mu\mathrm{m}$ in width and $150\,\mu\mathrm{m}$ gap between neighbor strips. As for the signal readout, the 1024 strips are divided from the middle so that first 512 strips and the other 512 strips are readout from two sides of the PCB. However, contrary to traditional method, no soldered connector is used for LM1 modules. Instead, the electronics is always connected using Zebra elastomeric connector [13] on front-end electronics board, which increases the flexibility of connection. The metal brushes on the Zebra connectors are designed to stay contact with the footprints of the readout strips, enabling the transmission of electrical signals. The mounting position of the front-end electronics board is fixed by precision pins and the compression bars installed on the module.

3.3 Cosmic ray test bench at CEA Saclay

The cosmic ray test bench at Saclay occupies an area of $20\,\mathrm{m}^2$ and is able to scan the surface of NSW LM1 Micromegas modules by sliding a supporting tray (Figure 3.11). On the bench, there are 3 external trackers called Mcube detectors that are Micromegas telescopes initially designed for muon tomography [14]. The layers of external trackers are denoted as HH, HB and BH from top to bottom. Each reference Mcube detector covers an area of $1\,\mathrm{m}^2$ and consists of four $0.5\times0.5\,\mathrm{m}^2$ bulk-

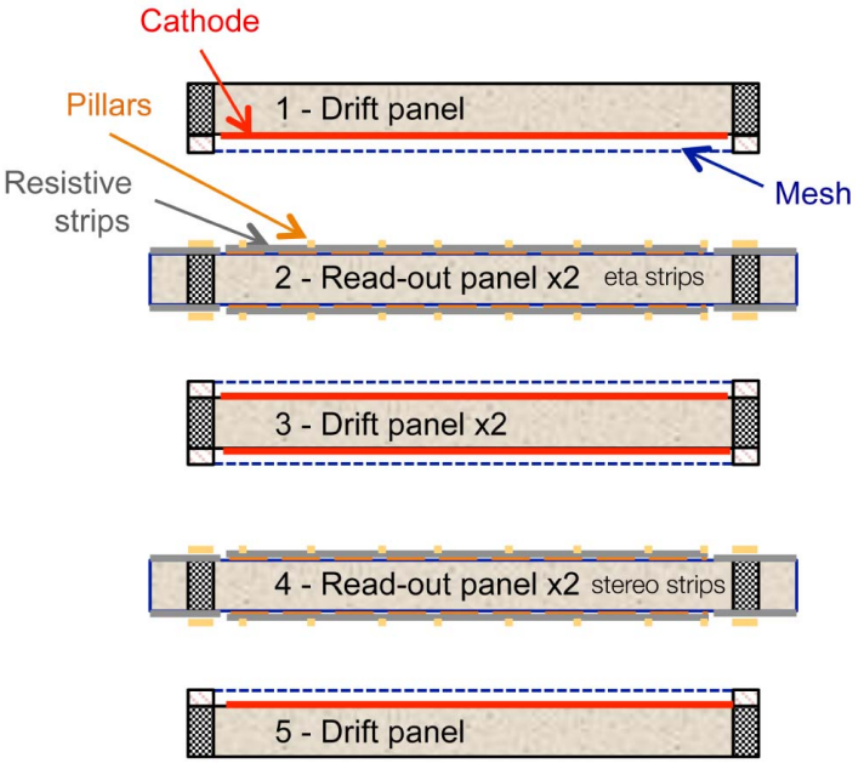

Figure 3.7 – Cross section view of NSW Micromegas illustrating the structure of 4 detecting layers. (Figure from [4].)

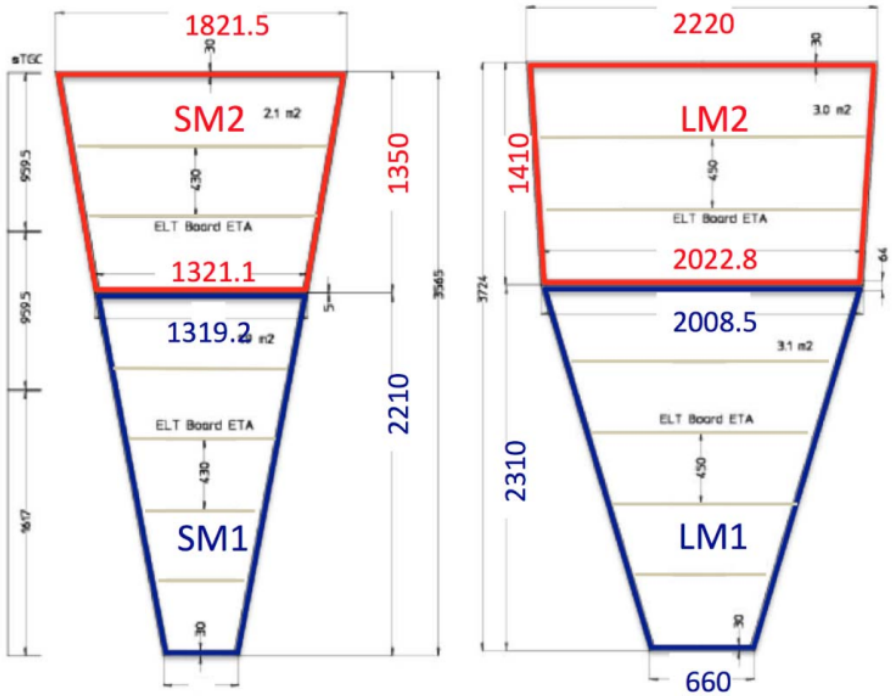

Figure 3.8 – Dimensions of different NSW Micromegas modules including non-sensistive area. LM1 quadruplet is the largest one among four types of detectors. (Figure from [4].)

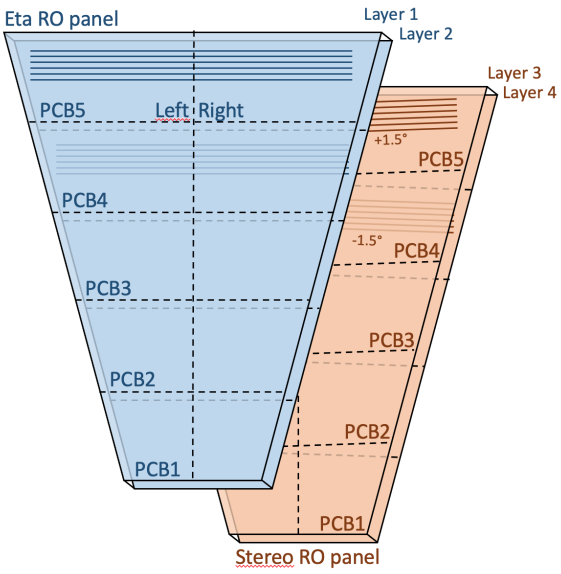

Figure 3.9 – Directions of readout strips on four readout planes in a quadruplet. (Figure from [11].)

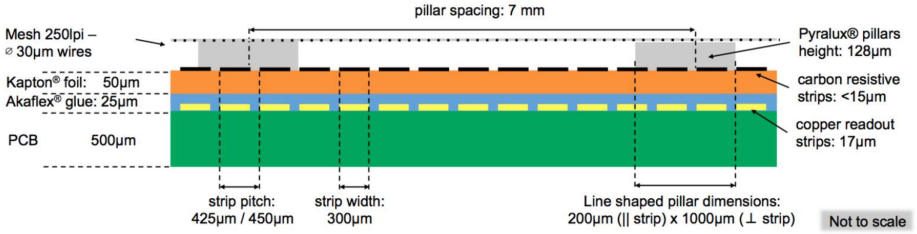

Figure 3.10 – Structure of the readout panel together with the mesh. (Figure from [11].)

Micromegas (Multigen2D) with a drift gap of 1 cm [7]. The Mcube system has a 2-dimensional readout. Therefore, a track of the cosmic muon, of which the average energy is 4 GeV [15], can be reconstructed by the three layers together. In order to save electronics channels, the 1024 strips of one Multigen2D detector are multiplexed into only 61 channels [16]. These external trackers work with 95 % Argon+5 % Isobutane mixture provided by an independent gas system.

Given that the development for LM1 cosmic ray characterization took place before the readiness of VMM electronics [17] which is currently used on NSW, the cosmic test bench at Saclay chose the available Deadtimeless Readout Electronics ASIC for Micromegas [18] as the readout electronics. DREAM, developed at CEA for CLAS12 experiment [19], is able to cope with Micromegas detectors with high strip capacitance (200 pF for 2 strips on PCB5 in a measurement) while keeping the signal to noise ratio larger than 10. This setup of electronics for cosmic test bench has been validated in both CLAS12 experiment and muon tomography [20].

The signal readout of both the NSW modules and Mcube are achieved via a data acquisition system based on DREAM electronics. A Front End Unit (FEU) board consists of 8 DREAM ASIC chips and is placed inside the crate. Since one DREAM corresponds to 64 channels and there are 8 FEU for the readout of LM1 module, the test bench is then competent to take data of 4096 strips at the same time. However, the LM1 module contains about 20,000 strips in total and thus around 4,000 strips

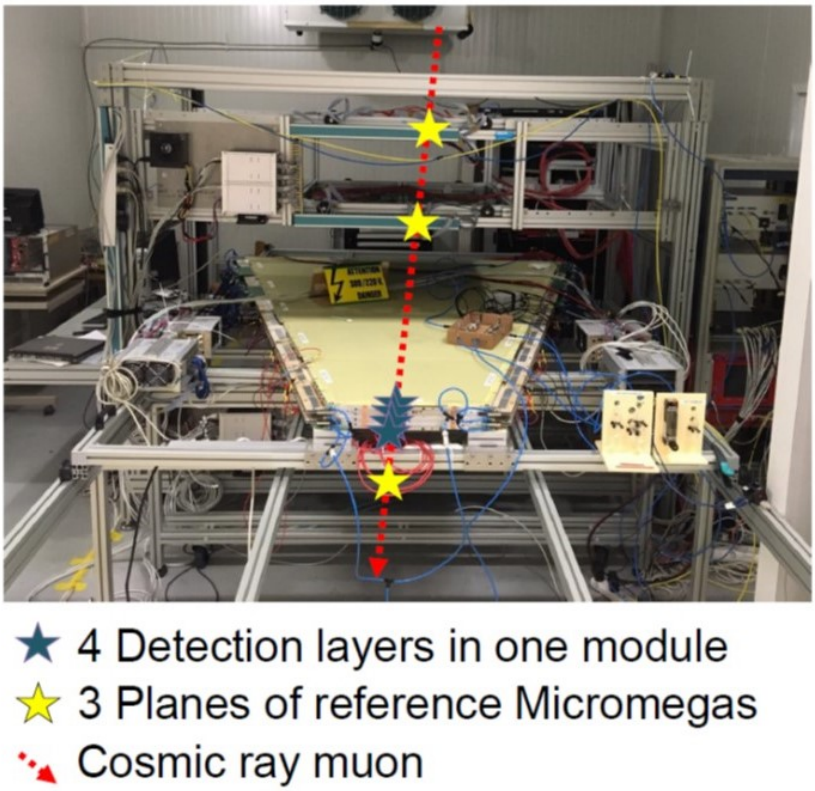

Figure 3.11 – A photo showing the setup of Saclay cosmic bench. 3 layers of Mcube system is included together with the LM1 module ready for test.

per PCB. Connecting DREAMs directly to the zebra line on LM1 means the cosmic bench is able to scan only one PCB of LM1 module at a time, which is not only time consuming but also fail to profit of the full sensitive area of the external trackers. As a solution to this scheme, electronics channels are adapted to zebra lines via a multiplexing strategy. The idea is to use the adapter to associate one channels to two strips. Considering the low cosmic ray multiplicity of LM1 module (only 3-4 strips for a muon event), it is possible to design a multiplexing circuit with a special pattern of connection to save electronics channels. A multiplexing factor of 2 has been decided as the final option, as it maintains a good signal to noise ratio while fully making use of the coverage of Mcube system.

3.4 Test protocol

Every NSW LM1 quadruplet is installed on the cosmic test bench after assembly and quality checks described in [11]. The module can be sent to CERN for NSW installation only if it has passed through the validation procedures on the cosmic bench.

The humidity is among the many factors (dust, panel planarity and so on) that affect the high voltage stability of Micromegas. If the humidity exceeds a certain limit in the gas gap, high voltage instabilities will show up upon the Micromegas modules. It has been observed that water may remain inside the PCB panel after washing and

cleaning, which can slowly evaporate into the gas gap, causing high leakage current or even sparks during operation of the detector. To speed up the drying-up, while flushing the working gas, modules are covered by plastic foils and heated from the bottom to get rid of humidity. Once the relative humidity (RH) reached as low as 20 % at 45 °C, the heaters are turn off. The module will cool down to room temperature around 20 °C after 12 hours. By monitoring the relative humidity of going-out gas, one is able to compare the humidity of the module before and after the heating. The RH is reduced from 37 % to 8 % through a 3-day heating process. The monitoring of this process is shown in Figure 3.12.

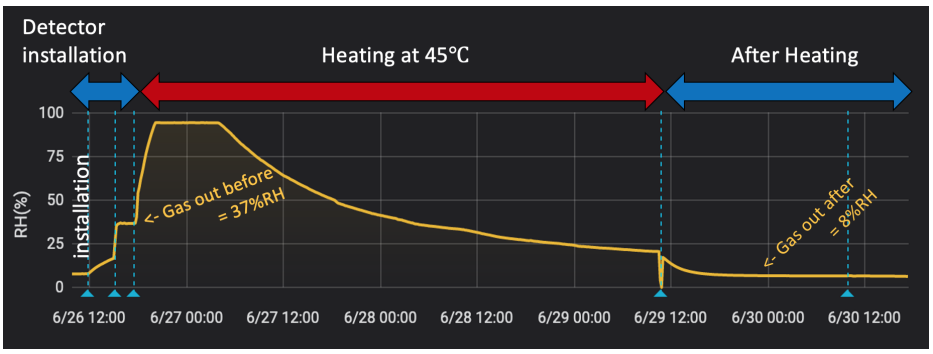

Figure 3.12 – The reduction of humidity by heating the LM1 module. The orange curve stands to the relative humidity of going-out gas, which represents the humidity inside the detector. Although the value of relative humidity depends on the temperature, in the end we still observed a great drop of the humidity after the module cooled down back to room temperature.

Once the module is verified to be dry enough, specifically when the relative humidity (RH) of going-out gas is lower than 10 %, the high voltage will be applied to the resistive strips. While the drift voltage is always 300 V for the 4 layers and can be easily achieved, the increase of the amplification voltage to 570 V requires a slow ramp up process. It turns out that the best results can be achieved only via a relatively slow and careful ramp-up of high voltage above all the 40 HV sectors. On the cosmic bench, the high voltage and corresponding current consumption are monitored by an automatic HV control program. To avoid tripping, a sector can rise up to the next HV step only when its current is low and stable after a certain time interval. In case the current fluctuates too much, the corresponding HV will be automatically reduced to a lower level for protection.

One more step before the actual data taking is to check the connection of Mux2 cards. As the Mux2 cards are always pressed to the module by metal compression bars, a careful cleaning is necessary before the mechanical installation of Mux2 cards on the module. This cleaning procedure makes sure that any dust or remaining glue from the tapes used in the production are removed from both the footprints on the module and the zebra lines on Mux2 cards. The first check of connection is by taking pedestal RMS of each electronics channel. A non-uniform pedestal may suggest some missing connection since the noise of a electronics channel is proportional to the capacitance. The known bad connections can then be improved by re-plugging of Mux2 card or adjusting the connectors of cables. The second check comes with a short data taking after the module is slid to the Mcube window. A short data taking is necessary because the multiplexing hides the missing connections in the noise run

of electronics pedestal. If the number of event counts in a channel is half of the others, it is very likely that the electronics channel in concern has a bad connection to one of its readout strips. The bad connections will be restored as good as possible before the HV scan and the long runs.

Due to the limited length of Mcube and the number of available electronics channels, the data taking has to be repeated for three times in order to scan all the strips in LM1 module. The test starts from PCB45, then moves to PCB23 and ends at PCB1 (Figure 3.13), which usually takes one week. For PCB3, 4 and 5, the surface beyond the Mcube acceptance will not be scanned because of the tight production schedule.

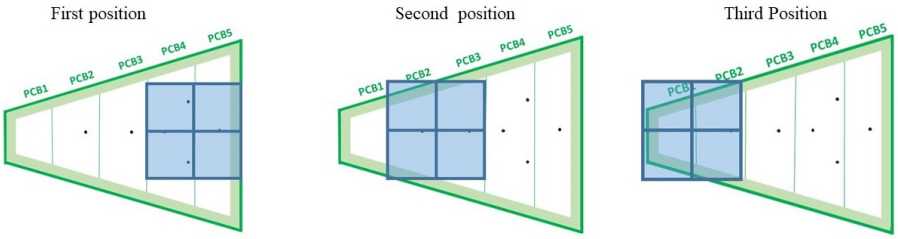

Figure 3.13 – The scheme of data taking for 5 PCBs. In order to scan all the 5 PCBs, the module needs to be at least posed at 3 positions. The blue square refers to the reference Mcubes, which are always fixed to the frame of cosmic bench. The offset between Mcube and the LM1 module along X direction can be obtained by data analysis after data taking and will be corrected before evaluating the performance of the LM1 module. (Figure from [11].)

3.5 Cosmic bench data analysis

The data analysis code of LM1 cosmic muon characterization [21] has been adapted from muon tomography studies and has been evolving to the last version of the analysis that was finished in 2020. It is divided into 4 steps that will be further illustrated:

1. Subtraction of pedestal: The amplitudes of electronics channels go through the common noise suppression, as well as the subtraction of mean amplitude value in the absence of a cosmic muon signal (the pedestal is subtracted to have equalisation). The suppression of a remaining common mode noise follows the pedestal subtraction: While the 50 samples are collected, the baseline amplitudes of all strips of a given Front-End-Unit (FEU) electronics are interpreted to be the common mode and are moved coherently.

2. Hit finding: After the subtraction of the pedestal and the suppression of the common mode noise, only the signals that have amplitudes 5 times than the standard deviation of channel pedestal are considered to be "hits".

3. Clustering: The neighboring hits gathered to form clusters. Since signals are readout in a multiplexing pattern, the conversion from electronics channels to strips requires a dedicated demultiplexing algorithm.

4. Track to cluster matching: The cluster matching algorithm associates muon tracks to the reconstructed clusters on each layer by an interpolation. Requirements

on the quality of the track are applied. A count of detected or undetected events gives the efficiency of each strip.

The above mentioned stages are all configured by a general configuration file. This configuration file is uniquely linked to the analysis of a specific data taking, where the geometric setup of the cosmic bench, the path to the pedestal as well as signal files, the cluster reconstruction algorithm, the arrangement of readout electronics and so on, are defined for the programs at each stage.

3.5.1 Subtraction of pedestal

The pedestals are calculated as the mean values of amplitudes without response to cosmic muon. In the pedestal taking, the amplitudes are recorded according to random triggers. The pedestals for all channels in one FEU are shown in Figure 3.14. Here Figure 3.15 shows an event display of 8 DREAMs in a FEU when muon passes through the LM1 module. 32 samples are collected for every event, with a sampling period of 60 ns. While pedestal subtraction is applied to the signals, the baseline of strips are also moving coherently for a given FEU. Their remaining common mode will also be suppressed. By the end of this stage, the information of pedestals is recorded in a text file while the processed signals are stored into root files.

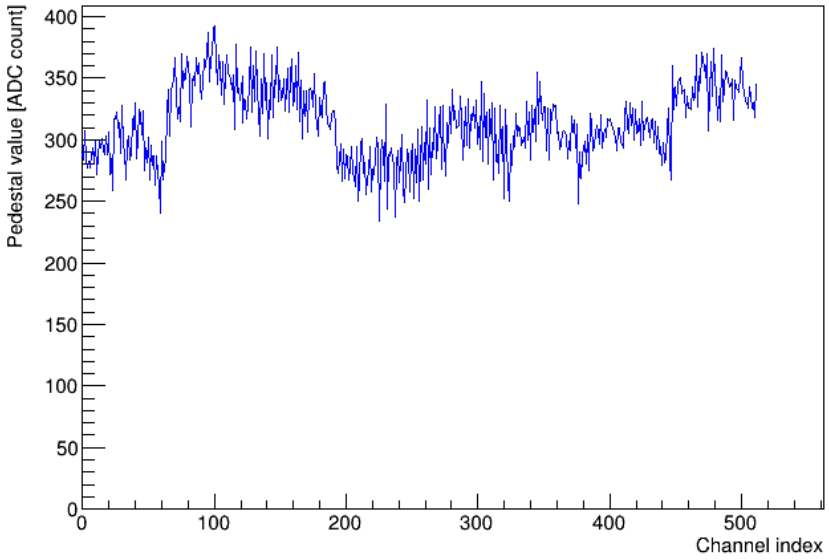

Figure 3.14 – The pedestal values of all channels on a FEU board during a pedestal taking.

3.5.2 Hit finding

The standard deviations of pedestals are obtained along with their mean amplitudes and are usually about 10-15 ADC counts. The hits are then selected according to the 5 times pedestal RMS criteria. Therefore, the amplitude of hits is supposed to be larger than 50-75 ADC units in most cases. The selected hits are saved as another root file, ready for the process of clustering. Considering that the connectors to the zebra line on the Mux2 card can be worn out over time, replacement of the zebra line connectors is necessary, which involves unplugging and re-plugging the readout cables

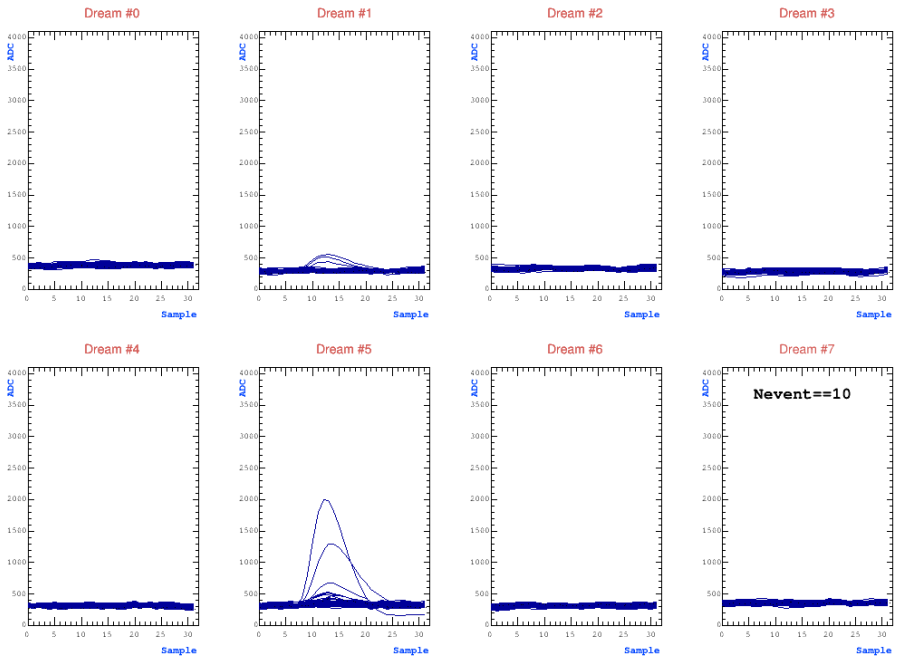

Figure 3.15 – An event display extracted from the raw data for 8 DREAMs on a FEU board. Signals from two DREAMs are observed, since these two DREAMs are fixed in the same X and Y locations of the module but on different layers. Pedestals around 256 are visible, as no correction is applied.

to the zebra line connectors. However, the readout cable can be inserted to the socket of the zebra line connector either way round, bringing the possibility of connecting them in an inverted way by mistake. The hit finding algorithm therefore includes the flexibility of handling inverted zebra line connection, such that the data analysis can be carried out regardless of this type of mistake. When an inverted zebra line connection happens, as the example presented in Fig 3.16, the mistake can be easily identified by comparing the physical position of the hit on the LM1 module with the cosmic muon predicted by the external trackers. Once identified, the mistake can be fixed by the hit finding algorithm as long as the identified inverted connection is manually labelled out in the corresponding configuration file.

3.5.3 Clustering

Clustering is performed separately on each layer, since the amplification is independent in the four gas gaps. The objective of clustering is to convert the "hit map" (Figure 3.17(a)) of electronics created by "hit finding", to a "cluster map" (Figure 3.17(b)) that records the positions of reconstructed clusters per detecting layer.

Due to the fact that one electronics channel is linked to 2 strips via the Mux2 card in the way indicated in Fig 3.18, referred to as "multiplexing", it is impossible to determine the position of a single hit. The demultiplexing is thus necessary in order to perform the reconstruction of clusters. To begin with, the hit with highest amplitude is chosen and matched with other hits according to a channel-to-strips map created in configuration file for this run. For every matching, both combinations are considered, assuming the hit comes from either of the two strips associated to each

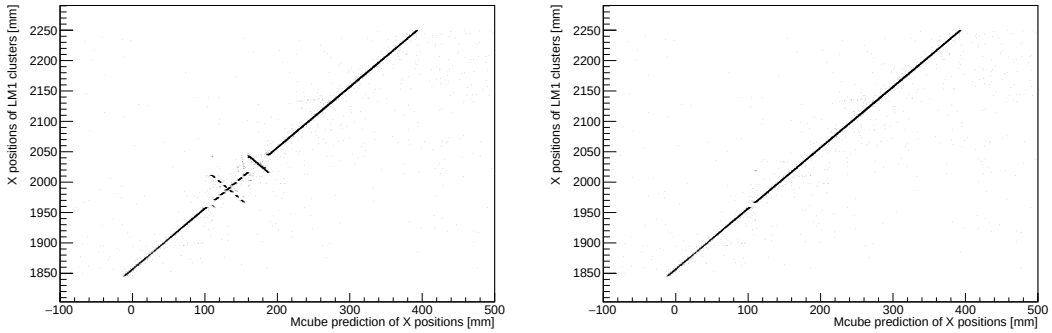

(a) (b)

Figure 3.16 – The correlation of X position between Mcube prediction and LM1 clusters for M35 PCB5 layer2. The offset of X position is not set to zero in this plot. (a) The correlation in the presence of an inverted cable connector. (b) The correlation after taking into account the inversion of cable connector in the configuration of data analysis.

channel. Two strips are considered to be neighbors if they are within the interval of 2 strips, or in another word, 0.9 mm from each other. Once the neighbors are found, the responding strips of both hits are fixed and the two hits are merged into a cluster. The demultiplexing algorithm then loops over the rest of the hits, trying to form a cluster as large as possible, provided that one possible strip of the next hit turns out to be the neighbor of a determined strip in the growing cluster. The clustering of this cluster ends when no more neighbor strip can be found. After that, the clustering of another cluster begins in the same method, gathering remaining clusters into a new cluster. The clustering finishes until all hits are uniquely assigned to a cluster. In case that a hit can never find any neighbor for both of its associated strips, two unity size clusters are generated in the position of each strip. Given that time window of the reference Mcubes is 32 samples $\times$ 40 ns, the small flux of cosmic muon ensures a low rate of signal for the reconstruction of a single cosmic ray muon most of the time. The trigger rate of Mcubes is below 20 Hz due to its efficiency, the acceptance angle and the high threshold on the electronics side to work in auto trigger. Even if sometimes more than one correlated particles are produced in the cosmic ray shower (of which the size is in the scale of meter), the muon tracks may become difficult to reconstruct in the Mcubes, therefore making the event being rejected due to the low quality of the reconstructed track. As a result, mainly the events with one cosmic muon are used to study the performance of the LM1 Micromegas, so that the duplication of multiplexing has a negligible effect to cluster and will not bring any major bias due to the mixture of multiple muon tracks. It has been checked by comparing to the data taking without multiplexing that the deficit in efficiency due to multiplexing is small, as long as the detectors work in the nominal HV.

The charge of a cluster is defined to be the sum over the amplitudes of all the constituent hits. The position of the cluster is the average weighted strip number of its hits where the strip number is weighted by the amplitude. While a hit must come from a physical strip, the position of a cluster refers to the centroid position except cluster of unity size. By the end of this step, the properties of clusters are saved in a format easy for the analysis of track matching.

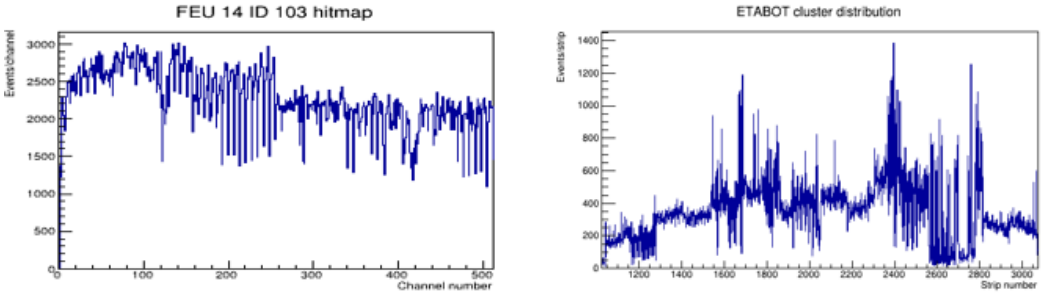

(a) Hit map (b) Cluster map

Figure 3.17 – Examples of (a) The "hit map" of electronics and (b) The "cluster map" of one detecting layer of the LM1 module during the cosmic bench characterization.

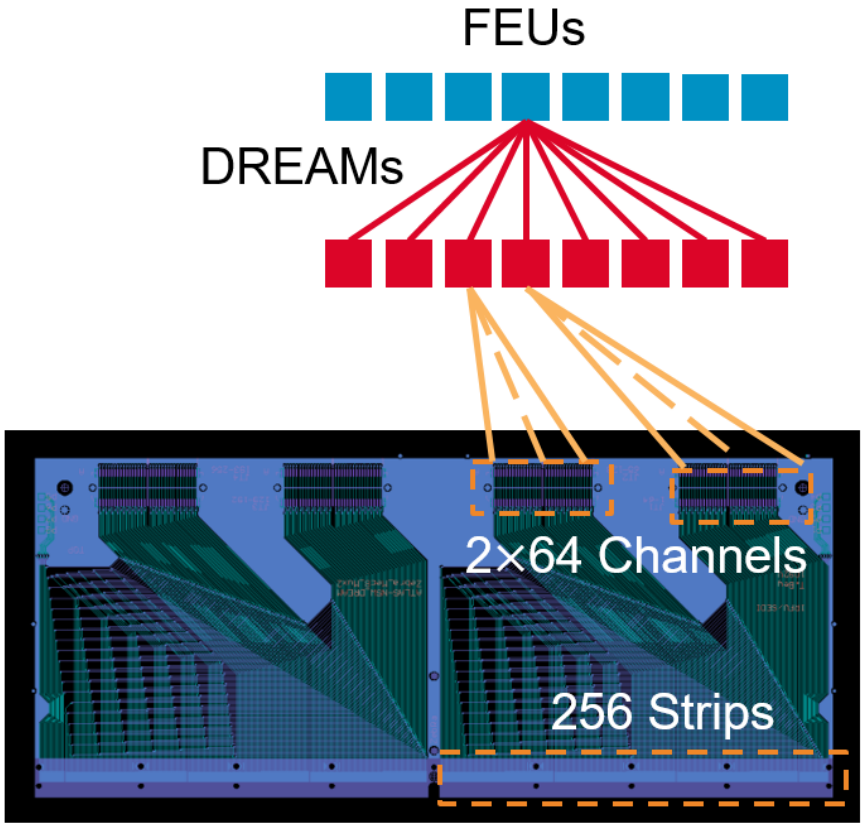

Figure 3.18 – Schematic view of the multiplexing readout. Each 128 electronics channels of 2 adjacent DREAM ASIC chips are associated to 256 readout strips of the LM1 module through the Mux2 card. The channel-to-strip projection is not always continuous, such that the granularity of the strips can be retained in cosmic ray tests.

3.5.4 Track to cluster matching

A Mcube track matches a cluster if the residual along X direction is smaller than the residual cut, which is set to 10 mm. However, selection is applied to both Mcube tracks and clusters before matching of a cosmic muon event.

Based on the signal readout of 3 Mcubes, the cosmic muon rays are reconstructed by a tomography program of which the essential idea is similar to the algorithm described in [20]. Considering the geometry of the cosmic bench, the selection of

good tracks requires muon rays with χ^2_X less than 2.5, χ^2_Y less than 10 and incident angle no more than 0.4 rad. Here X and Y are orthogonal axes of Mcubes. The cut in the Y direction is looser than that in the X direction because of worse resolution of the Mcubes along the Y direction. The Y is also the direction of readout strips stretching on the eta layers of LM1 module on cosmic bench. In some rare cases, there might be more than one possible muon rays that meet the requirement of good track, hence the selection of best track is introduced to keep the muon ray that has the minimum χ^2_X from those match the most clusters on 4 layers of LM1 module. Matching is only performed between the best Mcube track and reconstructed clusters. As for a zero match event, the best track is simply the good ray with minimal χ^2_X.

Once the Mcube track is determined, it is the time to select the clusters. For each layer, only the cluster with minimum residual in X with respect to the position predicted by Mcube track is chosen to be the response of the module on that layer. When applying the residual cut, this cluster with best reconstructed position could be removed if it is too far away from one predicted X position, yielding an inefficient event for the layer. A typical cut flow for cosmic muon events is listed in Table 3.1. The number of events used for matching is reduced by a factor of ∼10 from the initial data after the selection criteria.

Cut	Entries			
Mcube events	499949			
At least 1 track	334791			
At least 1 good track ($\chi^2_X < 2.5$, $\chi^2_Y < 10.0$ and incident angle < 0.4 rad)	54583			
	Layer 1	Layer 2	Layer 3	Layer 4
Geometric cut	44447	44142	43319	45297
Residual cut (10 mm)	38831	38186	36818	39884

Table 3.1 – Cut flow of cosmic muon analysis for Module 13 PCB4 and PCB5

The distribution of residuals that reveals the difference between the X position of best cluster and the prediction of Mcube track, is shown in Figure 3.19 left. Due to a translation along X direction, this distribution is not necessarily centered at 0 before offsetting the module. The offset has to be found for each data taking in order to make sure the matching is based on proper muon rays and clusters. In order to find the center of the residual distribution for the adjustment of module offset, the cluster residual is always fitted by a double Gaussian function per PCB per layer as a proxy of effect of the LM1 spatial resolution convoluted over muon angles, smeared by the imperfect alignment as well as the resolution of the external Mcube trackers. The fraction of the wider Gaussian in this fit is artificially restricted to be within 5 %, yielding a corresponding standard deviation around 3 mm. Although neither standard deviation of the double Gaussian fit can be interpreted to be the intrinsic spatial resolution of the detector, that of the wider component offers a reliable reference for setting the residual cut. After studying the dependence of efficiency on the choice of residual cut, it was decided to set the residual cut to 10 mm for all the measurements. This universal residual cut is from 3 to 5 times larger than the standard deviation of the wider Gaussian, thus ensures a good coverage of the real detector responses to the cosmic muon while excluding the clusters that are too far away from their predictions. From Figure 3.20, it can be seen that the cut of 10 mm locates on the plateau of efficiency, which means changing the criterion of residual cut by a reasonable amount

will hardly influence the measurement of efficiency. The residual cut should not be set to the turning point of the curve without any margin, otherwise the efficiency would be too sensitive to the performance of each individual PCB as well as the subtly of Mcube alignment during data taking. As a cross-check in Figure 3.19 right, the correlation between the best cluster position and the Mcube tracker prediction along X follows an expected linear relationship. The sparse random dots spread beyond the linear correlation are considered to be the noise and are therefore effectively excluded from the efficient events, thanks to the residual cut.

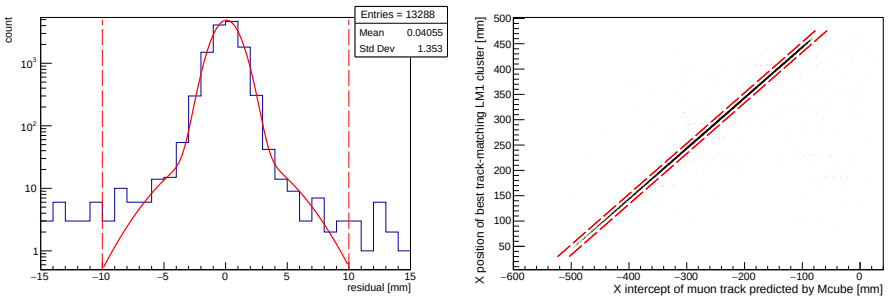

Figure 3.19 – Left: The cluster residual distribution of Module 11 PCB1 Layer 1 before applying the residual cut. The red curve represents the double Gaussian fit. Right: The corresponding correlation of X positions between best reconstructed clusters and their predictions by the external trackers. The dashed lines in both plots indicates the *10 mm* residual cut.

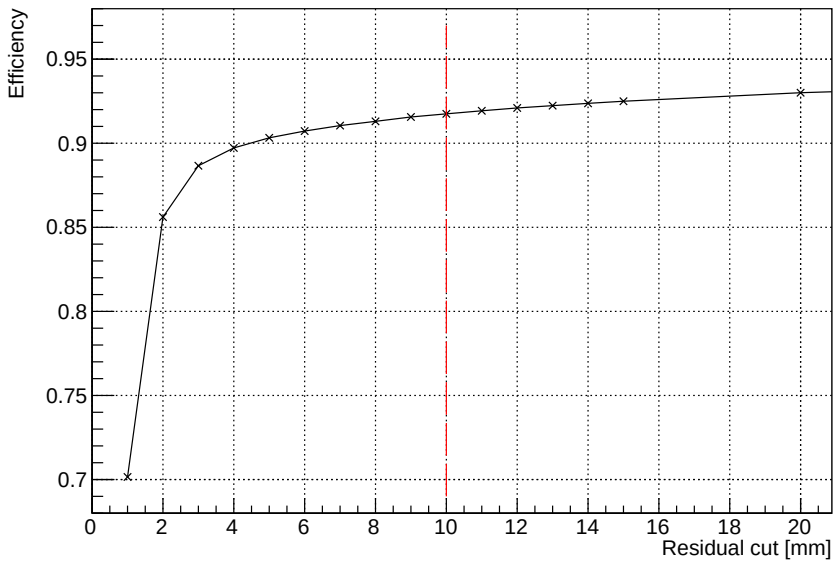

Figure 3.20 – The efficiency of LM1 module with different criteria of residual cut. The 10 mm residual cut is indicated by the red dashed line, corresponding to an efficiency of about *92%*.

3.6 Performance of modules

3.6.1 Efficiency

Each matching cluster that passes the residual cut will be assigned a position in the module. Besides the layer and the X position is known from the clustering, the Y position of the cluster is also given by the Mcube track thanks to the 2D readout of Mcube detectors. Although the resolution along Y is not as good as that in X, this method is still powerful enough to perform the 2D characterization for LM1 modules. The efficiency is studied at the base of every HV sector and summarized per PCB per layer. The overall efficiency for each layer or each PCB is the average weighted efficiency over the corresponding HV sectors. The weight used for the average is the inverse of the squared error of efficiency in the HV sector, in order to ensure the sensitive area of each sector is properly taken into account in the average. The choice of weight is based on the assumption of a constant efficiency, following which the number of accepted events in a given amount of time for each sector is proportional to its area, so that effectively the sensitive area is proportional to the inverse of the squared relative statistical error. i.e. a HV sector with larger sensitive area reconstructs more cosmic muon events (which also means a smaller error of efficiency) and therefore should have a greater contribution to the average of efficiency. For this reason, the data taking is supposed to have more or less same amount of cosmic muon events recorded by Mcubes for different coverage of a LM1 module, otherwise the weight of PCBs that accept more events will be overestimated because of lower statistical fluctuation. Here the errors of efficiency are obtained along with the efficiency itself via the TEfficiency class of Root [22] on 1σ confidence level. Despite the asymmetric errors of Poisson statistics, the up and down errors are symmetrized to a single number, so as to simplify the analysis workflow. The symmetrization of up and down errors is justified as their absolute values are generally very close to each other for a given HV sector.

However, considering the fact that the acceptance of Mcube detectors is smaller than the Y-width of PCB 3,4 and 5, the efficiency on the borders of these PCBs cannot be studied and will not be included in the final results. The count of cluster matching on the rest of the area gives a so-called raw efficiency, which does not take into account the effect of bad connections or the passivation on edges. Even though the connection is always carefully checked via inspecting "hit map" before data taking, remaining glues, degrading of Mux2 cards or even broken zebra lines may still lead to a loss of efficiency that is hidden behind multiplexing. In order to correct this underestimation of efficiency caused by bad connection of electronics, the strips with efficiency less than 10 % in a data taking will be excluded from the calculation of efficiency. Meanwhile, the edge passivation can be observed on PCB1, 2 and 3 by Mcubes on the cosmic bench, which will produce a large inefficient area if we look at the 2D distribution of efficiency. This impact of edge passivation is corrected by introducing a global margin factor to the border of the module instead of simply using the geometric edges. As an example, the efficiency of a module is summarized to each layer in Tab 3.2 and to each PCB in Tab 3.3. The efficiency significantly goes up for PCB1 after excluding the effect of edge passivation. Yet the difference is smaller for PCB 2 and 3 since their proportion of passivated area is lower compared to that of PCB1.

Layer	Raw Efficiency	Efficiency excluding bad connections	Efficiency excluding passivated areas
L1/Eta top	0.86 ±0.11	0.88±0.11	0.89±0.03
L2/Eta bottom	0.85 ±0.06	0.87±0.05	0.88±0.03
L3/Stereo top	0.84 ±0.06	0.86±0.05	0.88±0.03
L4/Stereo bottom	0.87 ±0.08	0.88±0.07	0.89±0.03

Table 3.2 – Mean efficiencies of the four layers of Module 13.

Layer	Raw Efficiency	Efficiency excluding bad connections	Efficiency excluding passivated areas
PCB1	0.72 ±0.06	0.74±0.5	0.91±0.04
PCB2	0.82 ±0.03	0.86±0.01	0.92±0.03
PCB3	0.86 ±0.03	0.91±0.02	0.91±0.02
PCB4	0.87 ±0.05	0.88±0.03	0.88±0.03
PCB5	0.85±0.04	0.88±0.01	0.88±0.01

Table 3.3 – Mean efficiencies per PCB for Module 13.

When looking at the final efficiency values after two corrections, the module achieved not only the relative high efficiency per individual layer (90 %), but also an overall good homogeneity for all the 4 layers (<4 %). An explicit view of the efficiency comes from the efficiency map (Figure 3.21), which is the combined 2D distribution of efficiency from the data taking at 3 locations on cosmic bench. The blue area near the small base is due to the edge passivation while some circular inefficient spots come from the interconnections that support the mechanical structure of the quadruplet. Figure 3.22 shows the efficiency per layer of every module validated on the cosmic bench. Generally speaking, they were all fulfilling the requirements during the cosmic muon characterization period at Saclay.

3.6.2 Charge homogeneity

In addition to the efficiency, the charge of matching clusters are also studied to validate the properties of LM1 modules in terms of gain. The charge distribution of different HV sectors are fitted with Landau function and the Most Probable Value (MPV) obtained from this fit is chosen to represent the charge in ADC unit for the sector (Figure 3.24). Although the actual number of gain relies on the transfer function of electronics which heavily depends on the connection scheme, especially the capacitance of the connected readout strip, it is still possible to estimate the level of gain by some simulations.

With the setup of electronics on the cosmic bench, the total input capacitance including capacitance of the strip, the cable, the cross-talk as well as the parasitic capacitance of the Mux2 card, is about 280 pF on PCB1. As longer strips bring larger capacitance and stronger cross-talk, the total input capacitance increases to 520 pF

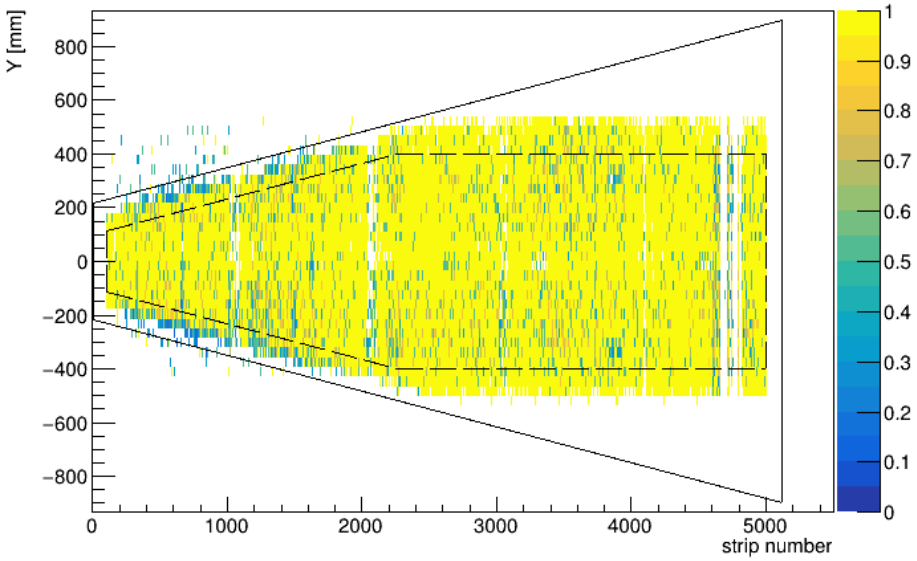

Figure 3.21 – 2D efficiency map of Module 11 layer 2, where the bins in yellow stand for efficiency higher than 95 %. The solid lines outline the nominal sensitive area of this layer. But the area taken into account for efficiency calculation is indicated by dashed lines, which excludes both the surface inactivated by edge passivation and the area beyond Mcube acceptance. Low efficiency caused by passivation can be seen near the small base of the trapezoid between the solid lines and dashed lines.

on PCB5. At the average strip length, the corresponding capacitance is inferred to be about 400 pF. By contrast, the transfer function of DREAM electronics decreases with the input capacitance. At 280 pF, 400 pF and 520 pF, the values of transfer function according to the simulation are 8.4, 6.7 and 5.8, in the unit of bin/fC.

The estimation of the gain uses the value of transfer function at average strip length, which is 6.7 bin/fC. As simulated by Heed [23] and presented in Figure 3.23, the primary ionization occurs in a 5 mm gas gap gives 47.4 primary electrons (N_{PI}) in average. The momentum and the angular distributions of cosmic ray is accounted for by adopting a phenomenological model [24]. By multiplying the amplitude factor to the MPV value of charge distribution in ADC unit and then dividing the number by the scale of primary ionization, one gets the absolute gain about 7,000. For illustration, the explicit calculation of this estimation is done in Equation 3.1.

$$Gain = \frac{ADC}{e \times f_{Mux2}^{Response} \times N_{PI}} = \frac{350}{1.6 \times 10^{-19}\,\mathrm{C} \times 6.7\,\mathrm{fC}^{-1} \times 47.4} \approx 6888 \qquad (3.1)$$

It should be noted that the distribution of charge as well as the Landau fit need to be studied individually for each HV sector, since even a slightly different voltage in another sector is going to change the gain exponentially, which in the end blurs the total distribution because of two displaced Laudau peaks. The overall charge for each layer or each PCB still comes from the averaged weighted charge of constitutional HV sectors. But this time the weight is the inversed square error of MPV of the fit, which in principle still keeps a weight proportional to the sensitive area. Similar to the data processing of efficiency, there is also a charge map for the 2D graphic view of the performance, as shown in Figure 3.25. The 2D distribution of cluster charge has been

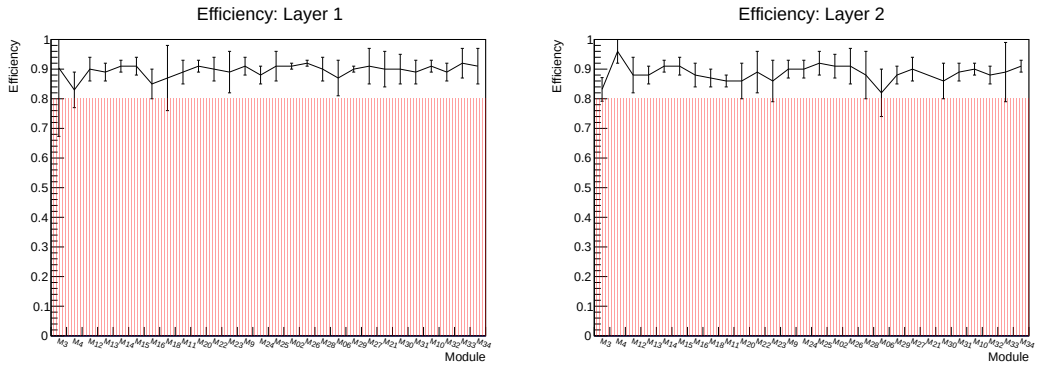

(a) L1

(b) L2

(c) L3

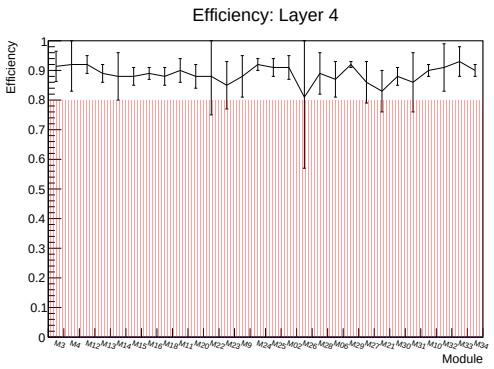

(d) L4

Figure 3.22 – Average efficiency per layer of LM1 modules. The uncertainty bars are the RMS evaluated from efficiencies of 10 HV sectors on the layer. Points above the red band fulfill the requirement of efficiency.

re-binned so that the gap of bad connections and the blank due to interconnection are even clearer on this map.

The average charge per layer is recorded for all the modules, of which the results are shown in Figure 3.26 The first data point here stands for module 3. The values are systematically higher than other modules because the signals are read out without a multiplexing scheme for this module. The Mux2 card enables one electronics channel to the associated two strip in the module, which almost doubles the capacitance attached to the channel and thus brings a lower amplitude. At nominal HV of 570 V, this lower amplitude caused by multiplexing introduces a slightly loss of efficiency.

Another attribute of charge in ADC unit is its reduction with the increase of connected impedance, which reflects the influence of transfer property of DREAM electronics. In an LM1 module, from the small base to the large base of the trapezoid, the strips become longer. When electronics are attached to longer strips, the corresponding capacitance also increases, which introduces a reciprocal relationship to the amplification factor. As a result, there is a tendency of charge going down with larger PCB numbers. Though the connection to strips is not exactly continuous on each PCB panel due to the multiplexing pattern, this trend turns out to be more or less matching the reciprocal of averaged strip lengths per PCB as shown in Figure 3.27, confirming the responding of the transfer function.

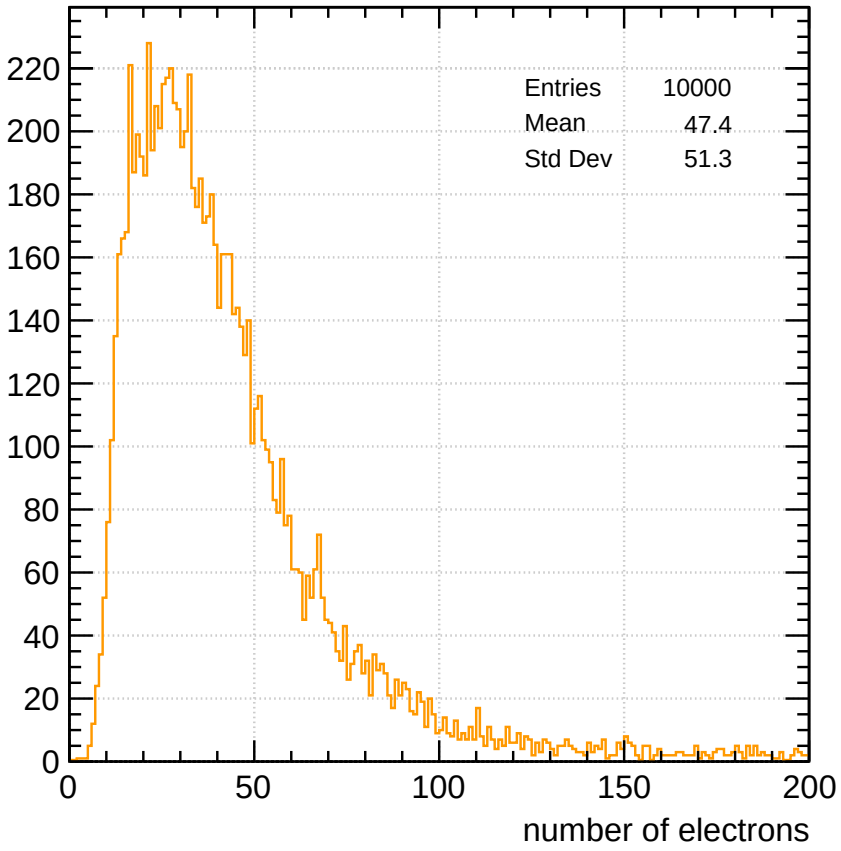

Figure 3.23 – The number of free electrons ionized by cosmic ray muons in a gas gap of 5 mm obtained from simulation. The gas medium is set to $93\,\%Ar + 7\,\%CO_2$ in the simulation.

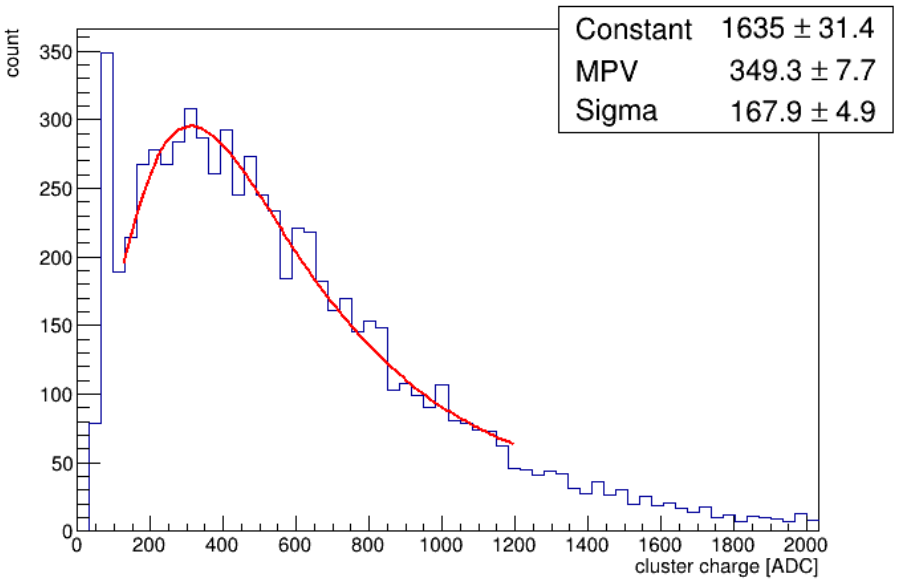

Figure 3.24 – The distribution of charge in ADC unit. This plot shows the charge of M13 PCB4 Layer 2, right HV sector. The small bump at low ADC is mixture of noise and partially reconstructed clusters.

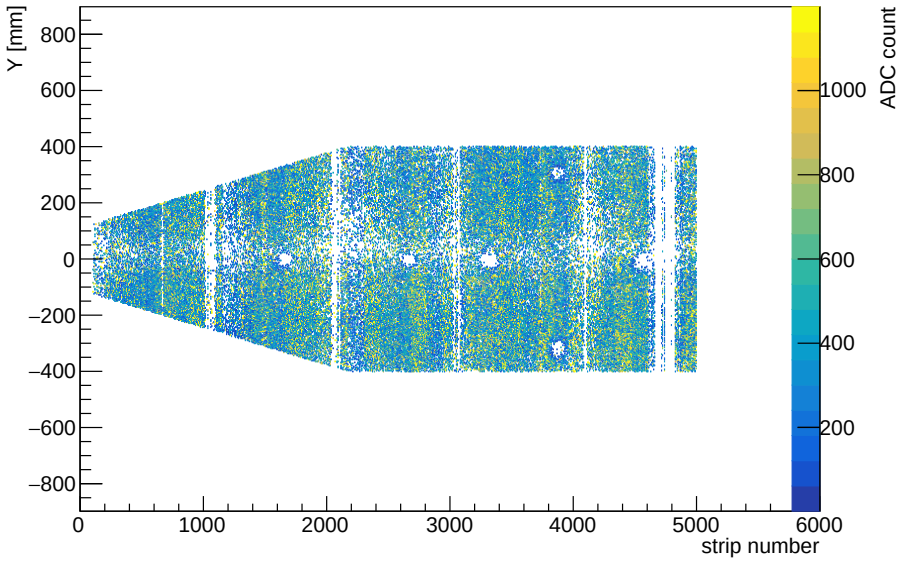

Figure 3.25 – The 2D charge map for Module 11 layer 2, all PCBs. The empty gaps are due to bad connections and passivation between PCBs. The 6 interconnections are clearly revealed on the map.

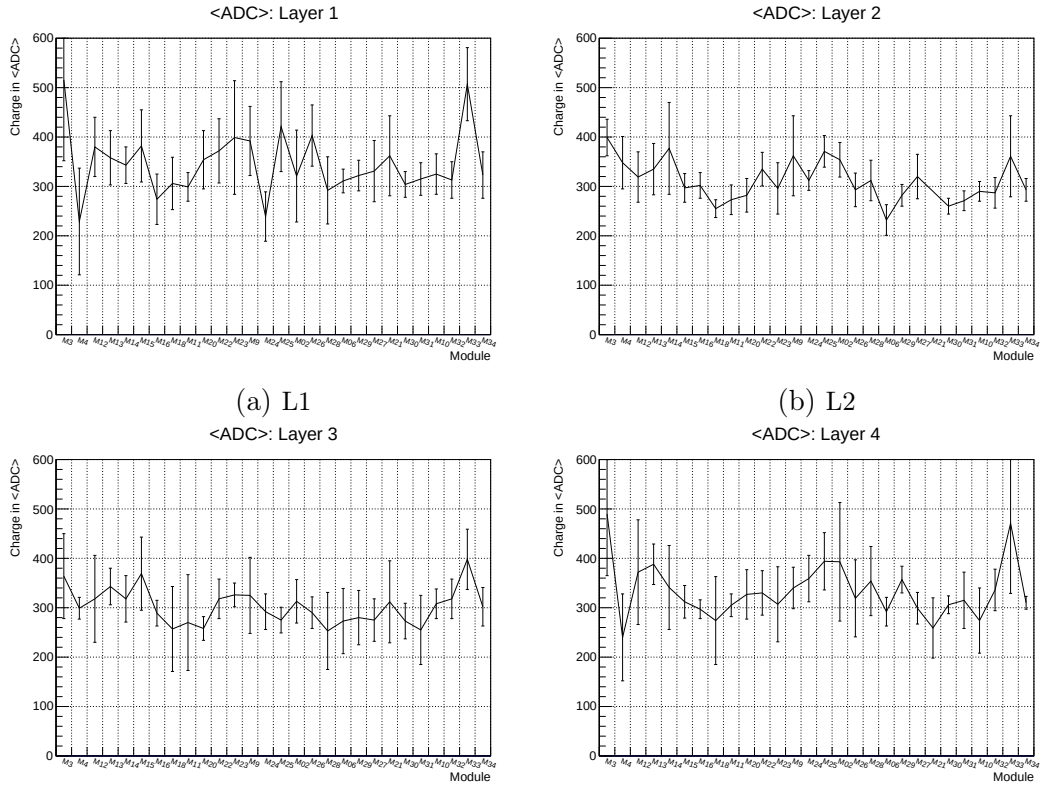

(a) L1 (b) L2

(c) L3 (d) L4

Figure 3.26 – Average charge in ADC unit per layer of LM1 modules. The uncertainty bars are the RMS evaluated from the charge of 10 HV sectors on the layer.

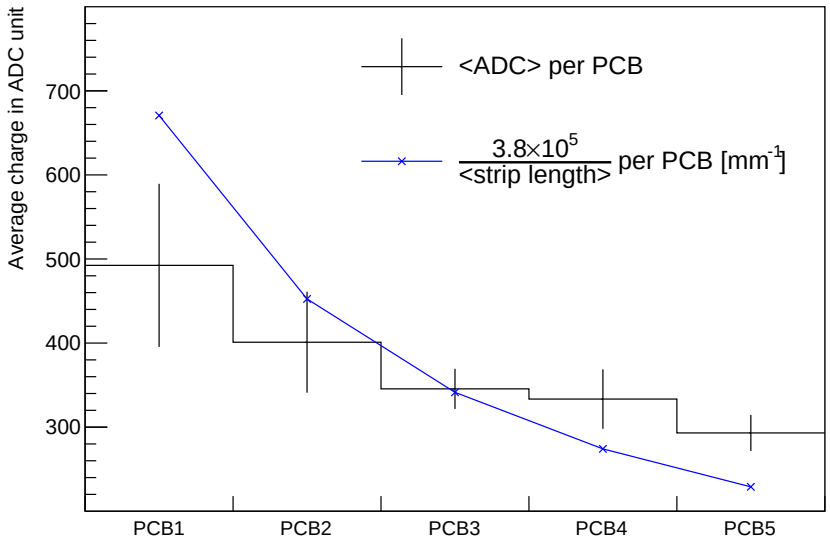

Figure 3.27 – Example taken from Module02: The dependence of charge in ADC unit on PCB. The reciprocal of average strip length per PCB are scaled for a better visualization. The regression of the gain roughly follows the reciprocal of average strip length.

3.6.3 The impact of interconnections

As mentioned in 3.2.2, interconnections are the mechanical points introduced to the design of NSW LM1 Micromegas to support the structure of the detector by well defining the gas gap, thus preventing the inflation of the detector. A close look of the interconnection is shown in Fig 3.28. However, the interface of an interconnection between resistive layer and metal mesh turns out to be susceptible to sparks, causing HV instability of the section or even serious damage in the adjacent area. Therefore, passivation was also applied to the area around interconnections.

The passivation of an interconnection consists of two parts, both on the resistive layer and on the metal mesh. In principle, the two parts of the passivation should well overlap each other. But a perfect overlap can hardly be realized in practice, which brings a even larger dead area than the passivated glue on the resistive layer. Moreover, the additional thickness of passivation around interconnections may deform the metallic mesh and thus locally increase the thickness of amplification gap, further reducing the efficiency of the detector near interconnections. Given that the LM1 modules are designed to be high precision trackers with good efficiency, the loss of efficiency due to the impact of interconnections should be carefully estimated.

This impact was studied for PCB4 over 10 different LM1 modules. The basic idea is to compare the efficiency between an interconnection-included area and a reference area that does not contain any interconnection. A graphic illustration can be seen in Fig 3.29, where 3 rectangles are outlined to cover each interconnection on PCB4. In order to minimize the effect of bad connections, the corresponding reference boxes are chosen to be parallel to the areas of interest. The reference boxes are also designed to have the same surface of the interconnection-included rectangles to ensure a reasonable comparison in term of statistics.

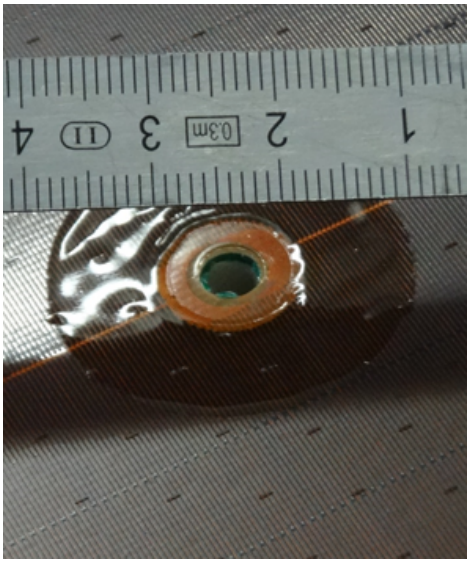

Figure 3.28 – Photo showing a real interconnection with passivation. The total diameter is *30 mm*.

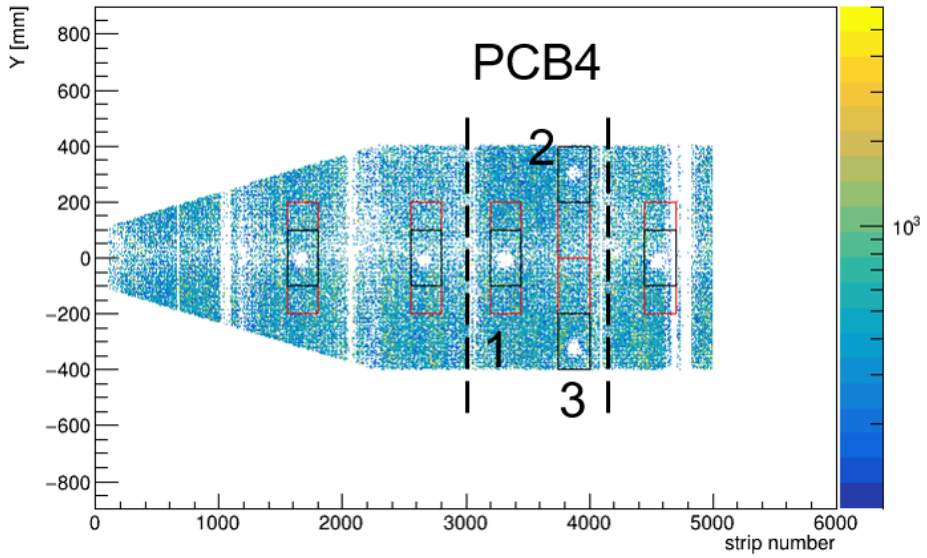

Figure 3.29 – A charge map showing the loss of efficiency due to interconnections. The impact of the three interconnections on PCB4 was estimated. Each box surrounded by black lines include one interconnection. The corresponding reference boxes are indicated in red.

$$\epsilon_{IC} = \epsilon_{Ref} \times \left(S_{Box} - S_{IC,geo} \times r_{actual/geo}\right) / S_{Box} \tag{3.2}$$

Equation 3.2 illustrates the relation between the efficiency of box including an interconnection and efficiency of the corresponding reference box, where ϵ_{IC} and ϵ_{Ref} are the efficiencies in the two boxes, S_{Box} is the surface of the boxes, $S_{IC,geo}$ is the geometric surface of an interconnection and $r_{actual/geo}$ is the ratio to be measured. Once the efficiencies are measured within the area with interconnection and the reference area, it is possible to know what is the actual dead area caused by an interconnection

compared to its geometric size.

After a series of surveys for 10 different modules, it turns out that the loss of efficiency due to interconnections is much larger than what one may expect based on the surface of the glue. The measured surface ratios $r_{actual/geo}$ for the three interconnections on PCB4 are shown in Figure 3.30. Generally speaking, the surface ratio between the consequent dead area on efficiency map and the geometric size of the interconnection is more than 3 according to the measurements. Assuming that the impact of interconnection is at the same level for different PCBs, an optimistic estimation using the factor of 3 would yield a loss of efficiency for the entire sensitive area, which is unfortunately an non-negligible number for Micromegas. Therefore, the passivation of interconnection has to be treated properly in the simulation of the detector to account for the loss of efficiency. The results of this estimation are also given to the construction team of Saclay who then makes efforts to minimize the surface of passivation around interconnections.

3.6.4 Intrinsic spatial resolution

Although the efficiency and gain are without doubt the two most crucial features of the NSW Micromegas modules, the spatial resolution is equally important when the detectors are operated during the actual data taking in ATLAS. As pointed out by the Technical Design Report [2], the precision trackers on the NSW have to measure the transverse momentum of passing muons within a precision of 10 % for 1 TeV muons in the full pseudo-rapidity of its coverage. This can be translated to a position resolution better than 100 µm per detecting layer for the Micromegas modules. The test beam is always a good approach to study the intrinsic spatial resolution of gaseous detectors, provided that the errors such as the imperfection of beam profile are well understood. Nonetheless, the unique setup of the cosmic test bench at Saclay also allows a simple estimation of intrinsic spatial resolution for LM1 Micromegas modules.

For the study of intrinsic spatial resolution using cosmic test data, the readout scheme of the electronics has to be specially prepared: the Mux2 card is no longer used, instead each electronics channel is connected to only one readout strip (Mux1). This choice of readout scheme is mostly due to the inevitable ambiguity of hit-to-strip conversion and the compromised signal-to-noise ratio with Mux2 readout. Even if the measurement of efficiency is not heavily affected by these effects, the clustering is prone to an incomplete reconstruction of charge, which smears determination of the charge center of the cluster. In contrast, data taking without multiplexing not only enhances the signal-to-noise ratio, but also avoids the potential mistake of demultiplexing in the analysis, both of which help improve the quality of cluster reconstruction. Given that the crossing point of cosmic muon track on the detecting layers is inferred from the charge centers of LM1 clusters, the distribution of residual of this inference, or in another word the spatial resolution, will significantly benefit from the Mux1 readout. Since there is no need for performing a scan of intrinsic spatial resolution, this measurement can focus on a single PCB. Therefore, the number of available electronics channels on the bench are still sufficient even without using multiplexing.

Considering the precision of the quantity to be measured, a strategy has to be worked out to reduce the dependence on the millimeter level predictions of muon tracks that are provided by the external trackers, as shown in Fig 3.31. The basic

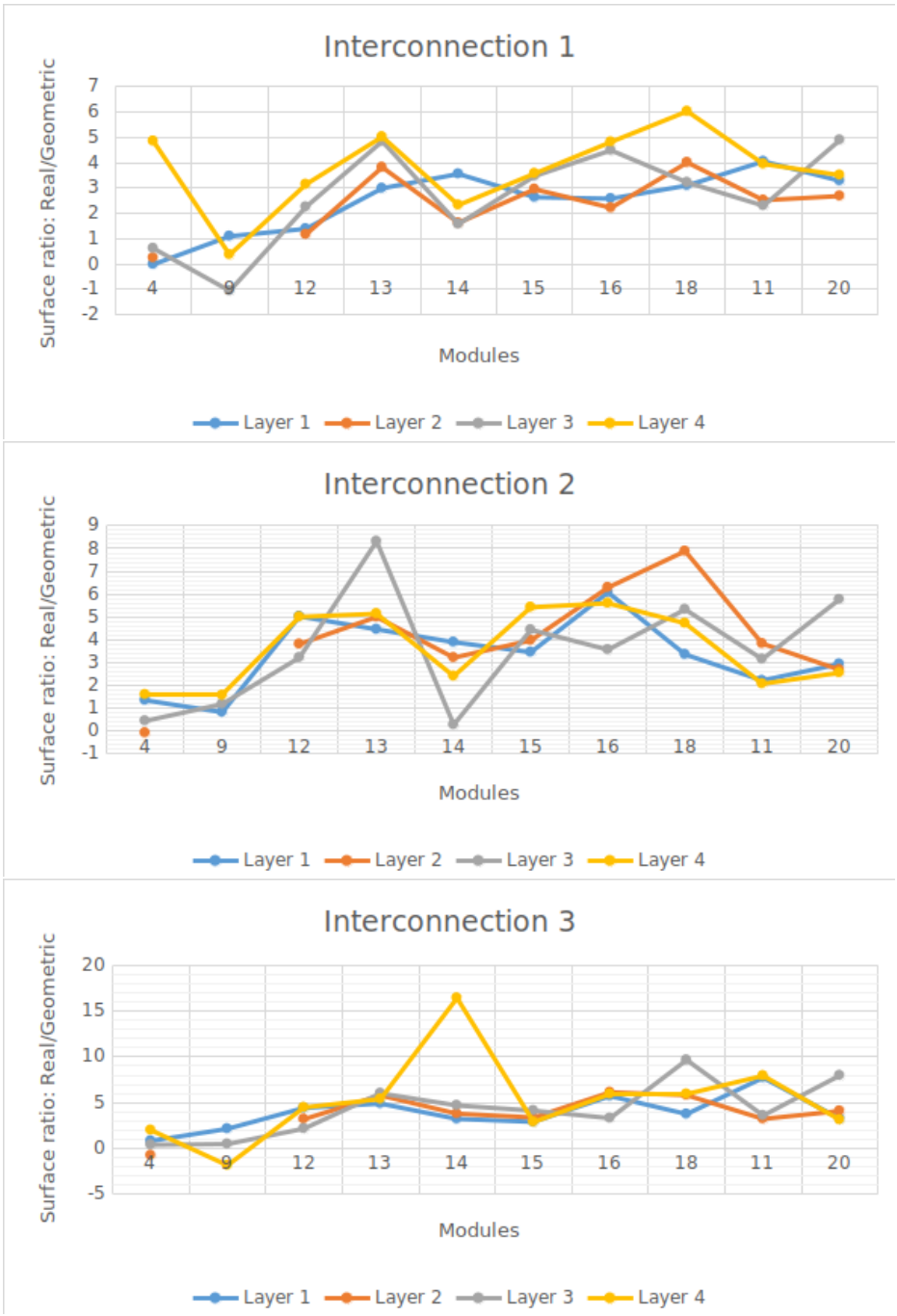

Figure 3.30 – The surface ratios $r_{actual/geo}$ indicating the actual dead area due to the three interconnections on PCB4 compared to their geometric sizes. If ϵ_{IC} occasionally happens to be slightly higher than ϵ_{Ref} in the measurement, negative $r_{actual/geo}$ can be reported.

principle is hence: for each cosmic muon reconstructed by the external trackers, the charge center of the LM1 clusters from the Layer1 and Layer2 are recorded if they both pass the track matching mentioned in 3.5.4. The charge center of LM1 cluster on each layer represents the position where the cosmic muon passes through the corresponding detecting layer. Given that the first two layers of LM1 module have parallel readout strips along the Y-direction, the difference in the X-position of the two clusters between Layer1 and Layer2 ($X1 - X2$) helps reveal the spatial resolution of LM1 Micromegas (the X, Y directions have been defined in 3.5.4). The residual of

the position difference in X-direction is the result of double smearing by two detecting layers, which suggests that in the vicinity of zero $angleX$ (the projection of the incident angle on X-axis), the standard deviation of the residual divided by $\sqrt{2}$ can be interpreted as the intrinsic spatial resolution of a single detecting layer.

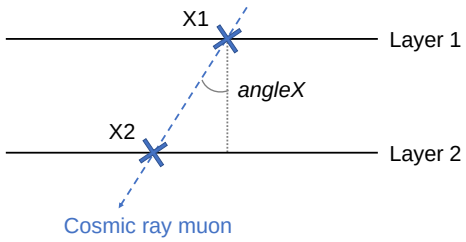

Figure 3.31 – Schematics showing the definitions of $X1-X2$ and $angleX$ for the measurement of intrinsic spatial resolution.

However, two major issues were discovered as the study unfolded. First, without any available external alignment, there is a limitation of the mechanical alignment for the external trackers at the level of several millimeters, which propagates a bias to the incident angle, adding an unknown offset to $angleX = 0$. More importantly, a correlation exists between $X1 - X2$ and $angleX$, which blurs the spatial resolution measured from any finite interval of $angleX$ even if the interval is close to 0. Solutions to these two difficulties are described in below.

In order to correct for the mechanic mis-alignment of the external trackers, each quarter of the 3-layer Mcube system is studied separately to achieve a small adjustment of the alignment parameters. The corrections include two parts: the optimization of the alignment parameters inside each quarter and offsetting different quarters along the X-axis. The directions of the readout panels of Multigen2D detectors are denoted as X and Y following the coordinate system of the cosmic bench and are each assigned with a number from 0 to 23 (Fig 3.32(a)). For the first part of the correction, the top left quarter is taken as an example for detail illustration: The bottom layer is used as reference such that the X, Y positions of 16, 17 readout panels are never changed in this stage of the correction. Then instead of reconstructing the tracks from all the three layers of Multigen2D (as it is done for the characterization of LM1 modules), the cosmic muon tracks are only reconstructed by 0, 1 together with 16, 17. On the horizontal plane, the mismatch of the reconstructed track with regards to the response of 8,9 is added to the alignment parameters of 8, 9 as correction. After that, muon tracks are reconstructed by 8, 9 and 16, 17 to check its consistency with the response of 0, 1. Similarly, the horizontal offsets in X and Y are added to the alignment parameters of 0, 1. This two procedures are repeated for a few iterations until the muon tracks reconstructed by 16, 17 and 0, 1 (8, 9) match the response of 8, 9 (0, 1). The configuration of the Multigen2D detectors and the distributions of residual for one of them after the alignment is presented in Fig 3.32. The same adjustment is carried out on the other three quarters as well. In the second part, the offset along X-axis between different quarters is observed by the LM1 module. If nothing is done after the correction within individual quarters of the Mcube, the Left and Right halves of a PCB panel of the LM1 module will show different central values of cluster residuals. To compensate for the inter-quarter misalignment, the top left

quarter of the Mcube is chosen to be the baseline while the discrepancy is added to 2, 11 and 19 as a global offset. The effect of adjusting the X-offset between Mcube quarters is shown in Fig 3.33.

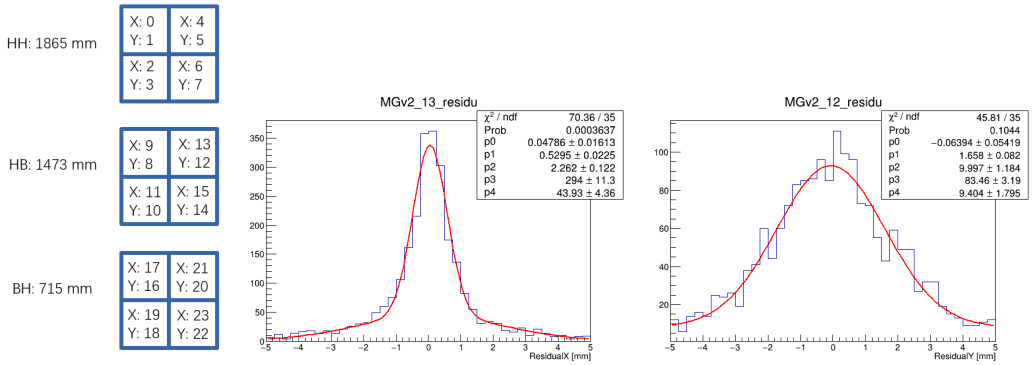

(a) (b) (c)

Figure 3.32 – The illustration of Mcube alignment within individual quarters. (a) The indices and directions of Multigen2D readout panels, as well as the heights of 3 layers. (b) The residual of one Multigen2D in X direction centers at zero after the alignment in the corresponding quarter of Mcube. (c) The residual of one Multigen2D in Y direction centers at zero after the alignment in the corresponding quarter of Mcube.

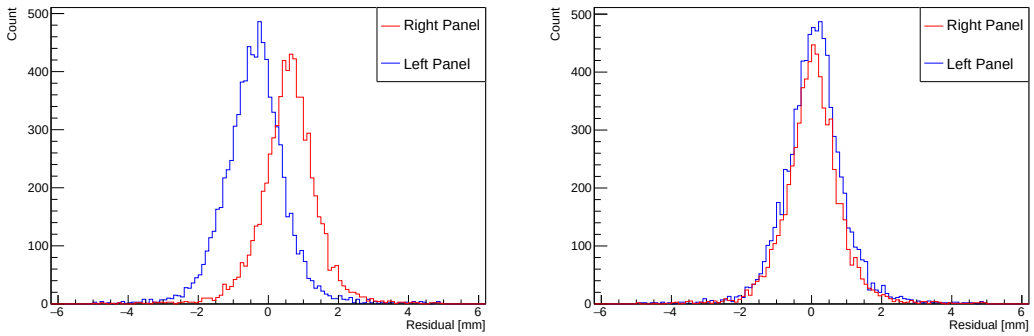

(a) Before correction (b) After correction

Figure 3.33 – The distributions of cluster residual for M12 Layer1 PCB1 before and after the second part of the alignment. The distributions are separated into left and right halves of the PCB panel to emphasis the improvement brought by the alignment.

Regarding the angle correction, in Fig 3.34(a) a 2-D histogram of "$X1 - X2$ vs $angleX$" is drawn for cosmic muons with angleX smaller than 0.35 rad (or 20°). A linear fit is performed to determine the specific amount of correction required for a given angleX (Fig 3.34(b)). The result of the linear fit is added to the variable $X1-X2$ as a function of $angleX$, so that the average of $X1-X2$ no longer depends on $angleX$. From the same 2-D histogram after angle correction (Figure 3.34(c)), the $X1-X2$ in the central bin of $angleX$ ($-0.05 < angleX < 0.05$) is projected to a 1-D histogram in Fig 3.34(d) and fitted by a Gaussian function between [−0.45 mm, 0.45 mm]. Since the σ of the Gaussian is the standard deviation of the residual distribution being

measured twice, the intrinsic spatial resolution should be this standard deviation divided by $\sqrt{2}$, which is 110 µm.

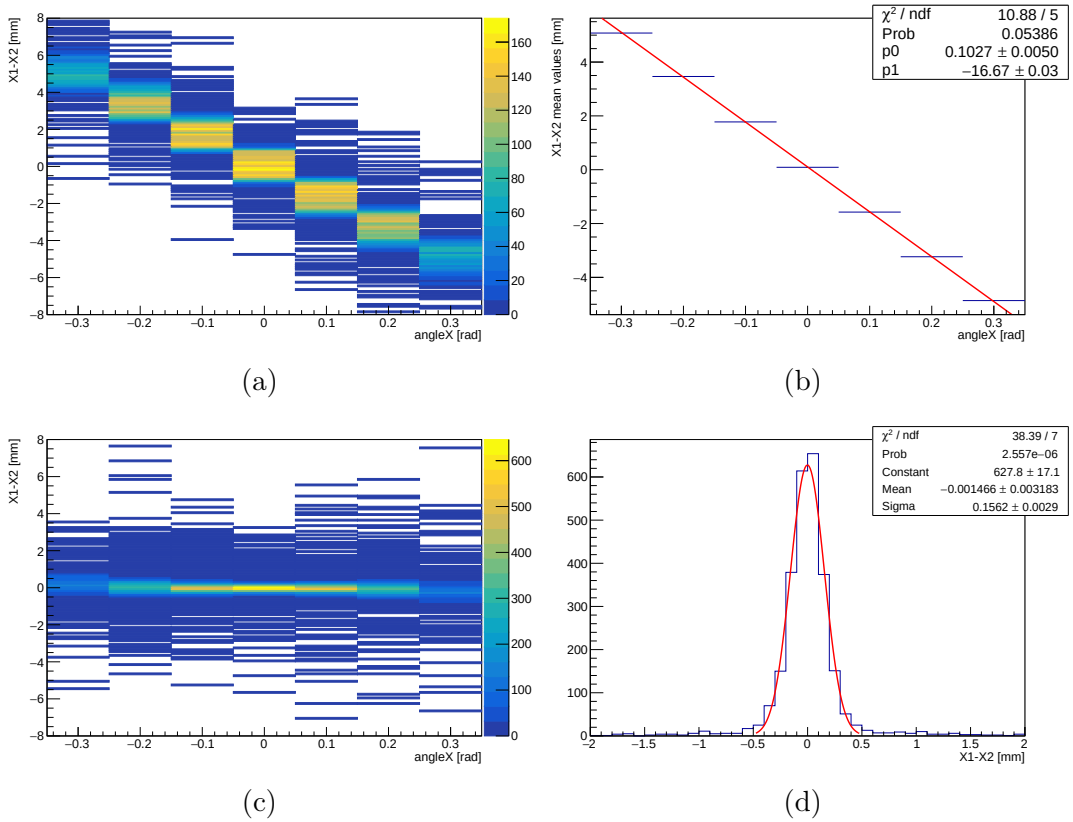

Figure 3.34 – The distributions of cluster residual for M12 Layer1 PCB1 before and after the second part of the alignment. The distributions are separated into left and right halves of the PCB panel to emphasize the effect of the alignment. (a) $X1 - X2$ vs $angleX$ before angle correction. (b) The linear fit for angle correction. (c) $X1 - X2$ vs $angleX$ after angle correction. (d) Gaussian fit of $X1 - X2$ for the bin $-0.05 < angleX < 0.05$.

The estimation made with cosmic bench data proves that the level of intrinsic spatial resolution for a LM1 Micromegas module is within the specifications of the NSW Technical Design Report.

3.6.5 Performance of the detector using isobutane gas mixture

Poor HV performance of NSW Micromegas modules is a common issue frequently reported in all consortia of production when the detectors are operated with 93 %Ar + 7 %CO_2 as working gas. The suppression of sparking can be achieved to some extent by the passivation technique mentioned in 3.2.3. Meanwhile, an alternative solution has also been tested, which involves the replacement of the initial gas mixture with 93 %Ar + 5 %CO_2 + 2 %iso-C_4H_{10} (isobutane). The presence of isobutane greatly reduces the amplitude of amplification HV needed for reaching the efficiency plateau.

This gas mixture with isobutance is also available on the cosmic test bench at Saclay. Some Mux2 data was taken for PCB1 of Module25 while circulating 93 %Ar + 7 %CO_2 in the gas gaps. As it is shown in Fig 3.35, an efficiency over 90 % on Layer2

can be achieved using the isobutance gas mixture under 515 V. Comparing with the HV performance and the efficiency of the 93 %Ar + 7 %CO_2 data in Fig 3.36, it is evident that the LM1 module is able to maintain the efficiency at lower HV in isobutane gas mixture while keeping more working sectors.

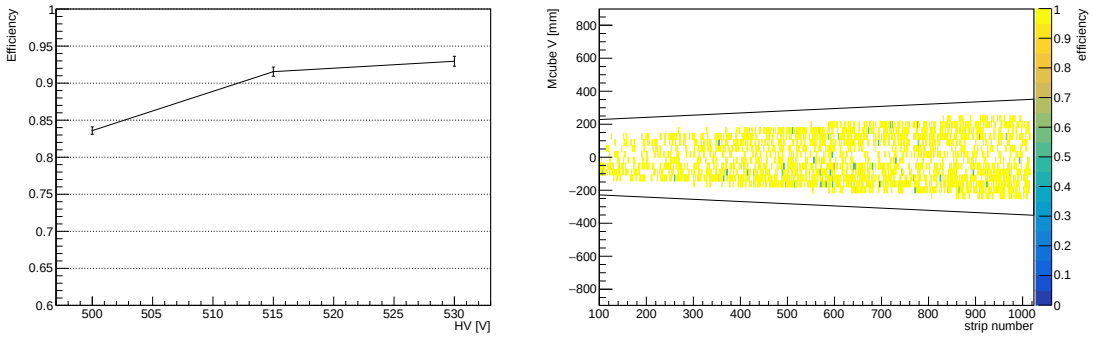

(a) (b)

Figure 3.35 – The efficiency of M25 PCB1 Layer2 using 93 %Ar + 5 %CO_2 + 2 %iso-C_4H_{10} gas mixture. (a) HV scan of efficiency. (b) Efficiency map of M25 PCB1 Layer2 at 515 V.

	Left	Right
Layer 1	0.86	0.88
Layer 2	0.94	0.90
Layer 3	0.24	0.14
Layer 4	0.93	0.89

(a) 93 %Ar + 7 %CO_2

	Left	Right
Layer 1	0.86	0.87
Layer 2	0.93	0.90
Layer 3	0.87	0.87
Layer 4	0.94	0.89

(b) 93 %Ar + 5 %CO_2 + 2 %$isobutane$

Figure 3.36 – The HV status and efficiency of 8 sectors on M25 PCB1 using two different gas mixtures. For the 93 %Ar+7 %CO_2 mixture, the nominal HV is 570 V. Those sectors unable to sustain nominal HV are labelled in red. For the isobutance gas mixture, the efficiencies are measured at 515 V.

Even though there are signs showing that the isobutane gas mixture is very likely to outperform the initial choice of working gas, a major concern with the isobutane is its aging effect on the detector. For this reason, dedicated beam test was carried out in the Gamma Irradiation Facility (GIF++) at CERN, studying long term degradation of the performance for NSW Micromegas modules. No significant evidence shows that the 93 %Ar + 7 %CO_2 gas mixture is better than the isobutane gas mixture in terms of aging. In February 2022, in view of the improvement of stability and experience in aging, ATLAS made the final decision to change the nominal gas to 93 %Ar + 5 %CO_2 + 2 %iso-C_4H_{10}.

3.7 Summary

Cosmic ray muons provide a powerful tool for the scan and characterization of large area detectors. The cosmic test bench at Saclay is efficient to characterize the performance of ATLAS NSW LM1 Micromegas in terms of efficiency, charge homogeneity, and even intrinsic spatial resolution. Serving as both trigger and external tracker, the Mcube system records cosmic rays and reconstructs their tracks within the acceptance area. While the acceptance of Mcubes is unable to cover the full surface of LM1 Micromegas modules with the given scheme and the pressing time schedule, the test of all readout strips is still possible thanks to the sliding tray and multiplexing readout strategy. Data taking at 3 different locations along the tray rail is enough for the scan of all 5 PCBs in a LM1 Micromegas. Meanwhile, the Mux2 cards adapt DREAM electronics on FEU boards to LM1 module by associating 2 strips to one electronics channel in a carefully-designed pattern so that the total number of channels is reduced by a factor of 2, while the granularity of strips is still retained.

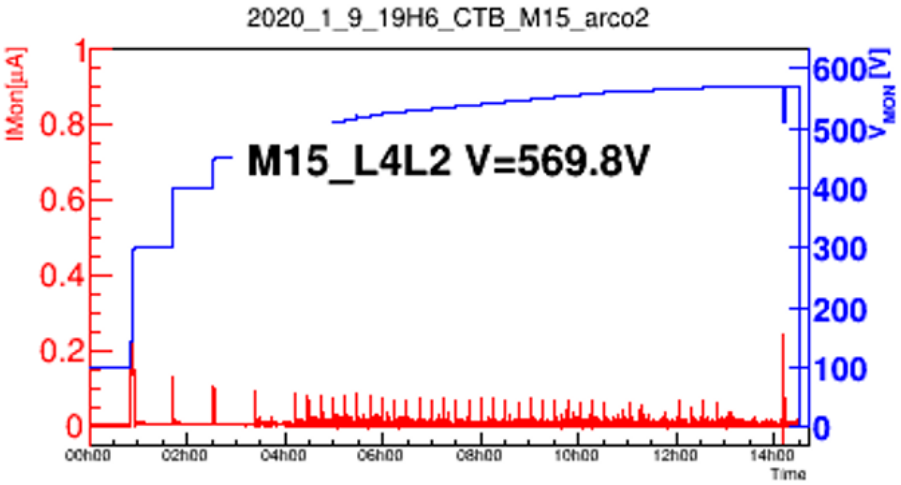

Figure 3.37 – The ramp-up of a sector on M15. The high voltage steadily rises up to the nominal HV.

A complete test protocol has been established for the cosmic muon characterization of NSW LM1 Micromegas at Saclay. Covering the LM1 Micromegas with a plastic tent, the heating on cosmic bench effectively accelerates the drying of modules. The high voltage ramp-up takes place only after the relative humidity of going-out gas reaches below 10 %. An example of HV ramp-up is presented in Fig 3.37. Considering the fragility of HV status for a Micromegas as large as a NSW LM1 quadruplet, an automatic program is hereby introduced to controls the HV ramping up of the module through monitoring and reacting to the leak current in real time. The program prevents rising up the HV of a sector to next preset level unless the current is stable enough according to a certain criteria. All sectors in the module can smoothly achieve the nominal HV of 570 V after 12 hours if everything goes well and without the presence of bad sector. A check of pedestals is always necessary after the installation of the module but before the actual data taking. The immediate output of pedestal

taking offers important clues to some possible connection issues. Once the LM1 module is pushed to the data taking position between Mcube layers HH and HB, a short run will be launched. The "hit map" of this short run can further indicate some other suspicious connection problems so that they can be fixed without going through the entire data analysis process. The entire data taking contains scans of the LM1 module at 3 locations. Given that the change of Mux2 card is necessary when switching to the next data taking location, the connection of electronics has to be done at least three times for a module.

The data analysis of cosmic bench at Saclay is another crucial part of cosmic test, from which the statistics summary will be produced as a basic reference of validation and the input of database. Each step of the analysis program uses root files to pass the processed information in a format easier for the next step to handle. The pedestal and signal samples collected by DREAM electronics go through the pedestal subtraction, hit finding, clustering and are finally matched with cosmic muon rays reconstructed by Mcubes, yielding output such as efficiency maps and charge maps. A demultiplexing algorithm is applied to the clustering stage, for the signals of two strips are readout by only one electronics channel with the help of Mux2 card. In addition to the analysis of LM1 module, there is also another program taking care of the track reconstruction of cosmic muon rays for Mcubes. The possible muon rays reconstructed by Mcubes are selected and matched to the LM1 clusters at the final phase of the analysis.

The data analysis mostly focuses on two properties of LM1 modules: efficiency and charge. Both efficiency and charge are studied in a basis of HV sector. While efficiency of a sector can be obtained by simply counting cluster-track matching events, the Landau function is chosen to fit MPV of the charge distribution. The summary of efficiency and charge per PCB and per layer requires a weighted average over the constitutional HV sectors, where the weight refers to the reverse of squared error in order to represent the surface of sensitive area for each sector. Excluding the effect of bad connections as well as edge passivation, the final efficiencies are able to reveal the intrinsic performance of the detector and the homogeneity for different layers. Based on the same exclusion as final efficiencies, analysis of charge also monitors the charge homogeneity of the tested module. The modules validated on cosmic bench meet the validation requirement and show a good performance in terms of efficiency and charge. The study of intrinsic spatial resolution of LM1 modules with cosmic bench data confirms that the produced detectors satisfy the designed tracking precision. An alternative working gas mixture for NSW Micromegas containing isobutane has been tested on cosmic bench at Saclay. Preliminary results show a positive effect on the detector performance and that the HV stability is improved without compromising the efficiency. Finally, this gas mixture has been chosen for the operation of NSW Micromegas during Run 3.

After the production and validation at Saclay, the LM1 modules are transported to CERN, where they are qualified and assembled into large Micromegas double-wedge chambers together with the LM2 quadruplets. A first HV test is performed for each chamber to further validate the HV performance after assembly. Furthermore, around 70 % of the Micromegas chambers are also put into a HV test under high irradiation at GIF++, so that the behaviour of the detectors can be measured at different incident fluxes. Current instability as well as sparking effects are monitored in the tests at GIF++, since they are likely to affect the performance in the expected 15 years of operation of NSW. Then the Micromegas chambers receive mechanical and services

integration before being equipped with electronics and assembled with sTGC wedges to form sectors. During the commissioning, the sectors are installed on the NSWs, with services and electronics boxes connected. Both of the NSWs have been lowered to the ATLAS cavern at P1 of CERN (Fig 3.38).

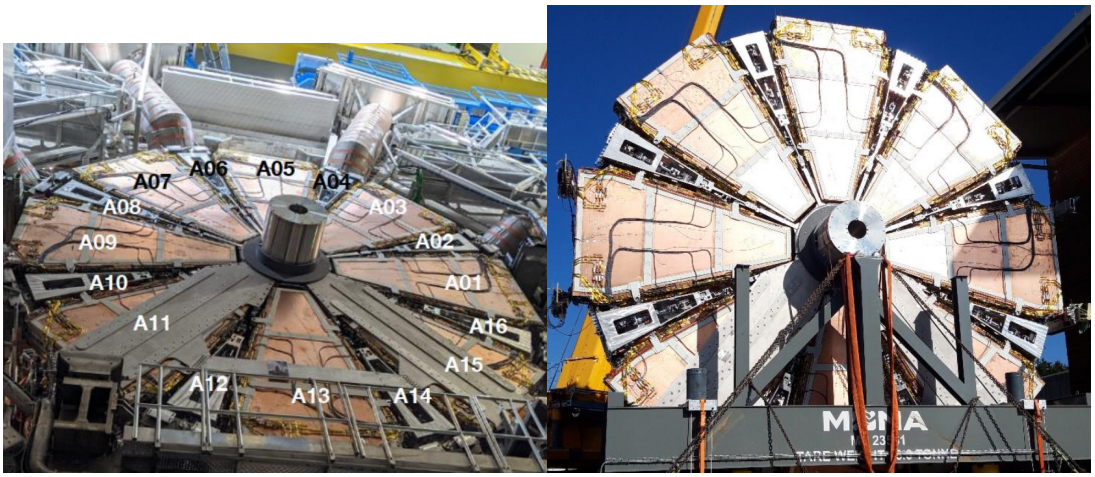

(a) NSW A in ATLAS cavern (b) NSW C in transportation

Figure 3.38 – Photos of ATLAS NSWs

In Run 3, the NSWs are operational and have already become part of the ATLAS muon spectrometer for the data taking. More work is still going on to fully exploit the benefit of the NSW upgrade, so as to further enhance the performance of the muon spectrometer in terms of both trigger and track reconstruction. As an indispensable step of the detector production, the cosmic bench test carried out at Saclay is a key to the success of the NSW upgrade.

References

[1] The ATLAS Collaboration, "Technical Design Report for the Phase-II Upgrade of the ATLAS Muon Spectrometer", Tech. Rep. CERN-LHCC-2017-017. ATLAS-TDR-026, Dec. 2017 (cit. on p. 36).

[2] T. Kawamoto, S. Vlachos, L. Pontecorvo, *et al.*, "New Small Wheel Technical Design Report", Tech. Rep. CERN-LHCC-2013-006. ATLAS-TDR-020, Jun. 2013, ATLAS New Small Wheel Technical Design Report. [Online]. Available: https://cds.cern.ch/record/1552862 (cit. on pp. 36, 61).

[3] The ATLAS Collaboration, "Measurement of the muon reconstruction performance of the ATLAS detector using 2011 and 2012 LHC proton–proton collision data", *Eur. Phys. J.*, vol. C 74, p. 3130, 2014. DOI: https://doi.org/10.1140/epjc/s10052-014-3130-x (cit. on p. 36).

[4] F. Jeanneau, "Design and Construction of Large Size Micromegas Chambers for the ATLAS Upgrade of the Muon Spectrometer", no. ATL-MUON-PROC-2016-004, Jul. 2016 (cit. on pp. 36, 37, 40, 42).

[5] *ATLAS muon spectrometer: Technical Design Report* (Technical design report. ATLAS). Geneva: CERN, 1997. [Online]. Available: http://cds.cern.ch/record/331068 (cit. on p. 36).

[6] Y. Benhammou, "Precision tracking with small-strip Thin Gap Chamber (sTGC): from Test Beam to ATLAS NSW Upgrade", *PoS*, vol. EPS-HEP2013, p. 486, 2013. DOI: 10.22323/1.180.0486 (cit. on p. 37).

[7] I. Giomataris, R. De Oliveira, S. Andriamonje, *et al.*, "Micromegas in a bulk", *Nucl. Instrum. Meth.*, vol. A560, pp. 405–408, 2006. DOI: 10.1016/j.nima.2005.12.222. arXiv: physics/0501003 [physics] (cit. on pp. 37, 43).

[8] Y. Giomataris, P. Rebourgeard, J. Robert, and G. Charpak, "Micromegas: a high-granularity position-sensitive gaseous detector for high particle-flux environments", *Nuclear Instruments and Methods in Physics Research Section A: Accelerators, Spectrometers, Detectors and Associated Equipment*, vol. 376, no. 1, pp. 29–35, 1996, ISSN: 0168-9002. DOI: https://doi.org/10.1016/0168-9002(96)00175-1. [Online]. Available: https://www.sciencedirect.com/science/article/pii/0168900296001751 (cit. on p. 37).

[9] F. Sauli and A. Sharma, "Micropattern Gaseous Detectors", *Annual Review of Nuclear and Particle Science*, vol. 49, pp. 341–388, 1999. DOI: 10.1146/annurev.nucl.49.1.341 (cit. on pp. 37, 38).

[10] P. Colas, I. Giomataris, and V. Lepeltier, "Ion backflow in the Micromegas TPC for the future linear collider", *Nucl. Instrum. Meth. A*, vol. 535, M. Jeitler, M. Krammer, M. Regler, and G. Badurek, Eds., pp. 226–230, 2004. DOI: 10.1016/j.nima.2004.07.274. arXiv: physics/0412057 (cit. on p. 37).

[11] J. Allard, N. Andari, M. Anfreville, *et al.*, "The large inner micromegas modules for the atlas muon spectrometer upgrade: construction, quality control and characterization", *Nuclear Instruments and Methods in Physics Research Section A: Accelerators, Spectrometers, Detectors and Associated Equipment*, vol. 1026, p. 166 143, 2022, ISSN: 0168-9002. DOI: https://doi.org/10.1016/j.nima.2021.166143. [Online]. Available: https://www.sciencedirect.com/science/article/pii/S0168900221010330 (cit. on pp. 41, 43, 44, 46).

[12] K. Fabian, "Signal Formation Processes in Micromegas Detectors and Quality Control for large size Detector Construction for the ATLAS New Small Wheel", Theses, Julius-Maximilians-Universität Würzburg, Jul. 2017 (cit. on p. 41).

[13] *Zebra*, https://www.fujipoly.com/usa/products/zebra-elastomeric-connectors/ (cit. on p. 41).

[14] S. Bouteille, D. Attié, P. Baron, *et al.*, "Large resistive 2D Micromegas with genetic multiplexing and some imaging applications", *Nucl. Instrum. Meth.*, vol. A834, pp. 187–191, 2016. DOI: 10.1016/j.nima.2016.08.006 (cit. on p. 41).

[15] J. Autran, D. Munteanu, T. Saad Saoud, and S. Moindjie, "Characterization of atmospheric muons at sea level using a cosmic ray telescope", *Nuclear Instruments and Methods in Physics Research Section A: Accelerators, Spectrometers, Detectors and Associated Equipment*, vol. 903, pp. 77–84, 2018, ISSN: 0168-9002. DOI: https://doi.org/10.1016/j.nima.2018.06.038. [Online]. Available: https://www.sciencedirect.com/science/article/pii/S0168900218307599 (cit. on p. 43).

[16] S. Procureur, R. Dupré, and S. Aune, "Genetic multiplexing and first results with a 50x50cm^2 Micromegas", *Nucl. Instrum. Meth.*, vol. A729, pp. 888–894, 2013. DOI: 10.1016/j.nima.2013.08.071 (cit. on p. 43).

[17] T. Alexopoulos, D. Antrim, C. Bakalis, *et al.*, "The VMM readout system", *Nucl. Instrum. Meth. A*, vol. 955, p. 163 306, 2020. DOI: 10.1016/j.nima.2019.163306 (cit. on p. 43).

[18] D. Attie, S. Aune, P. Baron, *et al.*, "The readout system for the clas12 micromegas vertex tracker", in *2014 19th IEEE-NPSS Real Time Conference*, 2014, pp. 1–11 (cit. on p. 43).

[19] V. Burkert *et al.*, "The CLAS12 Spectrometer at Jefferson Laboratory", *Nucl. Instrum. Meth. A*, vol. 959, p. 163 419, 2020. DOI: 10.1016/j.nima.2020.163419 (cit. on p. 43).

[20] S. Bouteille, "Development and applications of micro-pattern gaseous detectors for muon tomography", Ph.D. dissertation, Département de Physique Nucléaire (ex SPhN), France, 2017. [Online]. Available: https://tel.archives-ouvertes.fr/tel-01759508 (cit. on pp. 43, 50).

[21] T. Chevalerias, "Characterization of large Micromegas detectors for the New Small Wheel project and search for four top quark production with the ATLAS detector at the LHC", Theses, Université Paris-Saclay, Jul. 2019. [Online]. Available: https://tel.archives-ouvertes.fr/tel-02268557 (cit. on p. 46).

[22] R. Brun and F. Rademakers, "Root — an object oriented data analysis framework", *Nuclear Instruments and Methods in Physics Research Section A: Accelerators, Spectrometers, Detectors and Associated Equipment*, vol. 389, no. 1, pp. 81–86, 1997, New Computing Techniques in Physics Research V, ISSN: 0168-9002. DOI: https://doi.org/10.1016/S0168-9002(97)00048-X. [Online]. Available: https://www.sciencedirect.com/science/article/pii/S016890029700048X (cit. on p. 53).

[23] I. B. Smirnov, "Modeling of ionization produced by fast charged particles in gases", *Nucl. Instrum. Meth. A*, vol. 554, pp. 474–493, 2005. DOI: 10.1016/j.nima.2005.08.064 (cit. on p. 55).

[24] J. A. Smith and N. M. Duller, *Journal of Geophysical Research*, vol. 64, p. 2297, 1959 (cit. on p. 55).

Chapter 4

Overview of W-boson mass measurements

Contents

As a quantity tightly linked to the BEH mechanism and spontaneous symmetry breaking described in Section 1.1.3, the mass of the W-boson is a fundamental parameter of the SM. While the W-boson mass can be determined from the precisely known values of the fine-structure constant, the Fermi constant and the mass of the Z-boson at the lowest order, the higher order loop corrections, denoted as Δr, are also predicted by the SM, bringing dependencies on the gauge boson coupling and the masses of the heavy particles in the SM. In particular, Δr is sensitive to the top-quark mass and to the Higgs-boson mass. However, in extended theories, the correction terms also receive contributions from additional particles and interactions of new physics. Therefore, comparing the W-boson mass measured from the experiments and the value predicted by theoretical calculations not only allows the consistency check the of the SM, but may also reveal a hint of the physics beyond the SM.

4.1 The history of W-boson mass measurements

Since the W-boson mass is a such an important probe for the consistency check of the SM as well as a possible indication of new physics, countless efforts have been devoted to the precise determination of the W-boson mass from experiments. It all started in 1983, when the mass of the W-boson was firstly measured during its discovery at CERN SPS $p\bar{p}$ (proton-antiproton) collider by UA1 at a center-of-mass energy of 546 GeV and UA2 at 630 GeV [1]. Given the six and four W candidates found by the two experiments, the value of the W-boson mass was measured to be 81 $\pm$ 5 GeV and 80^{+10}_{-6} GeV. The measurements were followed by those of the Tevatron $p\bar{p}$ collider with the CDF and D0 detectors at a center-of-mass energy of 1.8 TeV in Run 1 (1987-1996) and at 1.96 TeV in Run 2 (2002-2011) [2]–[5]. The combined value of the measurements from the two experiments gives a W-boson mass of 80.387 $\pm$ 0.016 GeV. In the LEP electron-positron collider, the ALEPH, DELPHI, L3 and OPAL collaborations performed the measurement at center-of-mass energies between 161-209 GeV using $e^+e^- \to W^+W^-$ process. The combined value of the W-boson mass at LEP is 80.376 $\pm$ 0.033 GeV [6]–[9]. In 2018, ATLAS published its first W-boson mass measurement at 7 TeV center-of-mass energy: 80.370 $\pm$ 0.019 GeV [10]. Before 2021, the average of the direct measurements achieves a result of 80.379 $\pm$ 0.013 GeV, an extraordinary result approaching the frontier of the experimental techniques. However, when compared with the SM predictions using the latest top mass and Higgs mass results, the prediction of 80.354 $\pm$ 0.007 GeV can hardly set tight constraint to new physics, as the comparison is limited by the experimental precision.

LHCb recently released its proof-of-concept measurement of the W-boson mass at

13 TeV using 1.7 fb^{-1} luminosity, giving 80.354 $\pm$ 0.032 GeV, which is largely dominated by statistics [11]. A future measurement of the W-boson mass at LHCb using the full LHC Run 2 data is expected to bring partial cancellation of PDF uncertainties with the ATLAS measurement. A more recent publication of CDF II data, with an integrated luminosity of 8.8 fb^{-1} $p\bar{p}$ collision at 1.96 TeV, presents by far the most precise single measurement of the W-boson mass: 80.433 $\pm$ 0.009 GeV [12]. The precision of the CDF II result has exceeded the combination of all the previous measurements excluding LHCb, approaching the accuracy of the state-of-the-art theoretical prediction. However, a 7σ tension with respect to the SM is also observed by CDF II, which requires confirmation from other experiments, emphasizing the needs for new W-boson mass measurements at LHC with improved systematic uncertainties as well as the reprocessing the 7 TeV ATLAS data using improved method of statistical analysis. A new on-going measurement of the W-boson mass at ATLAS with the specialized datasets (Section 4.3.2) will be described in Chapter 8.

4.2 The methodologies of the precision W-boson mass measurements

The precision measurement of the W-boson mass started from the LEP era. As an electron positron collider, LEP produced the W-bosons in pairs via the annihilation of an electron and a positron. After the production, the W^+W^- pair decays subsequently in three modes: The fully hadronic decay results in four jets, of which the total energy adds up to the center-of-mass energy; the semi-leptonic decay yields a dijet product, a lepton signature and the missing energy in the detector brought by the neutrino; the fully leptonic decay comes with low statistics and significant missing energy in the detector. The reconstruction of the W-boson from jets at LEP benefited from the low event rate and the clean environment of the collisions. Also, thanks to the known total energy in the electron-positron collisions, in the case of the leptonic decays, the neutrino energy can be inferred from the conservation of the total energy and of the total momentum in three dimensions. The direct mass reconstruction method was used at LEP at 172, 183 and 189 GeV center-of-mass energies based on the fully hadronic decay and the semi-leptonic decay. Despite the lower branch ratio, the measurement based on the semi-leptonic decay mode had clean signal and no contribution from the dijet pairing problem compared with the fully hadronic decay model. As a result, the two decay modes yielded similar precision. In addition to the direct reconstruction of the W-boson invariant mass, LEP also determined the W-boson mass by measuring the W^+W^- production cross-section at the threshold center-of-mass energy around 161 GeV [13]–[16]. The precision of the threshold analysis is limited by the small size of the dataset taken at 161 GeV.

At hadron colliders, the measurement of the W-boson mass relies on the production of W-boson via the Drell-Yan process, as described in Section 1.2. In constract to LEP, the direct reconstruction of the W-boson invariant mass is extremely challenging regardless of the W-boson decay mode. In the hadronic decay, the QCD background is orders of magnitude higher than the electroweak production of the W-boson. In the leptonic decay, the conservation of the four momentum can no longer be used at hadron colliders to infer the momentum and the direction of the neutrino. For the above reasons, all W-boson mass measurements at hadron colliders are based

on the study of the leptonic decays of the W-boson with the help of the template fit method for statistics inference. The basic principle of the template fit method, as illustrated in Figure 4.1, is to generate the kinematic distributions associated to the leptonic decay of the W-boson, but with different hypothetical values of the W-boson mass in the simulation. And these simulated kinematic distributions with different hypotheses of the W-boson mass are referred to as templates. The W-boson mass hypothesis of the template that is closest to the corresponding kinematic distribution of the data is taken to be the most probable value of the W-boson mass from the measurement. In order to avoid the bias brought by the experimenter-expectancy effect, when using the template fit, an unknown offset has to be added to the value of the W-boson mass for the production of the templates and is only removed after the measurements are compatible in all channels as well as categories, and the analysis procedure is finalized. In the simplest test statistic of the template fit method, for instance, measurements [10]–[12], the most probable value of the W-boson mass is inferred from statistics without taking into account the bias introduced by the systematic effects. This method of statistical inference is usually referred to as the χ^2 offset method. The systematic uncertainties in the χ^2 offset method are taken into consideration later on by fitting the systematic variations as pseudo data and studying the offsets in the central value of the fit brought by the variations. A more advanced technique of statistical inference based on the template fit method, known as profile likelihood fit, has been recently introduce to the W-boson mass analysis [17], which corrects for the small systematic biases and allows to use the power of data to constrain the systematic uncertainties. Consequently, the profile likelihood fit improves both the accuracy (the central value) and the precision (the total uncertainty) of the measurement, with respect to the χ^2 offset method. More detailed discussions about the template fit method will be covered in Section 8.1.

Despite its success in the measurement of the W-boson mass, one major limitation of the template fit method arises from the systematic uncertainty in the modelling of the underlying transverse momentum distribution of the W-boson (p_{T}^{W}) in the simulation. Conventionally, the modelling of p_{T}^{W} is extrapolated from the well measured transverse momentum distribution of the Z-boson (p_{T}^{Z}). However, the extrapolation from p_{T}^{Z} to p_{T}^{W} is inclined to introduce large modelling uncertainty to the measurement. For example, in the ATLAS measurement of the W-boson mass at 7 TeV center-of-mass energy [10], the systematic uncertainty on the p_{T}^{W} modelling amounts to as high as 6 MeV out of the 19 MeV total uncertainty. One possible solution to constrain the p_{T}^{W} modelling uncertainty is to perform a direct measurement of the p_{T}^{W} spectrum with fine granularity and use it as the input to the W-boson mass analysis. Given that the neutrino in the leptonic decay of the W-boson escapes the detection, this p_{T}^{W} measurement relies on the precise measurement of the hadronic system in a clean collision environment, which would only be feasible at ATLAS by analyzing the specialized low pile-up dataset that will be introduced in Section 4.3. The measurement of the p_{T}^{W} spectrum using the low pile-up data and the propagation of the p_{T}^{W} uncertainty from the direct measurement to the W-boson mass analysis will be discussed in Chapter 7 and Section 8.3.2, respectively. The signal modelling and the background estimation of the W-boson analyses will be covered in Chapter 5. Chapter 6 will give a detailed description of the physics objects used in the analyses.

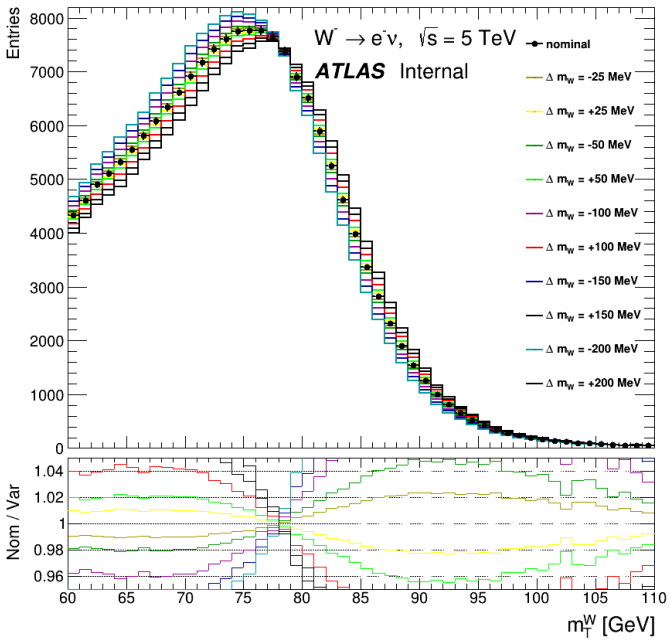

Figure 4.1 – An illustration of the template fit method for the measurement of the W-boson mass. Templates of the reconstructed level kinematic distribution assuming different values of the W-boson mass are compared with the nominal simulation. The sensitivity to the W-boson mass can be appreciated from the changes in the land-shape.

4.3 ATLAS low pile-up data

For *pp* collisions at LHC, no more than 1 hard inelastic process happens in every bunch crossing. However, additional inelastic *pp* collision may occur in the same bunch crossing along with the hard process. The number of those additional inelastic *pp* collisions per bunch crossing other than the one containing the hard process, is referred to as pile-up. The high instantaneous luminosity reached by the LHC implies a high pile-up environment. For instance, the average pile-up ($<\mu>$) of the 13 TeV Run 2 dataset is 33.7 [18]. And it is the combination of all the individual collisions that yields the signals seen by the detectors. As a result, deteriorated detector resolution and enhanced soft QCD background largely affect the measurements of W-boson production, imposing significant challenges to the precision measurement of the W-boson mass performed in ATLAS. Fortunately, even though low pile-up requires low instantaneous luminosity, the cross-sections for W and Z-boson production are large enough at LHC that a considerable amount of samples can still be collected within a few days of low instantaneous luminosity [19]. For these reasons, dedicated low pile-up data was taken during LHC Run 2 to help improve the relevant precision measurements.

4.3.1 General information of the datasets

The average pile-up is as high as 15-60 for typical LHC Run 2 runs. But for the low pile-up datasets that serve the needs of electroweak precision measurements, such as the measurement of the W-boson mass, $<\mu>$ is set to a much lower value. Putting

aside the performance of the LHC machine, the optimization of $<\mu>$ is essentially a trade-off between fast accumulation of samples and high proportion of triggered events with only one collision vertex [20]. Higher instantaneous luminosity comes with higher $<\mu>$, which means that the events pass the trigger much more frequently but the fraction of events with only one interaction is reduced. Toward another extremity, if $<\mu>$ approaches zero, almost all the triggered events have exactly one interaction, which enhances the experimental precision. This will be discussed in Section 4.3.2 with more details. However, the low instantaneous luminosity in this data taking condition will result in a longer time for the acquisition of sufficient statistics. Considering the above two aspects, the final decision of $<\mu>$ is made to be around 2 for the Run 2 low pile-up datasets as a middle ground.

The Run 2 low pile-up *pp* collision data used in the work of this thesis covers two center-of-mass energies: 5.02 TeV and 13 TeV [21], [22]. The 5.02 TeV *pp* collision data was recorded in 2017, with an integrated luminosity of 255 pb^{-1}. The corresponding number of W-boson events after selection is estimated to be about 1.45 million. The total luminosity uncertainty of 5.02 TeV data is 1 %. In 2017, ATLAS collected 147 pb^{-1} of low pile-up data at 13 TeV. Another round of low pile-up data taking was performed at 13 TeV in 2018, of which the integrated luminosity is 191 pb^{-1}. The total integrated luminosity of 13 TeV low pile-up data amounts to 338 pb^{-1}, providing 4.36 million W-boson events after selection. The combined 2017 and 2018 low pile-up data at 13 TeV has a total luminosity uncertainty of 0.92 %. The uncertainties in the integrated luminosity of the low pile-up datasets are determined following the method discussed in [19], using the LUCID-2 detector [23] for the primary luminosity measurement and complemented by the measurements using the inner detector and calorimeters. The luminosity-weighted distribution of $<\mu>$ for full Run 2 *pp* collision data at 13 TeV is shown in Fig 4.2, where the low pile-up data is contrasted by the other datasets from 2015 to 2018.

4.3.2 The physics interest of low pile-up conditions

The existing W-boson mass measurement at ATLAS using 7 TeV data [10] reveals clear difficulties related to the impact of pile-up on the study of W-boson production. The multiple proton interactions as high as $< \mu > \approx 9$ degrades the detector response to the hadronic system recoiling against the W decay products in the transverse plane (a.k.a. the recoil or u_{T}). The poor resolution of the recoil weakens the ability of the data to constrain the modelling of the W transverse momentum (p_{T}^{W}) distribution, leading to a large systematic uncertainty in the p_{T}^{W} modelling. Furthermore, since some kinematic distributions used for the extraction of the W-boson mass, such as the neutrino missing transverse momentum $p_{\mathrm{T}}^{\mathrm{miss}}$ and the W transverse mass m_{T}, are based on the u_{T} distribution, the statistical sensitivity of these observables to the W-boson mass are hence reduced. On top of that, soft QCD background (multijet) in high pile-up conditions is also a limiting factor of the total uncertainty. These three disadvantages are the main limitations of further improving the precision of m_W measurements using high pile-up datasets in ATLAS.

Given that no good modelling of p_{T}^{W} to the desired precision of a resolution better than ∼6-7 GeV exists to describe the data of u_{T} [24], p_{T}^{W} has to be extrapolated from p_{T}^{Z} after parton shower tuning in most cases. Both the experimental measurement of p_{T}^{Z} and the extrapolation contribute to the modelling uncertainty of p_{T}^{W}. However,

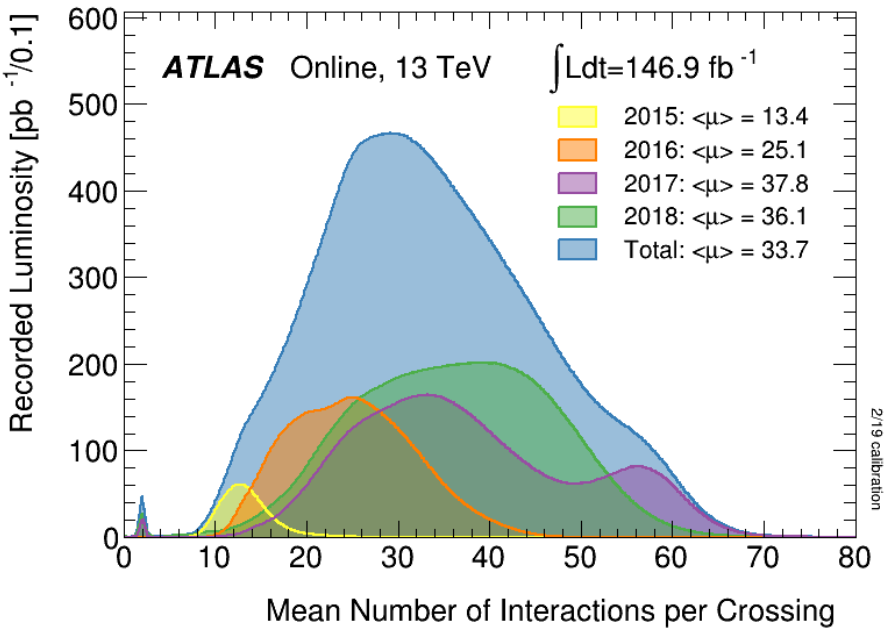

Figure 4.2 – Luminosity-weighted distribution of average interactions per bunch crossing for the full Run 2 *pp* collision data at 13 TeV. The little bump on the very left side of the plot indicates the 13 TeV low pile-up data recorded in 2017 and 2018 [18].

the theoretical uncertainty of the Z to W extrapolation is not only debatable but also crucial to the total uncertainty of the W-boson mass. Following this strategy, the p_{T}^{W} uncertainty is estimated to be more than 6 MeV in the W-boson mass measurement by ATLAS at the center-of-mass energy of 7 TeV, according to a quadratic sum of uncertainties related to parton shower tuning, the charm quark mass and perturbative calculation of parton shower as well as its corresponding missing higher order uncertainties. With the low pile-up data, it will be possible to directly measure the p_{T}^{W} spectrum instead of performing the theoretical extrapolation from p_{T}^{Z}. An uncertainty about 1-2 % with bin width close to 6-7 GeV is desired for the direct measurement, which is expected to halve the related QCD modelling uncertainty in the W-boson mass. The ratio of W^{+} over W^{-} p_{T} distributions will also achieve a good precision thanks to the cancellation of experimental systematics, rendering better constraints on the theoretical modelling of W-boson production. More detailed discussion of p_{T}^{W} and m_W measurement using Run 2 low pile-up data will be covered in Chapter 7 and Chapter 8.

From the experimental side, the Run 2 low pile-up datasets taken at two center-of-mass energies have slightly different features. The data recorded at $\sqrt{s}$=13 TeV comes with a better detector calibration and more signal candidates in total, while the $\sqrt{s}$=5.02 TeV dataset has in principle smaller underlying event and cleaner signals, including a lower fraction of the multijet background that cannot be reliably simulated. Consequently, the measurements of m_W at two center-of-mass energies are complimentary for their own advantages in different experimental aspects. From the theoretical side, it is very interesting to study the energy dependence of p_{T}^{W} spectrum, since the distribution is expected to vary by 20-30 % between 5.02 and 13 TeV. Another effect is that the fraction of charm-induced W-boson production increases rapidly from 5.02 to 13 TeV, which means that the precise measurements at both

centre-of-mass energies will help understand the impact of heavy flavor quarks on p_{T}^{W} spectrum. These studies relevant to the measurement of the p_{T}^{W} spectrum will benefit to the constraint on the physics modelling in the m_W measurement.

References

[1] G. Arnison *et al.*, "Experimental observation of isolated large transverse energy electrons with associated missing energy at s=540 gev", *Physics Letters B*, vol. 122, no. 1, pp. 103–116, 1983, ISSN: 0370-2693. DOI: https://doi.org/10.1016/0370-2693(83)91177-2. [Online]. Available: https://www.sciencedirect.com/science/article/pii/0370269383911772 (cit. on p. 74).

[2] B. Abbott *et al.*, "Measurement of the w boson mass", *Phys. Rev. D*, vol. 58, p. 092 003, 9 Sep. 1998. DOI: 10.1103/PhysRevD.58.092003. [Online]. Available: https://link.aps.org/doi/10.1103/PhysRevD.58.092003 (cit. on p. 74).

[3] T. Affolder *et al.*, "Measurement of the w boson mass with the collider detector at fermilab", *Phys. Rev. D*, vol. 64, p. 052 001, 5 Jul. 2001. DOI: 10.1103/PhysRevD.64.052001. [Online]. Available: https://link.aps.org/doi/10.1103/PhysRevD.64.052001 (cit. on p. 74).

[4] V. M. Abazov *et al.*, "Improved W boson mass measurement with the dø detector", *Phys. Rev. D*, vol. 66, p. 012 001, 1 Jul. 2002. DOI: 10.1103/PhysRevD.66.012001. [Online]. Available: https://link.aps.org/doi/10.1103/PhysRevD.66.012001 (cit. on p. 74).

[5] V. M. Abazov *et al.*, "Combination of cdf and d0 results on the W boson mass and width", *Phys. Rev. D*, vol. 70, p. 092 008, 9 Nov. 2004. DOI: 10.1103/PhysRevD.70.092008. [Online]. Available: https://link.aps.org/doi/10.1103/PhysRevD.70.092008 (cit. on p. 74).

[6] S. Schael *et al.*, "Measurement of the W boson mass and width in e+e- collisions at LEP", *The European Physical Journal C*, vol. 47, p. 309, 2006. DOI: 10.1140/epjc/s2006-02576-8 (cit. on p. 74).

[7] J. Abdallah *et al.*, "Measurement of the mass and width of the W boson in e+e- collisions at $\sqrt{s}$= 161–209 GeV", *The European Physical Journal C*, vol. 55, p. 38, 2008. DOI: 10.1140/epjc/s10052-008-0585-7 (cit. on p. 74).

[8] The L3 Collaboration, "Measurement of the mass and the width of the W boson at LEP", *The European Physical Journal C*, vol. 45, p. 569, 2006. DOI: 10.1140/epjc/s2005-02459-6 (cit. on p. 74).

[9] G. Abbiendi *et al.*, "Measurement of the mass and width of the W boson", *The European Physical Journal C*, vol. 45, p. 307, 2006. DOI: 10.1140/epjc/s2005-02440-5 (cit. on p. 74).

[10] The ATLAS Collaboration, "Measurement of the W-boson mass in pp collisions at $\sqrt{s} = 7$ TeV with the ATLAS detector", *The European Physical Journal C*, vol. 78, p. 110, 2018. DOI: 10.1140/epjc/s10052-017-5475-4 (cit. on pp. 74, 76, 78).

[11] The LHCb collaboration, "Measurement of the w boson mass", *Journal of High Energy Physics*, vol. 2022, no. 1, Jan. 2022. DOI: 10.1007/jhep01(2022)036 (cit. on pp. 75, 76).

[12] CDF collaboration *et al.*, "High-precision measurement of the w boson mass with the cdf ii detector", *Science*, vol. 376, no. 6589, pp. 170–176, 2022. DOI: 10.1126/science.abk1781. eprint: https://www.science.org/doi/pdf/10.1126/science.abk1781. [Online]. Available: https://www.science.org/doi/abs/10.1126/science.abk1781 (cit. on pp. 75, 76).

[13] R. Barate *et al.*, "Measurement of the w mass in e+e- collisions at production threshold", *Physics Letters B*, vol. 401, no. 3, pp. 347–362, 1997, ISSN: 0370-2693. DOI: https://doi.org/10.1016/S0370-2693(97)00460-7. [Online]. Available: https://www.sciencedirect.com/science/article/pii/S0370269397004607 (cit. on p. 75).

[14] P. Abreu *et al.*, "Measurement and interpretation of the w-pair cross-section in e+e- interactions at 161 gev", *Physics Letters B*, vol. 397, no. 1, pp. 158–170, 1997, ISSN: 0370-2693. DOI: https://doi.org/10.1016/S0370-2693(97)00226-8. [Online]. Available: https://www.sciencedirect.com/science/article/pii/S0370269397002268 (cit. on p. 75).

[15] M. Acciarri *et al.*, "Measurement of w-pair cross sections in e+e- interactions at s=172 gev and w-decay branching fractions", *Physics Letters B*, vol. 407, no. 3, pp. 419–431, 1997, ISSN: 0370-2693. DOI: https://doi.org/10.1016/S0370-2693(97)00802-2. [Online]. Available: https://www.sciencedirect.com/science/article/pii/S0370269397008022 (cit. on p. 75).

[16] K. Ackerstaff *et al.*, "Measurement of the mass of the w boson in e+e- collisions at s=161gev", *Physics Letters B*, vol. 389, no. 2, pp. 416–428, 1996, ISSN: 0370-2693. DOI: https://doi.org/10.1016/S0370-2693(96)01452-9. [Online]. Available: https://www.sciencedirect.com/science/article/pii/S0370269396014529 (cit. on p. 75).

[17] A. Collaboration, "Improved W boson Mass Measurement using 7 TeV Proton-Proton Collisions with the ATLAS Detector", CERN, Geneva, Tech. Rep., 2023. [Online]. Available: https://cds.cern.ch/record/2852059 (cit. on p. 76).

[18] *Run2Lumi*, https://twiki.cern.ch/twiki/bin/view/AtlasPublic/LuminosityPublicResultsRun2 (cit. on pp. 77, 79).

[19] "Luminosity determination for low-pileup datasets at $\sqrt{s} = 5$ and 13 TeV using the ATLAS detector at the LHC", Jul. 2020 (cit. on pp. 77, 78).

[20] B. Alvarez Gonzalez, L. Aperio Bella, A. J. Armbruster, *et al.*, "Physics potential of 200 pb^{-1} of *pp* collisions with low pile-up at $\sqrt{s} = 13$ TeV", CERN, Geneva, Tech. Rep., Aug. 2017. [Online]. Available: https://cds.cern.ch/record/2280709 (cit. on p. 78).

[21] A. Collaboration, "Precision measurements of W and Z transverse momentum spectra with the ATLAS detector at $\sqrt{s} = 5.02$ TeV and 13 TeV", CERN, Geneva, Tech. Rep., 2023, Paper draft for STDM-2018-17. [Online]. Available: https://cds.cern.ch/record/2856303 (cit. on p. 78).

[22] "Luminosity determination in *pp* collisions at $\sqrt{s} = 13$ TeV using the ATLAS detector at the LHC", Dec. 2022. arXiv: 2212.09379 [hep-ex] (cit. on p. 78).

[23] G. Avoni, M. Bruschi, G. Cabras, *et al.*, "The new lucid-2 detector for luminosity measurement and monitoring in atlas", *Journal of Instrumentation*, vol. 13, no. 07, P07017, Jul. 2018. DOI: 10.1088/1748-0221/13/07/P07017. [Online]. Available: https://dx.doi.org/10.1088/1748-0221/13/07/P07017 (cit. on p. 78).

[24] "Prospects for the measurement of the W-boson transverse momentum with a low pileup data sample at $\sqrt{s} = 13$ TeV with the ATLAS detector", CERN, Geneva, Tech. Rep., 2017, All figures including auxiliary figures are available at https://atlas.web.cern.ch/Atlas/GROUPS/PHYSICS/PUBNOTES/ATL-PHYS-PUB-2017-021. [Online]. Available: https://cds.cern.ch/record/2298152 (cit. on p. 78).

Chapter 5

W signal modelling and background estimation

Contents

5.1 MC samples in ATLAS Run 2 low pile-up data analyses

As mentioned earlier in Section 4.3, dedicated data-taking was carried out during Run 2 at low average interactions per bunch crossing, so as to help the precision electroweak measurements, such as the W transverse momentum (p_{T}^{W}) and the W-boson mass (m_W).

The signal process considered in the p_{T}^{W} and the m_W analyses is the W-boson production via the proton-proton collision described in Section 1.2, then followed by the leptonic decay of the given W-boson. Only electron and muon are referred to as leptons in the signal process, while W-boson decaying into tau and neutrino is one major electroweak background in the analyses. A few Feynman diagrams of this process at leading-order (LO) and next-to-leading-order (NLO) are shown in Figure 5.1 for illustrative purpose. Since the pile-up distributions are adjusted to those of the datasets, no further pile-up reweighting needs to be applied to the MC samples.

In order to model the signal process, the top-quark related background as well as the electroweak background, MC16 production campaigns are launched to fully simulate and reconstruct the ATLAS Monte Carlo (MC) samples. These MC samples are set to match the special data taking conditions at low pile-up, specifically the pile-up overlay, the topo-cluster noise threshold of the calorimeter and the corresponding trigger menu.

The main signal event samples for W and Z production are generated using the Powheg [1]–[4] event generator using the CT10 global PDF set [5]. For the simulation of the parton shower, Powheg is interfaced to Pythia8 [6] using the AZNLO tune [7]. The effect of QED final state radiation in the Powheg+Pythia8 samples is

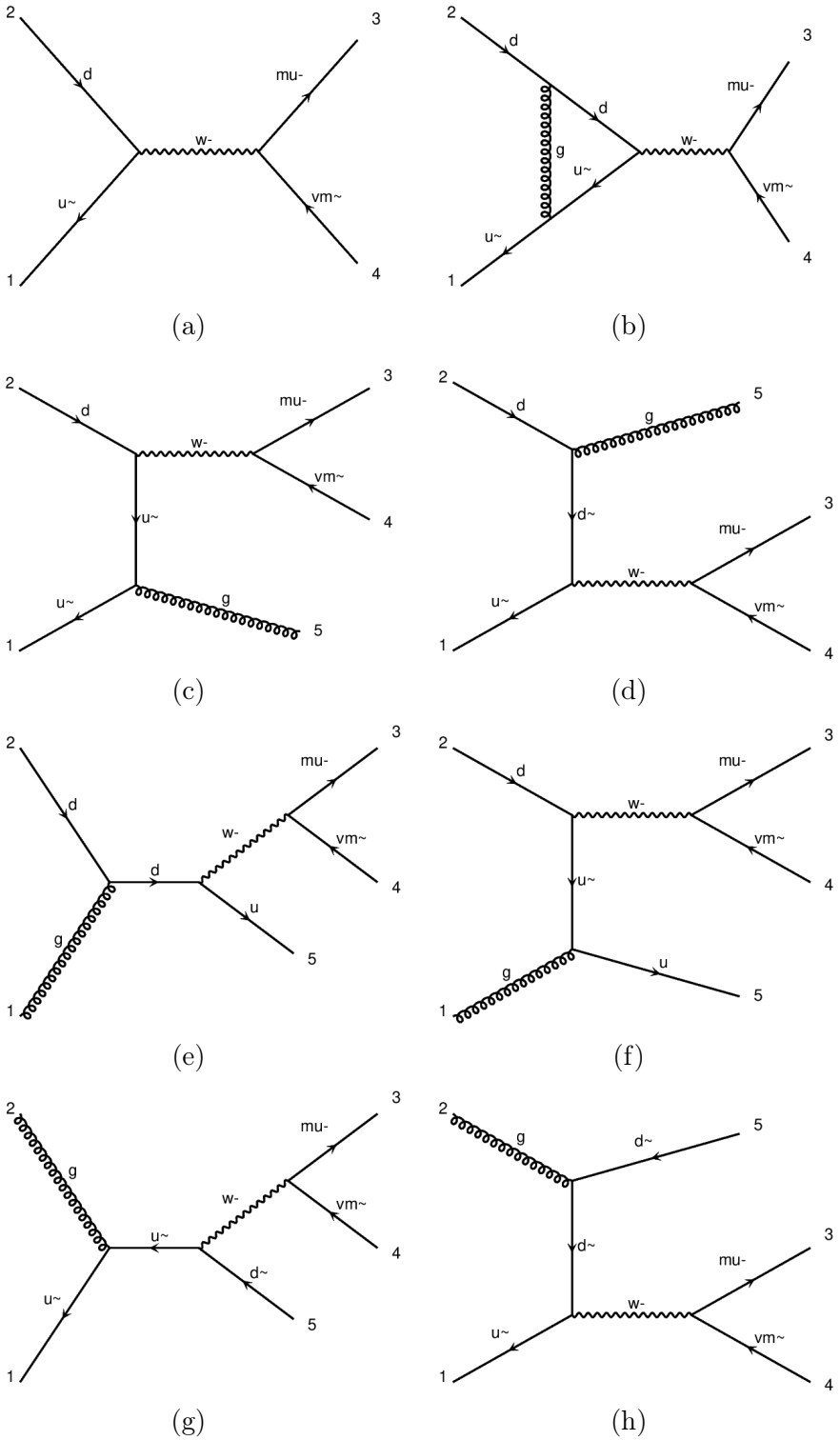

Figure 5.1 – The LO and NLO processes of W^- production and decaying into a pair of μ-ν, where the d-quark, $\bar{u}$-quark and gluon are involved as initial partons. (a) LO process. (b) Virtual loop. (c)(d) Gluon emission. (e)(f)(g)(h) Quark emission.

simulated by Photos++ [8]. The cross-sections of W and Z processes are normalized to NNLO calculation performed using the DYTURBO [9], [10] program with the MMHT2014nnlo PDF set [11]. Given that the uncertainties on the choice of the PDF

set plus the PDF set internal uncertainties ($\sim 3-4\%$), the dependence of factorization and renormalization scales ($< 1\%$), as well as the uncertainty of strong coupling constant α_S ($\sim 1-2\%$), a conservative total uncertainty of 5% is assigned to the event count predictions normalized using these cross-sections.

Single top-quark production (Wt, t-channel and s-channel) and top-quark pair-production $t\bar{t}$ are generated with Powheg+Pythia8 as well, among which the cross-section of $t\bar{t}$ at 5.02 TeV is taken from the Top++ prediction [12] reported by CMS [13]. Various combinations of di-bosons background ($VV, V = W, Z$) are produced with Sherpa [14] in all the decay channels for at least one real lepton in the final state. Cross-section uncertainties of 10% are assigned to the top-quark related background and the di-boson background, except for $t\bar{t}$ process, of which the cross-section uncertainty is 7%.

The effect of multiple interactions per bunch crossing (pile-up) is modelled by overlying the simulation of minimum bias events over the hard-scattering event. The minimum bias events are generated with Pythia8 using NNPDF2.3LO [15] as the global PDF set and A3 tune [16]. The soft QCD background (multijet or MJ) is derived via a data-driven method described in Section 4.4.

5.2 Object definitions and event selection

The reconstruction of primary vertices requires at least two charged-particle tracks. The primary vertex with the highest $\sum p_{\mathrm{T}}^2$ of all associated tracks is considered to be the hard-scattering vertex. The distribution of z-position of the primary vertex in the simulation is corrected to the data using a data-driven method in Z events. The 5.02 TeV simulation is adapted to perfectly match the data out-of-box. However, at 13 TeV, the data and simulation do not match very well, which mainly originates from the slightly different beam spots in 2017 and 2018 datasets. The residual acceptance effects due to different z-position distribution of the primary vertex can be corrected by reweighting the MC by the data/MC ratio taken from $\mathrm{Z}\to ee$ and $\mathrm{Z}\to \mu\mu$ selections, such that the data and MC distributions by construction match each other well after the reweighting. Despite marginal impact on p_{T}^W measurement, further studies might be required in the future to understand whether or not the effect of this correction is also negligible in the m_W analysis.

An electron is reconstructed from the clusters of energy deposition in the calorimeter that can be associated to a track in the ID, while a muon is reconstructed as a track crossing the muon spectrometer and the ID. Both types of object have to pass the kinematic cut $p_{\mathrm{T}}^{\ell} > 25$ GeV. A cut at 25 GeV, above the p_{T} cut in the lepton trigger, is chosen so as to avoid the migration of events from outside the kinematic region brought by the relatively low resolution of p_{T} used in the trigger. Considering the acceptance of the detector, the electron is limited to $|\eta| < 2.47$, excluding the transitional region of the calorimeter $1.37 < |\eta| < 1.52$. The muon is required to satisfy $|\eta| < 2.4$. As for lepton identification, the electron candidates must reach the Medium LH identification criteria [17]. Track isolation is applied to the lepton isolation selection, for which the nearby activity is measured by tracks in a cone of size $\Delta R < 0.2$ around the lepton candidate (ptcone20). The electron candidates have to be isolated according to ptcone20/Min(pT, 50 GeV). The muon candidates are required to pass the Medium identification criteria [18] and be isolated by the ptcone20/Min(pT,

50 GeV) track isolation criteria.

The lepton candidates of the $W \to \ell\nu$ and $Z \to \ell\ell$ analyses must originate from at least one primary vertex that is associated with at least two ID tracks. A trigger is supposed to be fired for at least one muon candidate with p_{T} above 14 GeV or loose-likelihood identified electron with p_{T} above 15 GeV. Two impact parameters are introduced in order to select the primary vertex. The longitudinal impact parameter of a lepton track is the distance between the track and the primary vertex along the beam line (Δz_0) times the $\sin\theta$ of the track. This quantity is required to fulfill $|\Delta z_0 \times \sin\theta| < 0.5$ mm. The second parameter describing the impact in the transverse plane, known as the significance of the transverse impact parameter, is defined to be the transverse impact parameter ($d0$) of the lepton track with respect to the nominal beam line divided by its estimated uncertainty ($\sigma(d0)$). The significance has to satisfy $|d0|/\sigma(d0) < 5$ for electron candidates and $|d0|/\sigma(d0) < 3$ for muon candidates.

Regarding W-boson production, the neutrino kinematics needs to be calculated at a high precision, which can only be achieved by the measurement of the hadronic recoil (u_{T}). In a proton-proton collision, due to the QCD initial state radiation of gluon or quark, the vector boson gains a non-zero momentum in the transverse plane, formulated by:

$$\vec{p}_{\mathrm{T}}(W/Z) = \vec{p}_{\mathrm{T}}^{\,lepton1} + \vec{p}_{\mathrm{T}}^{\,lepton2} = -\Sigma\vec{p}_{\mathrm{T}}^{\,ISR\,q,g} = -\vec{u}_{\mathrm{T}} \tag{5.1}$$

the left hand side $\vec{p}_{\mathrm{T}}(W/Z)$ denotes the transverse momentum of the vector boson and $\vec{p}_{\mathrm{T}}^{\,lepton}$ is the transverse momentum of the leptons. The hadronic recoil, $\vec{u}_{\mathrm{T}}$ is therefore the transverse momenta of the partons from the initial state radiation at detector level. The hadronic recoil turns out to be an important quantity in the m_W measurement. With the use of particle flow objects (PFOs [19]) as input ingredients to the reconstruction of u_{T} in Run 2, instead of reconstructing the vector sum of all topo-clusters [20], u_{T} has become an even more powerful tool for the precise determination of neutrino transverse momentum, according to:

$$\vec{E}_{\mathrm{T}}^{\mathrm{miss}} = \vec{p}_{\mathrm{T}}^{\,\nu} = -(\vec{u}_{\mathrm{T}} + \vec{p}_{\mathrm{T}}^{\,\ell}) \tag{5.2}$$

$\vec{E}_{\mathrm{T}}^{\mathrm{miss}}$ is the missing transverse energy of the neutrino. The W-boson transverse mass m_{T} is then derived from the kinematic information of the charged lepton and of the neutrino as follows:

$$m_{\mathrm{T}} = \sqrt{2p_{\mathrm{T}}^{\ell}E_{\mathrm{T}}^{\mathrm{miss}}(1 - \cos\Delta\phi)} \tag{5.3}$$

here $\Delta\phi$ is the azimuthal opening angle between $\vec{p}_{\mathrm{T}}^{\,\ell}$ of the charged lepton and neutrino $\vec{E}_{\mathrm{T}}^{\mathrm{miss}}$. Another critical quantity ΣE_{T}, defined to be the scalar sum of the p_{T} of all PFOs, represents the total event activity. ΣE_{T} is related to the resolution of the u_{T} measurement and grows with $p_{\mathrm{T}}^{V} = u_{\mathrm{T}}$. In order to represent the activity from underlying event, pile-up as well as the emissions beyond the order of V + 1 jet process,

$$\Sigma\bar{E}_{\mathrm{T}} = \Sigma E_{\mathrm{T}} - u_{\mathrm{T}} \tag{5.4}$$

is introduced to correct the event activity by the directed recoil activity, disentangling the dependence of ΣE_{T} on boson dynamics.

5.2.1 W analysis event selection

Candidates of $W \to \ell\nu$ ($\ell = \mu, e$) events are recorded in the data with single-lepton triggers. The primary, unprescaled triggers are used in both 5.02 and 13 TeV datasets. $HLT\_e15\_lhloose\_nod0\_L1EM12$ single-lepton trigger is required for electron, where at least one reconstructed electron with E_{T} larger than 15 GeV and passing loose identification is required. HLT_mu14 is applied to muons, requiring p_{T} of the muon to be higher than 14 GeV.

W events are selected to contain exactly one identified and isolated lepton candidate satisfying the criteria of object definitions. In order to suppress the Z background, any event with additional leptons of the same flavour with p_{T} higher than 20 GeV meeting certain identification criteria is vetoed. Background fraction, in particular the multijet background, can be effectively reduced once the following two kinematic cuts are applied to the events in addition to the lepton kinematic cut: $E_{\mathrm{T}}^{\mathrm{miss}}$>25 GeV and m_{T} >50 GeV. The three cuts of lepton p_{T}, $E_{\mathrm{T}}^{\mathrm{miss}}$ and m_{T} are kept coherent, such that an optimal trade-off can be achieved in balancing background rejection and signal selection efficiency.

An overview of pre-selection, object selection and event selection for W candidates is summarized in Table 5.1.

Pre-selection		
GRL	Pass Good Run List	
Vertex	Number of primary vertex ≥ 1	
Object selection		
	Electron	Muon
p_{T}	p_{T} >25 GeV	p_{T} >25 GeV
η	$\lvert\eta\rvert < 1.37$ or $1.52 < \lvert\eta\rvert < 2.47$	$\lvert\eta\rvert < 2.4$
Identification	MediumLH	Medium
Isolation	$ptcone20/Min(p_{\mathrm{T}}, 50\,\mathrm{GeV})$<0.1	$ptcone20/Min(p_{\mathrm{T}}, 50\,\mathrm{GeV})$<0.1
Trigger	$HLT\_e15\_lhloose\_nod0\_L1EM12$	HLT_mu14
Event selection		
N leptons	Exactly one electron or muon	
$E_{\mathrm{T}}^{\mathrm{miss}}$	$E_{\mathrm{T}}^{\mathrm{miss}} = \lvert\vec{u}_{\mathrm{T}} + \vec{p}_{\mathrm{T}}^{\,\ell}\rvert$ >25 GeV	
m_{T}	m_{T} >50 GeV	

Table 5.1 – Summary of pre-selection, object selection and event selection for W-boson candidates in low pile-up data

5.2.2 Calibration of vertex selection efficiency

In the leptonic decay of a W-boson, due to the neutrino in the decay product, only the association of the single lepton to the primary vertex can be performed via the impact parameter cuts. The second track used in the search of vertex has to rely on the hadronic activities associated to the W-boson production, either jets or the underlying event. What is more complicated is that the single lepton used in the vertex association may actually originate from pile-up rather than the hard-scattering,

especially in the case of electron. The reconstructed vertices associated to the tracks of these leptons will not be selected as the event primary vertex due to the leptons not passing the impact parameter cuts. Although Z-boson selected events are generally used to calibrate the W-boson analyses, the two reconstructed leptons in a Z event help the vertex selection become almost independent of the hadronic activities and hardly influenced by the effects that lead to vertex selection inefficiency in W events.

It has been found that the efficiency of lepton matching the primary vertex is not well reproduced by the simulation of W events with Powheg+Pythia8 in the low p_{T} region [21], mainly due to a mis-modelling in the underlying events. The effect of this mis-modelling is studied by comparing between the data and the MC the fraction of $Z \to \mu\mu$ events with 0 or 1 additional tracks (excluding the two leptons in the decay product) matching the z-position of the hard interaction. A significant discrepancy is found between data and MC in the low p_{T} region where the majority of the W-bosons is produced. Therefore, a dedicated correction of vertex selection efficiency is derived for W events.

The correction of vertex selection efficiency relies on the extraction of the efficiency of lepton matching the primary vertex as a function of boson p_{T}, in three categories of events: with 0, 1, or more than 1 additional tracks matching the z-position of the hard interaction. The inefficiency in each category of events $(1 - \epsilon(p_{\mathrm{T}})_i)$ is obtained from W simulation. The fraction of number of events falling into each category $(frac(p_{\mathrm{T}})_i)$ is extracted from Z events as a function of $p_{\mathrm{T}}^{\ell\ell}$, separately for data and simulation. The overall efficiency for a given sample S, to be either data or a MC simulation, can be expressed in:

$$\begin{aligned}\epsilon(p_{\mathrm{T}})_S = & \, frac(p_{\mathrm{T}})_{(0,S)} \cdot \epsilon(p_{\mathrm{T}})_{(0,Powheg+Pythia8)} \\ & + frac(p_{\mathrm{T}})_{(1,S)} \cdot \epsilon(p_{\mathrm{T}})_{(1,Powheg+Pythia8)} \\ & + frac(p_{\mathrm{T}})_{(>1,S)} \cdot \epsilon(p_{\mathrm{T}})_{(>1,Powheg+Pythia8 \to S)}\end{aligned} \tag{5.5}$$

While $1-\epsilon(p_{\mathrm{T}})_{(0,Powheg+Pythia8)}$ and $1-\epsilon(p_{\mathrm{T}})_{(1,Powheg+Pythia8)}$ are simply the inefficiencies of lepton matching primary vertex for 0 or 1 additional tracks from Powheg+Pythia8 simulation, a 2D-reweighting is applied to the Powheg+Pythia8 W simulation to match the $(\sum E_{\mathrm{T}}^{charged} \equiv \sum E_{\mathrm{T}}$ of tracks close to the interaction point, $p_{\mathrm{T}}^{\ell\ell})$ distribution in the target sample S before determining $\epsilon(p_{\mathrm{T}})_{(>1,Powheg+Pythia8 \to S)}$.

In the nominal case for p_{T}^{W} analysis where the data is studied by unfolding, the Powheg+Pythia8 simulation is corrected by a function of boson p_{T}:

$$\epsilon(p_{\mathrm{T}})_{data} / \epsilon(p_{\mathrm{T}})_{Powheg+Pythia8} \tag{5.6}$$

In the p_{T}^{W} analysis, the uncertainty on the vertex selection efficiency due to mis-modelling in the underlying events is estimated by comparing two generators that are known to model underlying events differently. So, in order to estimate only the residual difference between the two MC setups generated in different ways, Sherpa is first reweighted to Powheg in $(p_{\mathrm{T}}^{true,V}, y)$, then calibrated to Powheg+Pythia8 nominal signal samples (following the same procedure as how Powheg is calibrated to data). After that, the difference in the results obtained with calibrated Sherpa and the nominal Powheg+Pythia8 is taken as the generator systematic uncertainty and propagated to the analysis chain.

5.3 Modelling of boson kinematics and physics corrections

The inclusive $Z \to \ell\ell$ and $W \to \ell\nu$ cross-sections are six-dimensional due to the two final-state leptons coming with fixed masses. A factorization of the differential cross-section has been demonstrated and successfully implemented in the 7 TeV ATLAS m_W measurement [20]:

$$\begin{aligned}\frac{\mathrm{d}\sigma}{\mathrm{d}p_1\mathrm{d}p_2} = &\left[\frac{\mathrm{d}\sigma(m)}{\mathrm{d}m}\right]\left[\frac{\mathrm{d}\sigma(y)}{\mathrm{d}y}\right]\left[\left.\frac{\mathrm{d}\sigma(p_\mathrm{T})}{\mathrm{d}p_\mathrm{T}}\right|_y \frac{\mathrm{d}\sigma(y)}{\mathrm{d}y}^{-1}\right] \\ &\times \left[(1+\cos^2\theta) + \sum_{i=0}^{7} A_i(p_\mathrm{T}, y, m) P_i(\cos\theta, \phi)\right]\end{aligned} \tag{5.7}$$

The four factorized quantities are related to the di-lepton (or boson) system. p_1 and p_2 are the lepton and anti-lepton four momenta. m, p_T and y are the invariant mass, transverse momentum and rapidity of the di-lepton system. If lepton refers to the negatively charged lepton from W^- or Z-boson as well as the neutrino from a W^+ boson, then θ and ϕ are the polar angle and the azimuth of the lepton in the rest frame of the di-lepton system. A_i's are the numerical angular coefficients representing the fraction of each helicity-state cross-section of the boson production, depending on boson transverse momentum, rapidity and mass. However, an approximation is introduced as discussed in the 7 TeV measurement that the dependence of A_i's on the final state invariant mass can be neglected. Each of the angular coefficient is multiplied by a spherical harmonic of order zero, one or two, noted as P_i in the formula.

The above factorization facilitates a simplified modelling of the mass-distribution $\mathrm{d}\sigma(m)/\mathrm{d}m$, the boson rapidity distribution y as well as the eight angular coefficients A_i predicted by fixed-order calculation, and the boson-p_T distribution at a given rapidity $\mathrm{d}\sigma(p_\mathrm{T})/\mathrm{d}p_\mathrm{T}|_y$, which can be described by resummation or tuned parton shower as discussed in Section 1.2.

5.3.1 Parameterization of boson resonance

The boson resonance ($\mathrm{d}\sigma(m)/\mathrm{d}m$) in Equation 5.7 is parameterized by a Breit-Wigner distribution. To start with, the gauge interactions and couplings are expressed as:

$$\begin{aligned}\mathcal{L}_{NC} &= \sum_{i=\gamma,Z} \alpha_i \bar{f}\gamma_\mu(v_{f_i} - a_{f_i}\gamma^5) f V_i^\mu \\ \mathcal{L}_{CC} &= \alpha_W V_{f\bar{f}'}\gamma_\mu(1-\gamma^5) f W^\mu\end{aligned} \tag{5.8}$$

where the gauge coupling constants α_i, the generation-mixing terms $V_{f\bar{f}'}$ and the vector and axial couplings v_i, a_i for the incoming and outgoing fermions are summarized for the gauge bosons in Table 5.2.

Using the same set of notation, the parton-level $q\bar{q} \to \ell\ell$ and $q\bar{q}' \to \ell\nu$ cross-

Vertex	$\gamma f\bar{f}$	$Zf\bar{f}$	$Wf\bar{f}'$
α_i	α_{em}	$G_\mu m_Z^2/(2\sqrt{2}\pi)$	$G_\mu m_W^2/(\sqrt{2}\pi)$
v_i	Q_f	$I_{3f} - 2Q_f \sin^2\theta_W$	I_{3f}
a_i	0	I_{3f}	I_{3f}
V_i	1	1	$V_{ff'}$

Table 5.2 – The SM gauge coupling constants, fermion vector and axial-vector coupling factors as well as the generation mixing terms. $V_{ff'}$ is known from the CKM matrix.

sections at leading order are written as:

$$\begin{aligned} \hat{\sigma}(\hat{s}) &\propto \sum_{i,j} \alpha_i \alpha_j V_i V_j B_{ij} P_{ij}(\hat{s}) \\ B_{ij} &= (v_i v_j + a_i a_j)_{in}(v_i v_j + a_i a_j)_{out} \\ P_{ij}(\hat{s}) &= \hat{s} \frac{(\hat{s} - m_i^2)(\hat{s} - m_j^2) + m_i m_j \Gamma_i \Gamma_j}{\left[(\hat{s} - m_i^2)^2 + (m_i\Gamma_i)^2\right]\left[(\hat{s} - m_j^2)^2 + (m_j\Gamma_j)^2\right]} \end{aligned} \tag{5.9}$$

The summation runs over the exchanged gauge bosons in the s-channel. In the case of charged-current interactions mediated by W-boson, the indices i, j only take one value, while in the neutral-current interactions mediated by γ and Z-boson they take two values. This is interpreted as i=j representing the squared amplitude corresponding to the exchange of a given boson in the diagonal and the cross terms when i≠j describing the contribution of γ-Z interference. The mass and width of a gauge boson i are denoted to be m_i and Γ_i. $\hat{s}$ stands for the available energy for the parton-level process.

The formula above is known as the fixed-width parameterization and was commonly used in the MC generators. An alternative parameterization, as used in the Z peak studies in LEP [22] and in the earlier m_W measurement [20], is the running-width form, where every factor of $m\Gamma$ is substituted by $\frac{\hat{s}}{m}\Gamma$, such that

$$P'_{ij}(\hat{s}) = \hat{s} \frac{(\hat{s} - m'^2_i)(\hat{s} - m'^2_j) + \frac{\hat{s}^2}{m'_i m'_j}\Gamma'_i \Gamma'_j}{\left[(\hat{s} - m'^2_i)^2 + (\frac{\hat{s}}{m'_i}\Gamma'_i)^2\right]\left[(\hat{s} - m'^2_j)^2 + (\frac{\hat{s}}{m'_j}\Gamma'_j)^2\right]} \tag{5.10}$$

When the running-width Breit-Wigner parameterization is used, the physical masses and widths of the gauge bosons should be taken from the PDG values [23] for the nominal simulation.

The two parameterizations are equivalent up to a redefinition of boson resonance parameters [24]:

$$\begin{aligned} m_i &= m'_i / \sqrt{1 + (\Gamma'_i/m'_i)^2} \\ \Gamma_i &= \Gamma'_i / \sqrt{1 + (\Gamma'_i/m'_i)^2} \end{aligned} \tag{5.11}$$

The W and Z samples produced by Powheg+Pythia8 are reweighted using the photon couplings in the vicinity of the Z peak defined as $\alpha_{em}(s)$, taking into account theoretical inputs for lepton loops as well as a mixture of theory and measurements for the

quark contributions:

$$\alpha_{em}(s) = \frac{\alpha_{em}(0)}{1 - \Delta\alpha(s)}$$
$$\Delta\alpha(s) = \frac{\alpha_{em}(0)}{3\pi}(13.4955 + 3\ln s) + 0.00165 + 0.00299\ln(1+s) \tag{5.12}$$

The experimental value of G_μ is taken for the weak boson couplings as a constant.

So far, the formalism of boson resonance doesn't consider the real photon emission corrections. In ATLAS, those corrections are applied to the simulation with Photos as an afterburner, such that photon emissions are generated based on the event record returned by the Powheg+Pythia8, modifying the lepton kinematics in the final state. In Photos [8], multiple photon radiation is generated in the full available phase space starting from the Born-level final state without QED radiation, where the emission of each photon is calculated according to the corresponding QED matrix element. After each emission, the available phase space is updated by excluding the emitted real photon in the vertex, as illustrated in Figure 5.2, so that another iteration is carried out using the same perturbative accuracy. The iteration comes to an end when the energy of the emitted photon is 10^{-7} times smaller than the parent lepton in the decay rest frame.

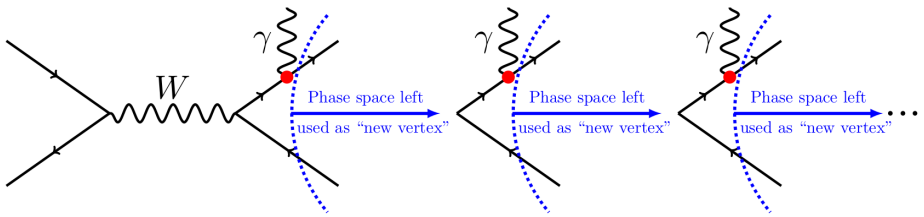

Figure 5.2 – The iterative calculation of QED FSR applied in ATLAS using Photos. Figure taken from [25].

5.3.2 Boson rapidity and transverse momentum

For the m_W measurement, the differential cross-section as a function of boson rapidity, $\mathrm{d}\sigma(y)/\mathrm{d}y$, is modelled with fixed-order perturbative QCD predictions at $\mathcal{O}(\alpha_S^2)$ in the perturbative expansion of the strong coupling constant using the CT18ANNLO PDF set [26].

Given that most gauge bosons generated for the analyses come with a low transverse momentum in the region p_{T}^W <30 GeV, the predictions of the boson transverse momentum cannot rely solely on fixed-order perturbative QCD calculations. The non-perturbative effects of QCD are accounted for by parton showers to predict the transverse momentum spectrum of vector boson at a given boson rapidity $\mathrm{d}\sigma(p_{\mathrm{T}})/\mathrm{d}p_{\mathrm{T}}|_y$ in equation 5.7. The AZNLO tune of Powheg+Pythia8 [7] is chosen to be the parameter setup of parton shower. The CTEQ6L1 PDF set [27] is used for the parton shower.

As it is revealed in the measurement of W transverse momentum with low pile-up data, the default prediction of rapidity-inclusive boson transverse momentum significantly deviates from the data. In order to avoid starting off the analysis with a clearly known non-optimal modelling that is due to bring bias to the physics results, a

data-driven correction is applied to the boson transverse momentum at particle-level, such that a good data-MC agreement is observed on boson transverse momentum at reco-level. The particle-level reweighting functions are derived based on center-of-mass energy, boson charge and the choice of reco-level kinematic distribution as observable. More detailed description of this reweighting technique will be covered in Section 7.3.

5.3.3 Angular coefficients

At leading order without QCD ISR, the vector bosons are only transversely polarized during the production. The angular distributions of the decay leptons only depend on the polar angle of the lepton in the boson rest frame. At higher orders, the non-zero transverse momentum brought by QCD ISR affects the polarization states of the bosons. Consequently, azimuthal asymmetries arise in the angular distribution of the decay leptons [28]–[31]. The polarization of the W and Z boson is completely embodied in the eight A_i's of equation 5.7. The dependence of the differential cross-section on the polar and the azimutal angles of the lepton in the boson rest frame is written down explicitly by:

$$\begin{aligned}\frac{\mathrm{d}\sigma}{\mathrm{d}p_{\mathrm{T}}^2\mathrm{d}y\mathrm{d}m\mathrm{d}\cos\theta d\phi} = \frac{3}{16\pi}\frac{\mathrm{d}\sigma}{\mathrm{d}p_{\mathrm{T}}^2\mathrm{d}y\mathrm{d}m} \times [&(1+\cos^2\theta) + A_0\frac{1}{2}(1-3\cos^2\theta) \\ &+ A_1\sin 2\theta\cos\phi \\ &+ A_2\frac{1}{2}\sin^2\theta\cos 2\phi \\ &+ A_3\sin\theta\cos\phi \\ &+ A_4\cos\theta \\ &+ A_5\sin^2\theta\cos\phi \\ &+ A_6\sin 2\theta\sin\phi \\ &+ A_7\sin\theta\sin\phi]\end{aligned} \tag{5.13}$$

Making use of the completeness of the spherical harmonics, the A_i's can be extracted via the projector defined as follows [32]:

$$< P_i(\theta,\phi) >= \frac{\int_{-1}^{1}\mathrm{d}\cos\theta\int_0^{2\pi}\mathrm{d}\phi\mathrm{d}\sigma(\theta,\phi)P_i(\theta,\phi)}{\int_{-1}^{1}\mathrm{d}\cos\theta\int_0^{2\pi}\mathrm{d}\phi\mathrm{d}\sigma(\theta,\phi)} \tag{5.14}$$

Such that

$$\begin{aligned}&A_0 = 4 - 10 < \cos^2\theta >, A_1 = 5 < \sin(2\theta)\cos\phi >, \\ &A_2 = 10 < \sin^2\theta\cos(2\phi) >, A_3 = 4 < \sin\theta\cos\phi >, \\ &A_4 = 4 < \cos\theta >, A_5 = 5 < \sin^2\theta\sin(2\phi) >, \\ &A_6 = 5 < \sin(2\theta)\sin\phi >, A_7 = 4 < \sin\theta\sin\phi >\end{aligned} \tag{5.15}$$

represent the ratios of helicity cross-sections with respect to the unpolarized one. The angles θ and ϕ are defined in a boson rest frame with arbitrary momentum along the z-axis, known as the Collins-Soper (CS) frame [33].

According to the measurement of Z A_i's at 8 TeV [34], the fixed-order NNLO perturbative QCD predictions of the angular coefficients describe well the data. A_i's

depend on boson mass, p_{T} and rapidity. Since the dependence on boson mass is relatively weak, the predictions are made with a fixed boson mass. However, it is understood that the angular correlations between the two decay leptons due to the polarization of the mother vector boson, are not properly modelled in the baseline simulation of Powheg+Pythia8 that produces W and Z samples. The generator only reaches NLO accuracy in QCD and predicts negative A_0 as $p_{\mathrm{T}}^{true,V}$ approaches 0. For this reason, the original angular coefficients are reweighted to NNLO predictions as what is done in the 7 TeV m_W analysis.

With CT10NNLO PDF set [35], DYTURBO predicts the angular coefficients as functions of boson p_{T} and rapidity, individually for W^+, W^- and Z. Noting A_i the initial prediction of an angular coefficient and A_i' an alternative prediction, the $\cos(\theta)$ and ϕ of the events are reweighted by the following weight:

$$w = \frac{1 + \cos^2\theta + \sum_{i=0}^{7} A_i'(p_{\mathrm{T}}, y) P_i(\cos\theta, \phi)}{1 + \cos^2\theta + \sum_{i=0}^{7} A_i(p_{\mathrm{T}}, y) P_i(\cos\theta, \phi)} \tag{5.16}$$

where the angular coefficients of Powheg+Pythia8 appear in the denominator and those of DYTURBO at $\mathcal{O}(\alpha_S^2)$ appear in the numerator.

5.4 Estimation of the MJ background

In addition to the electroweak and top-quark related background described in Section 5.1, multijet (MJ) background also contaminates the events with single W or Z-boson final states. The MJ background originates from semi-leptonic decays of heavy quarks, in-flight pion decays. And in the case of electron channels, MJ may come from pion faking an electron or photon conversion as well. In W events, although the MJ background is in principle well rejected by the lepton isolation selection and kinematic cuts on m_{T} and $E_{\mathrm{T}}^{\mathrm{miss}}$, a non-negligible contribution is still attributed to both the large jet production cross-section and the limited resolution of $E_{\mathrm{T}}^{\mathrm{miss}}$. In contrast, the MJ contribution is much smaller in Z channels due to the requirement of two opposite-sign, well-identified and isolated leptons. MJ background can hardly be simulated precisely at detector-level because its effect after signal selection is essentially a large production cross-section multiplied by a tiny efficiency. Good control is demanded for both quantities in order to obtain the accurate shape and the yield of the MJ background, which is not easily achievable. Instead, based on what has been proposed in [36], a data-driven method is used for the estimation of MJ background and the relevant uncertainties in the low pile-up p_{T}^W and m_W measurements [37].

The W-boson phase-space in the signal region (SR) that is used for the main measurement of p_{T}^W spectrum, is defined by the following selections:

— $p_{\mathrm{T}}^{\ell} > 25\,\mathrm{GeV}$ and $|\eta_{\ell}| < 2.4$.
— $E_{\mathrm{T}}^{\mathrm{miss}} > 25\,\mathrm{GeV}$.
— $m_{\mathrm{T}} > 50\,\mathrm{GeV}$.
— Lepton isolation as ptcone20/Min(pT,50 GeV)<0.1.

It is shown in [38] that ptcone20/Min(pT,50 GeV) tightens the lepton isolation consistently at high u_{T} region and ensures a good compatibility between electron and muon channels.

Four regions are defined by relaxing the kinematic cuts and inverting the lepton isolation selection (Figure 5.3):

— Signal region (SR): Isolated leptons and signal phase-space for p_{T}^{ℓ}, $E_{\mathrm{T}}^{\mathrm{miss}}$ and m_{T}.
— Fit region (FR): Isolated leptons, but without cut on $E_{\mathrm{T}}^{\mathrm{miss}}$ or on m_{T}.
— Control region 1 (CR1): Anti-isolated leptons (ptcone20/Min(pT, 50 GeV)>0.1) and relaxed kinematic cuts like FR.
— Control region 2 (CR2): Anti-isolated leptons with full kinematic cuts like SR.

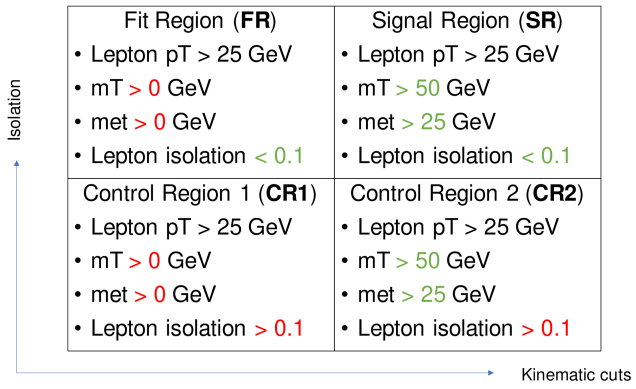

Figure 5.3 – The definition of four regions used in MJ study, according to the division of fiducial space and lepton isolation.

The basic idea of MJ estimation is to use the two MJ enriched control regions, CR1 and CR2, to infer the fraction and the shape of MJ background in SR. Considering that the MJ production is concentrated at lower values of p_{T}^{ℓ}, $E_{\mathrm{T}}^{\mathrm{miss}}$ and m_{T}, it is more practical to first determine the fraction of MJ in FR where m_{T} and $E_{\mathrm{T}}^{\mathrm{miss}}$ cuts are relaxed, such that the peak of the MJ distribution facilitates the convergence of the fraction fit:

$$N_{data}^{FR} = \alpha \cdot N_{EW+top}^{FR} + T \cdot N_{MJ}^{CR1} \tag{5.17}$$

N_{data}^{FR}, N_{EW+top}^{FR} and N_{MJ}^{CR1} stand for the total number of data events in FR, expected contribution from electroweak and top-quark related process in FR and the number of MJ events in CR1 ($N_{MJ}^{CR1} = N_{data}^{CR1} - N_{EW}^{CR1}$). T is the scale of MJ template in FR to be determined by the fit, while α represents an overall normalization of contribution from electroweak and top-quark related process approximately equal unity, within the uncertainties in luminosity and production cross-sections. Then the MJ yield in FR is given by:

$$N_{MJ}^{FR} \approx T \cdot N_{MJ}^{CR1} \tag{5.18}$$

While SR and CR2 share the same set of kinematics cuts, FR and CR1 also share another set of kinematics cuts. The only differences between these two sets of kinematics cuts are the additional selections on m_{T} and $E_{\mathrm{T}}^{\mathrm{miss}}$ in SR and CR2. Therefore,

the yield in FR can be extrapolated to the yield in SR with a transfer factor ϵ derived from the two control regions:

$$N_{MJ}^{SR} = \epsilon N_{MJ}^{FR} = \frac{N_{MJ}^{CR2}}{N_{MJ}^{CR1}} \times N_{MJ}^{FR} = \frac{N_{data}^{CR2} - N_{EW+top}^{CR2}}{N_{data}^{CR1} - N_{EW+top}^{CR1}} \times N_{MJ}^{FR} \tag{5.19}$$

The shape of MJ template used in the fraction fit in FR, as well as the expected MJ shape in SR, has to be derived from CR1 and CR2, respectively.

Section 5.4.1 will describe a dedicated correction applied to the MJ estimation so as to eliminate a bias in the recoil construction in CR1 and CR2. Section 5.4.2 and 5.4.3 explain how the yield and the shape of MJ in SR are obtained. Section 5.4.4 is about the uncertainty sources of MJ estimation for p_{T}^{W} analysis. Section 5.4.5 summarizes the results of MJ for p_{T}^{W} analysis.

5.4.1 Recoil isolation correction

During the recoil reconstruction for a W event, all the PFOs are used for the given event, but excluding the cone of $\Delta R = 0.2$ around the selected lepton. The energy of pile-up and underlying event removed in this cone is subsequently compensated by looking at another cone with the same size centered at the same $|\eta|$ but in an azimuth away from any lepton or hard activity. The energy in this selected cone is added to the recoil, with its orientation aligned to the direction of the removed lepton. In SR and FR, the leptons are isolated, meaning they are typically away from jets and are surrounded by soft activities. The removal and replacement of the cone does not introduce a bias to the recoil. However, in anti-isolated regions, the lepton in interest is on average close to a jet. Replacing the cone around the lepton with another cone of soft activities removes the hard contribution and biases the recoil reconstruction. The m_{T} and $E_{\mathrm{T}}^{\mathrm{miss}}$ are affected by this bias, since the computation of their values uses the recoil as input.

The projection of the recoil along the direction of the lepton momentum $u_{||}^{\ell} = \vec{u}_{\mathrm{T}} \cdot \frac{\vec{p}_{\mathrm{T}}^{\ell}}{|\vec{p}_{\mathrm{T}}^{\ell}|}$, is pertinent to the bias, since the magnitude in its direction is affected by this cone replacement on average. In the absence of bias, $u_{||}^{\ell}$ is mostly independent on lepton isolation, whereas the dependence of $u_{||}^{\ell}$ on ptcone20 indicates the bias. The quantity ptcone20, sum of transverse momentum of tracks around a lepton, is correlated to the energy to be removed around the lepton, even though the neutral components are not accounted for in ptcone20. So, a correction to recoil u_{T} as a function of ptcone20 is proposed:

$$\vec{u}_{\mathrm{T}}^{corr} = \vec{u}_{\mathrm{T}}^{baseline} + (k_{iso} \times ptcone20)\frac{\vec{p}_{\mathrm{T}}^{\ell}}{|\vec{p}_{\mathrm{T}}^{\ell}|} \tag{5.20}$$

where $u_{\mathrm{T}}^{baseline}$ is the recoil before correction, and u_{T}^{corr} the recoil after the correction. The linear coefficient k_{iso} takes into account the possible difference in the scale between ptcone20 and the total energy removed in the cone around the lepton. Considering the correlation between ptcone20 (contributions from only the charged components) and the total energy of hard activity (both neutral and charged components) within the cone remains unknown, the coefficient k_{iso} has to be measured from the data by performing a linear fit:

$$< u_{||}^{\ell,baseline} >= -k_{iso} < ptcone20 > +b \tag{5.21}$$

Channel	k_{iso}
13 TeV $W^- \to e^-\nu$	1.179 ± 0.009
13 TeV $W^+ \to e^+\nu$	1.178 ± 0.009
13 TeV $W^- \to \mu^-\nu$	1.426 ± 0.004
13 TeV $W^+ \to \mu^+\nu$	1.429 ± 0.004
5.02 TeV $W^- \to e^-\nu$	1.141 ± 0.019
5.02 TeV $W^+ \to e^+\nu$	1.160 ± 0.020
5.02 TeV $W^- \to \mu^-\nu$	1.383 ± 0.009
5.02 TeV $W^+ \to \mu^+\nu$	1.422 ± 0.007

Table 5.3 – The fitted values of k_{iso} for 13 and 5.02 TeV, the uncertainty are the statistical uncertainty from the fitting.

The term b is the constant in the linear fit, representing the average $u_{||}^{\ell}$ in the anti-isolated regions. The correction procedure is shown Figure 5.4, where the large dependence of $u_{||}^{\ell}$ on ptcone20 is reduced to almost zero after the correction. The value of k_{iso} is fitted for each individual channel as the opposite of the slope in the linear fit performed between 5 and 25 GeV. The results of k_{iso} are listed in Table 5.3, in which the values are consistent for each lepton flavor at a given center-of-mass energy. The corrections needed for muons are larger than electrons, which is interpreted as the electron Bremsstrahlung energy leaking outside the cone is not fully removed from the recoil before the correction. The fraction fits in FR performed before and after the correction are compared in the left and middle columns of Figure 5.7, where the MJ template is taken from an anti-isolated slice in CR1. As an example, Figure 5.5 show the effect of the recoil isolation correction on the ptcone20/Min(pT, 50 GeV) scan in the electron and muon channels at 13 TeV. A strong impact is seen for the dependence of the fitted yield on the isolation range.

The bias discussed above is corrected for in the hadronic recoil reconstruction only for the MJ background estimation. In isolated regions, recoil reconstruction is consistent with applying no correction, as the value of ptcone20 is in general close to zero if the lepton isolation cut is satisfied.

5.4.2 Yield extrapolation

The determination of MJ yield in SR starts from the MJ fraction fit in FR. Given that the shape of MJ distribution in the FR is not known in the first place, it has to be inferred from the CR1. MJ background is the dominant contribution in CR1 due to the inverted lepton isolation and relaxed kinematic cuts. The data in CR1 subtracted by the small predicted contribution from the electroweak and top-quark related processes is expected to well represents the MJ distribution in CR1. However, the shape of MJ distribution is not independent of lepton isolation, which means the shape of MJ in CR1 is different from that in FR and should not be taken directly as the template for the fraction fit. In order to catch the dependence of MJ shape on lepton isolation in CR1, four consecutive anti-isolated slices are chosen, with isolation variable lays between [0.1, 0.2], [0.2, 0.3], [0.3, 0.4] and [0.4, 0.5]. In each slice A<ptcone20/Min(pT, 50 GeV)<B, the MJ shape for the normalized distribution of X in CR1, after the

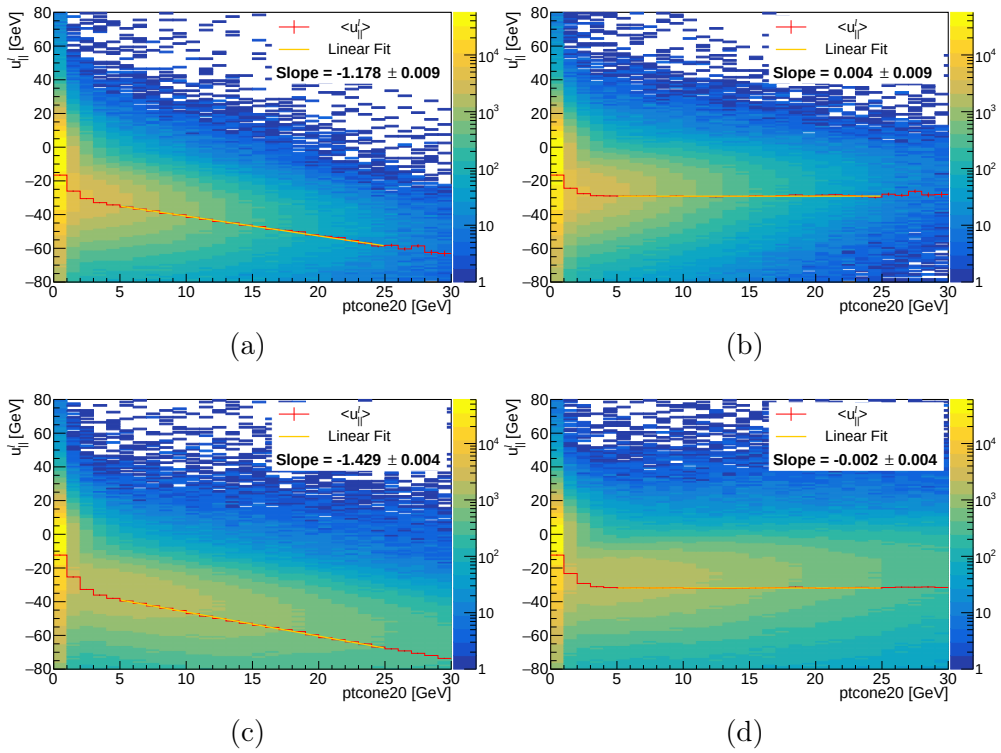

Figure 5.4 – $< u_{||}^{\ell} >$ as a function of ptcone20 before (left) and after (right) recoil isolation correction in CR1+FR of data for 13 TeV $W^+ \to e^+\nu$ channel (a)(b) and $W^+ \to \mu^+\nu$ channel (c)(d).

subtraction of EW and top-quark related processes, is defined to be:

$$H_{MJ}^{[A,B]}[X] = H_{data}^{[A,B]}[X] - H_{EW+top}^{[A,B]}[X] \tag{5.22}$$

The assumption that the MJ shape changes linearly with respect to the isolation variable is justified in Figure 5.6, so that the degree of change in MJ shape by every 0.1 of ptcone20/Min(pT, 50 GeV) is approximately:

$$\Delta^{CR1}[X] = \frac{1}{2}\left\{\frac{H_{MJ}^{[0.1,0.2]}[X] - H_{MJ}^{[0.3,0.4]}[X]}{2} + \frac{H_{MJ}^{[0.2,0.3]}[X] - H_{MJ}^{[0.4,0.5]}[X]}{2}\right\} \tag{5.23}$$

with which the MJ shape in FR is uniquely determined via:

$$H_{MJ}^{FR}[X] = H_{MJ}^{[0.1,0.2]}[X] + \Delta^{CR1}[X] \tag{5.24}$$

The correction term $\Delta[X]$ used in the above formula is purely built upon the MJ shapes in the chosen four anti-isolated slices of CR1. For MJ template taken from each of the four slices, its shape is corrected to $H_{MJ}^{FR}[X]$ in 5.24 then normalized to the initial integral of MJ distribution in that slice. For this reason, once the shape correction is implemented in CR1, no matter which anti-isolated slice the MJ template comes from, the fraction of MJ in FR determined by the fraction fit is always the same for a given observable X (Figure 5.8(b)(e) in constrast to (a)(c)). Significant improvement can be seen from the middle and right columns of Figure 5.7 after the shape correction in CR1.

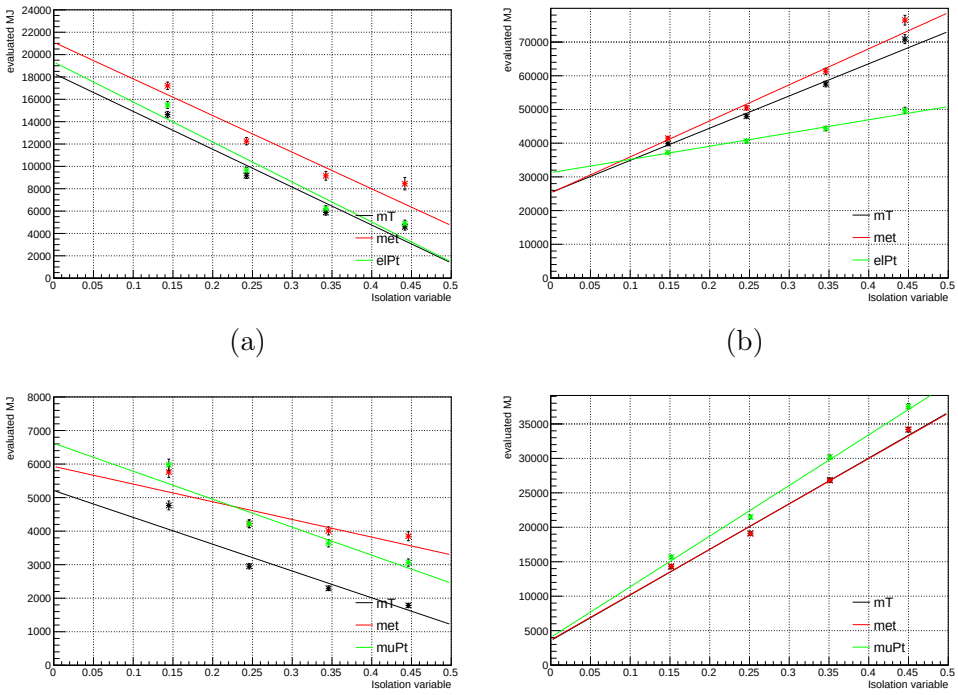

Figure 5.5 – The estimated total number of the MJ background in SR scanned as a function of the isolation. Each point represents an interval of anti-isolated region, of which the horizontal coordinate is the average ptcone20/Min(pT, 50 GeV) in the corresponding slice of CR2. The scans are shown for 13 TeV $W^+ \to e^+\nu$ (top) and $W^+ \to \mu^+\nu$ (bottom), without (left) and with (right) recoil isolation correction. No correction has ever been applied to the shape of MJ templates derived in CR1.

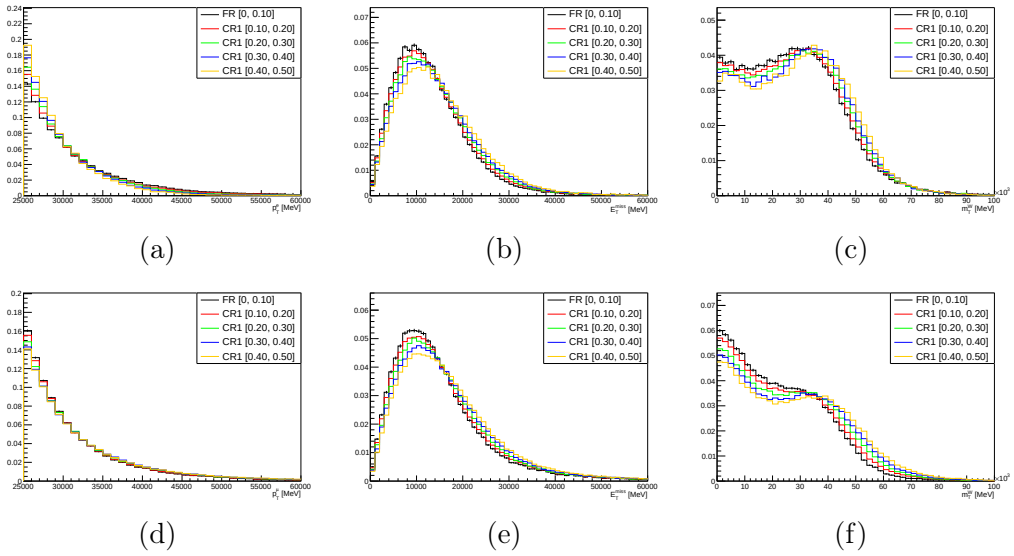

Figure 5.6 – Normalized MJ shapes in anti-isolated slices of CR1 and the shape corrected to FR for 13 TeV $W^+ \to e^+\nu$ (top) and $W^+ \to \mu^+\nu$ (bottom). (a)(d) p_{T}^{ℓ}, (b)(e) $E_{\mathrm{T}}^{\mathrm{miss}}$, (c)(f) m_{T}.

Once the yield in FR is known, one would expect equation 5.19 to tell the yield

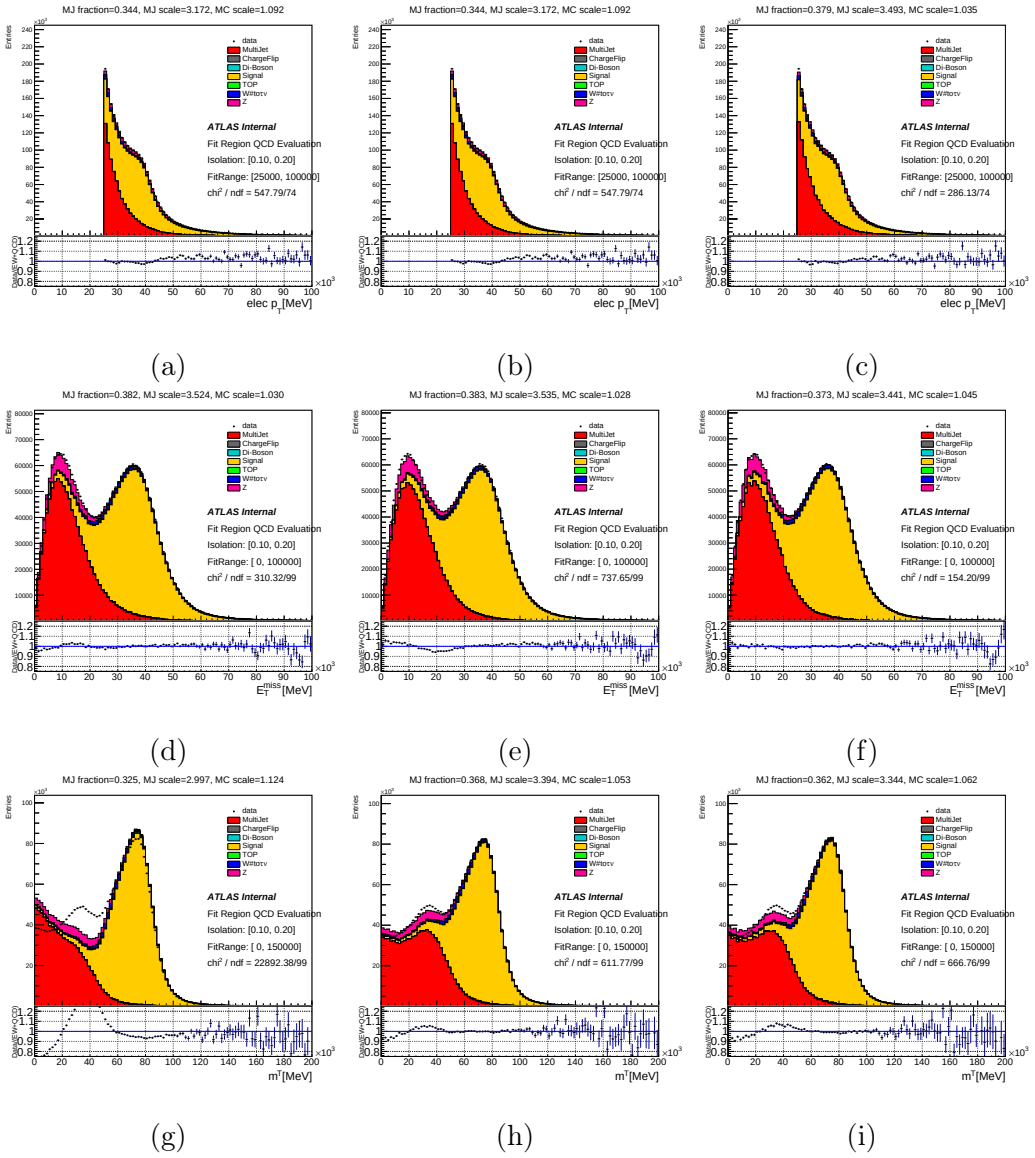

Figure 5.7 – $W^+ \to e^+\nu$ channel at 13 TeV. The FR post-fit control plots showing MJ fraction fit using p_{T}^{ℓ} (top), $E_{\mathrm{T}}^{\mathrm{miss}}$ (middle) and m_{T} (bottom) distributions. (a)(d)(g) Without recoil isolation correction or shape correction in CR1. (b)(e)(h) After recoil isolation correction but before shape correction in CR1. (c)(f)(i) With both recoil isolation correction and shape correction in CR1.

in SR. Yet the ratio of $\epsilon = N_{MJ}^{CR2}/N_{MJ}^{CR1}$ is not a constant because the efficiencies of the tighter $E_{\mathrm{T}}^{\mathrm{miss}}$ and m_{T} cuts in the control regions depend on lepton isolation. This dependence is visualized in Figure 5.8, where the value of isolation for each point is taken from the average value of isolation in individual anti-isolated slice of CR2. The anti-isolated slices in CR2 are defined consistently with CR1. For now, a simple linear relationship is assumed. A fair good match between the yield of data-driven method and the yield of $b\bar{b}$ and $c\bar{c}$ samples in Section 5.4.5 validates the assumption of the linear extrapolation.

With the known N_{MJ}^{FR} and the linear extrapolation of ϵ, the yield in SR becomes:

$$\begin{aligned} N_{MJ}^{SR}(ptcone20/Min(pT, 50\,GeV) = x) &= \epsilon(x) N_{MJ}^{FR} \\ &\approx k \cdot x + N_{MJ}^{SR}(ptcone20/Min(pT, 50\,GeV) = 0) \end{aligned} \tag{5.25}$$

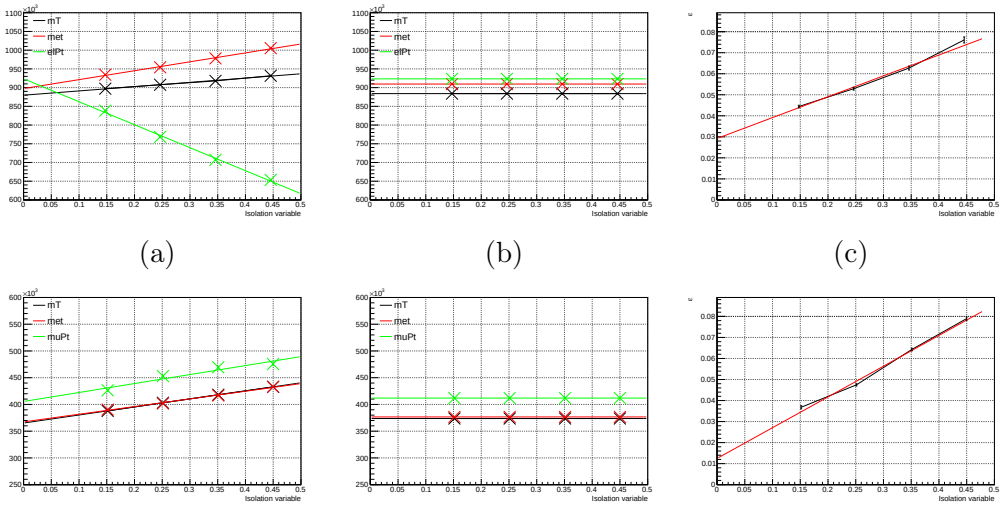

(a) (b) (c)

(d) (e) (f)

Figure 5.8 – Dependence of the predicted MJ yield in FR on the anti-isolated slices in CR1 before shape correction (left), after shape correction (middle) and the relation between *epsilon* and isolation variable (right) for $W^+ \to e^+\nu$ channel (a)(b)(c) and $W^+ \to \mu^+\nu$ channel (d)(e)(f) at 13 TeV.

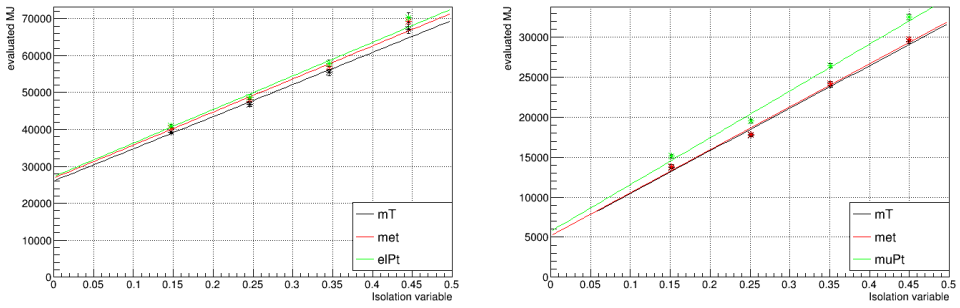

(a) $W^+ \to e^+\nu$ (b) $W^+ \to \mu^+$

Figure 5.9 – The extrapolation of MJ yield to SR for $W^+ \to e^+\nu$ channel (a) and $W^+ \to \mu^+\nu$ channel (b) at 13 TeV. Each point is located at the average isolation of the corresponding anti-isolated slice of CR2.

where x is the target of the extrapolation and k is the slope in Figure 5.9. The average value of isolation of the MJ background in SR is not zero and can only be inferred from appropriate MC samples. For this work, the average value of isolation of the MJ background in SR is investigated with $b\bar{b}$ and $c\bar{c}$ samples in the muon and anti-muon channels as shown in Table 5.11, which favors choosing a baseline value of x=0.025 as the extrapolation target. A similar study can hardly be carried out in the electron channels because of the significant contribution from mis-identified hadrons. It is assumed that the isolation distributions for pions are not very different than those for the leptons from heavy-flavor quark decays. Hence, the baseline extrapolation target being check in the muon channels applies to the electron channels as well.

While the baseline x=0.025 is considered the central value of the yield extrapolation, the difference of yield between x=0.025 and x=0 is taken as one source of MJ yield uncertainty due to the ambiguity of the extrapolation target.

It is observed that in the post-fit control distributions in FR there is a discrepancy between observation and total prediction, which can be possibly traced back to a mis-modelled dependence of the fraction fit on the jet activity. The effect of this mis-modelled dependence is studied by categorizing events as a function of recoil u_{T}, a quantity capable of representing the overall jet activity. The inclusive u_{T} distribution is therefore split into 5 intervals: [0, 20, 40, 60, 80, 1000] GeV. Once the fraction fit is performed in each slice of u_{T}, the post-fit agreement is in general better than the outcome of inclusive u_{T}, which confirms the dependence of the MJ template on u_{T}. Following the baseline method MJ yield estimation, the fraction fits are carried out in the 5 slices of u_{T} using $E_{\mathrm{T}}^{\mathrm{miss}}$ and m_{T} distributions. After that, the MJ yield is extrapolated to the SR in the corresponding u_{T} slice. The procedures are shown in Figure 5.10. Given that the cut p_{T}^{ℓ} >25 GeV is never relaxed in FR and CR1, a fraction fit based on p_{T}^{ℓ} does not benefit from the kinematic peak of MJ. Especially in the high u_{T} region where the Jacobian peak of W-boson production is no longer prominent either, the MJ distribution in p_{T}^{ℓ} becomes indistinguishable from the EW and top-quark related processes, causing convergence issue in the fraction fit. Therefore, p_{T}^{ℓ} distribution is not used in the estimation of MJ yield in slices of u_{T}. The estimation of MJ yield in slices of u_{T} offers not only a cross-check of the MJ shape in the SR (Figure 5.11), but also helps define a source of MJ yield uncertainty that is the difference between the nominal u_{T} inclusive yield and the sum of yields in u_{T} slices.

The correlation of u_{T}-dependence uncertainty across channels is understood by examining the response of the sum of yields towards the division of u_{T} spectrum in different channels. The MJ yield estimation is repeated upon a few alternative division of the entire u_{T} region, along with the inclusive one and the 5-slice split:

— 1 slice (u_{T}-inclusive): [0, 1000] GeV for u_{T}.
— 2 slices: [0, 50, 1000] for u_{T}.
— 4 slices: [0, 25, 50, 1000] for u_{T}.
— 5 slices (the systematic variation): [0, 20, 40, 60, 80, 1000] GeV for u_{T}.
— 10 slices: [0, 10, 20, 30, 40, 50, 60, 70, 80, 90, 1000] GeV for u_{T}.

The estimation of overall yield tends to inflate when more u_{T} slices are used (more degrees of freedom are given). In Figures 5.12 and 5.13, with 5 slices of u_{T}, the sum of yields approaches the plateau, which justifies the choice of using the sum of yields in 5 u_{T} slices as the systematic variation of this uncertainty source. Also strong correlation is observed both between two lepton flavours and between the two center-of-mass energies. It is hence concluded that the u_{T}-dependence yield uncertainty originates from the method of assessment itself and should be fully correlated across both charges, both lepton flavours and both center-of-mass energies.

5.4.3 Extraction of shape

The shape of MJ background in SR is determined from four anti-isolated slices in CR2, each one with ptcone20/Min(pT, 50 GeV) ranging within [0.1, 0.2, 0.3, 0.4, 0.5]. For any observable X such as p_{T}^{ℓ}, $E_{\mathrm{T}}^{\mathrm{miss}}$ and m_{T}, the shape extrapolation uses a formula similar to equation 5.24, with MJ shapes in CR1 replaced by those in CR2.

$$H_{MJ}^{SR}[X] = H_{MJ}^{[0.1,0.2]}[X] + \Delta^{CR2}[X] \tag{5.26}$$

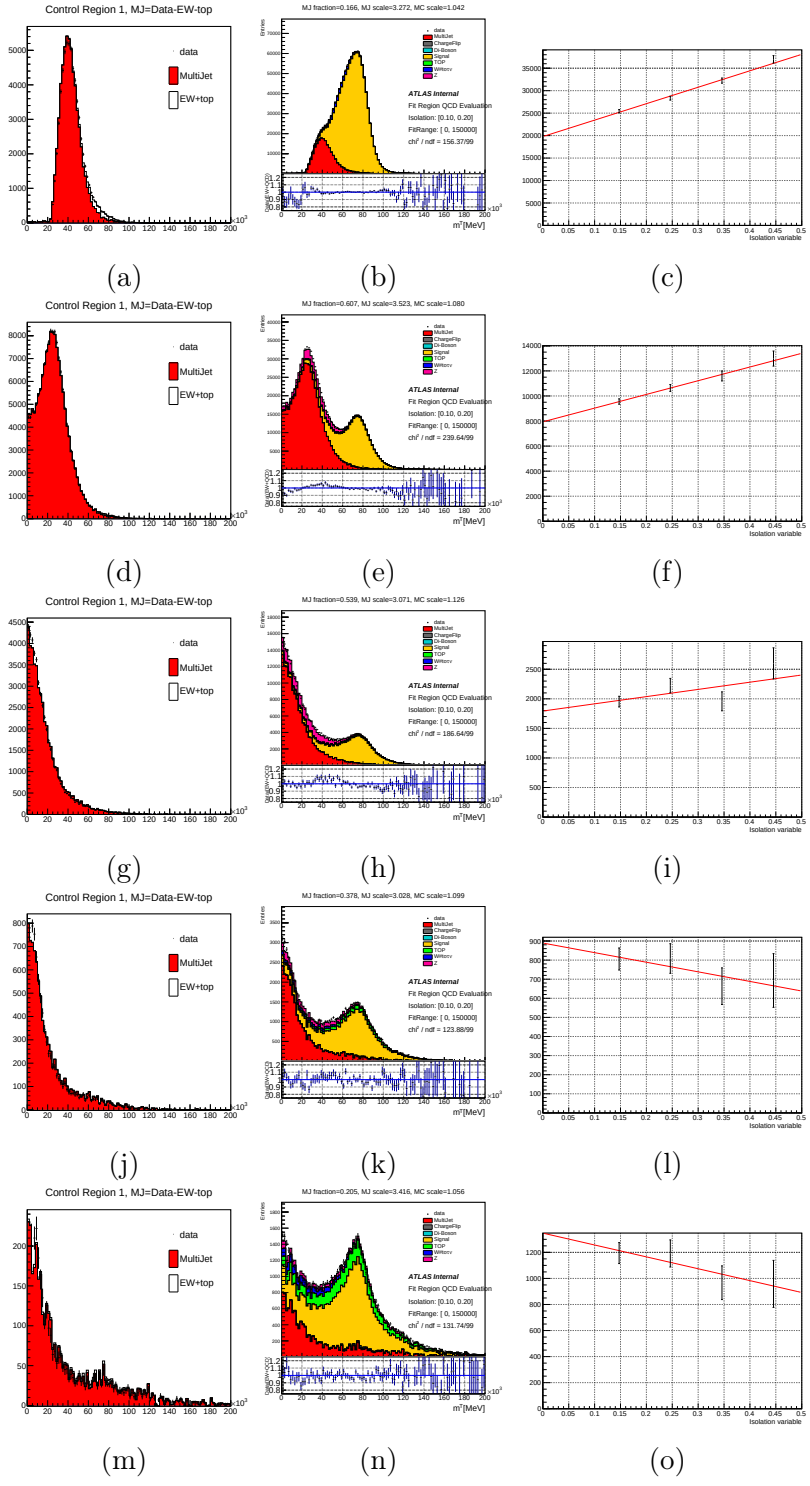

Figure 5.10 – MJ yield estimated in slices of u_{T}. Left: CR1 MJ shape template with shape correction implemented, middle: MJ fraction fit in FR, right: yield extrapolated to SR. (a)(b)(c): $u_{\mathrm{T}} \in$ [0,20] GeV, (d)(e)(f): $u_{\mathrm{T}} \in$ [20,40] GeV, (g)(h)(i): $u_{\mathrm{T}} \in$ [40,60] GeV, (j)(k)(l): $u_{\mathrm{T}} \in$ [60,80] GeV, (m)(n)(o): $u_{\mathrm{T}} \in$ [80,1000] GeV.

The shape extrapolation is shown in Figure 5.14. The statistical uncertainty in the MJ distribution in the SR follows the error propagation of equation 5.26, where in each anti-isolated slice of CR2 the corresponding statistical uncertainty comes from the data-EW-top subtraction per bin. The statistical uncertainty is bin-by-bin uncor-

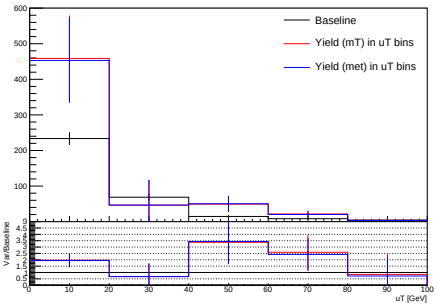

(a) 5.02 TeV $W^- \to \mu^- \nu$

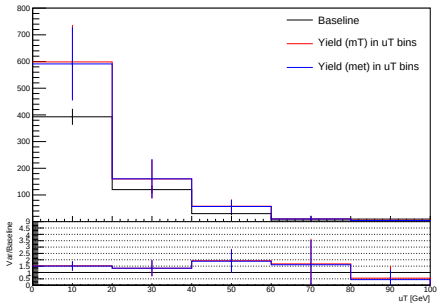

(b) 5.02 TeV $W^- \to e^- \nu$

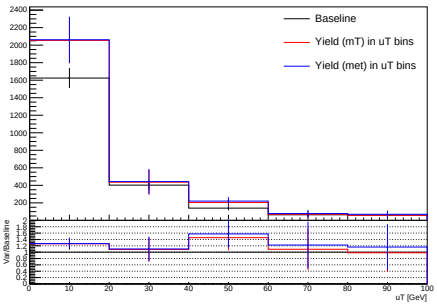

(c) 5.02 TeV $W^+ \to \mu^+ \nu$

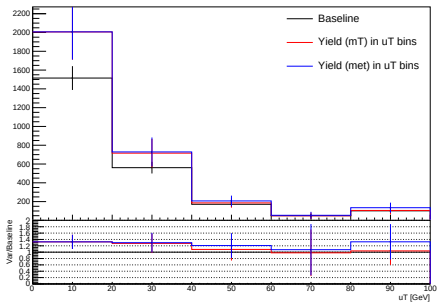

(d) 5.02 TeV $W^+ \to e^+ \nu$

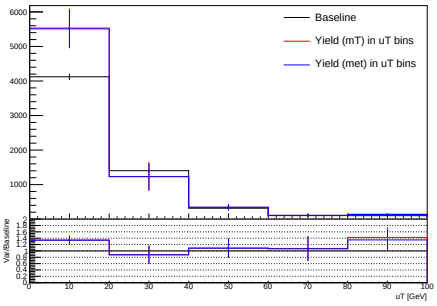

(e) 13 TeV $W^- \to \mu^- \nu$

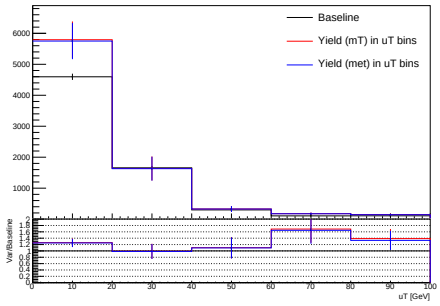

(f) 13 TeV $W^- \to e^- \nu$

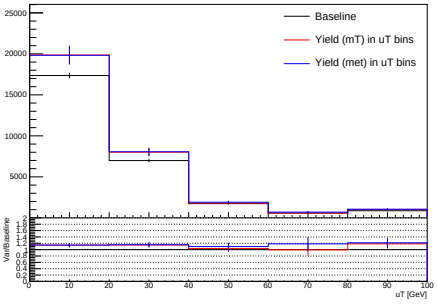

(g) 13 TeV $W^+ \to \mu^+ \nu$

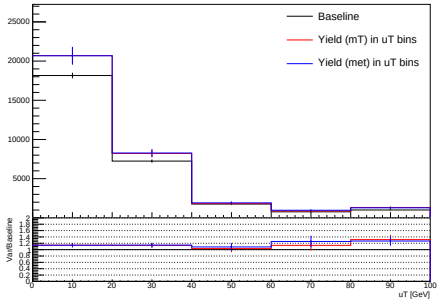

(h) 13 TeV $W^+ \to e^+ \nu$

Figure 5.11 – MJ background in SR compared in broad bins of u_{T} between u_{T}-sliced estimations and the baseline shape extrapolation. The last bin includes overflow.

related in this way. But in p_{T}^{W} analysis, a dedicated smoothing is applied to the region u_{T} >100 GeV in certain channels to improve the compatibility between electron and muon unfolded p_{T}^{W} spectra [38]. In this case, the shape variations of the smoothing parameters are correlated in the full u_{T} distribution, representing the MJ statistical

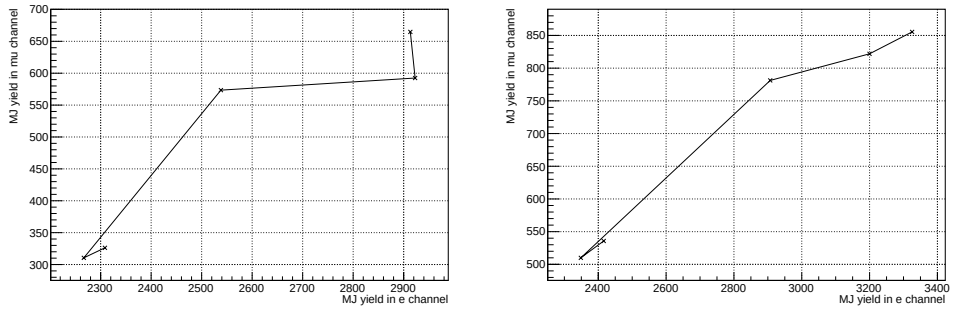

(a) 5.02 TeV W^- (b) 5.02 TeV W^+

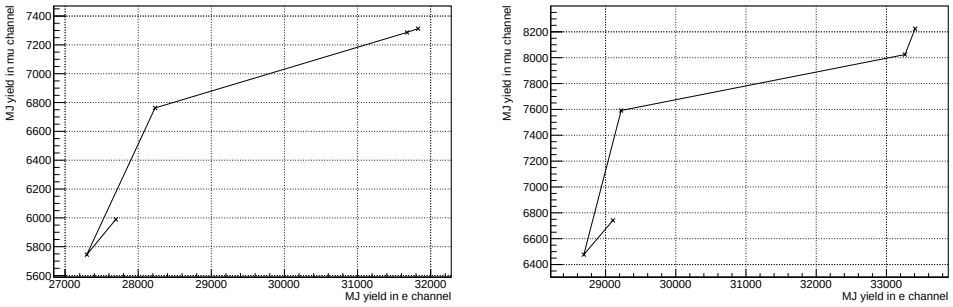

(c) 13 TeV W^- (d) 13 TeV W^+

Figure 5.12 – The MJ yield in $W \to e\nu$ channel (horizontal) and $W \to \mu\nu$ channel (vertical) depending on the number of u_{T} slices (1, 2, 4, 5, 10, the overall trend goes from bottom left to top right) used for the estimation of yield. A strong correlation is found in all cases.

uncertainty for u_{T} >100 GeV.

5.4.4 Sources of uncertainties

For the p_{T}^{W} analysis, the uncertainty in the MJ background estimation arises dominantly from three aspects: systematic uncertainties in the estimation of MJ yield in the SR, systematics in the determination of the shape in the SR and statistical uncertainty of the MJ distribution. Among them, the systematic uncertainties in yield and shape turn out to be correlated across the channels, while statistical uncertainty is uncorrelated between channels because of its statistical nature. Besides the above three major types of uncertainties, all sources of uncertainty have been investigated throughout the study of MJ background estimation and are listed below. These two sources of uncertainties are assumed to be uncorrelated between channels:

— The data and MC statistics: The statistical uncertainty from the limited data and MC samples is obtained from the error propagation of equation 5.26. The data and MC statistics is bin-by-bin uncorrelated in most cases. Only in the electron channels at 13 TeV, the statistical uncertainty in u_{T} >100 GeV is parameterized into shape variations by smoothing and hence becomes bin-by-bin correlated.

— Uncertainty in the yield caused by the linear extrapolation as a function of isolation. The linear extrapolation of the yield accounts for the statistical uncertainty in the control regions and the uncertainty of the MJ fraction in FR obtained from the fraction fit. For the nominal estimation, the impact of

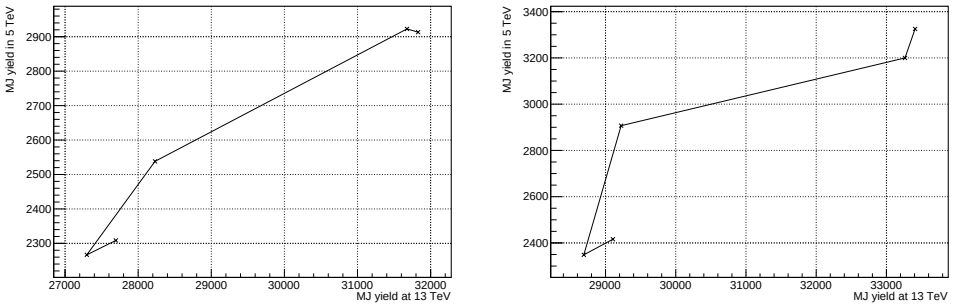

(a) $W^- \to e\nu$ (b) $W^+ \to e\nu$

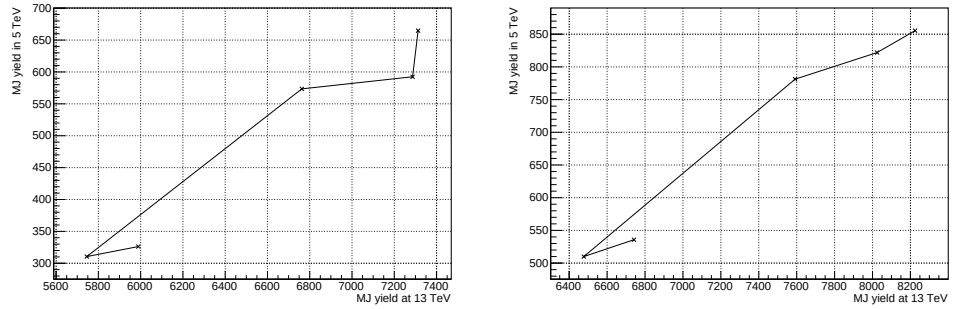

(c) $W^- \to \mu\nu$ (d) $W^+ \to \mu\nu$

Figure 5.13 – The MJ yield in 13 (horizontal) and 5.02 TeV (vertical) center-of-mass energies depending on the number of u_{T} slices (1, 2, 4, 5, 10, the overall trend goes from bottom left to top right) used for the estimation of yield. A strong correlation is found in all cases.

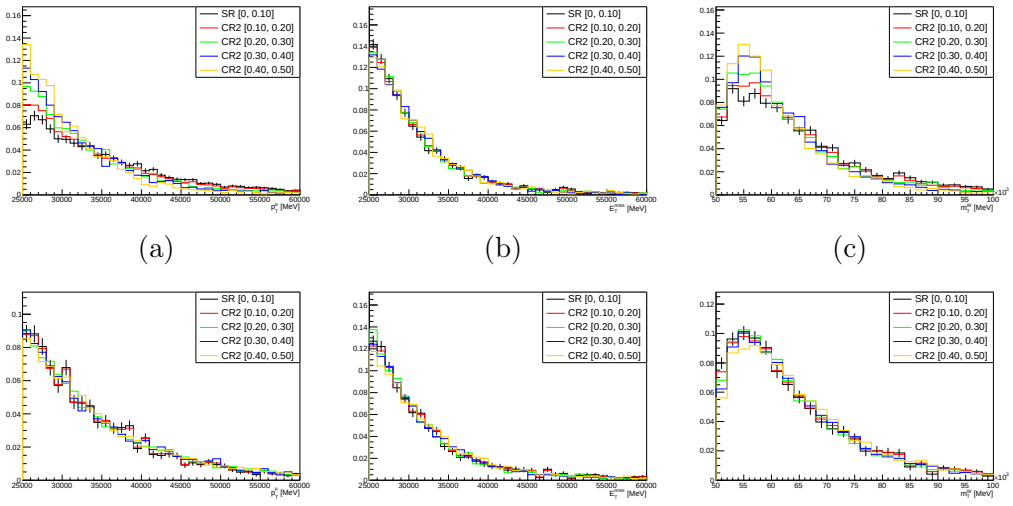

(a) (b) (c)

(d) (e) (f)

Figure 5.14 – Normalized MJ shapes in anti-isolated slices of CR2 and the shape corrected to SR for 13 TeV $W^+ \to e^+\nu$ (top) and $W^+ \to \mu^+\nu$ (bottom). (a)(d) p_{T}^{ℓ}, (b)(e) $E_{\mathrm{T}}^{\mathrm{miss}}$, (c)(f) m_{T}.

this uncertainty source turns out to be well covered by the leading systematic uncertainties of the yield. It is only included when presenting the uncertainty on the yield in slices of u_{T}.

The following uncertainties are correlated across channels, and across bins for a given

kinematic distribution:

— Uncertainty in the shape of MJ background in SR. This source of uncertainty is represented by the difference between the extrapolated shape in equation 5.26 and the shape of the [0.1, 0.2] anti-isolated slice in CR2. This source of uncertainty is propagated to the final result of MJ estimation.

— The dependence of the fitted and extrapolated MJ yields on u_{T}. This uncertainty affects the total yield of MJ in the SR. It is taken to be the difference between the central value of yield based on u_{T}-inclusive estimation and the sum of yields from u_{T}-sliced estimations.

— Uncertainties in the luminosity and in the cross-sections of the simulated MC samples. They appear in the subtraction of the EW and top processes from CR1 and CR2.

— Uncertainty in the choice of the extrapolation target for the isolation scan. This is assessed by changing the isolation target from 0.025 to 0. As long as the shape correction is applied to the CR1 templates, the impact of changing the isolation target on the yield is consistent among p_{T}^{ℓ}, m_{T} and $E_{\mathrm{T}}^{\mathrm{miss}}$. So, the arithmetic average of the impact on the yield over the three kinematic distributions is propagated to the final result of MJ estimation.

— The uncertainty in the yield due to the recoil isolation correction k_{iso} is estimated by changing the isolation correction by 10%, a number way more conservative than the fit uncertainty presented in Table 5.3.

For p_{T}^{W} analysis, the u_{T}-dependence of the fitted yield is important in all the W-boson decay channels. In the muon channels, the uncertainty in the choice of the extrapolation target is comparable to the u_{T}-dependence uncertainty. In terms of yield, other sources are found to be sub-dominant in comparison. Since the u_{T}-dependence uncertainty and the extrapolation target uncertainty are the two independent leading uncertainty sources, a quadratic sum of them is taken to be the total MJ yield uncertainty. The shape uncertainty is propagated to the analysis chain as variations. The data and MC statistical uncertainty in MJ estimation is only considered for u_{T} >100 GeV, where it is no longer negligible compared with the data statistical uncertainty of each u_{T} bin.

5.4.5 Summary of results

The final results of the MJ background estimation for p_{T}^{W} analysis are presented in this section for the eight individual channels. The yield in the SR is obtained by determining the yield in FR with the MJ template extracted from CR1, then extrapolated to the SR via the ratio of numbers of MJ events in CR2 over CR1. The yield is estimated using three kinematic distributions: p_{T}^{ℓ}, $E_{\mathrm{T}}^{\mathrm{miss}}$ and m_{T}. The total yield of MJ background based from the three distributions are summarized in Table 5.4 $\sim$ Table 5.7 for u_{T} inclusive estimation and u_{T}-sliced estimations. The central value of yield is taken to be the arithmetic average of the u_{T} inclusive estimation based on p_{T}^{ℓ}, $E_{\mathrm{T}}^{\mathrm{miss}}$ and m_{T}, since the three numbers are compatible with each other. The MJ yields between the two charges are within the tolerance of uncertainties as well. The absolute and relative uncertainties of MJ yields are shown in Tables 5.8 and 5.9, where the statistical uncertainty of the linear extrapolation of yield to the SR is included but only for reference.

As for the cross check of the shape extrapolation, the MJ shape extrapolated from

Distribution	u_{T} bin (GeV)	Electron Channel	Positron Channel	Δ
Lepton p_{T}	Inclusive	28041 ± 852	29362 ± 883	1321 ± 1227
m_{T}	[0,20]	19789 ± 615	20584 ± 641	795 ± 888
m_{T}	[20,40]	8023 ± 403	8176 ± 409	153 ± 574
m_{T}	[40,60]	1826 ± 168	1847 ± 173	21 ± 241
m_{T}	[60,80]	586 ± 92	919 ± 107	333 ± 141
m_{T}	[80,1000]	1086 ± 127	1415 ± 147	329 ± 194
m_{T}	Inclusive	26692 ± 805	28078 ± 834	1386 ± 1159
$E_{\mathrm{T}}^{\mathrm{miss}}$	[0,20]	19767 ± 614	20563 ± 640	796 ± 887
$E_{\mathrm{T}}^{\mathrm{miss}}$	[20,40]	8075 ± 406	8241 ± 412	166 ± 578
$E_{\mathrm{T}}^{\mathrm{miss}}$	[40,60]	1929 ± 178	1940 ± 182	11 ± 255
$E_{\mathrm{T}}^{\mathrm{miss}}$	[60,80]	696 ± 110	1011 ± 118	315 ± 161
$E_{\mathrm{T}}^{\mathrm{miss}}$	[80,1000]	1118 ± 134	1325 ± 139	207 ± 193
$E_{\mathrm{T}}^{\mathrm{miss}}$	Inclusive	27399 ± 826	28858 ± 857	1459 ± 1190

Table 5.4 – MJ background yield estimated from the lepton p_{T}, m_{T} and $E_{\mathrm{T}}^{\mathrm{miss}}$ distributions in the 13 TeV $W \to e\nu$ channel. Statistical uncertainties are quoted.

CR2 to SR is merged to broad bins and compared to the yields estimated in slices of u_{T} in Figure 5.11. Good agreement is found in these comparisons.

A further check of the data-driven MJ background estimation is achieved in muon channels by comparing with heavy-flavour quark decay MC samples, since the MJ background in the muon channels is supposed to be dominated by $b\bar{b}$ and $c\bar{c}$ decays. More information of the samples are provided in Tables 5.10. Even though the production cross-sections are greater than those of the signal and other backgrounds, the calculation of these processes carry significant uncertainties from the dijet production cross-section, $b/c \to \mu$ decay factions and fragmentation functions. After signal event selection and normalization to data luminosity, the number of $b\bar{b}$ and $c\bar{c}$ candidates are reported in Table 5.11, along with the average isolation in the SR. The shape comparison between the data-driven MJ background and the $b\bar{b}$ and $c\bar{c}$ samples is shown in Figures 5.15 and 5.16, where a certain degree of discrepancy is seen for the m_{T} distribution at 13 TeV.

The difference between the data-driven results and the MC samples can be attributed to a couple of reasons:

— The uncertainty in the generated cross-sections of MC samples.
— Background sources other than $b\bar{b}$ and $c\bar{c}$.
— Possible mis-modelling of $b\bar{b}$ and $c\bar{c}$ distributions bringing bias to cut efficiencies.

The estimated MJ yields in SR for p_{T}^{W} analysis are reminded in Table 5.12 for all channels, with central value and that of the yield uncertainty converted to a fraction of number of total candidates in data.

5.5 Total yields and control plots

The total expected yield passing the event selections of Section 5.2.1 is the sum of MC samples mentioned in Section 5.1 and the estimation of MJ background in

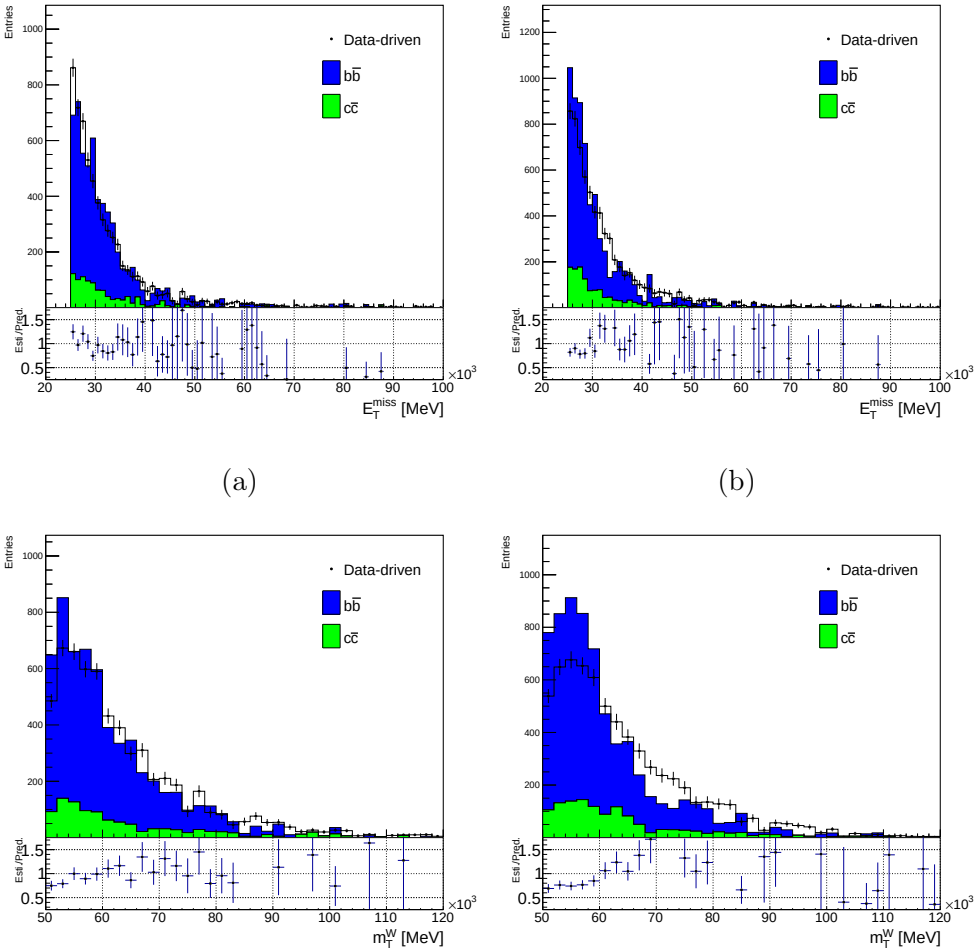

Figure 5.15 – Comparison of SR distributions of $E_{\mathrm{T}}^{\mathrm{miss}}$ (top) as well as m_{T} (bottom) in muon channels using $b\bar{b} + c\bar{c}$ MC samples and data-driven estimation at 13 TeV. (a)(c) $W^- \to \mu^-\nu$, (b)(d) $W^+ \to \mu^+\nu$. The MC samples are normalized to the yield of data-driven MJ background.

Section 5.4. The observed yields are compared with the expected yields in Table 5.13 for each W decay signal channel.

Control plots for 5.02 and 13 TeV low pile-up datasets are produced after applying all the selection in Table 5.1, as well as all the object corrections and physics corrections described in Sections 5.2 and 5.3. The total predictions including MJ are normalized to the integral of data to offer a better visualization of the agreement in the shapes. In the ratio panel, the shallow grey band represent the total systematic uncertainty that includes all the experimental uncertainties. Luminosity uncertainty is excluded in the error band because of the normalization. No modelling uncertainty is taken into account in the control plots. The brown band adds in quadrature the signal MC statistical uncertainty on top of the total systematics, coming with a tiny contribution everywhere over the spectra. The χ^2/ndf is calculated based on the full covariance matrix of statistical uncertainties and the above systematics accounting for bin-by-bin correlations.

The hadronic recoil u_{T} in Figure 5.17 is the reco-level observable for the measure-

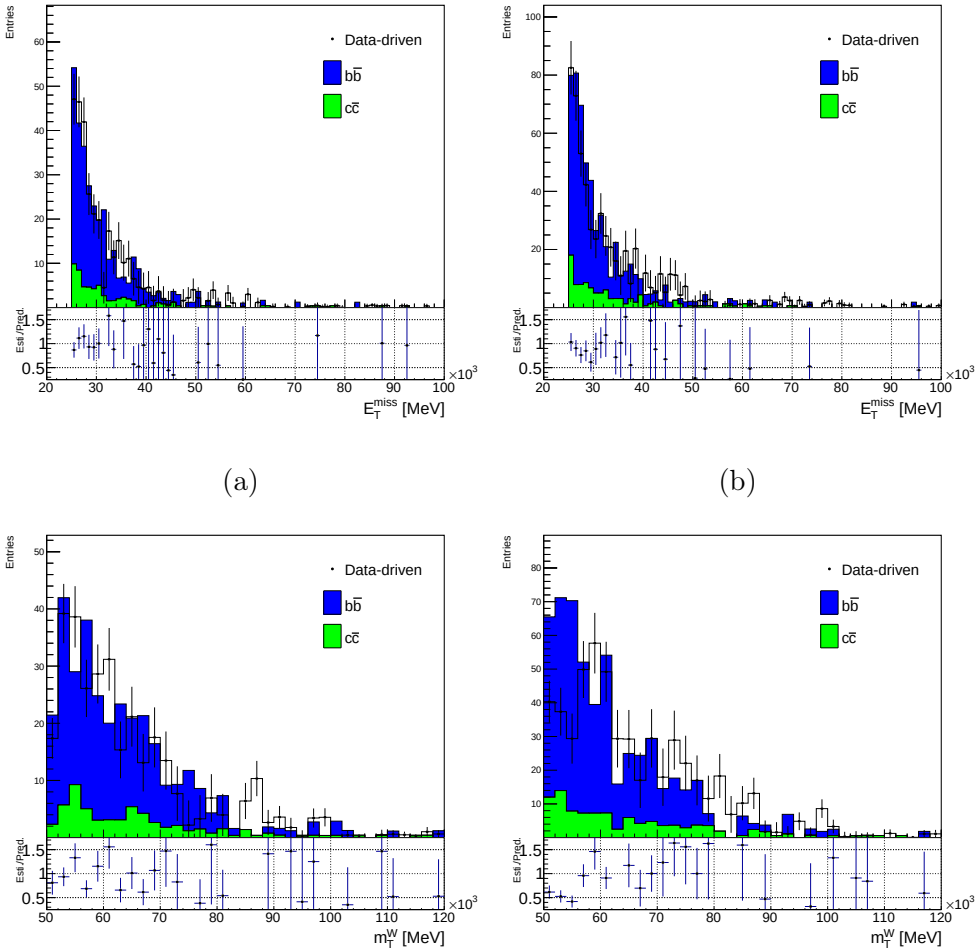

Figure 5.16 – Comparison of SR distributions of $E_{\mathrm{T}}^{\mathrm{miss}}$ (top) as well as m_{T} (bottom) in muon channels using $b\bar{b} + c\bar{c}$ MC samples and data-driven estimation at 5.02 TeV. (a)(c) $W^- \to \mu^-\nu$, (b)(d) $W^+ \to \mu^+\nu$. The MC samples are normalized to the yield of data-driven MJ background.

ment of p_{T}^{W}, while p_{T}^{ℓ} (Figure 5.18), m_{T} (Figure 5.19) and $E_{\mathrm{T}}^{\mathrm{miss}}$ (Figure 5.20) are commonly used observables for the m_W measurements.

Distribution	u_{T} bin (GeV)	Muon Channel	Anti-muon Channel	Δ
Lepton p_{T}	Inclusive	6123 ± 331	6924 ± 358	801 ± 488
m_{T}	[0,20]	5529 ± 233	5740 ± 247	211 ± 340
m_{T}	[20,40]	1115 ± 154	1512 ± 162	397 ± 224
m_{T}	[40,60]	291 ± 67	299 ± 69	8 ± 96
m_{T}	[60,80]	96 ± 34	167 ± 36	71 ± 50
m_{T}	[80,1000]	136 ± 29	160 ± 30	24 ± 42
m_{T}	Inclusive	5617 ± 296	6247 ± 312	630 ± 430
$E_{\mathrm{T}}^{\mathrm{miss}}$	[0,20]	5504 ± 233	5685 ± 246	181 ± 339
$E_{\mathrm{T}}^{\mathrm{miss}}$	[20,40]	1108 ± 153	1507 ± 162	339 ± 222
$E_{\mathrm{T}}^{\mathrm{miss}}$	[40,60]	290 ± 67	299 ± 69	9 ± 96
$E_{\mathrm{T}}^{\mathrm{miss}}$	[60,80]	95 ± 34	162 ± 36	67 ± 50
$E_{\mathrm{T}}^{\mathrm{miss}}$	[80,1000]	125 ± 28	153 ± 30	28 ± 41
$E_{\mathrm{T}}^{\mathrm{miss}}$	Inclusive	5638 ± 298	6304 ± 316	666 ± 434

Table 5.5 – MJ background yield estimated from the lepton p_{T}, m_{T} and $E_{\mathrm{T}}^{\mathrm{miss}}$ distributions in the 13 TeV $W \to \mu\nu$ channel. Statistical uncertainties are quoted.

Distribution	u_{T} Cut (GeV)	Electron Channel	Positron Channel	Δ
Lepton p_{T}	Inclusive	2248 ± 311	2405 ± 348	157 ± 467
m_{T}	[0,20]	2044 ± 242	2005 ± 263	-39 ± 357
m_{T}	[20,40]	422 ± 136	753 ± 151	331 ± 203
m_{T}	[40,60]	216 ± 42	188 ± 54	-28 ± 68
m_{T}	[60,80]	78 ± 37	61 ± 33	-17 ± 50
m_{T}	[80,1000]	58 ± 35	119 ± 47	61 ± 59
m_{T}	Inclusive	2181 ± 301	2269 ± 327	88 ± 444
$E_{\mathrm{T}}^{\mathrm{miss}}$	[0,20]	2060 ± 244	2010 ± 264	-50 ± 359
$E_{\mathrm{T}}^{\mathrm{miss}}$	[20,40]	428 ± 138	766 ± 153	338 ± 206
$E_{\mathrm{T}}^{\mathrm{miss}}$	[40,60]	232 ± 45	209 ± 60	-23 ± 75
$E_{\mathrm{T}}^{\mathrm{miss}}$	[60,80]	85 ± 41	70 ± 38	-15 ± 56
$E_{\mathrm{T}}^{\mathrm{miss}}$	[80,1000]	64 ± 38	129 ± 51	65 ± 64
$E_{\mathrm{T}}^{\mathrm{miss}}$	Inclusive	2258 ± 312	2356 ± 339	98 ± 461

Table 5.6 – MJ background yield estimated from the lepton p_{T}, m_{T} and $E_{\mathrm{T}}^{\mathrm{miss}}$ distributions in the 5.02 TeV $W \to e\nu$ channel. Statistical uncertainties are quoted.

Distribution	u_{T} Cut (GeV)	Muon Channel	Anti-muon Channel	Δ
Lepton p_{T}	Inclusive	321 ± 123	586 ± 148	265 ± 192
m_{T}	[0,20]	480 ± 89	614 ± 103	134 ± 136
m_{T}	[20,40]	34 ± 54	165 ± 63	131 ± 83
m_{T}	[40,60]	46 ± 22	57 ± 26	11 ± 34
m_{T}	[60,80]	24 ± 10	7 ± 12	-17 ± 16
m_{T}	[80,1000]	5 ± 7	7 ± 10	2 ± 12
m_{T}	Inclusive	293 ± 112	528 ± 132	235 ± 173
$E_{\mathrm{T}}^{\mathrm{miss}}$	[0,20]	474 ± 88	606 ± 102	132 ± 135
$E_{\mathrm{T}}^{\mathrm{miss}}$	[20,40]	34 ± 54	165 ± 63	131 ± 83
$E_{\mathrm{T}}^{\mathrm{miss}}$	[40,60]	47 ± 23	57 ± 25	10 ± 34
$E_{\mathrm{T}}^{\mathrm{miss}}$	[60,80]	22 ± 10	6 ± 12	-16 ± 16
$E_{\mathrm{T}}^{\mathrm{miss}}$	[80,1000]	4 ± 6	6 ± 7	2 ± 9
$E_{\mathrm{T}}^{\mathrm{miss}}$	Inclusive	298 ± 114	532 ± 133	234 ± 175

Table 5.7 – MJ background yield estimated from the lepton p_{T}, m_{T} and $E_{\mathrm{T}}^{\mathrm{miss}}$ distributions in the 5.02 TeV $W \to \mu\nu$ channel. Statistical uncertainties are quoted.

Channel	Electron	Positron	Muon	Anti-muon
MJ background yield	27377	28766	5792	6492
Stat. unc. (p_{T}^{ℓ})	852 (3.1%)	883 (3.1%)	331 (5.7%)	358 (5.5%)
Stat. unc. ($E_{\mathrm{T}}^{\mathrm{miss}}$)	826 (3.0%)	857 (3.0%)	298 (5.1%)	316 (4.9%)
Stat. unc. (m_{T})	805 (2.9%)	834 (2.9%)	296 (5.1%)	312 (4.8%)
Stat. arithmetic average	828 (3.0%)	858 (3.0%)	308 (5.3%)	329 (5.1%)
Extrapo. unc. (p_{T}^{ℓ})	2498 (9.1%)	2414 (8.4%)	1518 (26.2%)	1556 (24.0%)
Extrapo. unc. ($E_{\mathrm{T}}^{\mathrm{miss}}$)	2440 (8.9%)	2370 (8.2%)	1404 (24.2%)	1426 (22.0%)
Extrapo. unc. (m_{T})	2377 (8.7%)	2306 (8.0%)	1400 (24.2%)	1414 (21.8%)
Extrapo. arithmetic average	2438 (8.9%)	2364 (8.2%)	1440 (24.9%)	1465 (22.6%)
u_{T}-dependence unc.	4208 (15.4%)	4315 (15.0%)	1375 (23.7%)	1386 (21.3%)
Total unc.	4863 (17.8%)	4920 (17.1%)	1991 (34.4%)	2017 (31.1%)

Table 5.8 – The absolute and relative statistical uncertainty of MJ yield in the $W \to e\nu$ and $W \to \mu\nu$ channel at $\sqrt{s}$ =13 TeV.

Channel	Electron	Positron	Muon	Anti-muon
MJ background yield	2229	2344	304	549
Stat. unc. (p_{T}^{ℓ})	311 (14.0%)	348 (14.8%)	123 (40.5%)	148 (27.0%)
Stat. unc. ($E_{\mathrm{T}}^{\mathrm{miss}}$)	312 (14.0%)	339 (14.5%)	114 (37.5%)	133 (24.2%)
Stat. unc. (m_{T})	301 (13.5%)	327 (14.0%)	112 (36.8%)	132 (24.0%)
Stat. arithmetic average	308 (13.8%)	338 (14.4%)	116 (38.3%)	138 (25.1%)
Extrapo. unc. (p_{T}^{ℓ})	293 (13.1%)	352 (15.0%)	222 (73.0%)	240 (43.7%)
Extrapo. unc. ($E_{\mathrm{T}}^{\mathrm{miss}}$)	295 (13.2%)	345 (14.7%)	209 (68.8%)	221 (40.3%)
Extrapo. unc. (m_{T})	284 (12.7%)	332 (14.2%)	206 (67.8%)	220 (40.1%)
Extrapo. arithmetic average	291 (13.1%)	343 (14.6%)	212 (69.7%)	227 (41.3%)
u_{T}-dependence unc.	642 (28.8%)	841 (35.9%)	268 (88.2%)	295 (53.7%)
Total unc.	705 (31.6%)	909 (38.8%)	342 (112.5%)	372 (67.8%)

Table 5.9 – The absolute and relative statistical uncertainty of MJ yield in the $W \to e\nu$ and $W \to \mu\nu$ channel at $\sqrt{s}$ =5.02 TeV.

Process	$\sqrt{s}$	Data set	Generator	σ·BR·$\epsilon_{\mathrm{filter}}$ [nb]
$b\bar{b} \to \mu$	13 TeV	361250	Pythia8B+A14+NNPDF23LO	186
$c\bar{c} \to \mu$	13 TeV	361251	Pythia8B+A14+NNPDF23LO	58
$b\bar{b} \to \mu$	5.02 TeV	361250	Pythia8B+A14+NNPDF23LO	46
$c\bar{c} \to \mu$	5.02 TeV	361251	Pythia8B+A14+NNPDF23LO	14

Table 5.10 – MC simulation of $b\bar{b}$ and $c\bar{c}$ decay to muon.

Channel	$b\bar{b}$		$c\bar{c}$		$b\bar{b} + c\bar{c}$		Data-driven
	Yield	< ptcone20/Min(pT, 50 GeV) >	Yield	< ptcone20/Min(pT, 50 GeV) >	Yield	< ptcone20/Min(pT, 50 GeV) >	Yield
13 TeV $W^+ \to \mu^+\nu$	4365	0.0246 ± 0.0018	1067	0.0228 ± 0.0021	5433	0.0243 ± 0.0015	6492
13 TeV $W^- \to \mu^-\nu$	4436	0.0306 ± 0.0019	941	0.0243 ± 0.0023	5377	0.0295 ± 0.0016	5792
5.02 TeV $W^+ \to \mu^+\nu$	428	0.0282 ± 0.0025	111	0.0225 ± 0.0026	538	0.0270 ± 0.0020	549
5.02 TeV $W^- \to \mu^-\nu$	393	0.0292 ± 0.0026	100	0.0185 ± 0.0025	493	0.0270 ± 0.0021	304

Table 5.11 – The numbers of $b\bar{b}$ and $c\bar{c}$ events in $W^+ \to \mu^+\nu$ and $W^+ \to \mu^-\nu$ signal channel at $\sqrt{s}$ =13 TeV and 5.02 TeV, and the corresponding average value of `ptcone20/Min(pT, 50 GeV)`. The data-driven MJ background yield is included for comparison; all numbers are normalized to the integrated luminosity of the data.

	13 TeV		5.02 TeV	
Channel	Yield	Fraction	Yield	Fraction
$W^- \to e^-\nu$	27377 ± 4863	(2.88 ± 0.51)%	2229 ± 705	(0.81 ± 0.26)%
$W^+ \to e^+\nu$	28766 ± 4920	(2.38 ± 0.41)%	2344 ± 909	(0.54 ± 0.21)%
$W^- \to \mu^-\nu$	5792 ± 1991	(0.60 ± 0.21)%	304 ± 342	(0.11 ± 0.12)%
$W^+ \to \mu^+\nu$	6492 ± 2017	(0.52 ± 0.16)%	549 ± 372	(0.12 ± 0.08)%

Table 5.12 – Evaluation of MJ background yields at 13 TeV and 5.02 TeV.

Channel	Observed	Expected
5.02 TeV $W^+ \to e^+\nu$	430662	430930 ± 933
5.02 TeV $W^+ \to \mu^+\nu$	457223	457473 ± 429
5.02 TeV $W^- \to e^-\nu$	274375	276272 ± 726
5.02 TeV $W^- \to \mu^-\nu$	288026	289016 ± 384
13 TeV $W^+ \to e^+\nu$	1207652	1192055 ± 4930
13 TeV $W^+ \to \mu^+\nu$	1245755	1230252 ± 2042
13 TeV $W^- \to e^-\nu$	949297	947264 ± 4871
13 TeV $W^- \to \mu^-\nu$	964514	965341 ± 2012

Table 5.13 – Observed and expected event yields for each W decay channel after event selection. The uncertainty of the expectation is the quadratic sum of MC background statistics and multijet yield uncertainty.

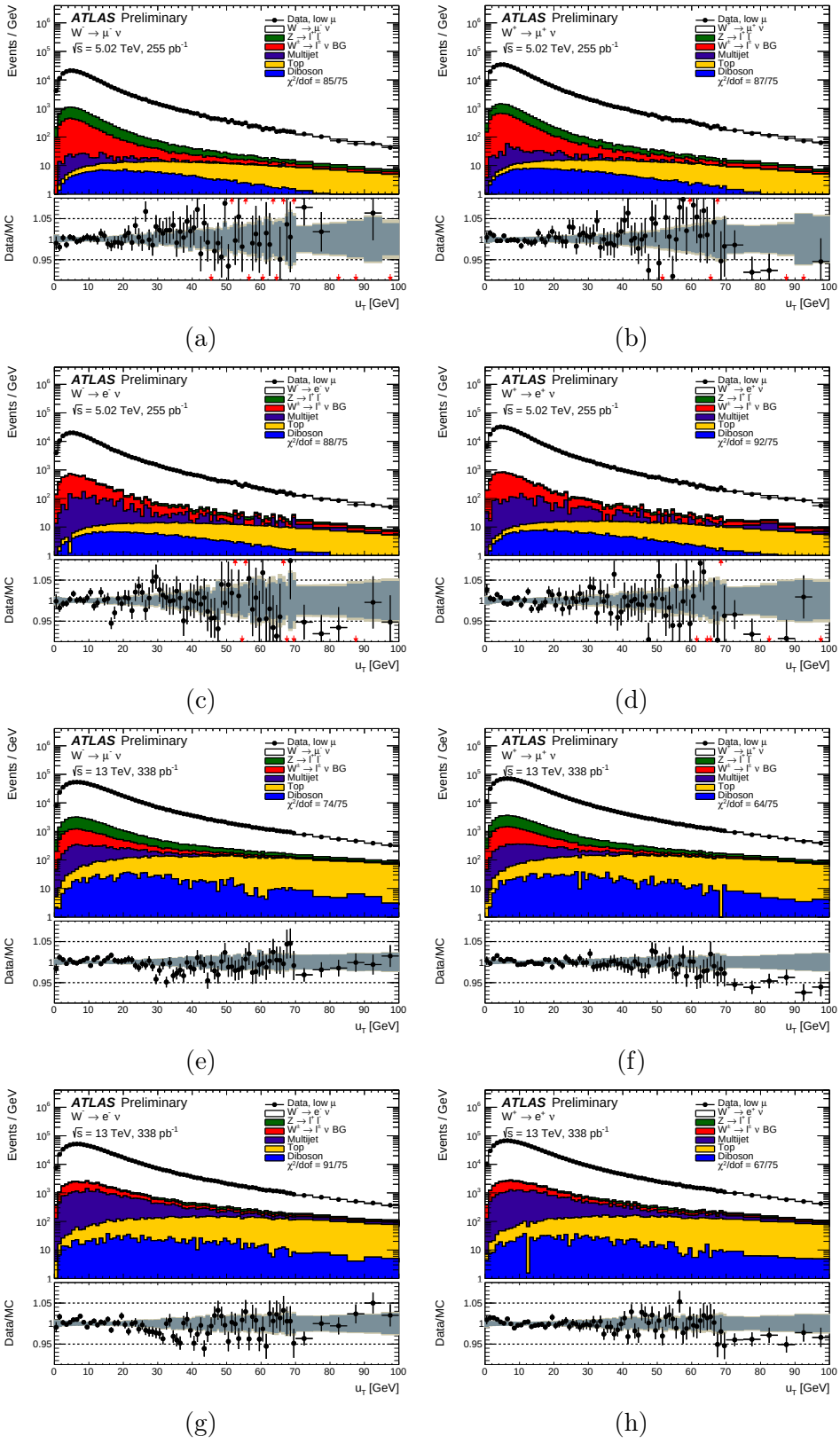

Figure 5.17 – u_{T} distribution in the muon and electron channels for the $\sqrt{s}$ =5.02 and 13 TeV datasets.

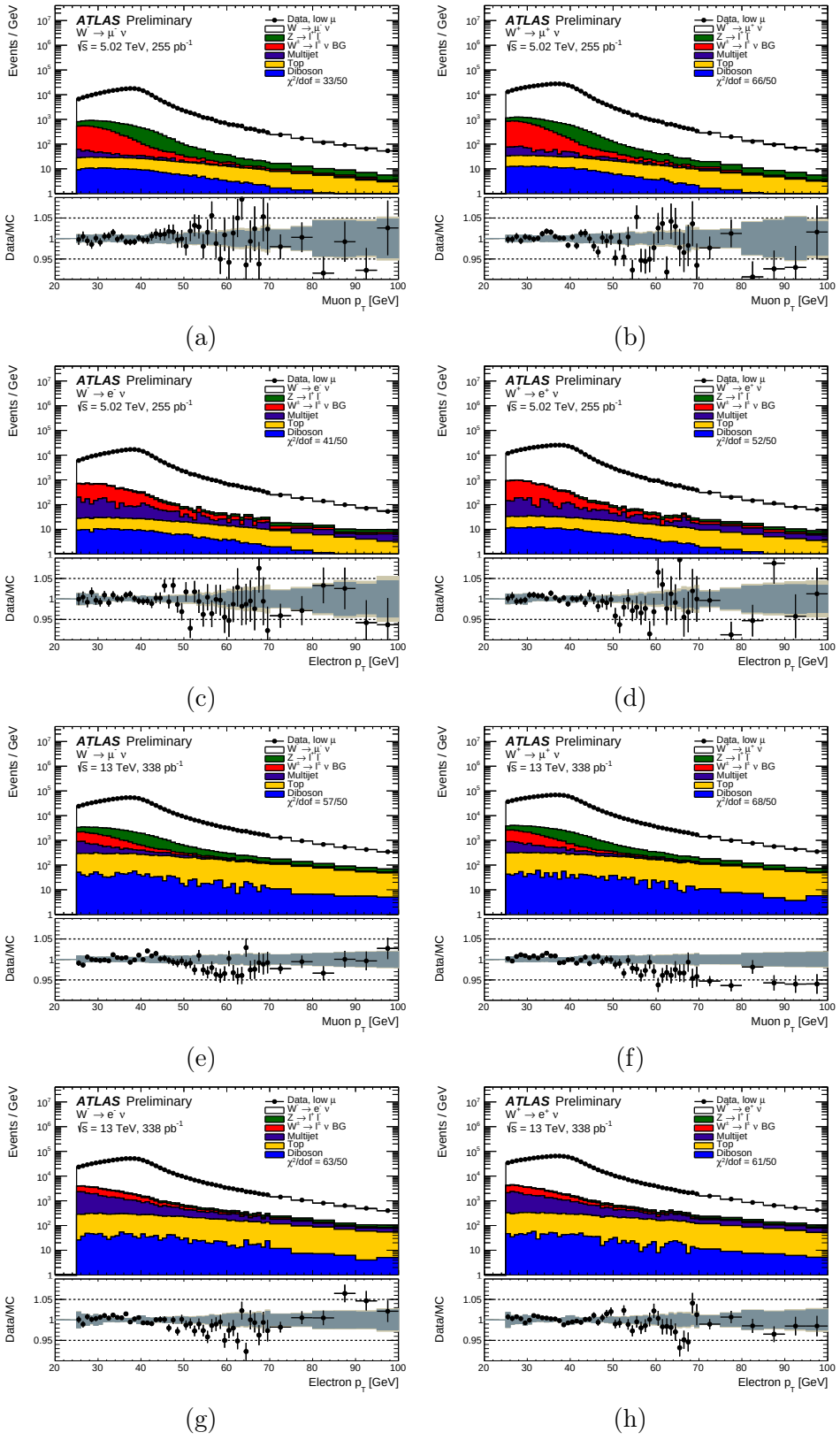

Figure 5.18 – Lepton p_{T} distribution in the muon and electron channels for the $\sqrt{s}$ =5.02 and 13 TeV datasets.

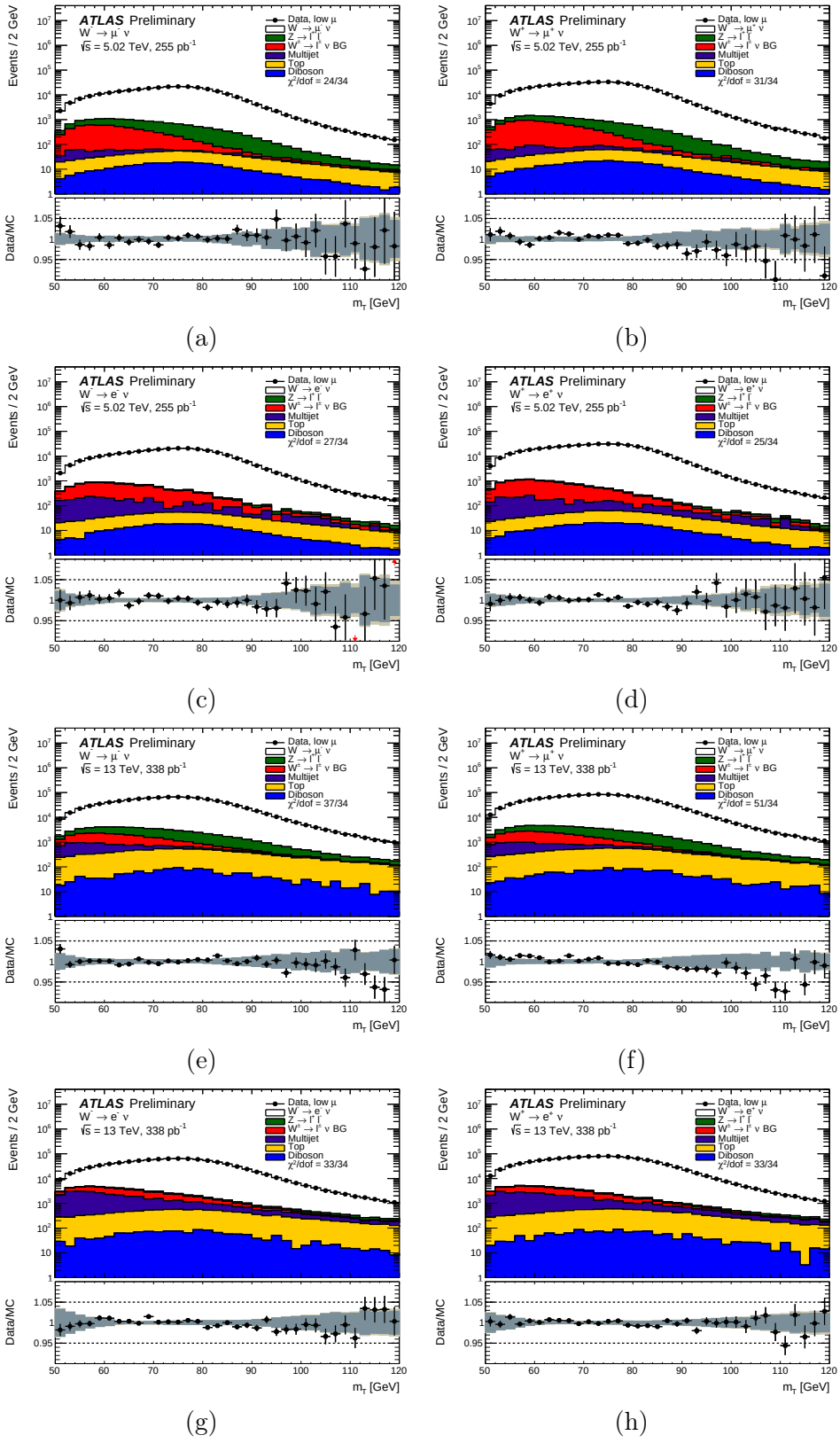

Figure 5.19 – m_{T} distribution in the muon and electron channels for the $\sqrt{s}$ =5.02 and 13 TeV datasets.

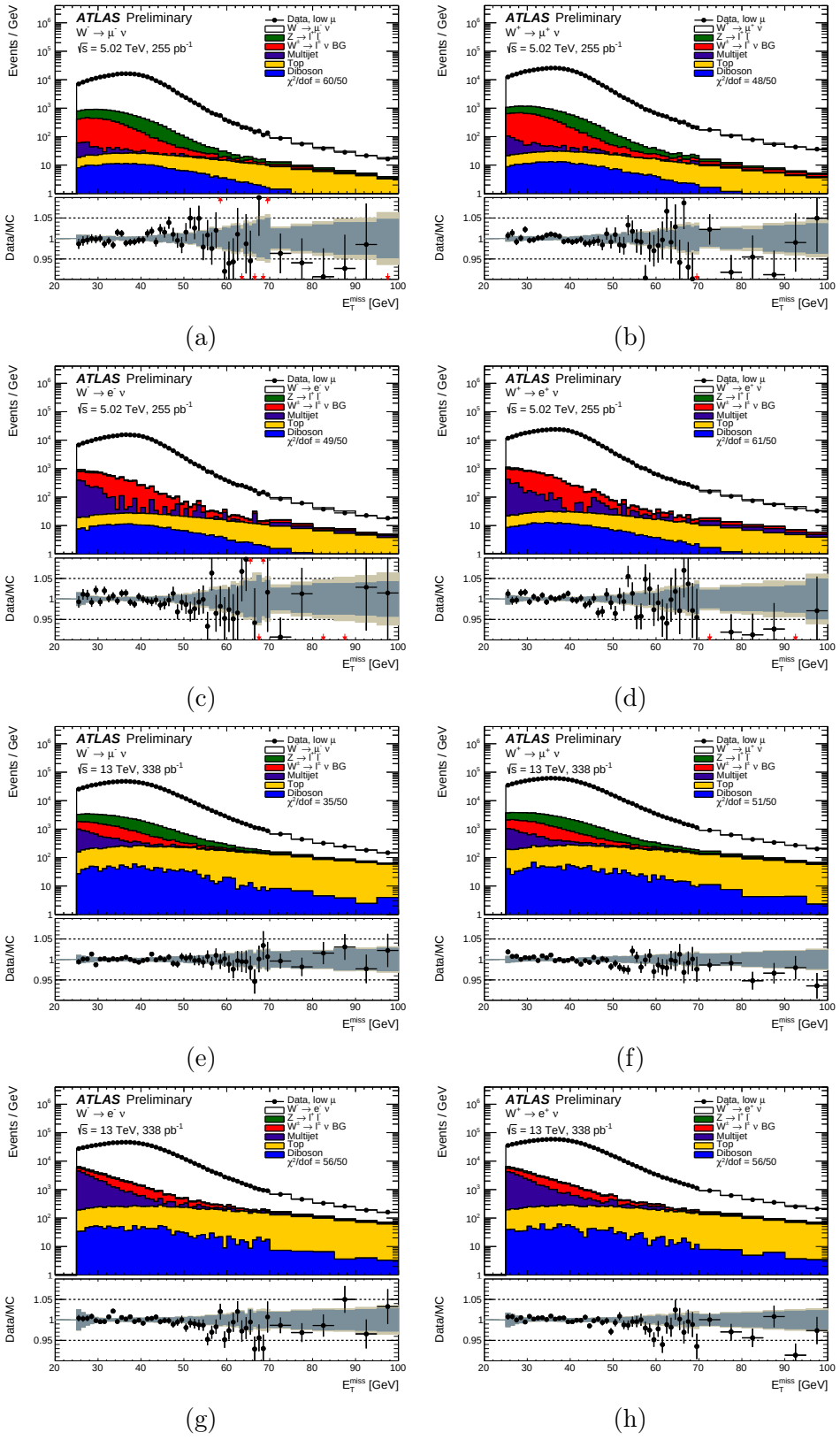

Figure 5.20 – $E_{\mathrm{T}}^{\mathrm{miss}}$ distribution in the muon and electron channels for the $\sqrt{s}$ =5.02 and 13 TeV datasets.

References

[1] P. Nason, "A new method for combining nlo qcd with shower monte carlo algorithms", *Journal of High Energy Physics*, vol. 2004, no. 11, p. 040, Dec. 2004. DOI: 10.1088/1126-6708/2004/11/040. [Online]. Available: https://dx.doi.org/10.1088/1126-6708/2004/11/040 (cit. on p. 86).

[2] S. Frixione, P. Nason, and C. Oleari, "Matching nlo qcd computations with parton shower simulations: the powheg method", *Journal of High Energy Physics*, vol. 2007, no. 11, p. 070, Nov. 2007. DOI: 10.1088/1126-6708/2007/11/070. [Online]. Available: https://dx.doi.org/10.1088/1126-6708/2007/11/070 (cit. on p. 86).

[3] S. Alioli, P. Nason, C. Oleari, and E. Re, "Nlo vector-boson production matched with shower in powheg", *Journal of High Energy Physics*, vol. 2008, no. 07, p. 060, Jul. 2008. DOI: 10.1088/1126-6708/2008/07/060. [Online]. Available: https://dx.doi.org/10.1088/1126-6708/2008/07/060 (cit. on p. 86).

[4] S. Alioli, P. Nason, C. Oleari, and E. Re, "A general framework for implementing nlo calculations in shower monte carlo programs: the powheg box", *Journal of High Energy Physics*, vol. 2010, p. 43, 6 Jul. 2010. DOI: 10.1007/JHEP06(2010)043. [Online]. Available: https://doi.org/10.1007/JHEP06(2010)043 (cit. on p. 86).

[5] H.-L. Lai, M. Guzzi, J. Huston, *et al.*, "New parton distributions for collider physics", *Phys. Rev. D*, vol. 82, p. 074 024, 2010. DOI: 10.1103/PhysRevD.82.074024. arXiv: 1007.2241 [hep-ph] (cit. on p. 86).

[6] T. Sjöstrand, S. Mrenna, and P. Skands, "A brief introduction to pythia 8.1", *Computer Physics Communications*, vol. 178, no. 11, pp. 852–867, 2008, ISSN: 0010-4655. DOI: https://doi.org/10.1016/j.cpc.2008.01.036. [Online]. Available: https://www.sciencedirect.com/science/article/pii/S0010465508000441 (cit. on p. 86).

[7] The ATLAS collaboration, "Measurement of the z/$\gamma*$ boson transverse momentum distribution in pp collisions at $\sqrt{s} = 7$tev with the atlas detector", *Journal of High Energy Physics*, vol. 2014, p. 145, 9 2014. DOI: https://doi.org/10.1007/JHEP09(2014)145. [Online]. Available: https://doi.org/10.1007/JHEP09(2014)145 (cit. on pp. 86, 94).

[8] Golonka, P. and Was, Z., "Photos monte carlo: a precision tool for qed corrections in z and w decays", *The European Physical Journal C - Particles and Fields*, vol. 45, pp. 97–107, 1 2006. DOI: https://doi.org/10.1140/epjc/s2005-02396-4. [Online]. Available: https://doi.org/10.1140/epjc/s2005-02396-4 (cit. on pp. 87, 94).

[9] S. Catani, L. Cieri, G. Ferrera, D. de Florian, and M. Grazzini, "Vector boson production at hadron colliders: a fully exclusive qcd calculation at next-to-next-to-leading order", *Phys. Rev. Lett.*, vol. 103, p. 082 001, 8 Aug. 2009. DOI: 10.1103/PhysRevLett.103.082001. [Online]. Available: https://link.aps.org/doi/10.1103/PhysRevLett.103.082001 (cit. on p. 87).

[10] S. Catani and M. Grazzini, "Next-to-next-to-leading-order subtraction formalism in hadron collisions and its application to higgs-boson production at the large hadron collider", *Phys. Rev. Lett.*, vol. 98, p. 222 002, 22 May 2007. DOI: 10.1103/PhysRevLett.98.222002. [Online]. Available: https://link.aps.org/doi/10.1103/PhysRevLett.98.222002 (cit. on p. 87).

[11] L. A. Harland-Lang, A. D. Martin, P. Motylinski, and R. S. Thorne, "Parton distributions in the lhc era: mmht 2014 pdfs", *The European Physical Journal C*, vol. 75, p. 204, 5 May 2015. DOI: 10.1140/epjc/s10052-015-3397-6. [Online]. Available: https://doi.org/10.1140/epjc/s10052-015-3397-6 (cit. on p. 87).

[12] M. Czakon and A. Mitov, "Top++: A Program for the Calculation of the Top-Pair Cross-Section at Hadron Colliders", *Comput. Phys. Commun.*, vol. 185, p. 2930, 2014. DOI: 10.1016/j.cpc.2014.06.021. arXiv: 1112.5675 [hep-ph] (cit. on p. 88).

[13] The CMS collaboration, "Measurement of the inclusive $t\bar{t}$ cross section in pp collisions at $\sqrt{s} = 5.02$ tev using final states with at least one charged lepton", *Journal of High Energy Physics*, vol. 2018, p. 115, 3 2018. DOI: https://doi.org/10.1007/JHEP03(2018)115. [Online]. Available: https://doi.org/10.1007/JHEP03(2018)115 (cit. on p. 88).

[14] S. Höche, F. Krauss, M. Schönherr, and F. Siegert, "Nlo matrix elements and truncated showers", *Journal of High Energy Physics*, vol. 2011, p. 123, 8 2011. DOI: 10.1007/JHEP08(2011)123. [Online]. Available: https://doi.org/10.1007/JHEP08(2011)123 (cit. on p. 88).

[15] R. D. Ball, V. Bertone, S. Carrazza, *et al.*, "Parton distributions with lhc data", *Nuclear Physics B*, vol. 867, no. 2, pp. 244–289, 2013, ISSN: 0550-3213. DOI: https://doi.org/10.1016/j.nuclphysb.2012.10.003. [Online]. Available: https://www.sciencedirect.com/science/article/pii/S0550321312005500 (cit. on p. 88).

[16] "The Pythia 8 A3 tune description of ATLAS minimum bias and inelastic measurements incorporating the Donnachie-Landshoff diffractive model", CERN, Geneva, Tech. Rep., 2016, All figures including auxiliary figures are available at https://atlas.web.cern.ch/Atlas/GROUPS/PHYSICS/PUBNOTES/ATL-PHYS-PUB-2016-017. [Online]. Available: https://cds.cern.ch/record/2206965 (cit. on p. 88).

[17] The ATLAS Collaboration, *The European Physical Journal C*, vol. 79, p. 639, 8 Aug. 2019. DOI: 10.1140/epjc/s10052-019-7140-6. [Online]. Available: https://doi.org/10.1140/epjc/s10052-019-7140-6 (cit. on p. 88).

[18] The ATLAS Collaboration, *The European Physical Journal C*, vol. 76, p. 292, 5 May 2016. DOI: 10.1140/epjc/s10052-016-4120-y. [Online]. Available: https://doi.org/10.1140/epjc/s10052-016-4120-y (cit. on p. 88).

[19] The ATLAS Collaboration, "Jet energy scale and resolution measured in proton-proton collisions at $\sqrt{s}$=13 tev with the atlas detector", *The European Physical Journal C*, vol. 77, p. 466, 7 Jul. 2017. DOI: 10.1140/epjc/s10052-017-5031-2. [Online]. Available: https://doi.org/10.1140/epjc/s10052-017-5031-2 (cit. on p. 89).

[20] The ATLAS Collaboration, "Measurement of the W-boson mass in pp collisions at $\sqrt{s} = 7\,\text{TeV}$ with the ATLAS detector", *The European Physical Journal C*, vol. 78, p. 110, 2018. DOI: 10.1140/epjc/s10052-017-5475-4 (cit. on pp. 89, 92, 93).

[21] J. Kretzschmar, F. Balli, and R. Stroehmer, "Samples and Physics modelling for low pile-up runs taken in 2017 and 2018", CERN, Geneva, Tech. Rep., 2019. [Online]. Available: https://cds.cern.ch/record/2657141 (cit. on p. 91).

[22] F. A. Berends, G. Burgers, W. F. L. Hollik, and W. L. van Neerven, "The standard Z peak", *Phys. Lett. B*, vol. 203, pp. 177–182, 1988. DOI: 10.1016/0370-2693(88)91593-6. [Online]. Available: https://cds.cern.ch/record/183706 (cit. on p. 93).

[23] P. Zyla *et al.*, "Review of Particle Physics", *PTEP*, vol. 2020, no. 8, p. 083C01, 2020, and 2021 update. DOI: 10.1093/ptep/ptaa104 (cit. on p. 93).

[24] D. Bardin, A. Leike, T. Riemann, and M. Sachwitz, "Energy-dependent width effects in e+e–annihilation near the z-boson pole", *Physics Letters B*, vol. 206, no. 3, pp. 539–542, 1988, ISSN: 0370-2693. DOI: https://doi.org/10.1016/0370-2693(88)91627-9. [Online]. Available: https://www.sciencedirect.com/science/article/pii/0370269388916279 (cit. on p. 93).

[25] N. Andari, M. Boonekamp, R. Hanna, and S. Camarda, "Measurement of m_W at 7 TeV: Physics modeling", CERN, Geneva, Tech. Rep., 2014. [Online]. Available: https://cds.cern.ch/record/1966965 (cit. on p. 94).

[26] T.-J. Hou, J. Gao, T. J. Hobbs, *et al.*, "New cteq global analysis of quantum chromodynamics with high-precision data from the lhc", *Phys. Rev. D*, vol. 103, p. 014 013, 1 Jan. 2021. DOI: 10.1103/PhysRevD.103.014013. [Online]. Available: https://link.aps.org/doi/10.1103/PhysRevD.103.014013 (cit. on p. 94).

[27] J. Pumplin, D. R. Stump, J. Huston, *et al.*, "New generation of parton distributions with uncertainties from global QCD analysis", *JHEP*, vol. 07, p. 012, 2002. DOI: 10.1088/1126-6708/2002/07/012. arXiv: hep-ph/0201195 (cit. on p. 94).

[28] E. Mirkes, "Angular decay distribution of leptons from w-bosons at nlo in hadronic collisions", *Nuclear Physics B*, vol. 387, no. 1, pp. 3–85, 1992, ISSN: 0550-3213. DOI: https://doi.org/10.1016/0550-3213(92)90046-E. [Online]. Available: https://www.sciencedirect.com/science/article/pii/055032139290046E (cit. on p. 95).

[29] E. Mirkes and J. Ohnemus, "W and z polarization effects in hadronic collisions", *Phys. Rev. D*, vol. 50, pp. 5692–5703, 9 Nov. 1994. DOI: 10.1103/PhysRevD.50.5692. [Online]. Available: https://link.aps.org/doi/10.1103/PhysRevD.50.5692 (cit. on p. 95).

[30] E. Mirkes and J. Ohnemus, "Angular distributions of drell-yan lepton pairs at the fermilab tevatron: order α_s^2 corrections and monte carlo studies", *Phys. Rev. D*, vol. 51, pp. 4891–4904, 9 May 1995. DOI: 10.1103/PhysRevD.51.4891. [Online]. Available: https://link.aps.org/doi/10.1103/PhysRevD.51.4891 (cit. on p. 95).

[31] E. Mirkes and J. Ohnemus, *Polarization effects in drell-yan type processes* $h_1 + h_2 \to (W, Z, \gamma*, J/psi) + X$, 1994. DOI: 10.48550/ARXIV.HEP-PH/9408402. [Online]. Available: https://arxiv.org/abs/hep-ph/9408402 (cit. on p. 95).

[32] R. Gauld, A. Gehrmann-De Ridder, T. Gehrmann, E. W. N. Glover, and A. Huss, "Precise predictions for the angular coefficients in Z-boson production at the LHC", *JHEP*, vol. 11, p. 003, 2017. DOI: 10.1007/JHEP11(2017)003. arXiv: 1708.00008 [hep-ph] (cit. on p. 95).

[33] J. C. Collins and D. E. Soper, "Angular distribution of dileptons in high-energy hadron collisions", *Phys. Rev. D*, vol. 16, pp. 2219–2225, 7 Oct. 1977. DOI: 10.1103/PhysRevD.16.2219. [Online]. Available: https://link.aps.org/doi/10.1103/PhysRevD.16.2219 (cit. on p. 95).

[34] The ATLAS collaboration, "Measurement of the angular coefficients in z-boson events using electron and muon pairs from data taken at $\sqrt{s} = 8$ tev with the atlas detector", *Journal of High Energy Physics*, vol. 2016, p. 159, 8 2016. DOI: https://doi.org/10.1007/JHEP08(2016)159. [Online]. Available: https://doi.org/10.1007/JHEP08(2016)159 (cit. on p. 95).

[35] J. Gao, M. Guzzi, J. Huston, *et al.*, "CT10 next-to-next-to-leading order global analysis of QCD", *Phys. Rev. D*, vol. 89, no. 3, p. 033 009, 2014. DOI: 10.1103/PhysRevD.89.033009. arXiv: 1302.6246 [hep-ph] (cit. on p. 96).

[36] The ATLAS Collaboration, "Measurement of w± and z-boson production cross sections in pp collisions at s=13 tev with the atlas detector", *Physics Letters B*, vol. 759, pp. 601–621, 2016, ISSN: 0370-2693. DOI: https://doi.org/10.1016/j.physletb.2016.06.023. [Online]. Available: https://www.sciencedirect.com/science/article/pii/S0370269316302763 (cit. on p. 96).

[37] T. Xu, "Measurements of W boson properties at $\sqrt{s}$=5 and 13 TeV with the ATLAS detector at the LHC", Theses, Université Paris Saclay (COmUE) ; University of science and technology of China, Sep. 2019. [Online]. Available: https://theses.hal.science/tel-02873298 (cit. on p. 96).

[38] T. Xu, M. Boonekamp, L. Aperio Bella, *et al.*, "Multi-jet background in low-pile-up runs taken in 2017 and 2018", CERN, Geneva, Tech. Rep., 2019. [Online]. Available: https://cds.cern.ch/record/2657146 (cit. on pp. 96, 106).

Chapter 6

Object reconstruction and calibration in W-boson measurements

Contents

6.1 Electron measurements

6.1.1 Electron reconstruction and selection

The offline electron and photon reconstruction in ATLAS in Run 2 is based on dynamic, variable-size clusters known as superclusters [1], so as to facilitate the energy recovery from bremsstrahlung photons or from photon-converted electrons. The dynamic clustering algorithm coordinates with dedicated calibration techniques to maintain the linear energy response and good stability as a function of pile-up.

An electron is defined to be an object comprising a cluster built from energy deposits in the calorimeter and a matched track or multiple tracks in the ID. An electron candidate is required to originate from the primary vertex, satisfying $|z_0| \cdot \sin(\theta)$ <0.5 mm and $|d_0|/\sigma_{d_0} < 5$. A converted photon is defined to be a cluster matching to a conversion vertex or several vertices, while an unconverted photon is a cluster matching to no electron track or conversion vertex.

The electron selection in the W-boson analyses consists of four requirements [2].

— Reconstruction: The object has to be reconstructed as an electron, judging from its energy deposit in the EM calorimeter and the track matching to the ID.

— Identification: The candidate for a prompt electron is required to pass a given working point (WP) of likelihood, where multiple quantities related to the calorimeter and the track are used to distinguish the prompt electron from light flavor jets, converted photons, or non-prompt electrons from the semi-leptonic decay of hadrons containing b or c quarks. The "MediumLLH" working point is chosen for the analyses, since it is found to render a good balance between efficiency and background rejection.

— Isolation: The reconstructed and identified electron needs to pass the isolation working point ptcone20/Min(pT, 50 GeV)<0.1.

— Trigger: The reconstructed and identified electron passing the isolation selection has to pass the trigger selection. For the single lepton trigger used in W-boson analyses, the trigger fires while at least one selected electron matches to the objects that fire the trigger.

The analyses use the combination of the above four requirements to select electrons, in order to improve the purity of electrons and reject backgrounds. The efficiencies of the selections may differ between data and simulation due to the complex data-taking and detecting environment, non-realistic simulation of tracks and clusters, mis-modelling of backgrounds and jet activities. This means that the electron distributions from the simulations have to be corrected for, in order to match instrumental inefficiencies in the data. The discrepancy between data and MC simulation are accounted for by scale factors (SF): the ratio of a given selection efficiency in the data over the predicted efficiency in MC. The total correction of selection efficiency applied to a single electron in W events is factorized into a product of the SFs for the four selection requirements:

$$W_{event}^{W\to e\nu} = SF_{reco} \cdot SF_{ID} \cdot SF_{Isolation} \cdot SF_{Trigger} \tag{6.1}$$

The efficiencies are measured with the tag-and-probe method using $Z \to ee$ events [3]. First, adequate kinematic cuts are applied to select $Z \to ee$ events, ensuring the purity and quality of the electron-positron pairs. Then, a tight selection is applied to one object in each pair to get the 'tag' while keeping the single electron trigger still matched, so that the trigger bias is removed. For events passing both the ordinary Z selection and the tight selection, the second object in the electron-positron pair is highly probable to be a prompt and isolated electron. And it is taken as 'probe' to measure the efficiency of a selection. The relevant systematic uncertainties are assessed by varying the requirements in the two levels of selection, which primarily evaluates the stability of the background subtraction.

For the low pile-up data taking, the $HLT\_e15\_lhloose\_nod0\_L1EM12$ unprescaled trigger is used for the electrons, which requires p_{T}^{e} >15 GeV, loose ID criteria and no isolation selection. The trigger efficiency is defined to be the fraction of reconstructed, MediumLLH-identified and isolated electrons passing the trigger selection. Given that both ID and isolation are applied to both electrons, background becomes negligible for the measurement of electron trigger efficiency.

The central values and uncertainties of electron reconstruction SFs are obtained by extrapolating the standard high pile-up SFs to the low pile-up conditions, for both the 5.02 and 13 TeV datasets, as a function of p_{T} in bins of η. The identification SFs are measured in-situ using $Z \to ee$ events of the low pile-up data, but separately for the two center-of-mass energies. The isolation and trigger SFs are measured using $Z \to ee$ events in the low pile-up data, combining 5.02 and 13 TeV datasets.

6.1.2 Electron calibration

The extraction of electron energy scale and resolution uses the same method as the high pile-up data [4]. For $Z \to ee$ events, the energy scale factors α_i is applied to the data to correct the measured energy E^{data} to the scale of the simulation E_{MC}, such that

$$E^{data} = E^{MC}/(1+\alpha_i) \tag{6.2}$$

The correction is implemented in η bins of the calorimeter cluster with the index i. The data are calibrated by multiplying the factor $1+\alpha_i$ after the derivation of the α_i factors.

The relative resolution of the measured electron energy is a quadratic sum of three contributions:

$$\frac{\sigma(E)}{E} = \frac{a}{\sqrt{E}} \oplus \frac{b}{E} \oplus c \tag{6.3}$$

The first term a is the stochastic fluctuations related to the development of the electromagnetic shower in the calorimeter. Since the development of the shower is linear to the energy E, the stochastic fluctuations of the development of the shower is therefore proportional to $1/\sqrt{E}$. The second term with b describes the electronics and pile-up noise, followed by a constant term c accounting for the non-uniformity of the detector. An additional smearing c_i' is applied to the simulation in each calorimeter bin of η, making the width of the MC mass distribution match that of the data:

$$\left(\frac{\sigma(E)}{E}\right)_i^{data} = \left(\frac{\sigma(E)}{E}\right)_i^{MC} \oplus c_i' \tag{6.4}$$

24 calorimeter bins of η are used to extract α and c' correction factors in-situ for the low pile-up runs [3]. Uncertainties are assigned to electron calibration according to the statistical uncertainties in α and c_i' factors, along with the systematics related to imperfect modelling of the calorimeter.

6.2 Muon measurements

6.2.1 Muon reconstruction and selection

The muon reconstruction and identification are based on the information of three sub-detectors: MS, ID and calorimeter. A muon candidate can be classified according to a few types, depending on the available information, and consequently the algorithm used for the reconstruction. The types of muon candidates relevant to the low pile-up data are listed below [5]:

- MuonStandAlone (SA): Muon candidates are identified by track reconstruction only in the MS. The MS-only track is extrapolated to the IP after accounting for the energy-loss in the calorimeter. The information of the muon candidate is determined by this Muon-Extrapolated (ME) track.
- Combined (CB): The reconstruction of the tracks comes from a combined fit using both ID and MS information. An ID track and a ME track are needed for the final fit, where the ID track is extrapolated outward to the MS to find additional segments.
- CaloTagged (CT): Muon candidates are identified via an ID track with p_{T} >5 GeV matching an energy deposit of a minimum ionization particle (MIP) in the calorimeter and being isolated.

For the muon reconstruction and identification of the Run 2 low pile-up datasets, the Medium working point (WP) is chosen as the muon selection criterion [6]. The tracks in both ID and MS are combined to fit the final reconstructed track of the muon (CB muon). The Medium WP in general provides very good acceptance, permille level fake rate, as well as small systematic uncertainties. For $0.1 < |\eta| < 2.5$, the Medium WP relies on CB muons with hits in no less than 2 MDT stations. For $|\eta| < 0.1$, CB muons with hits in 1 MDT station are allowed.

Given that the tracks are reconstructed separately in the ID and MS, the muon reconstruction efficiency can be factorized into a product of reconstruction efficiency in the ID, the reconstruction efficiency in the MS and the matching efficiency between the ID and MC measurements. Similar to the measurement of electron selection efficiency, a tag-and-probe method is also used for muons [7]. The efficiency to obtain a Medium muon is computed as:

$$\epsilon(Medium) \simeq \epsilon(ID|ME) \times \epsilon(ME|CT) \times \epsilon(Medium|ID \wedge ME) \tag{6.5}$$

Here $\epsilon(ID|ME)$ stands for the efficiency of and ID track measured with respect to a ME probe. $\epsilon(ME|CT)$ is the efficiency of an MS-only tracked measured with respect to a CT probe. The last term $\epsilon(Medium|ID \wedge ME)$ is a measurement of the combination and the medium identification criteria with respect to a two-track-probe, in which the ID and ME tracks are required to stay $\Delta R < 0.05$ with each other.

The muon objects have to satisfy $|z_0| \cdot sin(\theta)$ <0.5 mm and $|d_0|/\sigma_{d_0} < 3$ (track-to-vertex association requirements, or TTVA) to ensure they originate from the primary vertex (PV). Since the two requirements are not included in the muon identification criteria, their selection efficiency has to be studied independently. Muons passing the Loose identification criterion as well as $|\eta|$ <2.5 and p_{T} >10 GeV are used as probes. Considering that the TTVA efficiency doesn't rely on the choice of identification WP, the corrections can be directly applied to the Medium WP. The matches are realized by adding the TTVA selection.

The muon trigger efficiency is determined by the tag-and-probe approach. The tag is an isolated and triggered muon, while the probe is an isolated muon. The invariant mass of the muon pair falls in the kinematic window near the Z resonance peak. The main unprescaled trigger is HLT_mu14, which comes with a significantly lower threshold and no isolation requirement in contrast to the single-muon triggers used for high pile-up Run 2 data taking. The trigger efficiency is studied in three dimensions: p_{T}, η and ϕ, so as to meet the requirements of the analyses in which the physics results are highly dependent on p_{T} but are inclusive in ϕ. To estimate the impact of systematic uncertainties on muon trigger efficiency, the selection requirements of the probe and the matching window to the trigger object are varied, including the kinematics of the Z mass window, the tightness of isolation, detector azimuthal symmetry and the inclusion of interaction point (IP) cuts.

Muon isolation in the low pile-up W analyses uses the track based isolation ptcone20/Min(pT, 50 GeV)<0.1. The isolation selection efficiencies are studied with the tag-and-probe method in $Z \to \mu\mu$ candidates in both data and MC simulation. Given that the background level is estimated to be negligible, no background subtraction is done in the determination of the isolation efficiency in both the data and the MC. Muon isolation SFs, measured as a function of the probe muon η and p_{T}, are used in the analyses to correct the MC events to match the isolation selection efficiency in the data. The muon isolation SFs are derived using combined 5 and 13 TeV low pile-up datasets. The permille level isolation SF uncertainties are dominated by statistical uncertainties. Additional systematic sources include the range of pair invariant mass required in the selection, the probe quality, the tag-probe separation, the jet separation and the tag isolation.

6.2.2 Muon calibration

Muon momentum calibration involves the corrections to the momentum scale and resolution, as well as the sagitta bias. The corrections to momentum scale and resolution are applied to the muons in the simulation, bringing the scales and resolutions closer to the data, though at the expense of optimal performance.

The reconstructed muon tracks in the inner detector (ID tracks) and those in the muon spectrometer (ME tracks) receive separate corrections. The corrections are propagated from ID tracks and ME tracks to combined muon tracks (CB tracks) thanks to a reweighting of the two contributions. The muon calibration in terms of momentum scale and resolution is obtained from the high pile-up datasets [5] and cross-checked with low pile-up datasets using J/ψ and Z-boson samples. Generally speaking, after the implementation of the standard corrections, the agreement of both the scales and resolutions in MC with data is improved. The data-MC discrepancy for scale is at permille level most of the time. The residual difference can be mostly covered by systematic uncertainties related to calibration corrections. This implies that at least for p_{T}^{W} analysis, which is not very sensitive to muon momentum calibration, the high pile-up calibration can be applied to the low pile-up data. An improved muon calibration might be needed for the W-boson mass analysis, using dedicated in-situ derivation of muon momentum corrections for the low pile-up data.

The other part of muon calibration is the correction for charge-dependent momentum biases (sagitta bias). The misalignments within the ID, within the MS or between the ID and the MS can introduce sagitta bias to the muon momentum reconstruction. The effect of sagitta bias on the reconstructed muon transverse momentum is parameterized as:

$$p_{\mathrm{T}}^{meas} = \frac{p_{\mathrm{T}}^{reco}}{1 + q \times \delta_{sagitta} \times p_{\mathrm{T}}^{reco}} \tag{6.6}$$

p_{T}^{meas} is the measured (and biased) transverse momentum. p_{T}^{reco} represents the unbiased reconstructed transverse momentum. The sagitta bias, quantified by $\delta_{sagitta}$, is studied in bins of lepton η while ignoring the distribution in ϕ to suppress the statistical fluctuations. The sagitta bias is evaluated using a combination of three methods [8]:

— ID momentum measurement with electrons. From $Z \to ee$ or $W \to e\nu$ events, the charge bias of the electron track is determined by:

$$\delta_{sagitta} = \frac{< E/p_{track} >^{+} - < E/p_{track} >^{-}}{2 < p_{\mathrm{T}} >} \tag{6.7}$$

Here p_{track} is the track momentum recorded by the inner detector and E is the calibrated electron energy measured by the EM calorimeter. $p_{\mathrm{T}} = E \sin\theta$ is the transverse momentum of the electron derived from the charge-blind EM calorimeter measurement and the track direction. All the quantities are measured in η bins on average.

— $p_{\mathrm{T}}(\mu)$ method. The muon momentum bias is determined by comparing the p_{T} distribution of muons with that of the anti-muons in $Z \to \mu\mu$ events. The difference caused by electroweak effects is known from the simulation and turns out to be marginal. Therefore, the major difference between the p_{T} spectra is expected to arise from the sagitta bias.

— Z-mass method. The reconstructed Z-boson invariant mass peak from $Z \to \mu\mu$ events may have an offset from the expected value, which can be assigned to the sum of the sagitta biases of the two muon tracks. The measured biases are corrected iteratively, until the sagitta bias of each individual muon track converges and Z mass is independent of η and ϕ bins.

It is observed that the sagitta bias in the low pile-up data is around 10 times larger than in the MC simulation. A dedicated sagitta bias correction is derived by using the results differential in η from the Z-mass method corrected by an global offset $< \delta_{sagitta} >$. The overall offset of $< \delta_{sagitta} >$ is evaluated by adjusting its value until the ratio of positive and negative muon p_{T} spectra in $Z \to \mu\mu$ events becomes flat [6]. The data-MC difference is applied to the data to achieve a good agreement in data/MC comparison.

6.3 Hadronic recoil measurements

In the decay of the $W \to \ell\nu$ process, where the neutrino escapes the detection, the transverse momentum of the neutrino can only be inferred from the transverse momenta of all other particles produced in a p-p collision. The transverse momentum of the neutrino is not only required in the event selection for W-boson measurements, but also enters the reconstruction of the W transverse mass, a quantity of particular importance in the W-boson mass analysis. In order to determine neutrino kinematics from W decay in high-precision, the ATLAS analyses use the general methodology known as the hadronic recoil, according to which the vectorial and scalar sums of all particles from the initial state gluon and quark radiation are measured. In this way, the transverse momentum of the W-boson can be directly measured by $\vec{u}_{\mathrm{T}} + \vec{p}_{\mathrm{T}}^{W} = 0$. One step further, by combining the measurement of the charged lepton with the hadronic recoil, the neutrino transverse momentum can be inferred by making using of the momentum balance in the transverse plane.

The hadronic recoil has been implemented successfully in previous ATLAS analyses, for instance, the measurement of W-boson transverse momentum distribution at $\sqrt{s}$ =7 TeV [9] and the measurement of W-boson mass at $\sqrt{s}$ =7 TeV [10]. In contrast, the ATLAS standard $E_{\mathrm{T}}^{\mathrm{miss}}$ algorithm used for physics in high pile-up environment with track-based soft term (TST) is not suitable for the W analyses at low p_{T}^{V}, mostly because of the main $E_{\mathrm{T}}^{\mathrm{miss}}$ algorithm on reconstructed jets with a p_{T} threshold of about 20 GeV and the very limited response of the tracking term.

6.3.1 PFOs and hadronic recoil reconstruction

The hadronic recoil is calculated using an algorithm based on Particle Flow Objects (PFOs) [11], which helps the algorithm stay fully transparent regarding its application to $W \to \ell\nu$ events and the calibration with $Z \to \ell\ell$ events.

In the PFO algorithm, first the inner detector (ID) tracks are selected with the tight criteria, requiring at least nine hits in the silicon detectors and tracks not missing hits in the pixel detector when those hits are expected from the trajectory under the given operating conditions. The best recoil resolution is obtained by using the constituent PFO in the largest possible phase space, such that no extra cut is applied apart from the p_{T} >0.5 GeV requirement of the track reconstruction. The maximal

pseudo-rapidity corresponds to the coverage of the ATLAS FCAL up to $|\eta|$ =4.9 [12]. Tracks matching to either an electron or muon with $p_{\mathrm{T}} > 10\,\mathrm{GeV}$ identified by the medium criteria are removed. The rest of the tracks are then matched to a single calorimeter cluster constructed with the usual topo-cluster 4/2/0 algorithm calibrated to the electromagnetic (EM) scale [13]: Based on the cluster position and the track momentum, the expected energy deposit of the track of the particle in the calorimeter is computed. Topo-clusters of calorimeter cells start from cells with absolute energy measurements exceeding the expected energy by four times of the standard deviation of the expected noise (both electronics noise and contribution from the pile-up). After that, the adjacent cells with absolute energy two times above the noise are added iteratively to the topo-clusters, followed by a final addition of all the neighbouring cells. In case a single particle deposits energy in multiple clusters, the additional clusters within the geometric cuts are added to the system. The recovery of split showers is handled by a specific procedure. In the end, the difference of the expected calorimeter energy deposited by the track and the sum of the associated clusters is compared with the expected calorimeter noise. If the difference is compatible with zero within 1.5 σ, the clusters are removed, otherwise the remnant topo-cluster is retained.

The PFOs are divided into two separate types. The neutral PFOs (nPFOs) correspond to topo-clusters not associated to ID tracks of charged particles. The charged PFOs (cPFOs) correspond to the selected ID tracks. The cPFOs originating from vertices other than the primary vertex are removed by requiring $|z_0 \times sin(\theta)| < 2\,\mathrm{mm}$ from the primary vertex.

The reconstruction of the hadronic recoil needs to be transparent between W and Z, or between electron and muon decay channels for a precise calibration and well-understood correlations. Although both electrons and muons lose energy in the calorimeter, the nature of energy loss as well as the profile of the energy deposit is very different: while electrons develop showering in the material, muons lose energy mainly because of isolation. For this reason, the lepton-related difference between electron and muon have to be removed in the reconstruction algorithm. Empirically in ATLAS, removing a cone of radius $\Delta R < 0.2$ around the lepton axis is sufficient to eliminate those effects, while bringing a minor impact on the rest of the event reconstruction. In practice, this is achieved by excluding the PFOs inside the cone around the identified leptons from the calculation of the recoil. Subsequently, the bias caused by removing energy deposits from underlying event and pile-up in that cone is compensated for by looking for another cone of the same size and same $|\eta|$ but at a random ϕ position. The chosen replacement cone also needs to be $\Delta R > 0.4$ away from the recoil prior to this correction or from any lepton. After that, the activities in replacement cone are rotated in ϕ to the removed lepton direction and added vectorially to the recoil. The leptons considered in the removal procedure are required to be well measured and pass the criteria of $p_{\mathrm{T}} > 10\,\mathrm{GeV}$, medium ID and $|\eta| < 2.4$ for muons, or LooseLH+B-layer hit and $|\eta| < 2.47$ excluding the cracks for electrons.

The hadronic recoil in the transverse plane $\vec{u}_{\mathrm{T}}$ is the vectorial sum of all cPFOs and nPFOs:

$$\vec{u}_{\mathrm{T}} = \sum_i \vec{E}_{\mathrm{T},i}^{cPFO} + \sum_i \vec{E}_{\mathrm{T},i}^{nPFO} \tag{6.8}$$

The quantity u_{T} is the magnitude of the vector $\vec{u}_{\mathrm{T}}$.

6.3.2 Variables for the study of hadronic recoil

The characterization and calibration of the hadronic recoil are based on variables independent of the azimuthal ϕ angles of the event activities but directly correlated with the vector boson kinematics. In Z events, $\vec{p}_{\mathrm{T}}^{\ell\ell}$ is used to represent the transverse momentum of Z-boson. Two scalar quantities are built using the projection of $\vec{u}_{\mathrm{T}}$:

The component of the hadronic recoil perpendicular to the axis of Z-boson is defined as:

$$u_{\perp} = \frac{|\vec{p}_{\mathrm{T}}^{\ell\ell} \times \vec{u}_{\mathrm{T}}|}{p_{\mathrm{T}}^{\ell\ell}} \tag{6.9}$$

The component of the hadronic recoil parallel to the axis of Z-boson is:

$$u_{||} = \frac{\vec{p}_{\mathrm{T}}^{\ell\ell} \cdot \vec{u}_{\mathrm{T}}}{p_{\mathrm{T}}^{\ell\ell}} \tag{6.10}$$

$u_{\perp}$ is zero on average, and its spread reflects the hadronic recoil resolution in the perpendicular direction. Ideally, $u_{||}$ balances the Z-boson transverse momentum according to $u_{||} = -p_{\mathrm{T}}^{\ell\ell}$. However, this balance can hardly be fulfilled because of effects such as particles escaping detection, energy losses in dead material and the non-compensating nature of the calorimeter. Therefore, a non-zero bias of the momentum balance in the transverse plane almost always exists and is introduced to the study of the hadronic recoil, as a more convenient notation in many contexts:

$$b = u_{||} + p_{\mathrm{T}}^{\ell\ell} \tag{6.11}$$

The average of b is usually found to be positive. And the spread of b distribution indicates the hadronic recoil resolution in the parallel direction.

In W events, the useful projections of the hadronic recoil rely on the direction of charged lepton because of the neutrino in the decay product:

$$\begin{aligned} u_{\perp}^{\ell} &= \frac{|\vec{p}_{\mathrm{T}}^{\ell} \times \vec{u}_{\mathrm{T}}|}{p_{\mathrm{T}}^{\ell}} \\ u_{||}^{\ell} &= \frac{\vec{p}_{\mathrm{T}}^{\ell} \cdot \vec{u}_{\mathrm{T}}}{p_{\mathrm{T}}^{\ell}} \end{aligned} \tag{6.12}$$

In this way $u_{\perp}^{\ell}$ and $u_{||}^{\ell}$ provides the information of u_{T} in the direction related to event kinematics, similar to the quantities $u_{\perp}$, $u_{||}$ and b in Z events.

6.3.3 Hadronic recoil calibration and correction

The calibration procedure for the hadronic recoil is adapted from the method developed in the analysis of the 2011 7 TeV data [14]. The calibration uses Z-boson events as a standard candle, since the transverse kinematics of the final state lepton pair can be fully reconstructed and precisely measured, of which the resolution is one order of magnitude better than the hadronic recoil. Three steps are carried out in a sequence:

— Reweighting of MC to improve the modelling of $\sum \bar{E}_{\mathrm{T}}$ (defined in Equation 5.4).

— The azimuthal bias is corrected for.

— The resolution and the response of the two projections of $\vec{u}_{\mathrm{T}}$ in MC are corrected to match the data.

$\sum \bar{E}_{\mathrm{T}}$ reweighting

Despite the similarities between W and Z events that help the transfer of calibration at good accuracy, differences in the energy scale and the partons involved in the hard scattering lead to both different underlying events and the boson-p_{T} spectra. Therefore, the transfer of the calibration correction from Z to W relies on a calibration obtained as a function of $\sum \bar{E}_{\mathrm{T}}$ and p_{T}^{V}. Both the modelling of $\sum \bar{E}_{\mathrm{T}}$ and the correlation between $\sum \bar{E}_{\mathrm{T}}$ and p_{T}^{V} have to be corrected for in the MC, such that in each bin of p_{T}^{V} the MC distribution of $\sum \bar{E}_{\mathrm{T}}$ matches that of the data.

Three steps of event reweighting are implemented to obtain a correct modelling of event activity $\sum \bar{E}_{\mathrm{T}}$ and its correlation with p_{T}^{V} for the MC samples. A $(\sum \bar{E}_{\mathrm{T}}, p_{\mathrm{T}}^{\ell\ell})$ 2D reweighting is derived from the ratio of the data to Z simulation, where electron and muon channels are added together:

$$w_{2D}^{Z}(\sum \bar{E}_{\mathrm{T}}, p_{\mathrm{T}}^{\ell\ell}) = \frac{h_{2D}^{data,Z}(\sum \bar{E}_{\mathrm{T}}, p_{\mathrm{T}}^{\ell\ell})}{h_{2D}^{MC,Z}(\sum \bar{E}_{\mathrm{T}}), p_{\mathrm{T}}^{\ell\ell}} \tag{6.13}$$

Here h_{2D} stands for the normalized 2D distribution of $(\sum \bar{E}_{\mathrm{T}}, p_{\mathrm{T}}^{\ell\ell})$).

The second step of reweighting is applied to the W processes, where the residual of a few percent for $\sum \bar{E}_{\mathrm{T}}$ is observed between data and MC, if the above Z-based procedure is implemented without further correction (i.e. simply taking $w_{2D}^{Z}(\sum \bar{E}_{\mathrm{T}}, p_{\mathrm{T}}^{true,V})$). After the 2D reweighting, an improved modelling of $\sum \bar{E}_{\mathrm{T}}$ in W events is obtained by reweighting $\sum \bar{E}_{\mathrm{T}}$ in slices of u_{T}:

$$w_{j,sliced}^{W^{\pm}}(\sum \bar{E}_{\mathrm{T}}) = \frac{h_{j}^{data,W^{\pm}}(\sum \bar{E}_{\mathrm{T}})}{h_{j}^{MC,W^{\pm},Z2D}(\sum \bar{E}_{\mathrm{T}})} \tag{6.14}$$

h_j denotes the normalized $\sum \bar{E}_{\mathrm{T}}$ for a given slice j of u_{T} distribution in the data (the sum of signal and background predictions) for the numerator (denominator) after the W event selection. The index 'Z2D' suggests that the histogram in the denominator has gone through the 2D reweighting.

Since the above two steps of reweightings together modify the spectrum of boson p_{T} in an unintended way, a third reweighting is necessary to recover the initial spectrum of $p_{\mathrm{T}}^{V,true}$ in the full phase-space, so that the critical modelling of boson p_{T} in the MC is not affected:

$$w_{1D}^{W\pm}(p_{\mathrm{T}}^{true,V}) = \frac{h^{MC,W\pm,mod}(p_{\mathrm{T}}^{true,V})}{h^{MC,W\pm,orig}(p_{\mathrm{T}}^{true,V})} \tag{6.15}$$

The 1D histogram h is the modified (numerator) or original (denominator) $p_{\mathrm{T}}^{true,V}$ of simulated W events without selection cut. The final weight applied to W events in the simulation with the value of u_{T} in the corresponding slice j is given by $w_{2D}^{Z}(\sum \bar{E}_{\mathrm{T}}, p_{\mathrm{T}}^{\ell\ell}) \times w_{j,sliced}^{W^{\pm}}(\sum \bar{E}_{\mathrm{T}}) \times w_{1D}^{W\pm}(p_{\mathrm{T}}^{true,V})$.

Correction of recoil direction

Due to effects such as beam crossing angle, calorimeter non-uniformity and beam displacement, the direction of the recoil is not perfectly modelled in the simulation. Empirically, the correction is carried out by an additive offset as the difference between the mean values of the x, y components ($< u_x >$, $< u_y >$) of the recoil in data and

simulation. A linear dependence on $\sum \bar{E}_{\mathrm{T}}$ is assigned to the correction:

$$\begin{aligned} u_x^{MC,corr} &= u_x^{MC} + [(< u_x^{data} > - < u_x^{MC} >)(\sum \bar{E}_{\mathrm{T}})] \\ u_y^{MC,corr} &= u_y^{MC} + [(< u_y^{data} > - < u_y^{MC} >)(\sum \bar{E}_{\mathrm{T}})] \end{aligned} \tag{6.16}$$

The remaining discrepancy between data and MC for the direction of the recoil is below the data statistics of the Z events and is therefore considered as a fluctuation. The effect of the correction of the recoil direction has been observed having a negligible impact on u_{T}, confirming a weak correlation between the direction and the magnitude of the recoil.

Resolution and response corrections

The recoil resolution is derived by comparing the width of $u_{\perp}$ as well as the mean and width of the bias b in the data and in the simulation of Z events. The differences in both perpendicular and parallel directions are corrected individually.

The data-to-MC resolution correction for $u_{\perp}$ derived as the ratio $r(\sum \bar{E}_{\mathrm{T}}, p_{\mathrm{T}}^{\ell\ell}) = \sigma(u_{\perp})^{data}/\sigma(u_{\perp})^{MC}$. The ratio of $\sum \bar{E}_{\mathrm{T}}$ and $p_{\mathrm{T}}^{\ell\ell}$ is fitted in separate bins of $p_{\mathrm{T}}^{\ell\ell}$ as a function of $\sum \bar{E}_{\mathrm{T}}$:

$$\sigma(u_{\perp})(\sum \bar{E}_{\mathrm{T}}) = c + d \cdot \sqrt{\sum \bar{E}_{\mathrm{T}}} \tag{6.17}$$

The corrected value of $u_{\perp}$ in the simulation of W events is scaled to make the width match to that of the data, with $p_{\mathrm{T}}^{\ell\ell}$ replaced by $p_{\mathrm{T}}^{true,V}$:

$$u_{\perp}^{MC,corr} = u_{\perp}^{MC} \times r(\sum \bar{E}_{\mathrm{T}}, p_{\mathrm{T}}^{true,V}) \tag{6.18}$$

The correction of $u_{||}$ in the simulation of W events comprises a response and a resolution correction:

$$u_{||}^{MC,corr} =< u_{||}^{data} > +(< b^{data} > - < b^{MC} >) \cdot r_{||} + (u_{||}^{MC} - < u_{||}^{data} >) \cdot r_{||} \tag{6.19}$$

Here $< u_{||}^{data} > (\sum \bar{E}_{\mathrm{T}}, p_{\mathrm{T}}^{\ell\ell})$ averages over data in each bin of $(\sum \bar{E}_{\mathrm{T}}, p_{\mathrm{T}}^{\ell\ell})$. And the dependence on $p_{\mathrm{T}}^{\ell\ell}$ is fitted in each $\sum \bar{E}_{\mathrm{T}}$ bin linearly:

$$< u_{||}^{data} > (p_{\mathrm{T}}^{\ell\ell}) = e + f \cdot p_{\mathrm{T}}^{\ell\ell} \tag{6.20}$$

Similarly, $(< b^{data} > - < b^{MC} >)(\sum \bar{E}_{\mathrm{T}}, p_{\mathrm{T}}^{\ell\ell})$ is derived as the average of bias in bins of $(\sum \bar{E}_{\mathrm{T}}, p_{\mathrm{T}}^{\ell\ell})$ and fitted in each bin of $\sum \bar{E}_{\mathrm{T}}$ by a linear function of $p_{\mathrm{T}}^{\ell\ell}$. When the correction is applied to the simulation of W events, $p_{\mathrm{T}}^{\ell\ell}$ is replaced by $p_{\mathrm{T}}^{true,V}$.

6.3.4 Recoil calibration uncertainties

The uncertainties on the recoil calibration stem from the data statistics in the resolution and response correction, as well as the non-closure in the extrapolation from Z to W [12].

$\sum \bar{E}_{\mathbf{T}}$ reweighting uncertainty

The Sherpa MC samples are used as pseudo-data to perform a closure test of $\sum \bar{E}_{\mathrm{T}}$ reweighting procedure. The reweighting coefficients are derived from Sherpa W and Z events and applied to Powheg samples following the$\sum \bar{E}_{\mathrm{T}}$ reweighting procedures in Section 6.3.3. The reweighted Powheg is then compared with Sherpa in 2D

$(\sum \bar{E}_{\mathrm{T}}, p_{\mathrm{T}}^{true,V})$ distribution. The non-closure for the $\sum \bar{E}_{\mathrm{T}}$ distribution in each bin of $p_{\mathrm{T}}^{true,V}$ defines a systematic variation as a 2-point systematic uncertainty.

Resolution and response uncertainties

The MC statistical uncertainty are neglected, since the size of simulated MC samples is one order of magnitude larger than the size of data samples. In a given bin of $p_{\mathrm{T}}^{\ell\ell}$, the uncertainties of two parameters of the fitted resolution function $\sigma(u_{\perp})(\sum \bar{E}_{\mathrm{T}})$ stem from limited data statistics. The variations of these two parameters are transformed into 2 up and 2 down uncorrelated variations as the linear combinations of the initial uncertainty variations.

The diagonalization of the statistical uncertainty variations is also done for the two parameters in the fit of $< u_{||}^{data} > (p_{\mathrm{T}}^{\ell\ell})$ in bins of $\sum \bar{E}_{\mathrm{T}}$. The non-linearity of the response is accounted for by an alternative 2nd polynomial fit to $< u_{||}^{data} >$ as a function of $p_{\mathrm{T}}^{\ell\ell}$ in bins of $\sum \bar{E}_{\mathrm{T}}$. The variation with respect to the nominal linear fit is taken to be an additional source of uncertainty correlated over the $\sum \bar{E}_{\mathrm{T}}$ bins.

The extrapolation uncertainties are also considered, accounting for the potential detector response and resolution differences to the hadronic recoil between W and Z events. First, the W samples are reweighted in 2D $(\sum \bar{E}_{\mathrm{T}}, p_{\mathrm{T}}^{V})$ to match the distributions of the Z process. Then, the neutrino of the W is treated to be a charged lepton in the recoil reconstruction, with the cone replacement implemented in the exact way as what is done for an electron or a muon. In the end, the events with truth FSR photons are discarded in both W and Z samples to get rid of the difference between W and Z due to their different patterns of final state photon radiation. After that, $u_{||}$ and $u_{\perp}$ are computed using $\vec{p}_{\mathrm{T}}^{V,true}$, and compared between W and Z process. The extrapolation uncertainties are treated as correlated in the analyses.

References

[1] The ATLAS Collaboration, *Journal of Instrumentation*, vol. 14, no. 12, P12006, Dec. 2019. DOI: 10.1088/1748-0221/14/12/P12006. [Online]. Available: https://dx.doi.org/10.1088/1748-0221/14/12/P12006 (cit. on p. 126).

[2] The ATLAS Collaboration, *The European Physical Journal C*, vol. 79, p. 639, 8 Aug. 2019. DOI: 10.1140/epjc/s10052-019-7140-6. [Online]. Available: https://doi.org/10.1140/epjc/s10052-019-7140-6 (cit. on p. 126).

[3] T. Xu, H. Atmani, and L. Aperio Bella, "Electron corrections for low pile-up runs taken in 2017 and 2018", CERN, Geneva, Tech. Rep., 2019. [Online]. Available: https://cds.cern.ch/record/2657152 (cit. on pp. 127, 128).

[4] "Electron and photon energy calibration with the ATLAS detector using data collected in 2015 at $\sqrt{s} = 13$ TeV", CERN, Geneva, Tech. Rep., 2016. [Online]. Available: https://cds.cern.ch/record/2203514 (cit. on p. 127).

[5] The ATLAS Collaboration, *The European Physical Journal C*, vol. 76, p. 292, 5 May 2016. DOI: 10.1140/epjc/s10052-016-4120-y. [Online]. Available: https://doi.org/10.1140/epjc/s10052-016-4120-y (cit. on pp. 128, 130).

[6] A. Sydorenko, J. A. Kremer, and T. Xu, "Muon corrections for low pile-up runs taken in 2017 and 2018", CERN, Geneva, Tech. Rep., 2019. [Online]. Available: https://cds.cern.ch/record/2657116 (cit. on pp. 128, 131).

[7] N. M. Koehler, J. J. Junggeburth, F. Sforza, *et al.*, "Muon Efficiency Measurements on the Full Run 2 dataset", CERN, Geneva, Tech. Rep., 2019. [Online]. Available: https://cds.cern.ch/record/2665704 (cit. on p. 129).

[8] "Study of alignment-related systematic effects on the ATLAS Inner Detector tracking", CERN, Geneva, Tech. Rep., 2012. [Online]. Available: https://cds.cern.ch/record/1483518 (cit. on p. 130).

[9] *Phys. Rev. D*, vol. 85, p. 012 005, 1 Jan. 2012. DOI: 10.1103/PhysRevD.85.012005. [Online]. Available: https://link.aps.org/doi/10.1103/PhysRevD.85.012005 (cit. on p. 131).

[10] The ATLAS Collaboration, "Measurement of the W-boson mass in pp collisions at $\sqrt{s} = 7$ TeV with the ATLAS detector", *The European Physical Journal C*, vol. 78, p. 110, 2018. DOI: 10.1140/epjc/s10052-017-5475-4 (cit. on p. 131).

[11] The ATLAS Collaboration, "Jet energy scale and resolution measured in proton-proton collisions at $\sqrt{s}$=13 tev with the atlas detector", *The European Physical Journal C*, vol. 77, p. 466, 7 Jul. 2017. DOI: 10.1140/epjc/s10052-017-5031-2. [Online]. Available: https://doi.org/10.1140/epjc/s10052-017-5031-2 (cit. on p. 131).

[12] M. Li, J. Llorente Merino, F. Balli, *et al.*, "Hadronic recoil reconstruction and calibration for low pile-up runs taken in 2017 and 2018", CERN, Geneva, Tech. Rep., 2019. [Online]. Available: https://cds.cern.ch/record/2657182 (cit. on pp. 132, 135).

[13] The ATLAS Collaboration, *The European Physical Journal C*, vol. 77, p. 490, 7 Jul. 2017. DOI: 10.1140/epjc/s10052-017-5004-5. [Online]. Available: https://doi.org/10.1140/epjc/s10052-017-5004-5 (cit. on p. 132).

[14] A. Dimitrievska, N. Vranjes, M. Schott, and M. Boonekamp, "Measurement of m_W at 7 TeV: Hadronic recoil corrections", CERN, Geneva, Tech. Rep., 2015. [Online]. Available: https://cds.cern.ch/record/2013274 (cit. on p. 133).

Chapter 7

Measurement of the W-boson transverse momentum

Contents

7.1 The motivation of the p_{T}^{W} measurement

The measurement of the spectrum of the W-boson transverse momentum (p_{T}^{W}) is mainly driven by the needs for the W-boson mass measurement. The lepton p_{T} spectrum, as one important observable used for the extraction of the W-boson mass, is heavily dependent on the modelling of p_{T}^{W}. A well-controlled modelling of p_{T}^{W} distribution with a precision as good as around 1 % is required in the region of low p_{T}^{W} (below 20-30 GeV) [1]. The cross-section in this low p_{T} region, known as the Sudakov peak, cannot be predicted using only fixed-order perturbative QCD calculation, and has to be handled with either analytical resummation [2] or the description of parton shower [3].

In the previous ATLAS measurement of the W-boson mass [4], the modelling of p_{T}^{W} relies on the experimentally measured the Z-boson transverse momentum spectrum (p_{T}^{Z}) to tune the parton shower [5]. The tuning parameters are passed to the prediction of p_{T}^{W} spectrum, with an uncertainty due to the experimental precision of p_{T}^{Z} measurement. In addition, the parton shower PDF uncertainty also contributes to the uncertainty on the p_{T}^{W} modelling. Other uncertainty sources include the uncertainty in the masses of charm and bottom quarks, of which the impact can be estimated in Pythia 8 [3], as well as the uncertainty from the higher-order QCD corrections. While the variations of masses of charm and bottom quarks turn out to have a relatively small impact on the W-boson mass measurement, the uncertainty from the higher-order QCD corrections is much larger and has to be assessed carefully. The missing higher-order QCD corrections to the parton shower are estimated by the variations of the factorization scale (μ_F) for QCD ISR. Although these corrections are mostly correlated between the W and Z-boson productions initiated by light quarks (u, d and s), therefore cancelled out in the ratio of $p_{\mathrm{T}}^{W}/p_{\mathrm{T}}^{Z}$, there is a certain level of decorrelation due to the different fractions of heavy quarks involved in the production. In general, the QCD scales variations have been considered to be an unreliable way to estimate the missing higher-order QCD uncertainty, as they only provide an approximate size of the missing higher-order effect without an insured coverage. On top of that, these variations offer no indication about how the uncertainties are correlated across a distribution.

To overcome the difficulty brought by the extrapolation of p_{T}^{Z} to the p_{T}^{W} modelling, it is worth measuring the p_{T}^{W} spectrum directly from the data, so that the estimation of uncertainty using QCD scale variations will be avoided. In the low-mu data taking conditions, the improved recoil resolution is expected to bring a <2 % uncertainty in

p_{T}^{W} with a granularity of around 6 GeV in the Sudakov peak, which will greatly reduce the modelling uncertainty in m_W.

7.2 Methodology

The measurement of the p_{T}^{W} spectrum corresponds to a measurement of the differential Drell-Yan cross-section with a direct decay of the W-boson: $W \to \ell\nu$, where $\ell = e$ or μ. The measurement in the e and μ channels as well as in the combination are reported in a common fiducial region close to the definition of the event selection in Table 5.1, such that the extrapolation stays minimal:

— $W \to \ell\nu$: p_{T}^{ℓ} >25 GeV, $|\eta^{\ell}| < 2.5$, p_{T}^{ν} >25 GeV and m_{T} >50 GeV.

The lepton kinematics in this definition of this cross-section measurement is taken from the state before QED FSR (a.k.a at Born-level).

Due to the neutrino in the decay product of the leptonic decay of the W-boson, the kinematics of the boson cannot be fully reconstructed in the transverse plane using the decay product. Therefore, the p_{T}^{W} has to be inferred from the hadronic recoil u_{T}, which originates from the QCD ISR that gives the none-zero transverse momentum distribution to the boson.

The detector effects bias and smear the measurement of p_{T}^{W} via the hadronic recoil. In order to extract the true underlying p_{T}^{W} spectrum from the response of the detector, all the detector effects, such as the limited detector acceptance, the efficiency of the object reconstruction and the finite detector resolution, are accounted for by an unfolding procedure. For events passing both fiducial volume selection and reconstructed-level selection ($T\&R$), the migration from p_{T}^{W} at truth-level to u_{T} at reco-level, normalized to unity in each truth bin j, is described by the migration matrix in the simulation:

$$M_{ij} = \frac{N_{ij}}{\sum_k N_{kj}} \tag{7.1}$$

N_{ij} is the number of events in u_{T} bin i and p_{T}^{W} bin j. Weights at truth level and reconstructed level are kept separately for these events. The baseline binnings of the u_{T} and of the p_{T}^{W} spectrum after the optimization (Section 7.4) are chosen to be:

— u_{T}: 1 GeV bin size up to u_{T}=100 GeV, 5 GeV bin size for u_{T} ∈[100,200] GeV, 10 GeV bin size for u_{T} ∈[200,600] GeV.

— p_{T} at 5.02 TeV: [0, 7, 14, 21, 28, 35, 42, 49, 56, 63, 77, 92, 115, 145, 175, 220] GeV.

— p_{T} at 13 TeV: [0, 7, 14, 21, 28, 35, 42, 49, 56, 63, 77, 92, 115, 145, 175, 220, 310, 600] GeV.

Examples of migration matrices are shown in Figure 7.1. The non-diagonal feature of the migration is attributed to the large detector resolution in u_{T} as well as the detector response of $\langle u_{\mathrm{T}}/p_{\mathrm{T}}^{W} \rangle$ is below one and dependent on p_{T}^{W}, which can be understood as the recoil measurement suffers from the signal loss due to noise cuts, particles traversing beyong the detector acceptance as well as the non-compensating nature of the calorimeter. The conditional probability to observe a reconstructed value of u_{T} in bin i and a given truth value of p_{T}^{W} in bin j is defined by correcting for the efficiency in the migration matrix M_{ij}, which yields the response matrix R_{ij}:

$$R_{ij} = M_{ij}\epsilon_j \tag{7.2}$$

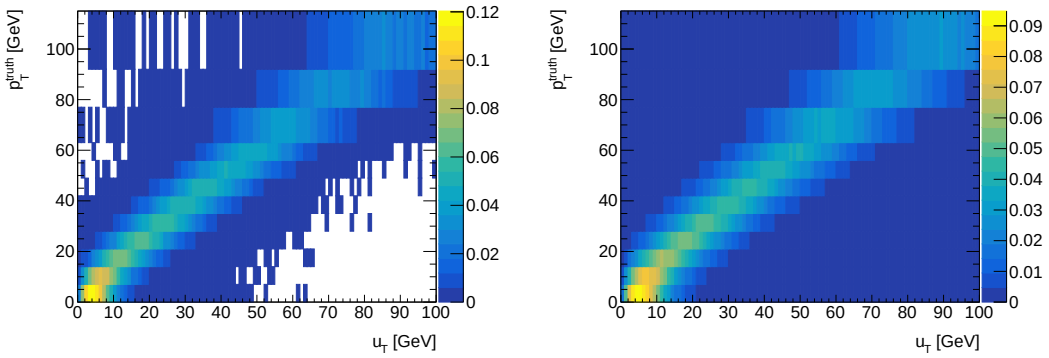

(a) (b)

Figure 7.1 – Examples of migration matrices for $W^- \to e\nu$ at (a) 5.02 TeV and at (b) 13 TeV.

And the efficiency of reconstructing a truth level signal, in bin j of p_{T}^W is:

$$\epsilon_j = \frac{N_j^{reco\&gen}}{N_j^{gen}} = \frac{\sum_i N_{ij}}{N_j^{gen}} \tag{7.3}$$

Here $N_j^{reco\&gen}$ refers to the number of events in a p_{T}^W bin j passing $T\&R$ selection cuts, and N_j^{gen} the number of events in the corresponding bin passing only the fiducial volume selection.

Starting from the underlying true distribution T after the fiducial cuts, the detector level distribution D in bins of u_{T} can be expressed in:

$$D_i = \sum_j R_{ij} T_j + B_i \tag{7.4}$$

The term B_i accounts for the presence of background after the reconstructed level cuts. Considering the fact that events beyond the fiducial volume can be reconstructed, an additional correction of purity has to be applied to the reconstructed level distribution in the unfolding by:

$$p_i = \frac{N_i^{reco\&gen}}{N_i^{reco}} = \frac{\sum_j N_{ij}}{N_i^{reco}} \tag{7.5}$$

The numerator of the purity correction in this formula covers the entire fiducial volume. The level of efficiency and purity corrections are shown in Figures 7.2.

Including the effect of purity correction, the best estimate of the underlying true p_{T}^W distribution determined by the unfolding procedure is given by:

$$\tilde{U}_j = \sum_i U_{ij}(D_i - B_i)p_i \tag{7.6}$$

where the unfolded spectrum estimating the underlying distribution T is presented by $\tilde{U}_j$. The unfolding transformation is symbolized by U_{ij}. Technically, the unfolding matrix U_{ij} in the analysis is determined by the iterative Bayesian regularized unfolding approach with the implementation of the D'Agostini iterative scheme [6][7]. For a given resolution of the unfolded spectrum, the number of unfolding iterations has to be chosen for the solution to minimize the total uncertainty as well as the possible bias. The optimization of the unfolding will be discussed in Section 7.4.

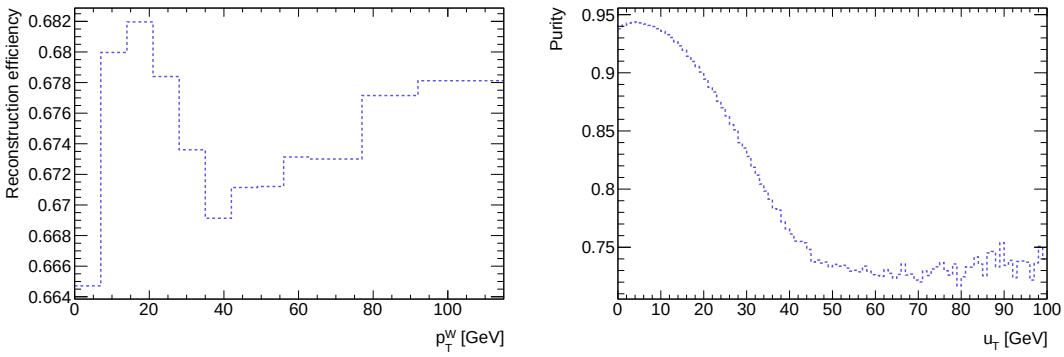

(a) (b)

Figure 7.2 – Example of (a) efficiency correction and (b) purity correction in 13 TeV $W^- \to e\nu$ channel.

Based on Equation 7.6, the uncertainties sources are divided to four types and propagated to the unfolded level following the corresponding procedure:

— Data statistics. The data distribution D_i is fluctuated at reconstructed level by bootstrap. The spread of toys after unfolding is taken to be the data statistical uncertainty at unfolded level.

— MC statistics. The unfolding transformation U_{ij} is varied by fluctuating the migration matrix, the efficiency correction and the purity correction via bootstrap. The spread of toys is considered to be the MC statistical uncertainty at unfolded level.

— Experimental systematics. The effect of the systematic variation is applied to the unfolding transformation U_{ij}, including migration matrix, efficiency correction and purity correction. After that, the change in the unfolded spectrum is taken to be the experimental systematic of the given source.

— Background uncertainty. The background estimation B_i at reconstructed level is varied according to the relevant systematics. The change in the unfolded spectrum is then the background systematic of source under study.

On the technical side, the boostrap method [8] is implemented by assigning a random weight to each event for each (pseudo) data set, defined as follows:

$$w = \mathcal{P}(n, 1) \tag{7.7}$$

where n is an integer randomly generated according to the Poisson distribution of unit mean, and $w = \mathcal{P}(n, 1)$ is the value of the Poisson probability to observe n events with an expectation of 1. The covariance matrices of data statistics and MC statistics are therefore the standard deviation of the N_{bs} bootstrap toys:

$$C_{kl}^{stat} = \frac{1}{N_{bs} - 1} \sum_{\alpha=1}^{N_{bs}} (\tilde{U}_k^\alpha - \langle \tilde{U} \rangle_k)(\tilde{U}_l^\alpha - \langle \tilde{U} \rangle_l) \tag{7.8}$$

with k and l looping all the bins. The systematic uncertainty is fully correlated across all the bins in the unfolded spectrum. Therefore, the elements of the covariance matrix for a given source of systematic a are:

$$C_{kl}^a = \delta\tilde{U}_k^a \delta\tilde{U}_l^a = (\tilde{U}_k^a - \tilde{U}_{Nom}^a)(\tilde{U}_l^a - \tilde{U}_{Nom}^a) \tag{7.9}$$

Then, the total covariance matrix for a given channel is expressed as a sum of all the uncertainty components:

$$C_{kl}^{tot} = C_{kl}^{stat,Data} + C_{kl}^{stat,MC} + \sum_{a} C_{kl}^{a} \tag{7.10}$$

with a running over all source of systematic uncertainties.

One major caveat of the unfolding procedure is that the hypothetical underlying distribution of a given physics variable in the simulation is not guaranteed to exactly match its true value, therefore causing a bias in the simulation of the migration matrix, as well as the efficiency and the purity corrections. While using the regularized iterative unfolding, this prior hypothesis bias introduces an uncertainty on the unfolded result. In ATLAS, it is recommended to estimate this source of uncertainty by following a procedure of data-driven closure test, of which the guiding principle is:

— The MC events passing $T\&R$ selections are reweighted at truth level to achieve the optimal agreement in shape at reconstructed level between data and MC for the physics observable under study. It has been checked that whether or not applying the reweighting to those events passing truth level selection but failing reconstruction selection doesn't change the result.

— For events passing $T\&R$ selections, the reconstructed-level MC distribution after the above truth level reweighting is unfolded as pseudo data using the migration matrix from the initial unreweighted MC.

— The unfolding bias is estimated by comparing the unfolded result with the reweighted truth distribution for events passing $T\&R$ selections.

Conventionally, the reweighting of the truth-level distribution is taken from the data-to-MC ratio at reconstructed level. But in the p_{T}^{W} measurement, due to the fact that the possible discrepancy (between the modelling of p_{T}^{W} and true physics) at truth-level may be smeared out at reconstructed level due to the large resolution, and that the proportionality between u_{T} and p_{T}^{W} is a function dependent on p_{T}^{W}, the reweighting has to use parameterized functions in p_{T}^{W} determined from a data-driven method described in Section 7.3, otherwise a simple reweighting of the data-to-MC ratio at reconstructed level will lead to large unfolding bias.

In parallel to the p_{T}^{W} measurement, the p_{T}^{Z} is carried using the same low pile-up datasets to validate the analysis strategy of unfolding the hadronic recoil to obtain the boson-p_{T} spectrum, since the p_{T}^{Z} can be measured by unfolding the u_{T} or by unfolding the $p_{\mathrm{T}}^{\ell\ell}$ distribution. The latter offers a precision of about one order of magnitude better than the former. In the end, it is shown that the results of p_{T}^{Z} measurements based on u_{T} and based on $p_{\mathrm{T}}^{\ell\ell}$ are compatible with each other, which validates method of unfolding the u_{T} distribution for the p_{T}^{W} measurement. The fiducial cross-section of Z production, along with the cross-section ratios, will be reported in Section 7.5.2.

7.3 p_{T}^{W} reweighting and bias uncertainties

The mis-modelling of p_{T}^{W} in the simulation brings large discrepancy of transverse momentum distribution at detector level between data and MC. It has been observed that the unfolding starting from this non-optimal initial distribution leads to a percent level unfolding bias as a source of uncertainty at unfolded level.

The analysis results can be optimized by reweighting the MC simulation according to a function of p_{T}^{W}, such that the best possible data to MC agreement on the

reconstructed u_{T} distribution is achieved, ensuring an unbiased unfolding result. This correction procedure is referred to as the p_{T} correction, of which the relevant uncertainties are derived from the possible variations of this correction. The form of p_{T} correction is derived from the following χ^2 minimization:

$$\begin{aligned} \chi^2 &= \sum_{ij} \Delta_i^T C_{ij}^{-1} \Delta_j \\ \Delta_i &= (D_i - B_i) - \sum_{ij} R_{ij} \times (w_{\mathrm{T}}(p_{\mathrm{T}}^W))_j \end{aligned} \tag{7.11}$$

Here Δ is the difference between the background subtracted data $(D_i - B_i)$ and the reconstruction level response (R_{ij}) of the simulation after the particle level reweighting $w(p_{\mathrm{T}}^W)$. The χ^2 is computed using the total covariance matrix at reconstructed level (C_{ij}). It was found that a satisfactory data-to-MC agreement can be realized by choosing the following form for the baseline reweighting function:

$$w_{\mathrm{T}}(p_{\mathrm{T}}^W) = N[(1 + a p_{\mathrm{T}}^W + b(p_{\mathrm{T}}^W)^2) \cdot (1 - c + c \cdot r_{NNPDF/CT10}(p_{\mathrm{T}}^W))] \tag{7.12}$$

The ratio $r_{NNPDF/CT10}(p_{\mathrm{T}}^W)$ is calculated by DYTURBO. It represents the correction in the full phase space, from the default PDF set (CT10 [9]) used in the Powheg [10]–[13] samples to a more modern PDF set: NNPDF3.0 [14]. The additional terms in the function adds more flexibility to the fit. The form of the baseline reweighting function is optimized separately for each centre-of-mass energy and for each charge of the boson. The correction is only derived over $0 < p_{\mathrm{T}}^W < 100\,\mathrm{GeV}$. The value of the correction is frozen at 100 GeV for any larger p_{T}^W. The average of correction functions in the e and μ channels are used because of the good compatibility between them.

The bias uncertainty related to this data driven p_{T} correction comprises three parts:

— Fit uncertainty: The uncertainty in the fit parameters.
— Parameterization uncertainty: The arbitrariness in the form of the reweighting function.
— Initial (p_{T}^W, y) distribution uncertainty: The potential mis-modelling in the correlation between boson p_{T} and rapidity.

The fit uncertainty is derived by repeating the fit of the p_{T}-correction, but using p_{T}-corrected migration matrix, as well as the efficiency and purity corrections in the MC. The new correction factor of p_{T}-reweighting given by the fit is compatible with 1, showing a small non-closure within the uncertainty due to the effect of averaging the p_{T} reweighting between the electron and muon channels. After the fit, based on the covariance matrix, the function parameters are transformed to be orthogonal and are parameterized by the corresponding nuisance parameters. Given that there are three parameters in the baseline fit of Equation 7.12, three variations of the fit uncertainty are produced following this prescription.

The parameterization uncertainty is determined by repeating the reweighting procedure of Equation 7.11, but replacing the baseline $w_{\mathrm{T}}(p_{\mathrm{T}}^W)$ with other functions:

$$Expo. \times Pol. : w_{\mathrm{T}}(p_{\mathrm{T}}^W) = N[(1 + a\,p_{\mathrm{T}}^W + b\,p_{\mathrm{T}}^{W\,2})(1 - c + \frac{c}{\tau} e^{-p_{\mathrm{T}}^W \cdot \tau})] \tag{7.13}$$

$$2nd - Order\ Pol. : w_{\mathrm{T}}(p_{\mathrm{T}}^W) = N[1 + a\,p_{\mathrm{T}}^W + b\,p_{\mathrm{T}}^{W\,2}] \tag{7.14}$$

$$Gaus. + Pol. : w_{\mathrm{T}}(p_{\mathrm{T}}^{W}) = N[(1 + a\,p_{\mathrm{T}}^{W} + b\,p_{\mathrm{T}}^{W)} + c\,G(p_{\mathrm{T}}^{W};\mu,d)] \quad (7.15)$$

$$Gaus. \times Pol. : w_{\mathrm{T}}(p_{\mathrm{T}}^{W}) = N[(1 + a\,p_{\mathrm{T}}^{W} + b\,p_{\mathrm{T}}^{W\,2})(1 - c + c\,G(p_{\mathrm{T}}^{W};\mu,\sigma))] \quad (7.16)$$

$$2\,Gaus + Pol. : w_{\mathrm{T}}(p_{\mathrm{T}}^{W}) = N[1 + a\,p_{\mathrm{T}}^{W} + b\,p_{\mathrm{T}}^{W\,2} + c\,G(p_{\mathrm{T}}^{W};\mu,d) + e\,G(p_{\mathrm{T}}^{W};\mu,f)] \quad (7.17)$$

Only the functions that bring a reasonable data-to-MC compatibility of u_{T} at reconstructed-level are chosen to be the variations for the parameterization uncertainty. After rejecting the functions leading to large χ^2 values of data-to-MC, Equation 7.13 is chosen to be the alternative function form at 13 TeV, while Equations 7.14 and 7.15 are taken to be the variations at 5.02 TeV, for W^+ and W^- respectively.

The uncertainty arising from the initial (p_{T}^{W}, y) distribution in the simulation is assessed by once again performing the reweighting procedure of p_{T}-correction, but starting from one of the following predictions of (p_{T}^{W}, y) in the simulation: DYTURBO [15][16] using CT10 PDF, DYTURBO using NNPDF3.0 PDF, Herwig7 [17] and Pythia [3]. The nominal MC is reweighted in 2D to the possible alternative prediction of (p_{T}^{W}, y). For each alternative prediction of (p_{T}^{W}, y), the form of reweighting function is chosen to be the one from 7.12 to 7.17 that gives the best description of data for u_{T} at reconstructed level. In the end, DYTurboCT10 is chosen to be the proxy of initial (p_{T}^{W}, y) uncertainty variation at 13 TeV while DYTurboNNPDF3.0 is chosen for all 5.02 TeV channels. These two choices give a reasonable data-MC agreement at reconstructed level and are the most conservative variations in the corresponding center-of-mass energy.

7.4 Optimization of Iterative Bayesian Unfolding

The guideline of measuring the p_{T}^{W} spectrum is to minimize the total uncertainty while reaching a fine resolution after unfolding. In particular, a low contribution from the unfolding bias uncertainty (approximately at 1 % level) will always be favoured, as a precise estimation of the bias uncertainty is extremely challenging in the context of this analysis. In order to achieve this goal, the two major parameters for the refinement of the Iterative Bayesian Unfolding, namely the bin width at truth level and the number of unfolding iterations, are optimized simultaneously in a dedicated study.

In each of the eight decay channels, the uncertainty on the unfolded spectrum is studied in bin widths of 5, 6, 7, 8 and 9 GeV in the low p_{T}^{W} region and with 1, 3, 5, 7, ..., 29 iterations of unfolding. In total the 75 versions of unfolding in a 2D mapping of bin width and number of iterations enable an optimization of both quantities. The optimization accounts for statistical uncertainty, experimental and background uncertainties, as well as bias uncertainties. Considering that the scheme of the optimization should be consistent with the combination of electron and muon channels and that the statistics is roughly the same in the two channels for a given charge at the same center-of-mass energy, the statistical uncertainties are always divided by a factor of $\sqrt{2}$, even though the study is performed per individual channel. Meanwhile, the experimental systematics, background uncertainties and bias uncertainties are considered correlated between the electron and the muon channels, since the dominating components among them are the recoil calibration uncertainty and the bias uncertainty that are correlated between the two channels. The total uncertainty in each channel is the quadratic sum of the above components.

The total uncertainties in various options of bin width and with different number of iterations are presented in Figures 7.3 and 7.4, where a linear interpolation between the centers of the two nearest bins is performed at a given value of p_{T}^{W}, so as to facilitate the comparison between the choices of bin width. It turns out that both the 5.02 TeV bin width and the 6 GeV bin width lead to a significantly larger uncertainty at both center-of-mass energies, mainly due to the large unfolding bias uncertainty. A wider binning tends to help reduce the total uncertainty in the p_{T}^{W} region thanks to not only the lower statistical uncertainty in each bin, but also a smaller bias uncertainty. Consequently, a bin width of 7 GeV is chosen for both 5 and 13 TeV, as a trade-off between the total uncertainty and the resolution. In this way, the 7 GeV bin width keeps a sufficiently low total uncertainty while preserving a reasonable resolution of the unfolded spectrum.

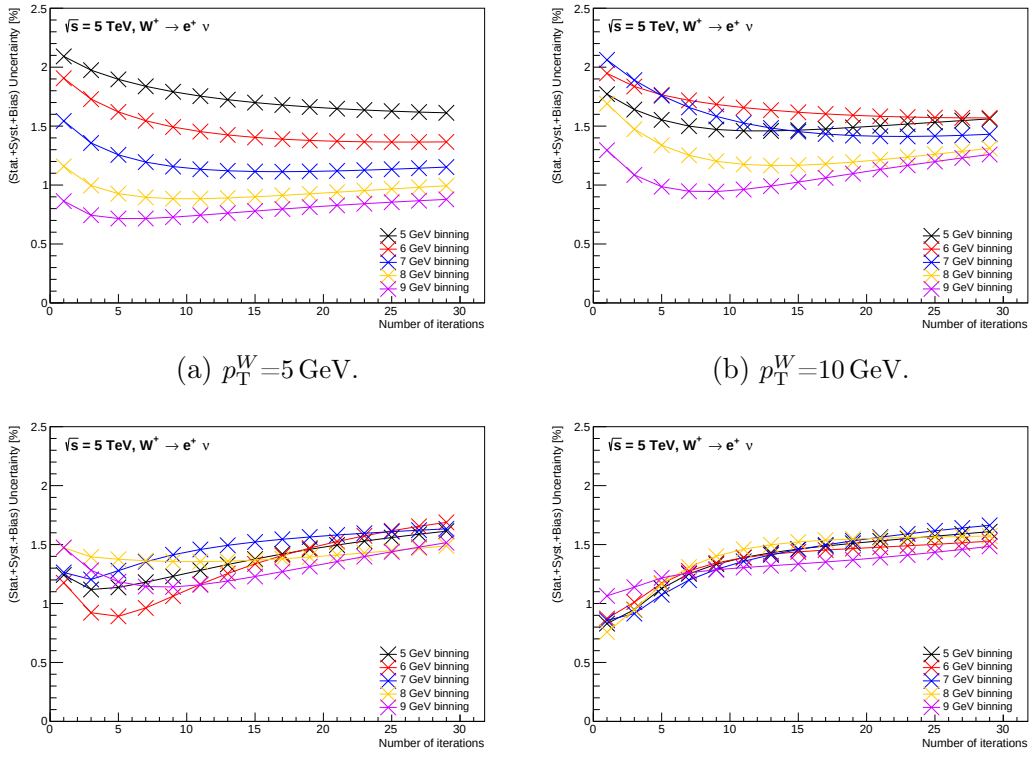

(a) p_{T}^{W}=5 GeV. (b) p_{T}^{W}=10 GeV.

(c) p_{T}^{W}=15 GeV. (d) p_{T}^{W}=20 GeV.

Figure 7.3 – Total uncertainty in various bin widths over different iterations for 5.02 TeV $W^{+} \to e\nu$ channel. The total uncertainty is interpolated to p_{T}^{W}=5, 10, 15, 20 GeV.

Once the bin width is chosen, the optimization is focused on the number of iterations, which is investigated separately for 5.02 and 13 TeV, as shown in Figures 7.5 and 7.6. The general tendency is that the increased number of iterations reduces the bias uncertainty but comes with a price of inflated both statistical and the other systematic uncertainties. The main guideline of choosing the number of iterations for a given bin width is to keep the bias uncertainty as low as possible in the p_{T}^{W} <10 GeV region, since the bias uncertainty is the least well understood uncertainty source in this region. If possible, the total uncertainty needs to be kept low as well, in addition to the low bias uncertainty. While reaching the best uncertainty in the region

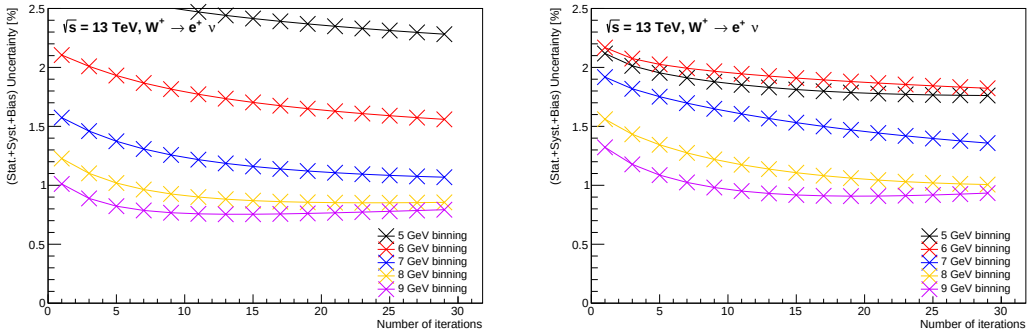

(a) p_{T}^{W}=5 GeV. (b) p_{T}^{W}=10 GeV.

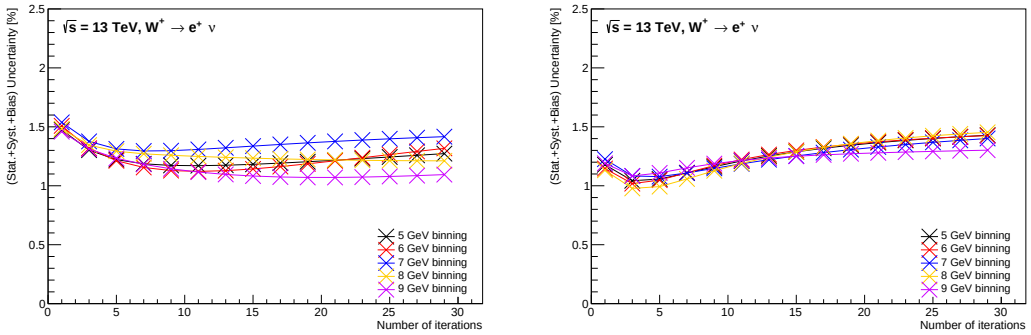

(c) p_{T}^{W}=15 GeV. (d) p_{T}^{W}=20 GeV.

Figure 7.4 – Total uncertainty in various bin widths over different iterations for 13 TeV $W^+ \to e\nu$ channel. The total uncertainty is interpolated to p_{T}^{W}=5, 10, 15, 20 GeV.

p_{T}^{W} <10 GeV, it is also necessary not to worsen the result at higher p_{T}^{W} unreasonably. Following all these criteria, at 13 TeV, a large number of iterations is preferred in the end, so as to keep the bias uncertainty better under control, especially in the p_{T}^{W} <10 GeV region. In this low p_{T} region, the other uncertainty components only increase very slowly after 20 iterations. For the 5.02 TeV channels, the effective drop of the bias uncertainties along with the relative slow increase of the statistical and the other systematic uncertainties brings a plateau of total uncertainty in the low p_{T}^{W} region, starting from around 9 iterations, even though the total uncertainty always increases with the number of iterations at above 15 GeV. The final decision of the unfolding optimization is to use a bin width of 7 GeV in the low p_{T}^{W} region for both center-of-mass energies, with 25 iterations of unfolding for 13 TeV and 9 iterations for 5.02 TeV.

7.5 Results

7.5.1 Unfolded data spectra and uncertainty break-down

The unfolded absolute different cross-sections are compared to the prediction of the Powheg+Pythia 8 samples with p_{T}^{W} reweighting correction in Figures 7.7 and 7.8. The ratios of the unfolded normalized differential cross-sections in different predictions to the unfolded data are shown in Figures 7.9 and 7.10. Putting aside the luminosity

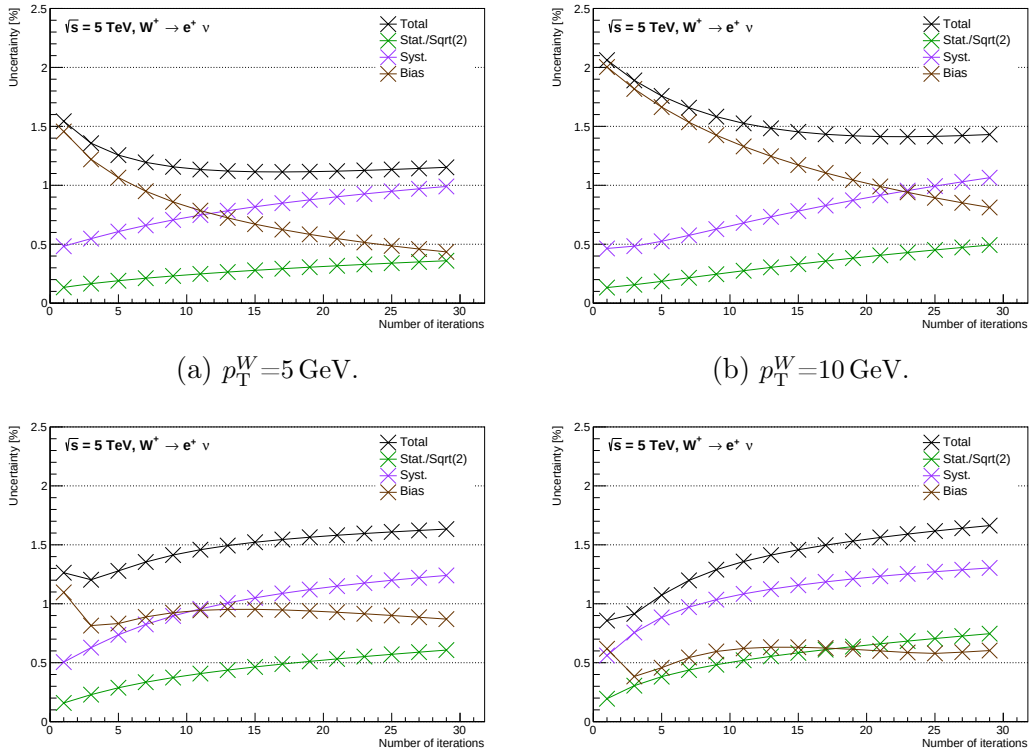

(a) p_{T}^{W}=5 GeV. (b) p_{T}^{W}=10 GeV.

(c) p_{T}^{W}=15 GeV. (d) p_{T}^{W}=20 GeV.

Figure 7.5 – Total uncertainty in various binnings over different iterations for 5.02 TeV $W^{+} \to e\nu$ channel. The total uncertainty is interpolated to p_{T}^{W}=5, 10, 15, 20 GeV.

uncertainty, the experimental uncertainties vary from about 2 % in the low p_{T}^{W} region to about 5 % (4 %) when p_{T}^{W} =100 GeV at 5.02 TeV (13 TeV). On top of that, the luminosity contributes to 1 % at 5.02 TeV and 0.92 % at 13 TeV. The predictions for comparison include Powheg+Pythia 8 AZNLO [5] without p_{T}^{W} correction, Pythia 8 AZ, Sherpa and DYRes [18][19]. For both center-of-mass energies, both lepton flavors and both W boson charges, a similar level of agreement with data is found for Powheg+Pythia8 AZNLO and Pythia 8 AZ. Sherpa predicts a softer spectrum while DYRes predicts a harder one.

The breakdown of the uncertainty at the reconstructed level is shown in Figures 7.11, 7.12 for the region 0< p_{T}^{W} <100 GeV. The absolute uncertainties at the unfolded level are shown in Figures 7.13, 7.14. The corresponding shape uncertainties at unfolded level are presented in Figures 7.15, 7.16, in which the central value and the uncertainty variations of the p_{T}^{W} distributions are normalized to unity when the uncertainty are calculated. The region of interest for p_{T}^{W} shown in the uncertainty breakdown plots at unfolded level is restricted to 0< p_{T}^{W} <63 GeV, although the measurement of the p_{T}^{W} spectra higher than 63 GeV is also performed in the analysis.

At the unfolded level, the total experimental uncertainty starts from 1 % at the lowest p_{T} bin and remains below around 2 % up to p_{T}=40 GeV in general. For p_{T} >40 GeV the uncertainty grows moderately at 13 TeV and increases steeply at 5.02 TeV. The data statistics, recoil calibration systematics, the signal generator systematic and bias uncertainties are the largest uncertainty components. The three first p_{T} bins receive

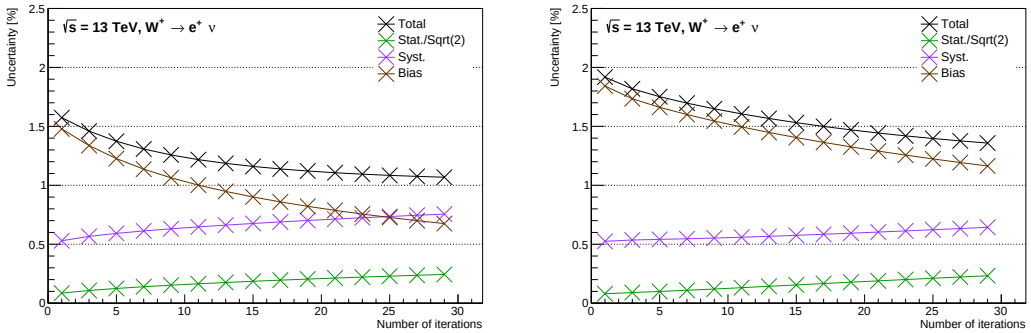

(a) p_{T}^{W}=5 GeV. (b) p_{T}^{W}=10 GeV.

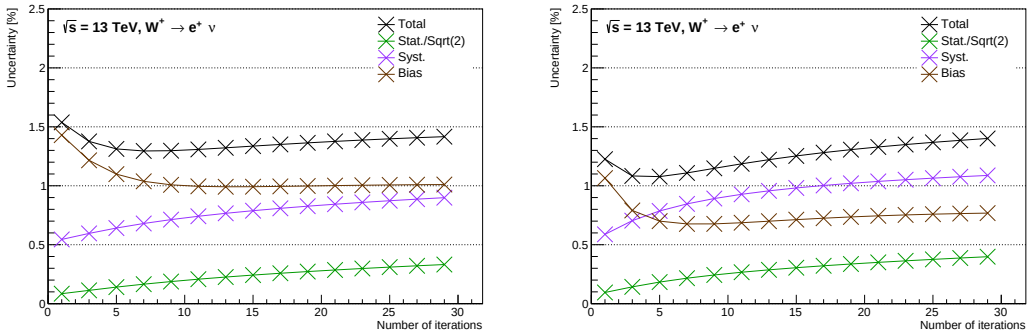

(c) p_{T}^{W}=15 GeV. (d) p_{T}^{W}=20 GeV.

Figure 7.6 – Total uncertainty in various binnings over different iterations for 13 TeV $W^+ \to e\nu$ channel. The total uncertainty is interpolated to p_{T}^{W}=5, 10, 15, 20 GeV.

a very important impact from the bias uncertainties. All the other remaining uncertainties are small in comparison, except for the background uncertainties at 13 TeV because of the larger multijet and $t\bar{t}$ contamination.

7.5.2 Channel combination

The combination of electron and muon channel cross-sections follows the standard prescription of the Best Linear Unbiased Estimator method (BLUE) [20][21] using the following χ^2 minimization:

$$\chi^2 = (X - \bar{X})^T C^{-1} (X - \bar{X}) \tag{7.18}$$

where X is the joint 2N-bin distribution in the electron and muon channels $X = \{X_1^e, ..., X_n^e; X_1^\mu, ..., X_n^\mu\}$ and $\bar{X} = \{\bar{X}_1, ..., \bar{X}_n; \bar{X}_1, ..., \bar{X}_n\}$ the vector of the average to be determined. The covariance matrix is of the size $2N \times 2N$:

$$C = \begin{pmatrix} C^e & C^{e\mu} \\ C^{e\mu} & C^\mu \end{pmatrix} \tag{7.19}$$

In this notation, the $N \times N$ matrices C^e and C^μ are the total covariance matrices derived in the electron and the muon channels according to Equation 7.10. And $C^{e\mu}$ reflects the sources of systematic uncertainty correlated between the two channels. The analytical solution to the minimization of the χ^2 is given by:

$$\bar{X} = (H^T C^{-1} H)^{-1} H^T C^{-1} X \tag{7.20}$$

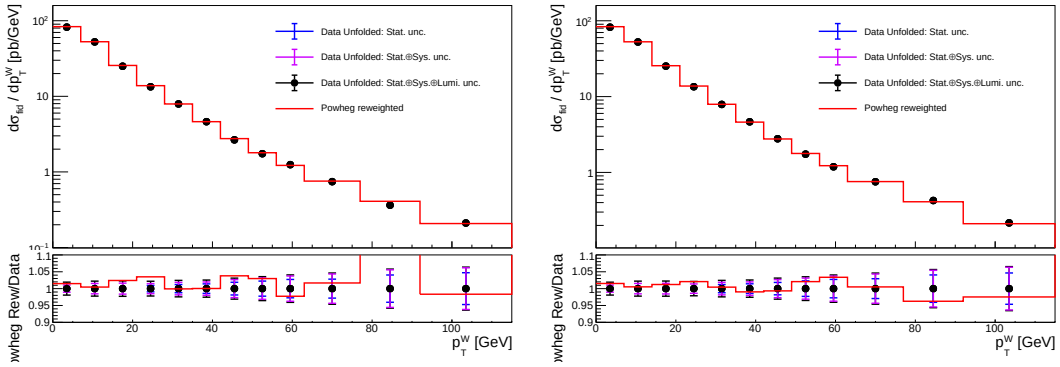

(a) $W^- \to e\nu$ (b) $W^- \to \mu\nu$

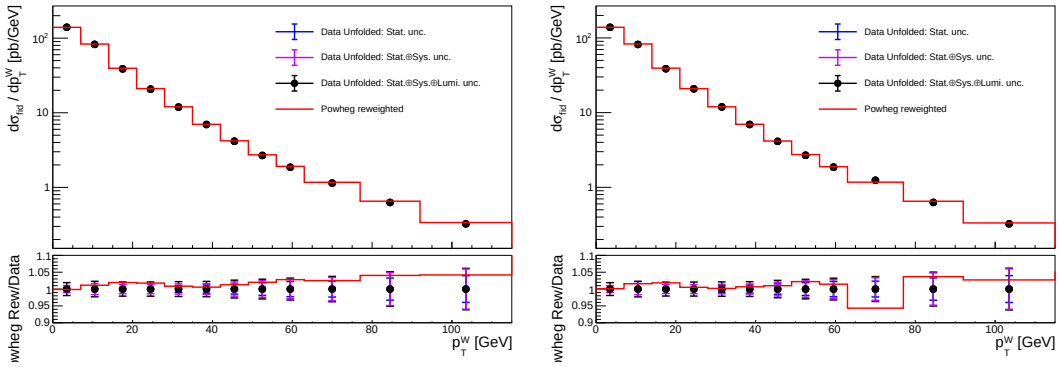

(c) $W^+ \to e\nu$ (d) $W^+ \to \mu\nu$

Figure 7.7 – Unfolded measurement results at $\sqrt{s}$=5.02 TeV compared with the nominal p_{T}-reweighted Powheg+Pythia 8 MC prediction. The bottom panel shows the prediction-to-data ratio.

with the $2N \times N$ matrix indicating the structure of the linear system:

$$H = \begin{pmatrix} 1 & & 0 \\ & \ddots & \\ 0 & & 1 \\ 1 & & 0 \\ & \ddots & \\ 0 & & 1 \end{pmatrix} \tag{7.21}$$

where the 2N lines correspond to the measured electron and muon spectra and the N columns correspond to the combined spectrum. In the end, the total covariance of the combination is solved by:

$$\bar{C} = H^T C^{-1} H^{-1} \tag{7.22}$$

This combination procedure is valid in the Gaussian limit and under the assumption that the uncertainties are constant in the covariance matrix, not depending on the value of the measured quantity. When it comes to luminosity or efficiency uncertainties that are the fixed fractions of the measured cross-section, a given relative source of uncertainty has a smaller impact for lower measured values, biasing the combination towards the lowest measured cross-section. A remedy of this issue would be to iterate the combination while rescaling the elements of the covariance matrix according to the

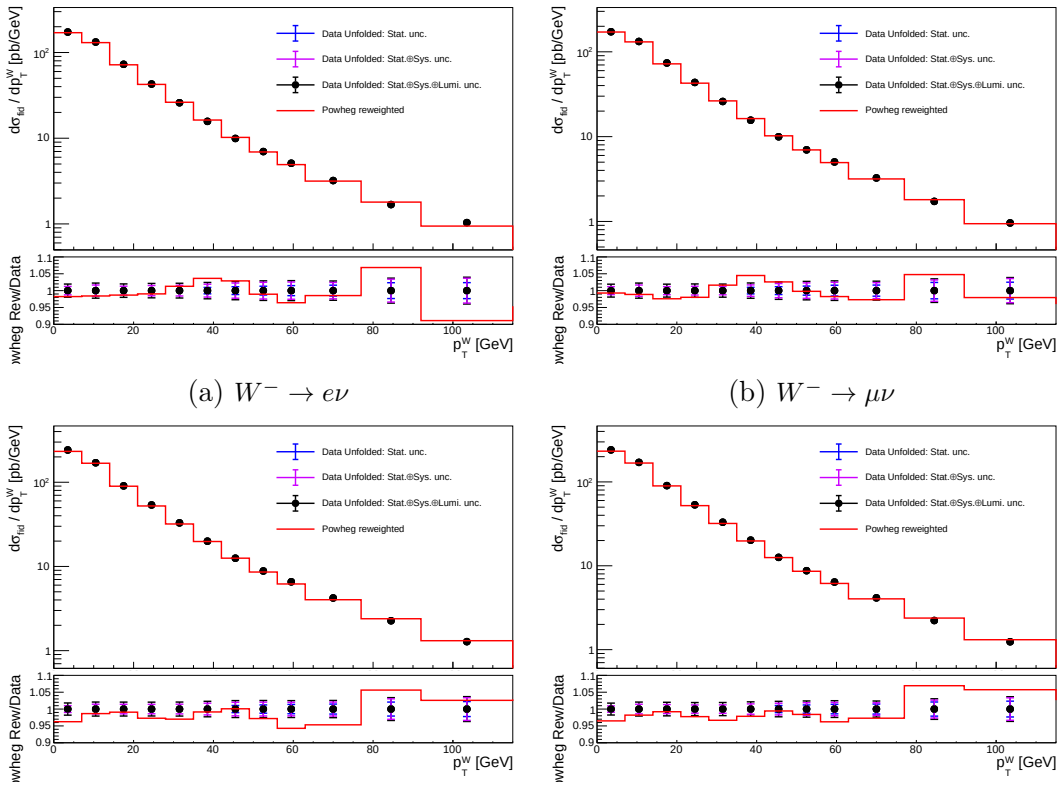

(a) $W^- \to e\nu$ (b) $W^- \to \mu\nu$

(c) $W^+ \to e\nu$ (d) $W^+ \to \mu\nu$

Figure 7.8 – Unfolded measurement results at $\sqrt{s}$=13 TeV compared with the nominal p_{T}-reweighted Powheg+Pythia 8 MC prediction. The bottom panel shows the prediction-to-data ratio.

combined uncertainties of the previous iteration [22]. In the p_{T}^W analysis, 4 iterations of combination are carried out, achieving stable results in the end.

The number of systematic sources involved in the combination is summarized in Table 7.1. In addition to the cross-section uncertainties of simulated background mentioned in Section 5.1, the experimental uncertainties considered in the p_{T}^W analysis have been described in Sections 6.1, 6.2 and 6.3. The multijet statistical uncertainties are also propagated to the unfolded level only in the region u_{T} >100 GeV, by fluctuating each bin separately according to its statistical uncertainty. The uncertainty variations are considered to be uncorrelated between channels. The multijet statistical uncertainties are accounted for in this way mainly because of their non-negligible contribution appearing only in the high p_{T} region. The multijet yield and shape uncertainties derived in Section 5.4 are, however, taken to be correlated across all the channels due to its methodological nature. The unfolding bias uncertainties represent the freedom in the underlying p_{T}^W distribution assumed in the MC for the simulation of the migration matrices as well as the selection efficiencies. All the 5 sources of unfolding bias uncertainty, including the 3 NPs of the fit uncertainty, the parameterization uncertainty and the initial (p_{T}, y) distribution uncertainty, are considered to be correlated between the electron and the muon channels for a given boson charge and at a given center-of-mass energy. The signal generator systematic uncertainty, taken as the difference in the result when Sherpa is used instead of the nominal Powheg, reflects the possible impact of alternative perturbative and non-perturbative

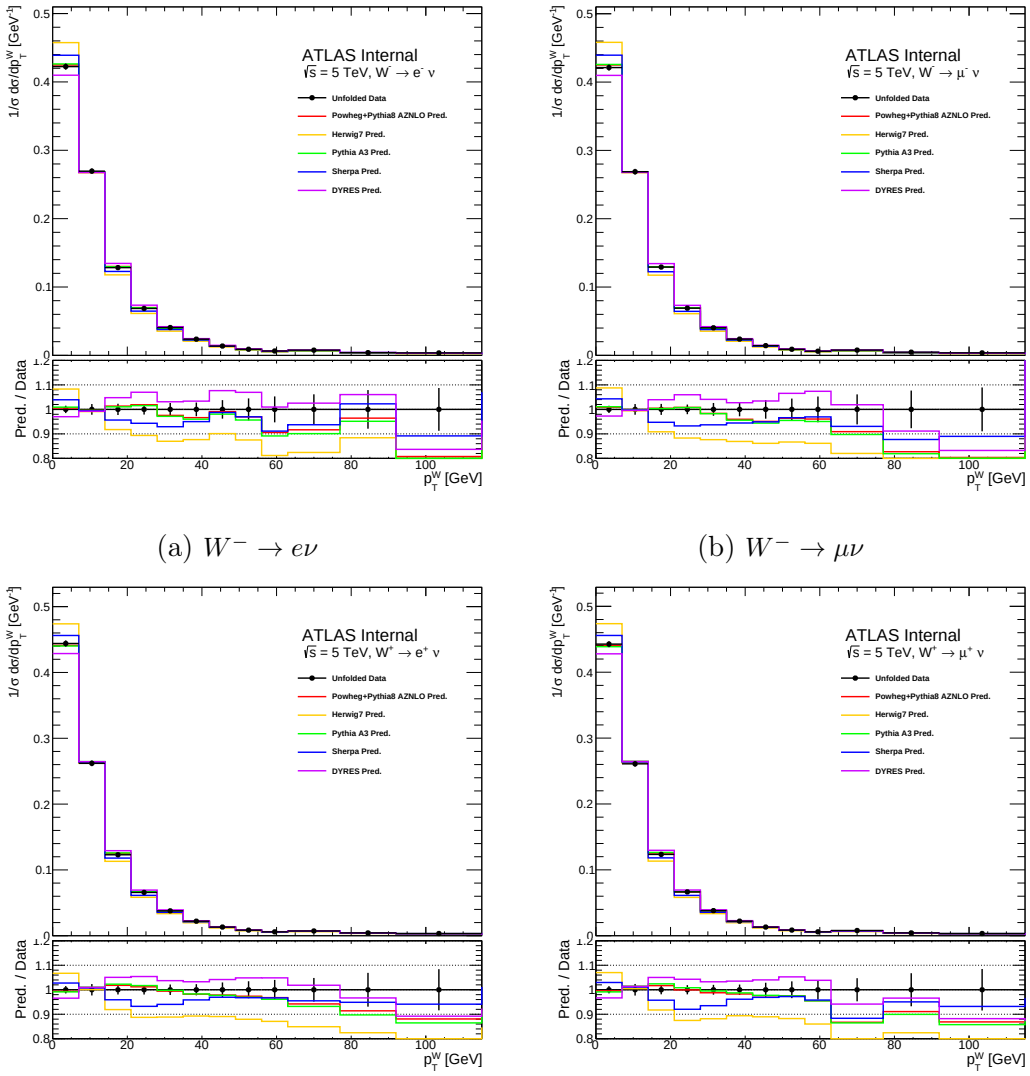

(a) $W^- \to e\nu$ (b) $W^- \to \mu\nu$

(c) $W^+ \to e\nu$ (d) $W^+ \to \mu\nu$

Figure 7.9 – Ratios of the normalized unfolded differential cross-sections by different predictions compared with the unfolded data at $\sqrt{s}$ =5.02 TeV.

QCD modellings for a fixed p_{T}^{W} distribution, which is therefore fully correlated across all the eight channels. A simplified description of the correlation model is shown in Table 7.2 for all the uncertainty components.

The p_{T}^{W} spectra are combined for both absolute differential cross-sections and normalized distributions. The combination results are shown in Figure 7.17, along with the uncertainty breakdown after the combination in Figure 7.18. The p_{T}^{Z} spectra shown in Figure 7.19 are measured from the $p_{\mathrm{T}}^{\ell\ell}$ distribution, combining $Z \to ee$ and $Z \to \mu\mu$ processes at each center-of-mass energy. The integrated fiducial cross-sections for W^+, W^- and Z production at 5.02 and 13 TeV are listed in Table 7.3. The cross-section ratios are presented in Table 7.4.

From Figure 7.20 to 7.24, the measurements of p_{T}^{W} and p_{T}^{Z} are compared with a variety of ATLAS MCs and the NNLO+NNLL DYTURBO predictions using several global PDF sets. Thanks to the high precision of the measurement, the data is

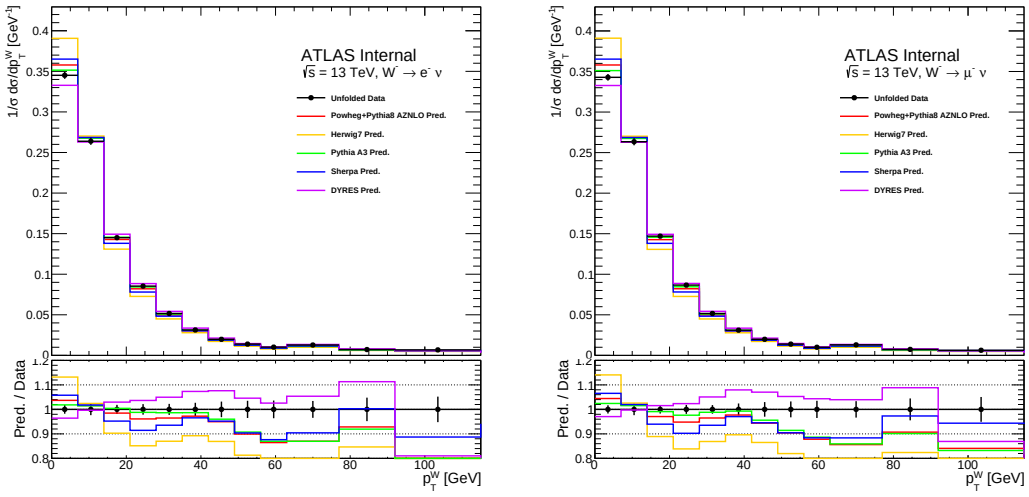

(a) $W^- \to e\nu$

(b) $W^- \to \mu\nu$

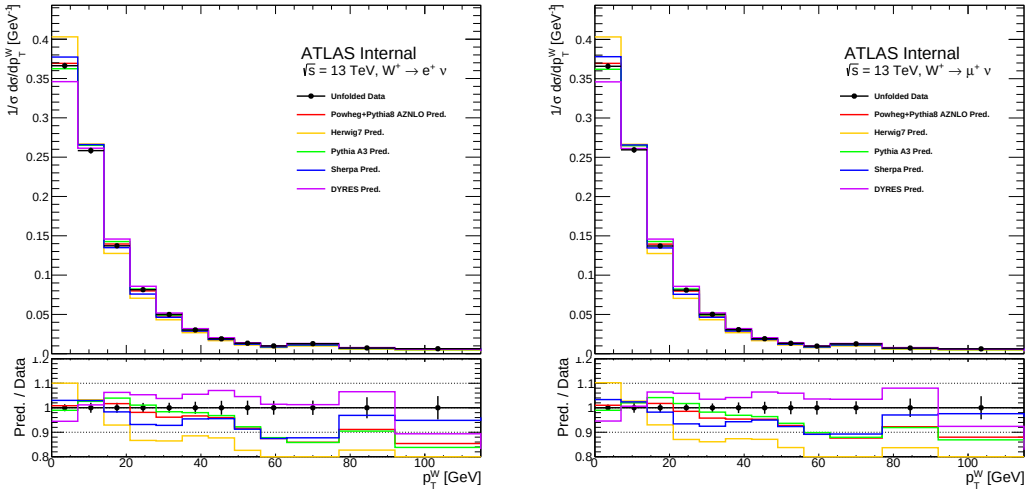

(c) $W^+ \to e\nu$

(d) $W^+ \to \mu\nu$

Figure 7.10 – Ratios of the normalized unfolded differential cross-sections by different predictions compared with the unfolded data at $\sqrt{s}$ =13 TeV.

discriminating in the Sudakov peak. In particular, percent-level precision is achieved in the measurement of W^+/W^- ratios. Small discrepancy can be appreciated from the comparison between the measurement and the theory predictions.

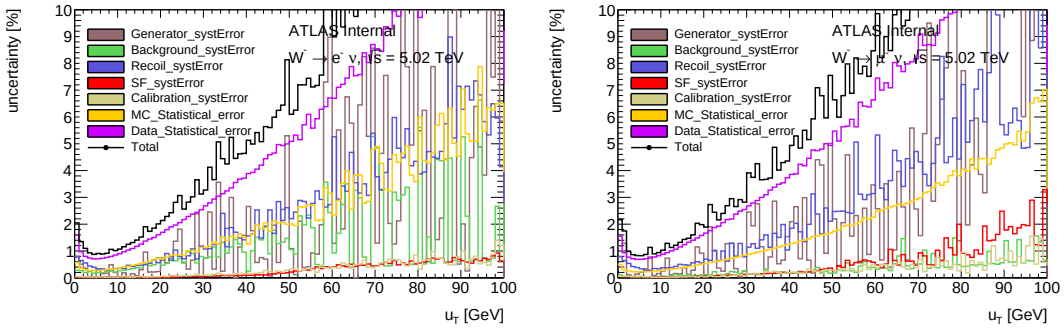

(a) $W^- \to e\nu$ (b) $W^- \to \mu\nu$

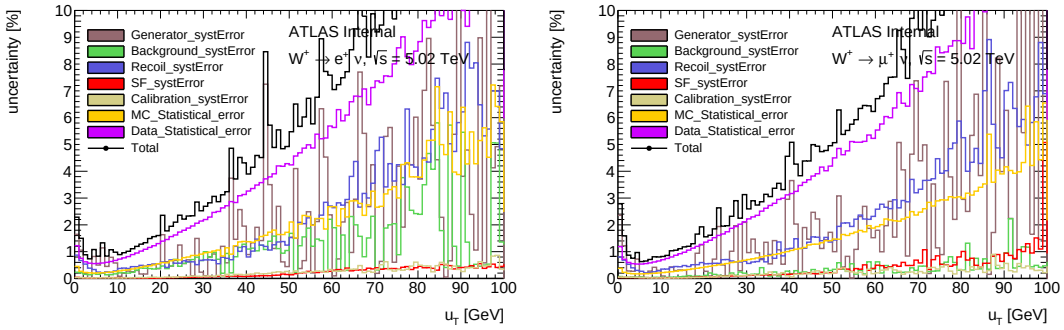

(c) $W^+ \to e\nu$ (d) $W^+ \to \mu\nu$

Figure 7.11 – Breakdown of uncertainties on the reconstructed level u_{T} distributions at $\sqrt{s}$ =5.02 TeV.

Uncertainty category	Nb. of sources at 5.02 TeV	Nb. of sources at 13 TeV
Electron calibration	108	108
Electron efficiencies	620	627
Muon calibration	48	48
Muon efficiencies	908	930
Recoil calibration	68	62
EW & Top backgrounds	24	22
Multijet background	11	11
Unfolding bias	5	5
Generator systematic	1	1
Total	1793	1814

Table 7.1 – Sources of systematic uncertainties in the p_{T}^{W} measurement at 5.02 and 13 TeV.

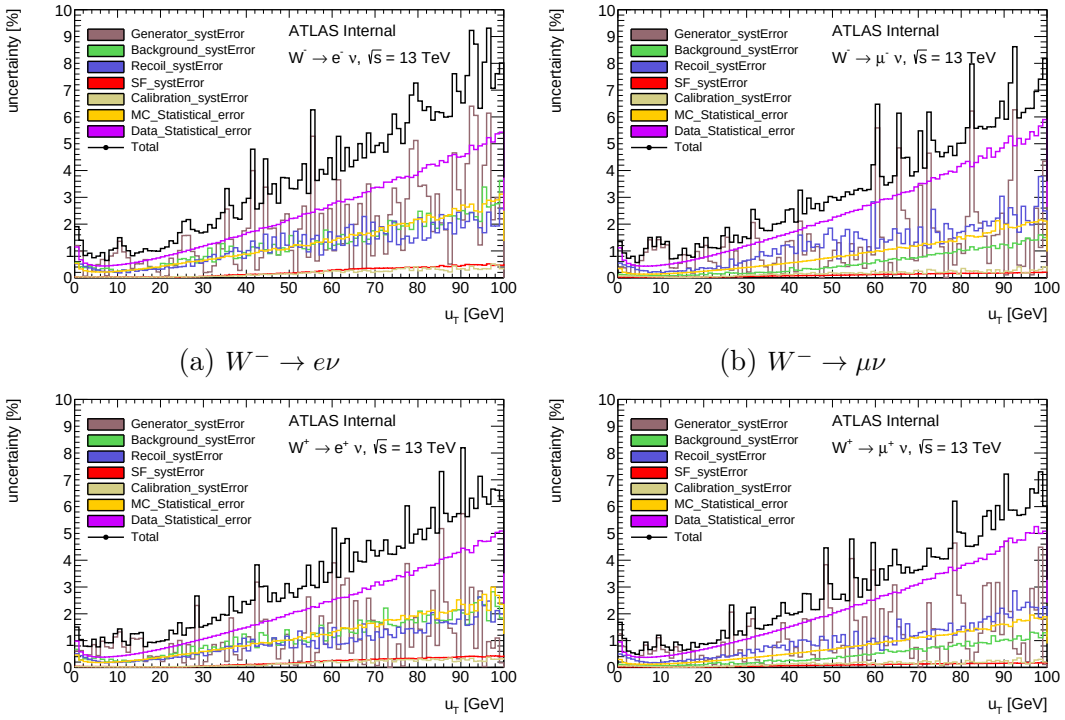

(a) $W^- \to e\nu$ (b) $W^- \to \mu\nu$

(c) $W^+ \to e\nu$ (d) $W^+ \to \mu\nu$

Figure 7.12 – Breakdown of uncertainties on the reconstructed level u_{T} distributions at $\sqrt{s}$ =13 TeV.

Source of uncertainty	W^+ vs. W^-	e vs. μ	5.02 vs. 13 TeV
Data & MC statistics	No	No	No
Lepton calibration & efficiencies	Full	No	Partial
Recoil calibration (Z-based)	Full	Full	No
Recoil calibration ($\sum \vec{E}_T$)	Full	Full	Full
EW & Top backgrounds	Full	Full	Full
Multijet background (statistics)	No	No	No
Multijet background (systematics)	Full	Full	Full
Unfolding bias	No	Full	No
Generator systematic	Full	Full	Full
Luminosity	Full	Full	No

Table 7.2 – A simplified description of the correlation model taken into account when combining the p_{T}^W spectra and calculating the integrals of fiducial cross-sections.

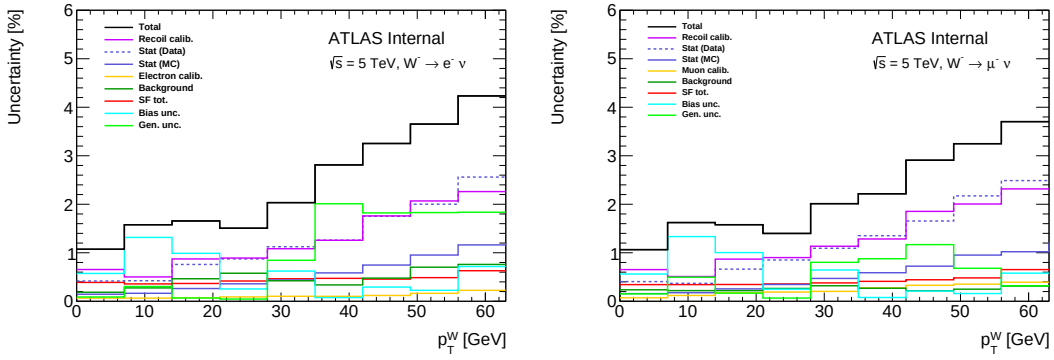

(a) $W^- \to e\nu$

(b) $W^- \to \mu\nu$

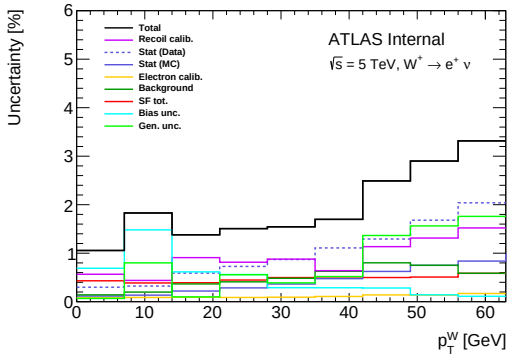

(c) $W^+ \to e\nu$

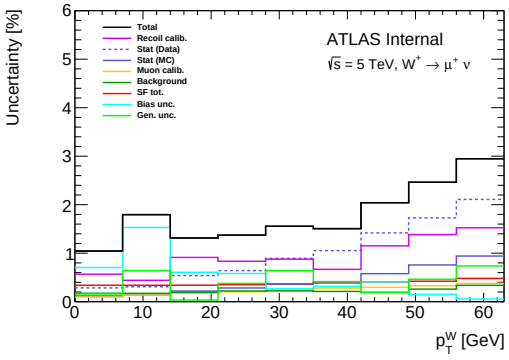

(d) $W^+ \to \mu\nu$

Figure 7.13 – Breakdown of absolute uncertainties on the unfolded level p_{T}^{W} distributions at $\sqrt{s}$ =5.02 TeV.

Process	Cross-section and uncertainties
5.02 TeV $W^+ \to l\nu$	2227.9 ± 2.6 (stat.) ± 7.8 (syst.) ± 23.1 (lumi.)
5.02 TeV $W^- \to l\nu$	1384.5 ± 2.1 (stat.) ± 5.4 (syst.) ± 14.5 (lumi.)
13 TeV $W^+ \to l\nu$	4571.4 ± 3.3 (stat.) ± 21.4 (syst.) ± 44.2 (lumi.)
13 TeV $W^- \to l\nu$	3485.8 ± 2.9 (stat.) ± 17.7 (syst.) ± 34.0 (lumi.)
5.02 TeV $Z \to ll$	333.0 ± 1.2 (stat.) ± 2.2 (syst.) ± 3.3 (lumi.)
13 TeV $Z \to ll$	780.3 ± 2.6 (stat.) ± 7.1 (syst.) ± 7.1 (lumi.)

Table 7.3 – Integrated fiducial cross-sections for W^+, W^- and Z productions in pb at 5.02 and 13 TeV.

Process	Ratio at $\sqrt{s}$ =5.02 TeV [pb]	Ratio at $\sqrt{s}$ =13 TeV [pb]
W^+/W^-	1.611 ± 0.003 (stat.) ± 0.004 (syst.)	1.312 ± 0.001 (stat.) ± 0.003 (syst.)
W^-/Z	4.16 ± 0.01 (stat.) ± 0.05 (syst.)	4.46 ± 0.01 (stat.) ± 0.07 (syst.)
W^+/Z	6.69 ± 0.02 (stat.) ± 0.08 (syst.)	5.84 ± 0.01 (stat.) ± 0.09 (syst.)
$W^\pm/Z$	10.85 ± 0.04 (stat.) ± 0.11 (syst.)	10.31 ± 0.02 (stat.) ± 0.15 (syst.)

Table 7.4 – Integrated cross-sections ratios at 5.02 and 13 TeV.

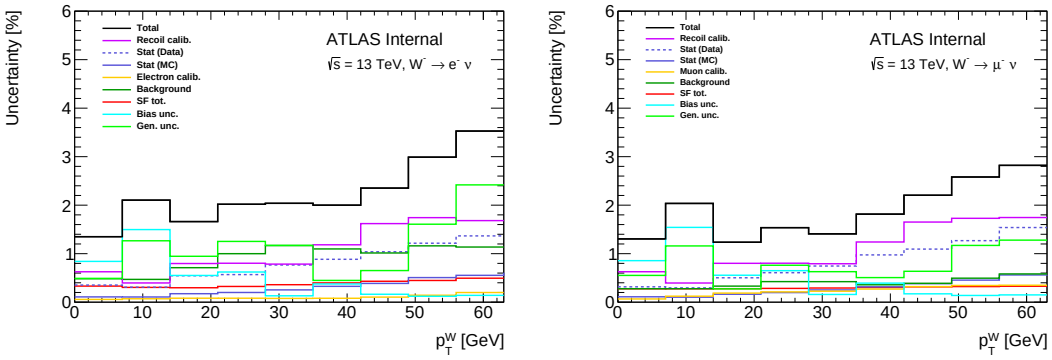

(a) $W^- \to e\nu$

(b) $W^- \to \mu\nu$

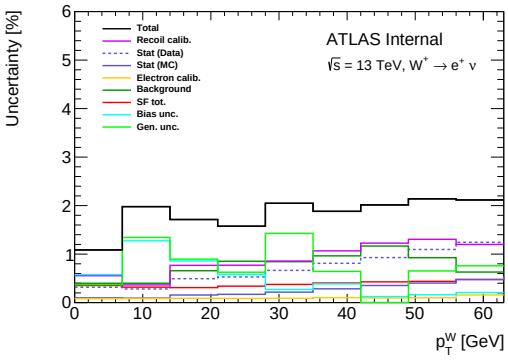

(c) $W^+ \to e\nu$

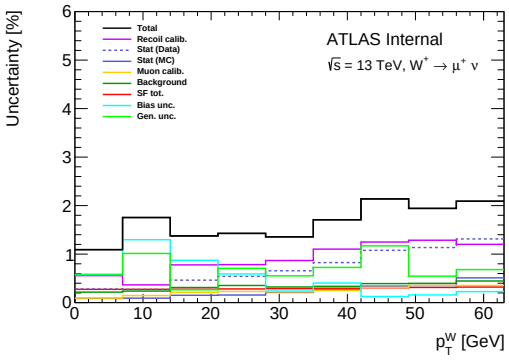

(d) $W^+ \to \mu\nu$

Figure 7.14 – Breakdown of absolute uncertainties on the unfolded level p_{T}^{W} distributions at $\sqrt{s}$ =13 TeV.

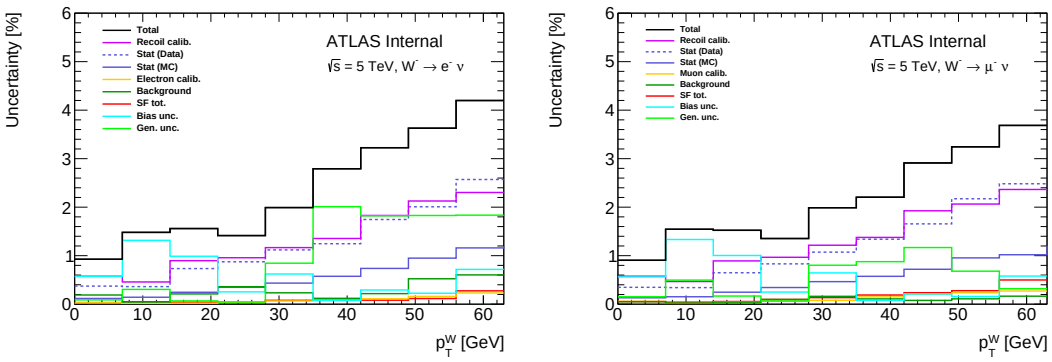

(a) $W^- \to e\nu$

(b) $W^- \to \mu\nu$

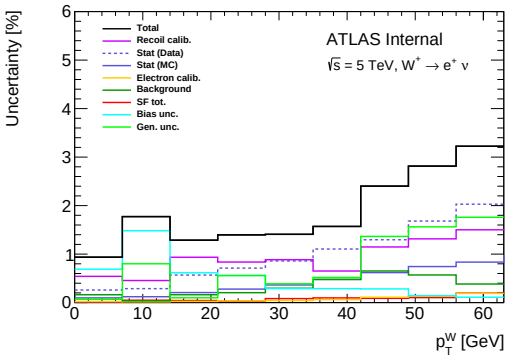

(c) $W^+ \to e\nu$

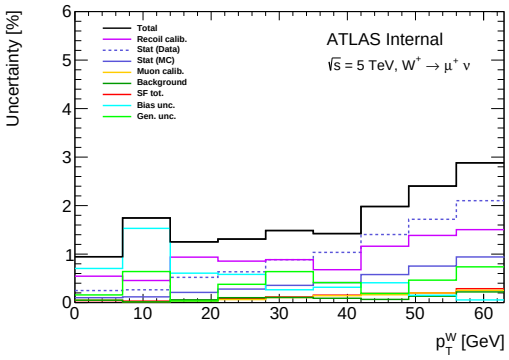

(d) $W^+ \to \mu\nu$

Figure 7.15 – Breakdown of shape uncertainties on the unfolded level p_{T}^{W} distributions at $\sqrt{s}$ =5.02 TeV.

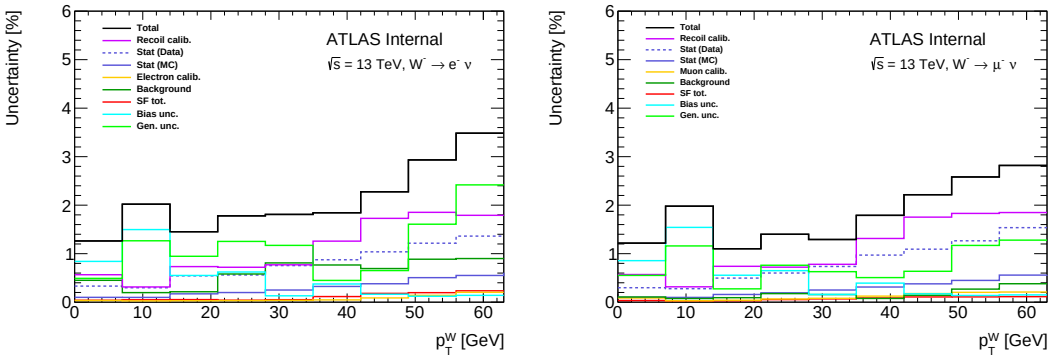

(a) $W^- \to e\nu$

(b) $W^- \to \mu\nu$

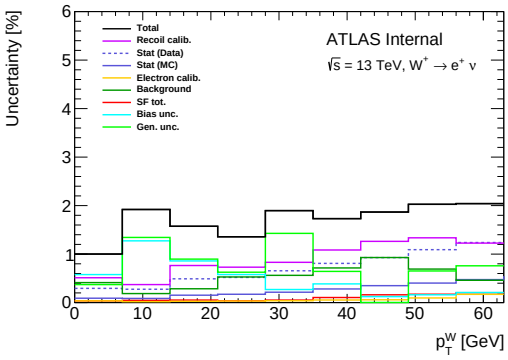

(c) $W^+ \to e\nu$

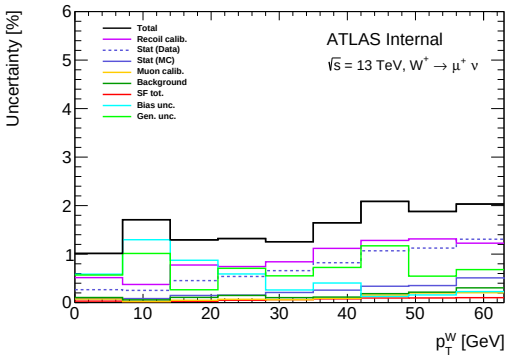

(d) $W^+ \to \mu\nu$

Figure 7.16 – Breakdown of shape uncertainties on the unfolded level p_{T}^{W} distributions at $\sqrt{s}$ =13 TeV.

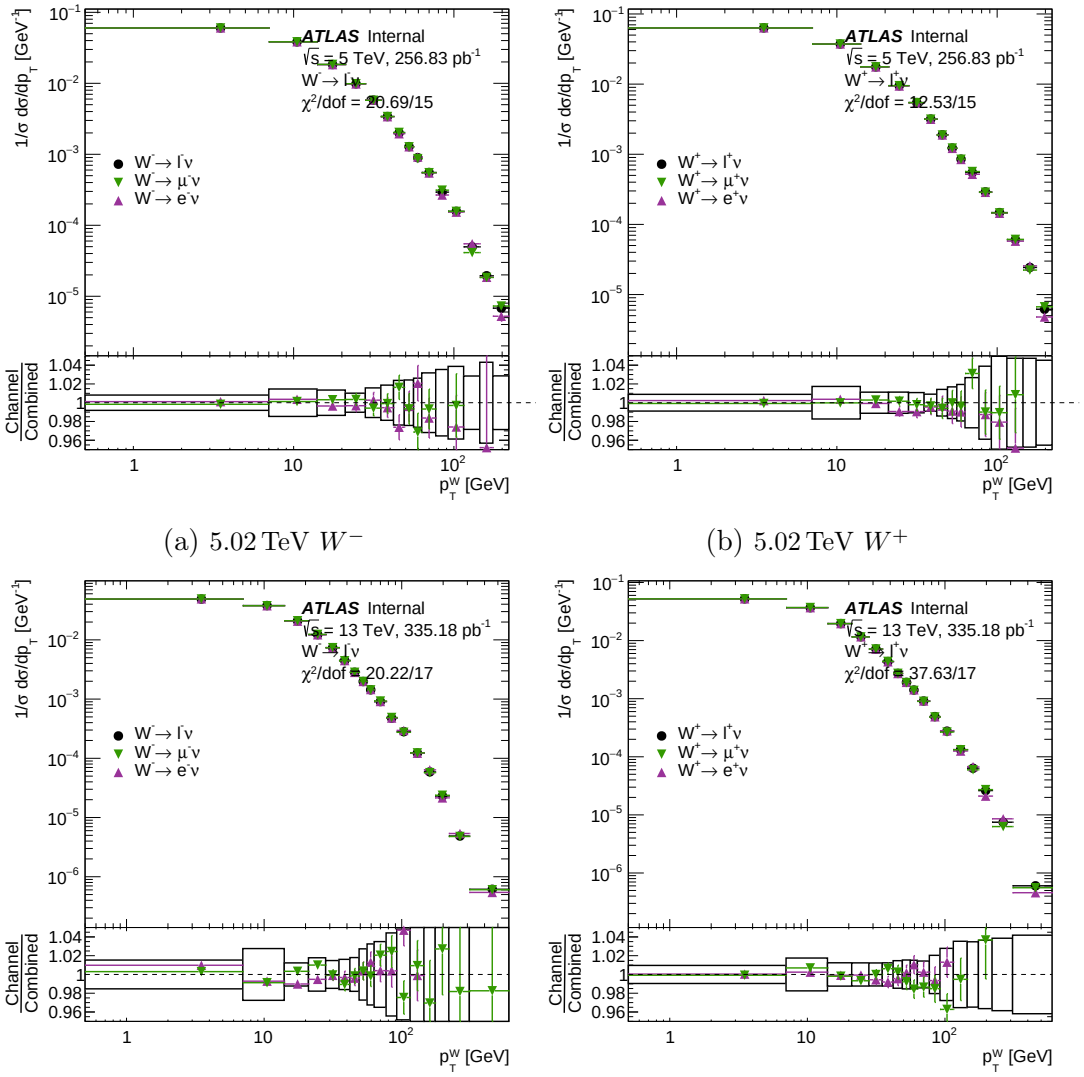

(a) 5.02 TeV W^- (b) 5.02 TeV W^+

(c) 13 TeV W^- (d) 13 TeV W^+

Figure 7.17 – Combination of the normalized p_{T}^{W} distributions.

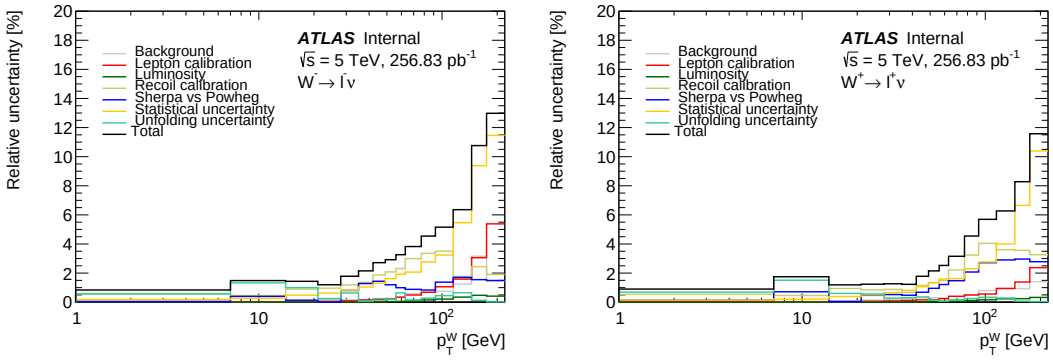

(a) 5.02 TeV W^- (b) 5.02 TeV W^+

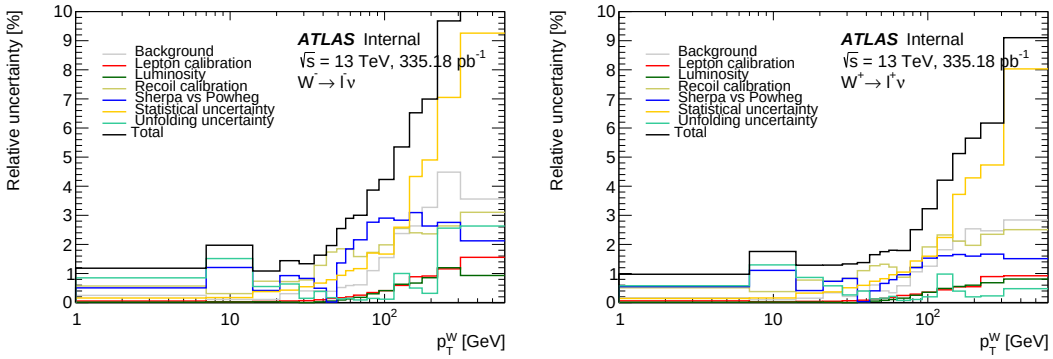

(c) 13 TeV W^- (d) 13 TeV W^+

Figure 7.18 – Breakdown of the uncertainties for the normalized p_{T}^{W} distributions.

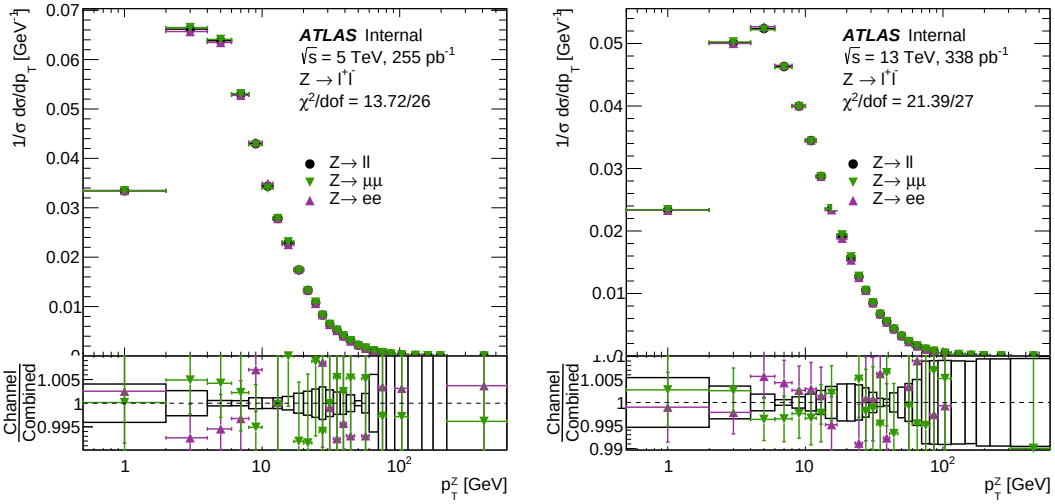

(a) 5.02 TeV (b) 13 TeV

Figure 7.19 – Combination of the normalized p_{T}^{Z} distributions.

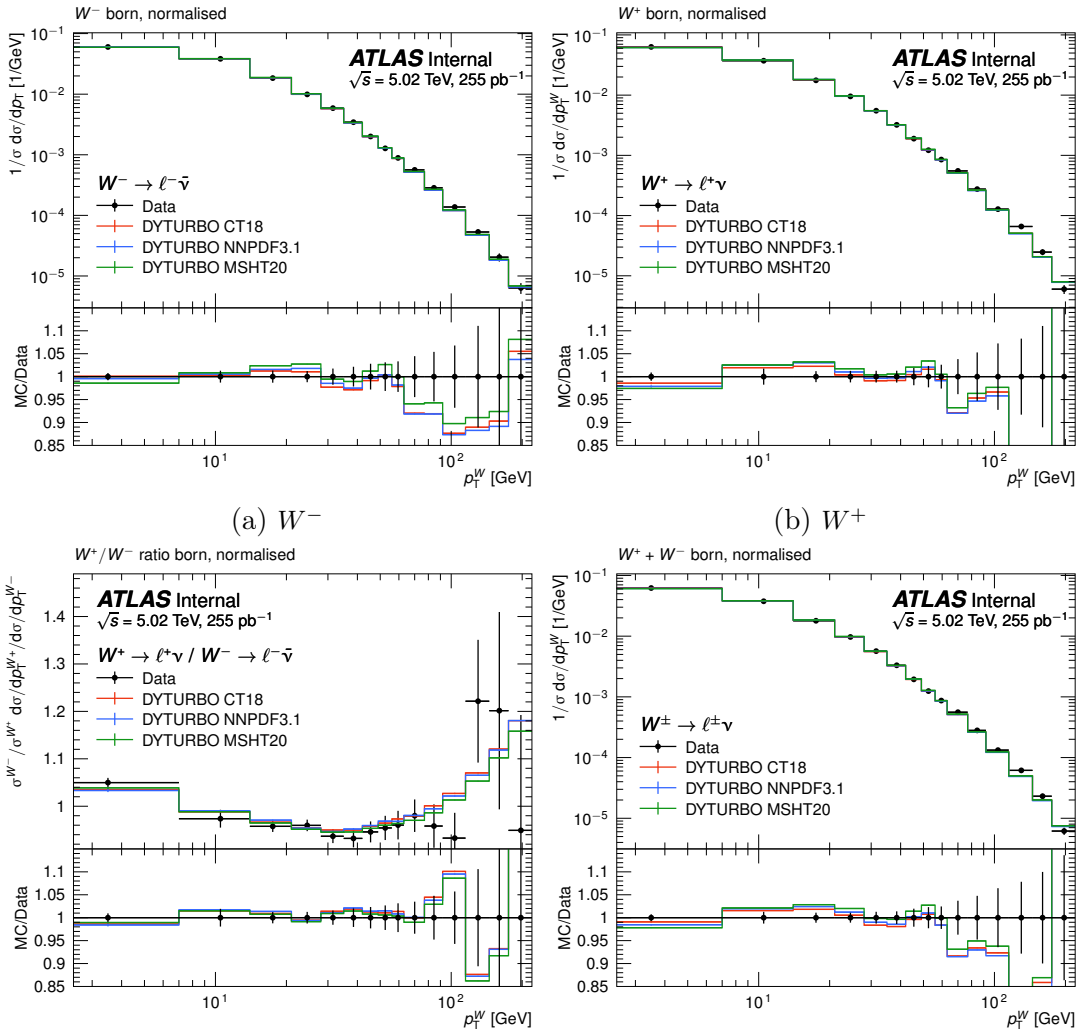

(a) W^- (b) W^+

(c) $W^+ + W^-$ (d) W^+/W^-

Figure 7.20 – Measurement of normalized p_{T}^{W} distributions at 5.02 TeV compared with DYTURBO predictions. The error bars of the data give the total measurement uncertainty.

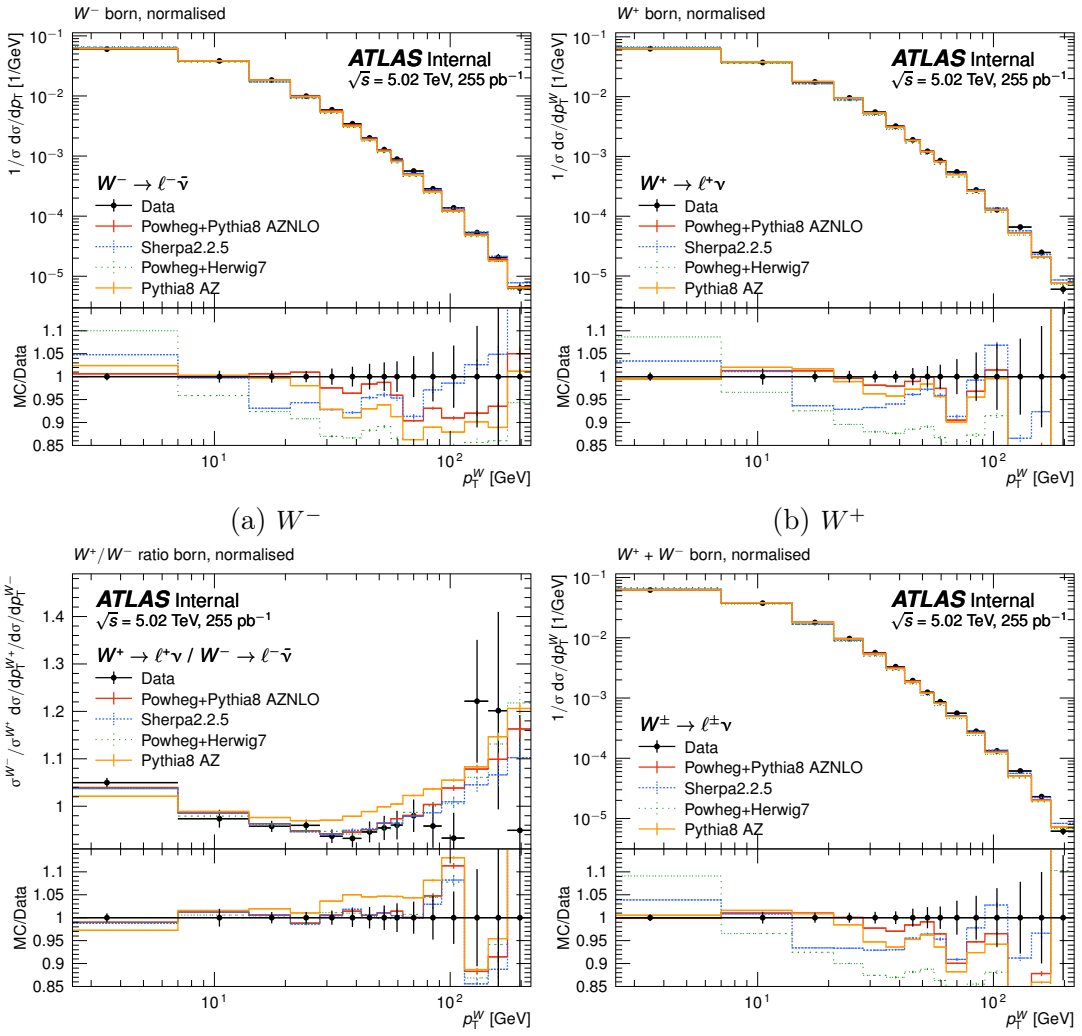

(a) W^- (b) W^+

(c) $W^+ + W^-$ (d) W^+/W^-

Figure 7.21 – Measurement of normalized p_{T}^{W} distributions at 5.02 TeV compared with MC predictions. The error bars of the data give the total measurement uncertainty.

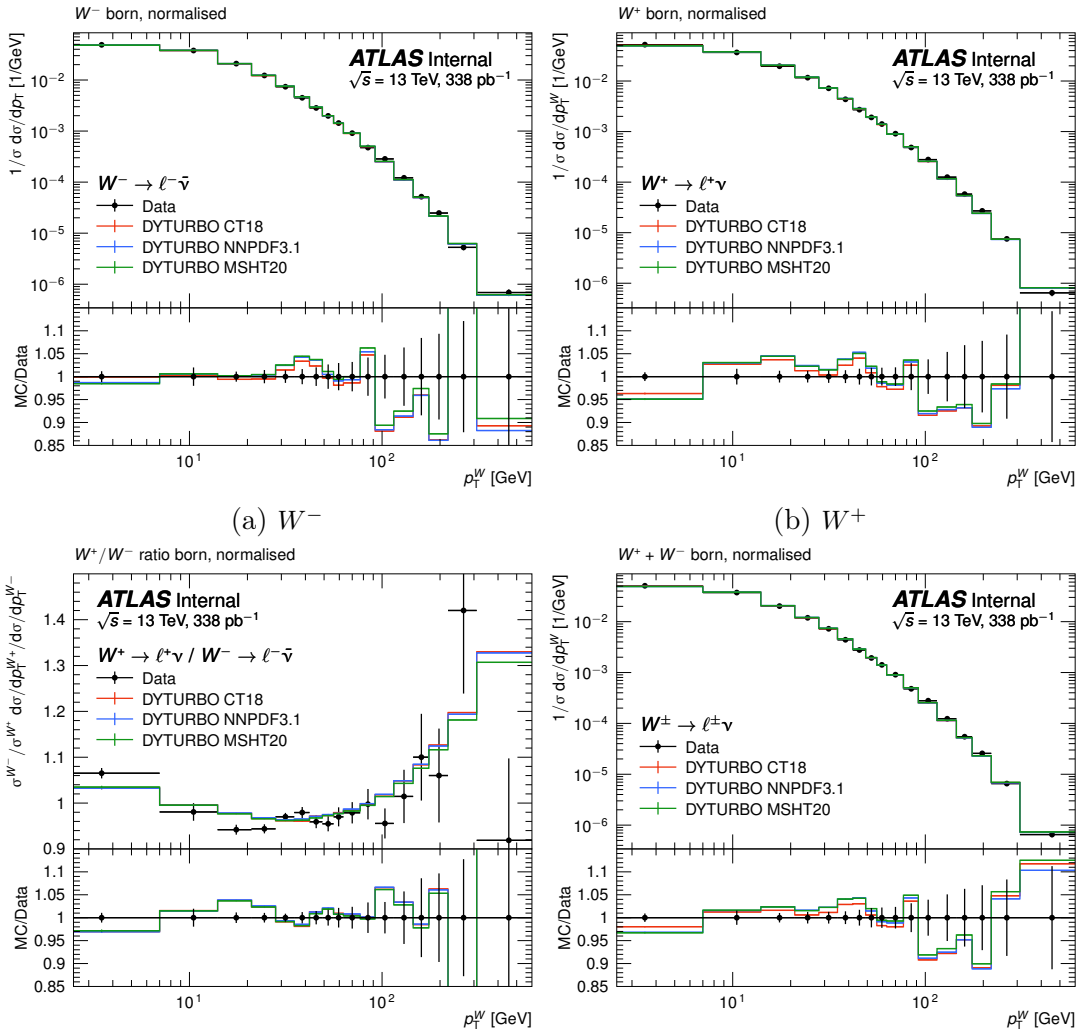

(a) W^- (b) W^+

(c) $W^+ + W^-$ (d) W^+/W^-

Figure 7.22 – Measurement of normalized p_{T}^{W} distributions at 13 TeV compared with DYTURBO predictions. The error bars of the data give the total measurement uncertainty.

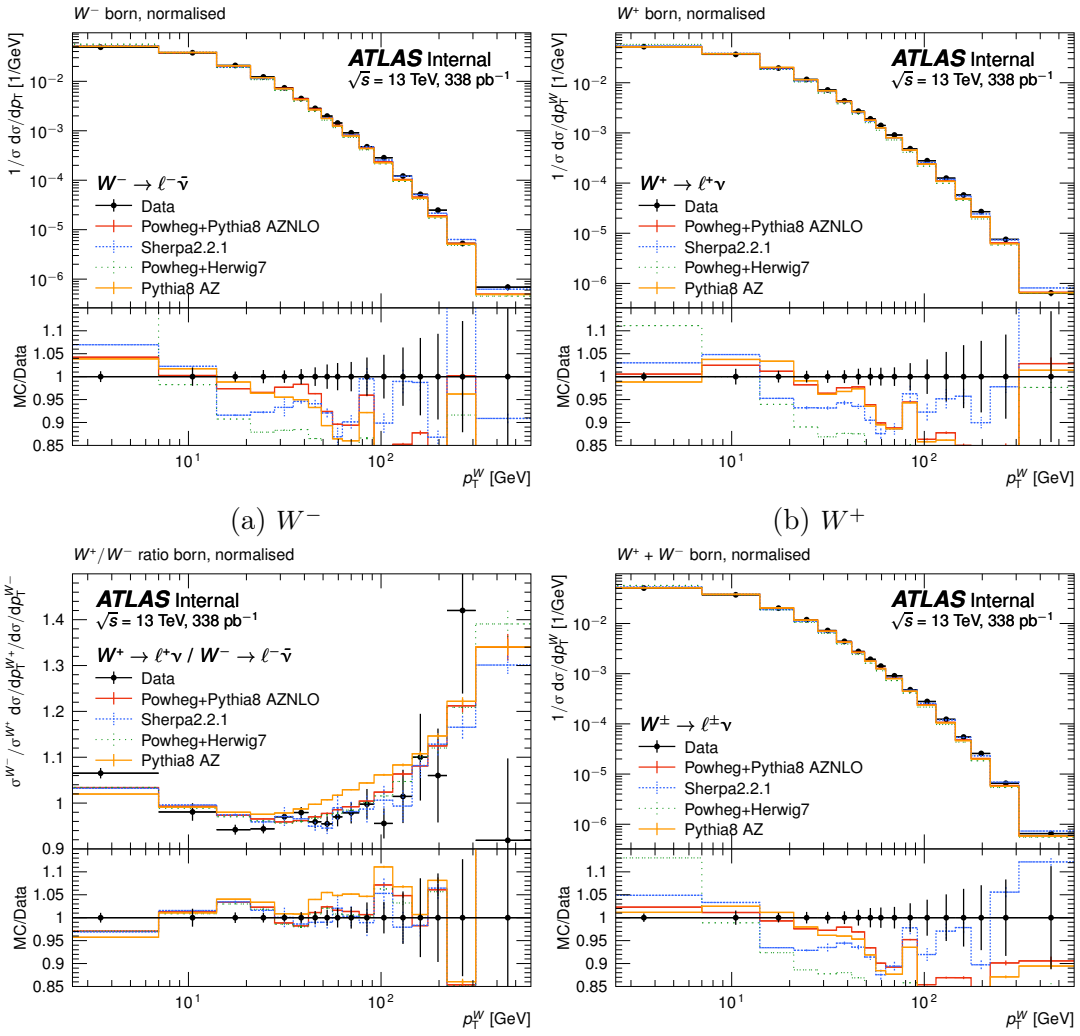

(a) W^- (b) W^+

(c) $W^+ + W^-$ (d) W^+/W^-

Figure 7.23 – Measurement of normalized p_{T}^{W} distributions at 13 TeV compared with MC predictions. The error bars of the data give the total measurement uncertainty.

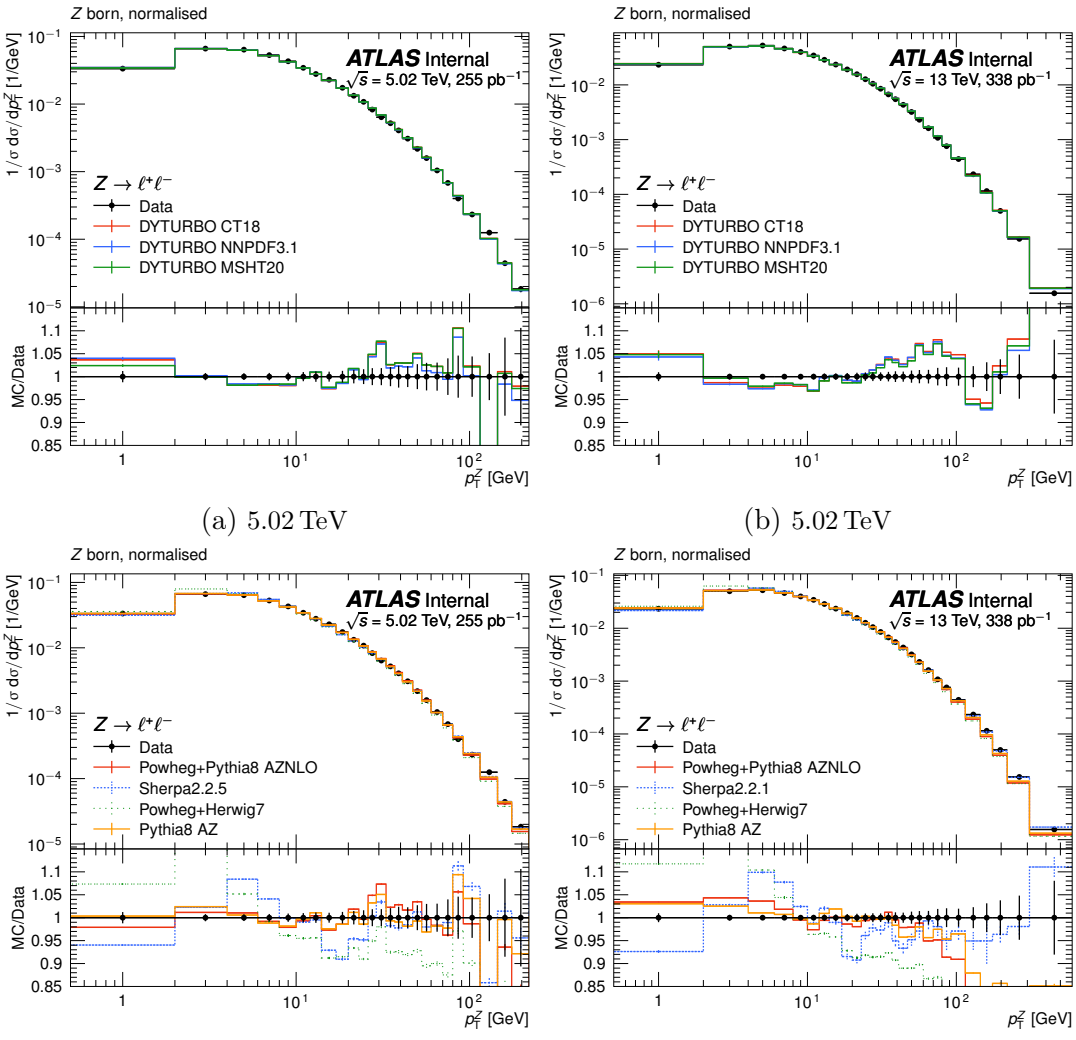

(a) 5.02 TeV (b) 5.02 TeV

(c) 13 TeV (d) 13 TeV

Figure 7.24 – Measurement of normalized p_{T}^{Z} distributions with DYTURBO (top) and MC (bottom) predictions. The error bars of the data give the total measurement uncertainty.

References

[1] "Prospects for the measurement of the W-boson transverse momentum with a low pileup data sample at $\sqrt{s} = 13$ TeV with the ATLAS detector", CERN, Geneva, Tech. Rep., 2017, All figures including auxiliary figures are available at https://atlas.web.cern.ch/Atlas/GROUPS/PHYSICS/PUBNOTES/ATL-PHYS-PUB-2017-021. [Online]. Available: https://cds.cern.ch/record/2298152 (cit. on p. 140).

[2] S. Catani, D. de Florian, G. Ferrera, and M. Grazzini, "Vector boson production at hadron colliders: transverse-momentum resummation and leptonic decay", *Journal of High Energy Physics*, vol. 2015, pp. 1–47, 12 2015. DOI: 10.1007/JHEP12(2015)047 (cit. on p. 140).

[3] T. Sjöstrand, S. Mrenna, and P. Skands, "A brief introduction to pythia 8.1", *Computer Physics Communications*, vol. 178, no. 11, pp. 852–867, 2008, ISSN: 0010-4655. DOI: https://doi.org/10.1016/j.cpc.2008.01.036. [Online]. Available: https://www.sciencedirect.com/science/article/pii/S0010465508000441 (cit. on pp. 140, 146).

[4] The ATLAS Collaboration, "Measurement of the W-boson mass in pp collisions at $\sqrt{s} = 7$ TeV with the ATLAS detector", *The European Physical Journal C*, vol. 78, p. 110, 2018. DOI: 10.1140/epjc/s10052-017-5475-4 (cit. on p. 140).

[5] The ATLAS collaboration, "Measurement of the $Z/\gamma*$ boson transverse momentum distribution in pp collisions at $\sqrt{s} = 7$TeV with the ATLAS detector", *Journal of High Energy Physics*, vol. 2014, p. 145, 9 2014. DOI: 10.1007/JHEP09(2014)145 (cit. on pp. 140, 149).

[6] G. D'Agostini, "A multidimensional unfolding method based on bayes' theorem", *Nuclear Instruments and Methods in Physics Research Section A: Accelerators, Spectrometers, Detectors and Associated Equipment*, vol. 362, no. 2, pp. 487–498, 1995, ISSN: 0168-9002. DOI: https://doi.org/10.1016/0168-9002(95)00274-X. [Online]. Available: https://www.sciencedirect.com/science/article/pii/016890029500274X (cit. on p. 142).

[7] G. D'Agostini, *Improved iterative bayesian unfolding*, 2010. arXiv: 1010.0632 [physics.data-an] (cit. on p. 142).

[8] B. Efron, "Bootstrap Methods: Another Look at the Jackknife", *The Annals of Statistics*, vol. 7, no. 1, pp. 1–26, 1979. DOI: 10.1214/aos/1176344552. [Online]. Available: https://doi.org/10.1214/aos/1176344552 (cit. on p. 143).

[9] H.-L. Lai, M. Guzzi, J. Huston, *et al.*, "New parton distributions for collider physics", *Phys. Rev. D*, vol. 82, p. 074 024, 2010. DOI: 10.1103/PhysRevD.82.074024. arXiv: 1007.2241 [hep-ph] (cit. on p. 145).

[10] P. Nason, "A new method for combining nlo qcd with shower monte carlo algorithms", *Journal of High Energy Physics*, vol. 2004, no. 11, p. 040, Dec. 2004. DOI: 10.1088/1126-6708/2004/11/040. [Online]. Available: https://dx.doi.org/10.1088/1126-6708/2004/11/040 (cit. on p. 145).

[11] S. Frixione, P. Nason, and C. Oleari, "Matching nlo qcd computations with parton shower simulations: the powheg method", *Journal of High Energy Physics*, vol. 2007, no. 11, p. 070, Nov. 2007. DOI: 10.1088/1126-6708/2007/11/070. [Online]. Available: https://dx.doi.org/10.1088/1126-6708/2007/11/070 (cit. on p. 145).

[12] S. Alioli, P. Nason, C. Oleari, and E. Re, "Nlo vector-boson production matched with shower in powheg", *Journal of High Energy Physics*, vol. 2008, no. 07, p. 060, Jul. 2008. DOI: 10.1088/1126-6708/2008/07/060. [Online]. Available: https://dx.doi.org/10.1088/1126-6708/2008/07/060 (cit. on p. 145).

[13] S. Alioli, P. Nason, C. Oleari, and E. Re, "A general framework for implementing nlo calculations in shower monte carlo programs: the powheg box", *Journal of High Energy Physics*, vol. 2010, p. 43, 6 Jul. 2010. DOI: 10.1007/JHEP06(2010)043. [Online]. Available: https://doi.org/10.1007/JHEP06(2010)043 (cit. on p. 145).

[14] R. D. Ball, V. Bertone, S. Carrazza, *et al.*, "Parton distributions for the LHC run II", *Journal of High Energy Physics*, vol. 2015, no. 4, Apr. 2015. DOI: 10.1007/jhep04(2015)040 (cit. on p. 145).

[15] S. Catani and M. Grazzini, "Next-to-next-to-leading-order subtraction formalism in hadron collisions and its application to higgs-boson production at the large hadron collider", *Phys. Rev. Lett.*, vol. 98, p. 222 002, 22 May 2007. DOI: 10.1103/PhysRevLett.98.222002. [Online]. Available: https://link.aps.org/doi/10.1103/PhysRevLett.98.222002 (cit. on p. 146).

[16] S. Catani, L. Cieri, G. Ferrera, D. de Florian, and M. Grazzini, "Vector boson production at hadron colliders: a fully exclusive qcd calculation at next-to-next-to-leading order", *Phys. Rev. Lett.*, vol. 103, p. 082 001, 8 Aug. 2009. DOI: 10.1103/PhysRevLett.103.082001. [Online]. Available: https://link.aps.org/doi/10.1103/PhysRevLett.103.082001 (cit. on p. 146).

[17] J. Bellm *et al.*, "Herwig 7.0/Herwig++ 3.0 release note", *Eur. Phys. J. C*, vol. 76, no. 4, p. 196, 2016. DOI: 10.1140/epjc/s10052-016-4018-8. arXiv: 1512.01178 [hep-ph] (cit. on p. 146).

[18] S. Catani, D. de Florian, G. Ferrera, and M. Grazzini, "Vector boson production at hadron colliders: transverse-momentum resummation and leptonic decay", *Journal of High Energy Physics*, vol. 2015, no. 12, pp. 1–47, Dec. 2015. DOI: 10.1007/jhep12(2015)047 (cit. on p. 149).

[19] G. Bozzi, S. Catani, G. Ferrera, D. de Florian, and M. Grazzini, "Production of drell–yan lepton pairs in hadron collisions: transverse-momentum resummation at next-to-next-to-leading logarithmic accuracy", *Physics Letters B*, vol. 696, no. 3, pp. 207–213, 2011, ISSN: 0370-2693. DOI: https://doi.org/10.1016/j.physletb.2010.12.024. [Online]. Available: https://www.sciencedirect.com/science/article/pii/S0370269310014036 (cit. on p. 149).

[20] L. Lyons, D. Gibaut, and P. Clifford, "How to combine correlated estimates of a single physical quantity", *Nuclear Instruments and Methods in Physics Research Section A: Accelerators, Spectrometers, Detectors and Associated Equipment*, vol. 270, no. 1, pp. 110–117, 1988, ISSN: 0168-9002. DOI: https://doi.org/10.1016/0168-9002(88)90018-6. [Online]. Available: https:

//www.sciencedirect.com/science/article/pii/0168900288900186 (cit. on p. 150).

[21] A. Valassi, "Combining correlated measurements of several different physical quantities", *Nuclear Instruments and Methods in Physics Research Section A: Accelerators, Spectrometers, Detectors and Associated Equipment*, vol. 500, no. 1, pp. 391–405, 2003, NIMA Vol 500, ISSN: 0168-9002. DOI: https://doi.org/10.1016/S0168-9002(03)00329-2. [Online]. Available: https://www.sciencedirect.com/science/article/pii/S0168900203003292 (cit. on p. 150).

[22] H. Dembinski, M. Schmelling, and R. Waldi, "Application of the iterated weighted least-squares fit to counting experiments", *Nuclear Instruments and Methods in Physics Research Section A: Accelerators, Spectrometers, Detectors and Associated Equipment*, vol. 940, pp. 135–141, 2019, ISSN: 0168-9002. DOI: https://doi.org/10.1016/j.nima.2019.05.086. [Online]. Available: https://www.sciencedirect.com/science/article/pii/S0168900219307508 (cit. on p. 152).

Chapter 8

Measurement of the W-boson mass with low pile-up data

Contents

The measurement of the W-boson mass documented in this work uses the ATLAS Run 2 low pile-up data described in Section 4.3. A dedicated MC simulation campaign was launched to match the special data-taking conditions, as discussed in Section 5.1. The low pile-up W-boson mass measurement shares the same physics modelling corrections as well as detector calibrations with the p_{T}^W measurement. Dedicated efforts have been spent on the improvement of the statistical analysis for the extraction of m_W from the data.

8.1 Basic methodology

The extraction of m_W in hadron colliders are based on a template fit, where the impact of hypothetically changing the mass of the boson on the kinematic spectrum is described by a reweighting of the resonance peak [1]:

$$\frac{\mathrm{d}\sigma}{\mathrm{d}m} \propto \frac{m^2}{\left(m^2 - m_V^2\right)^2 + m^4\Gamma_V^2/m_V^2} \tag{8.1}$$

with m_V and Γ_V as the assumed values of the W-boson mass and width in the simulation, while m stands for the invariant mass of the W-boson. The W-boson mass templates with various assumed values of m_W are generated via reweighting the events in the baseline simulation according to Equation 8.1. The W-boson mass template that best describes the data indicates the most probable value of the W-boson mass inferred from the data. Considering the sensitivity of the kinematic distributions to m_W, the most common choices of observables used for the extraction of the W-boson mass in hadron colliders are lepton p_{T} and m_{T}. This can be understood as for the W-bosons at rest, the Jacobian edges of these two distributions are $m_V/2$ and m_V, respectively [2].

The conventional approach of conducting the template fit for the W-boson mass, known as the χ^2 offset method, will be briefly recapped in Section 8.1.1. The profile likelihood fit (pLH-fit), as an advanced fitting technique based on the template fit, is applied to the low pile-up W-boson mass analysis, of which the basic concept and notations will be formulated in Section 8.1.2.

8.1.1 The χ^2 offset method

The χ^2 is a test statistic that helps evaluate the discrepancy between the expected frequencies and the observed frequencies. When applied to histograms, it takes the following binned format. For instance, the Neyman's χ^2 is expressed as:

$$\chi^2 = \sum_{i=1}^{N_{bin}} \frac{(n_i - v_i)^2}{\sigma_i^2} \tag{8.2}$$

for which n_i and v_i are the number of entries in the i-th bin of the observed (pseudo) data and of the expectation predicted by the simulation. The bin-by-bin uncorrelated uncertainty showing up in the denominator is a quadratic sum of the statistical uncertainties in both data and MC simulation in that bin, denoted as:

$$\sigma_i \equiv \sigma_i^{datastat.} \oplus \sigma_i^{MCstat.} \tag{8.3}$$

Considering that the kinematic distributions of physics observables, such as p_{T}^{ℓ} and m_{T}, are dependent on the value of the W-boson mass in the simulation (m_W), the number of entries in each bin of a kinematic distribution is therefore a function of m_W, and can be expanded into Taylor series in the vicinity of $m_W = m_W^0$, the resonance peak of the W-boson:

$$v_i = v_i\left(\frac{m_W - m_W^0}{m_W^0}\right) = \sum_{j=0}^{\infty} \frac{v_i^{(j)}(0)}{j!}\left(\frac{m_W - m_W^0}{m_W^0}\right)^j \approx v_i(0) + v_i'(0)\left(\frac{m_W - m_W^0}{m_W^0}\right) \tag{8.4}$$

The change of the W-boson mass in the template (in general, $m_W - m_W^0 \approx$<100 MeV) is way smaller than the assumed central value of the W-boson mass ($m_W^0 \approx$80 400 MeV). This allows to take the linear approximation from the Taylor series, such that the Neyman's χ^2 becomes a 2nd-order polynomial function of m_W:

$$\chi^2(m_W) = \sum_{i=1}^{N_{bin}} \frac{\left[n_i - v_i(0) - v_i'(0)\left(\frac{m_W - m_W^0}{m_W^0}\right)\right]^2}{\sigma_i^2} \tag{8.5}$$

The χ^2 between data and the W-boson mass templates are computed at different assumed values of the W-boson mass and fitted by a parabola. The minimum of the curve is the most probable value of the W-boson mass $\hat{m}_W$ ($\chi^2(\hat{m}_W) = \chi^2_{Min}$), while the difference between $\hat{m}_W$ and the value of m_W satisfying

$$\chi^2(m_W) = \chi^2(\hat{m}_W \pm \Delta_{m_W}^{stat.}) = \chi^2_{Min} + 1 \tag{8.6}$$

is the statistical uncertainty of the measurement ($\Delta_{m_W}^{stat.}$). The systematic uncertainties are accounted for by replacing the (pseudo) data in the above procedure with the

systematic variation and determining the new minimum of the parabola fit. The offset between $\hat{m}_W$ and the new minimum is taken to be the uncertainty ($\Delta_{m_W}^{syst.\,p}$) arising from corresponding systematic source p.

In the end, the result of the measurement using the χ^2 offset method, in terms of central value and the associated uncertainties, is presented by:

$$\hat{m}_W \pm \Delta_{m_W}^{stat.} \oplus \sum_{\oplus p} \Delta_{m_W}^{syst.\,p} \tag{8.7}$$

The total uncertainty is a quadratic sum of statistical uncertainty and systematic uncertainties.

8.1.2 Profile likelihood fit

Despite the low CPU time consumption and the good numerical precision (typically at sub-MeV level for the m_W measurement) of the χ^2 offset method, the biases caused by systematics are not corrected in the probability model, therefore leading to a less accurate central value. Moreover, even though the measurement of the W-boson mass has sensitivity to the systematics to some extent, none of the systematic uncertainties is constrained by the kinematic distributions of the data in the χ^2 offset method, which is a shortcoming especially when the measurement is dominated by systematics.

A more powerful tool for the statistical analysis, also following the principle of the template fit, would be the binned profile likelihood fit (pLH-fit), for which the probability density function is parameterized by the parameter of interest (POI) and a series of nuisance parameters (NPs) to account for the normalization as well as the effect of systematics [3]:

$$\mathcal{P}(n_i, a_p|\alpha_{mW}, \alpha_p, \phi_{CME}, \gamma_i) = \prod_{i\in bins} Pois(n_i|v_i) \prod_{p\in syst.+\Gamma} f_p(a_p|\alpha_p) \tag{8.8}$$

— n_i is the observed number of events in the i-th bin of the histogram known from the (pseudo) data.
— v_i is the total predicted number of events in the ith bin of the histogram.
— α_{mW} is the parameter of interest (POI) that can be translated to m_W.
— α_p is the nuisance parameter in the probability model parameterizing the effect of systematic uncertainty. Conventionally, $\alpha_p = \pm 1$ corresponds to the distortion of ± 1 standard deviation on the kinematic spectrum brought by the systematic uncertainty.
— ϕ_{CME} is the free floating normalization factor for the prediction of the signal. The normalization factors are mainly introduced to account for the bias due to the effect of missing higher-order QCD calculation on the signal cross-section. The difference between the calculations of W^+ and W^- productions is considered to be weakly dependent on higher-order QCD correction. Hence one single ϕ_{CME} is shared by all the W-boson channels at each center-of-mass energy.
— γ_i is the parameter accounting for MC statistical uncertainty. The details of these parameters will be elaborated in Section 8.2.2. The collection of all γ_i is denoted as Γ.
— a_p is the central value of the auxiliary measurement for the systematic source p, known as the global observable. The prior knowledge of this systematic

source is embodied by the form of the constraint term f_p. The constraint term is usually a normal distribution with the conventional definition of NP, if nominal expectation for the main measurement has been corrected by the results of the auxiliary measurements (e.g. detector calibration) and a_p is defined in the unit of α_p.

The overall likelihood $\mathcal{P}$ is a product of Poisson likelihood for each bin and the constraint terms for systematics. The prediction of the Poisson likelihood is parameterized by a template morphing that consists of a polynomial interpolation and linear extrapolation:

$$I_{poly|lin.}(\alpha; I^0, I^+, I^-) = \begin{cases} \alpha(I^0 - I^-) & \alpha \leq -1 \\ \sum_{i=1}^{6} c_i \alpha^i & |\alpha| < 1 \\ \alpha(I^+ - I^0) & \alpha \geq 1 \end{cases} \tag{8.9}$$

with a set of coefficients c_i making the interpolation satisfy the continuity in the value $\eta(\alpha = \pm 1)$, the first derivative $d\eta/d\alpha|_{\alpha=\pm1}$ and the second derivative $d^2\eta/d\alpha^2|_{\alpha=\pm1}$ at the boundaries $\alpha = \pm 1$.

For multiplicative parameterization such as luminosity, the template morphing is written explicitly as:

$$\eta(\boldsymbol{\alpha}) = 1 + \sum_{p \in syst.} I_{poly|lin.}(\alpha_p; 1, \eta_p^+, \eta_p^-) \tag{8.10}$$

Here $\eta_p^\pm$ correspond to the deviation of η from unity brought by ± 1 standard deviation of systematic source p. And similarly for the additive parameterization, for example the shape of a distribution, the morphing takes the form:

$$h_i(\boldsymbol{\alpha}) = h_i^0 + \sum_{p \in syst.} I_{poly|lin.}(\alpha_p; h_{p,i}^0, h_{p,i}^+, h_{p,i}^-) \tag{8.11}$$

where h_i^0 is the content of the i-th bin at nominal value, α_p is the NP that parameterizes the effect of systematics, $h_{p,i}^\pm$ are the changes in bin content brought by ± 1 standard deviation of the systematic source p. Conventionally, one sets $h_{p,i}^0 = h_i^0$.

The Poisson likelihood for each bin adopts the form of an extended p.d.f., taking into account the contribution from background in the total prediction. Specifically, in the W-boson mass fit one has:

$$v_i = \phi_{CME} \cdot v_i^{sig} + \alpha_{lumi.} \cdot v_i^{bkg} + v_i^{MJ} \tag{8.12}$$

where v_i^{sig} is the MC prediction of the signal process, v_i^{bkg} the prediction of the simulated background and v_i^{MJ} the data-driven estimation of the multijet background described in Section 5.4. v_i^{sig} is parameterized by the effect of systematic uncertainties as well as that of the hypothetical change in the W-boson mass. The parameterization of both sources follows Equation 8.11. v_i^{bkg} can be varied by the cross-section uncertainty of each simulated background process, of which the uncertainty templates are also morphed according to Equation 8.11. The uncertainties arising from the data-driven method are assigned to v_i^{MJ}, with the parameterization of Equation 8.11. The normalization of the signal prediction is parameterized by the free floating parameter ϕ_{CME}, while the luminosity measurement parameterized by $\alpha_{lumi.}$ accounts for the normalization of the simulated background. The template morphing of the luminosity uncertainty takes the form of Equation 8.10. No normalization is applied to the result of data-driven estimation of the multijet background.

The setup and the execution of the profile likelihood fit used in this work are handled by HistFactory [3] interfaced to RooFit [4]. The most probable values of the fit parameters are inferred from the (pseudo) data by minimizing the Negative Logarithm of the Likelihood (NLL), which is an approach mathematically equivalent to maximizing the likelihood but with a considerable numerical advantage. The calculation of the first derivative of the NLL leads to the most probable values of the fit parameters, requiring:

$$\frac{\partial NLL}{\partial x} = 0 \tag{8.13}$$

with x looping over all fit parameters.

The calculation of the errors on the fit parameters consists of two steps. Firstly, the Hessian matrix $\mathcal{H}$ (the matrix of secondary derivatives) of the NLL with respect to the fit parameters is computed:

$$\mathcal{H} = \left(\frac{\partial^2 NLL}{\partial x \partial y} \right) \tag{8.14}$$

with x and y independently looping over all fit parameters. The post-fit uncertainties of the POI and the NPs can be assessed by the retrieving the diagonal elements of the inverse of the Hessian matrix $\mathcal{H}^{-1}$, producing what is referred to as the Hesse Error in the context of RooFit. In the second step, after the calculation of the Hesse Error, the ± 1 standard deviation of a given fit parameter can be found by performing a scan of the likelihood contour along this parameter and solving the two points fulfilling $\Delta NLL = 0.5$. This is similar to solving Equation 8.6 in the χ^2 offset method. But in a profile likelihood fit, this formula is applicable to all fit parameters. The uncertainty derived in the second step is denoted as the Minos Error. The computation of the Minos Error is more time consuming than the Hesse Error.

The Hesse Errors are symmetric and are only the approximate post-fit errors of the fit parameters, since they are computed from the secondary derivative at the minimum of the NLL and dependent on the minimization path being taken. In most cases the Hesse Errors are lower than the true errors on the fit parameters, meaning that some validations might be necessary for one to understand if the values are reliable. In contrast, the Minos Errors are obtained from the scan of the likelihood contour beyond the minimum. Therefore, the Minos Errors are allowed to be asymmetric and are expected to better reflect the true errors on the parameters. Both the Hesse Error and the Minos Error on the POI are estimates of the total uncertainty on POI, including statistical uncertainties and systematic uncertainties. In order to ensure a reliable total uncertainty in m_W with optimized usage of computational resources, the Minos Error is always used for the POI in the profile likelihood fit, while the Hesse Error can be considered to attain a reasonable precision for the errors on the NPs.

Compared with the χ^2 offset method, the profile likelihood fit not only enables corrections to the small biases in the measurement caused by systematics, but also allows to constrain the systematic uncertainties with the statistical power of the dataset. The downsides of the profile likelihood fit and the possible remedies to these known issues are discussed in Section 8.2.

8.1.3 Configuration of the fit for m_W measurement

The full probability model of the low pile-up W-boson mass fit includes 8 decay channels. The main kinematic distribution is chosen to be m_{T} due to its better

sensitivity to the W-boson mass in the low pile-up datasets. A 2D categorization in u_{T} and η_{ℓ} is implemented in the probability model to facilitate the constraint of systematic uncertainties. The optimization of range and of the bin width of m_{T} and u_{T} has been studied in the 5 TeV $W^{-} \to e\nu$ channel, only taking into account the data statistics. Only the categorization in u_{T} is involved in this study. The baseline is set to be: 60< m_{T} <100 GeV with 2 GeV bin width, u_{T} <15 GeV with 5 GeV bin width. Each time, one of the following four quantities is varied to study its impact on the total uncertainty, as shown in Figure 8.1: (a) Range of m_{T}, (b) Bin width of m_{T}, (c) Range of u_{T} and (d) Bin width of u_{T}. In the end, the combination of 60< m_{T} <100 GeV with 2 GeV bin width and u_{T} <25 GeV with 5 GeV bin width is chosen for the input of the fit. Finer granularity or extended fit range bring marginal improvement to the statistical uncertainty. The categorization in lepton η is kept consistent with the ATLAS 7 TeV measurement [5] in general, mainly driven by the acceptance and performance of the detector systems. Therefore, the alignment of η_e and η_{μ} bins is unnecessary:

— Bin edges of $|\eta_e|$ categories: [0, 0.6, 1.2, 1.8, 2.47]

— Bin edges of $|\eta_{\mu}|$ categories: [0, 0.8, 1.4, 2.0, 2.4]

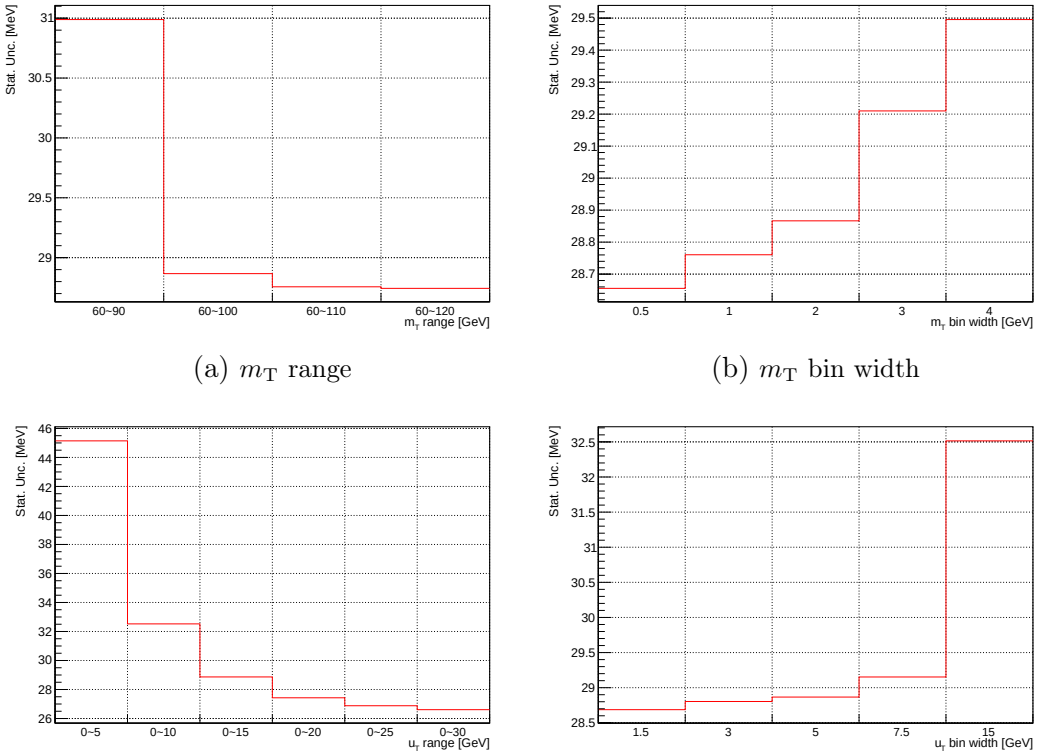

(a) m_{T} range

(b) m_{T} bin width

(c) u_{T} range

(d) u_{T} bin width

Figure 8.1 – The optimization of fit range and bin width for m_{T} and u_{T} using the signal MC in 5 TeV $W^{-} \to e\nu$ channel.

The 2D categorization effectively makes the fit a 3D measurement in (m_{T}, u_{T}, η_{ℓ}). The full information on the kinematic distribution is presented by the unrolled m_{T} distribution, where the m_{T} spectra in different categories are concatenated into a long 1D histogram. The preliminary control plots of the unrolled m_{T} distribution

are shown from Figure 8.2 and to Figure 8.5, where the total prediction is normalized to the data integral. Only the statistical uncertainties are presented in the control plots. The value of m_W is blinded in the simulation. The categorization in the plots first goes through the 4 η_ℓ categories in the first u_T category, then the 4 η_ℓ categories in the next u_T category, until the 4 η_ℓ categories in the last u_T category. The reconstructed level PDF reweighting in Section 8.3.3 has not been applied to the unrolled m_T distributions in the control plots.

Clear trends of discrepancy between data and simulation have been observed in the control plots. Some trends of discrepancy are repeated in different categories and shared by multiple channels, which might indicate that further improvement of physics modelling is necessary.

8.2 The improvement of profile likelihood fit

Despite clear advantages over the χ^2 offset method in terms of both accuracy (central value) and precision (total uncertainty), the use of profile likelihood fit is largely limited by two factors: CPU time consumption and the treatment of statistically correlated observables. The improvement for the first limitation is discussed in Sections 8.2.1 and 8.2.2. A few possible solutions related to the second limitation are mentioned in Section 8.2.3.

8.2.1 Reduction of nuisance parameters

Due to the calculation of the Hessian matrix during the minimization, the CPU time consumption goes up proportionally to the square of the number of fit parameters. As tested in an early stage of the analysis, a fit with several hundreds of fit parameters took about a few hours for a single CPU core to complete the minimization. An even larger number of fit parameters in the probability model would make the computation extremely expensive. Therefore, dedicated efforts were spent in studying the possible schemes of NP reduction in the probability model.

The large number of NP sources mainly originates from the experimental systematics such as the uncertainties related to the lepton selection efficiencies. However, instead of injecting each source of uncertainty one by one to the profile likelihood fit, a good approximation can be achieved by replacing the individual uncertainty variations with the error vectors of the corresponding covariance matrix. For the binned kinematic distribution of a given observable, the covariance matrix of systematics is written as:

$$C_{ij}^{syst} = \sum_p C_{ij}^p = \sum_p \left(H_i^p - H_i^{nom}\right)\left(H_j^p - H_j^{nom}\right) = \Sigma^T\Sigma \tag{8.15}$$

where i, j are the indices of bins (i,j=1, 2, 3 ... N_{bins}) of the kinematic distribution, $(\Sigma)_i^p = H_i^p - H_i^{nom}$, H^{nom} is the nominal spectrum and H^p is the systematic variation. By performing the diagonalization of the matrix C^{syst}, one obtains a set of error vectors Γ. The number of the error vectors is equal to the rank of C^{syst} and is no more than the number of bins of the distribution:

$$\Sigma^T\Sigma = C^{syst} = \Gamma^T\Gamma = \left(\sqrt{D}X_L\right)^T\left(\sqrt{D}X_L\right) \tag{8.16}$$

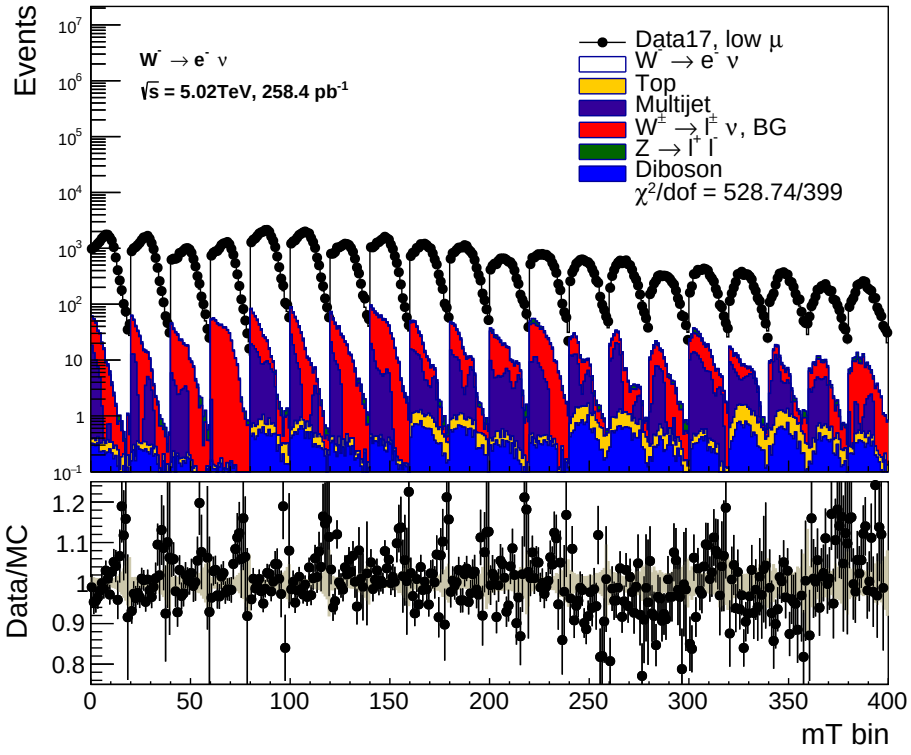

(a)

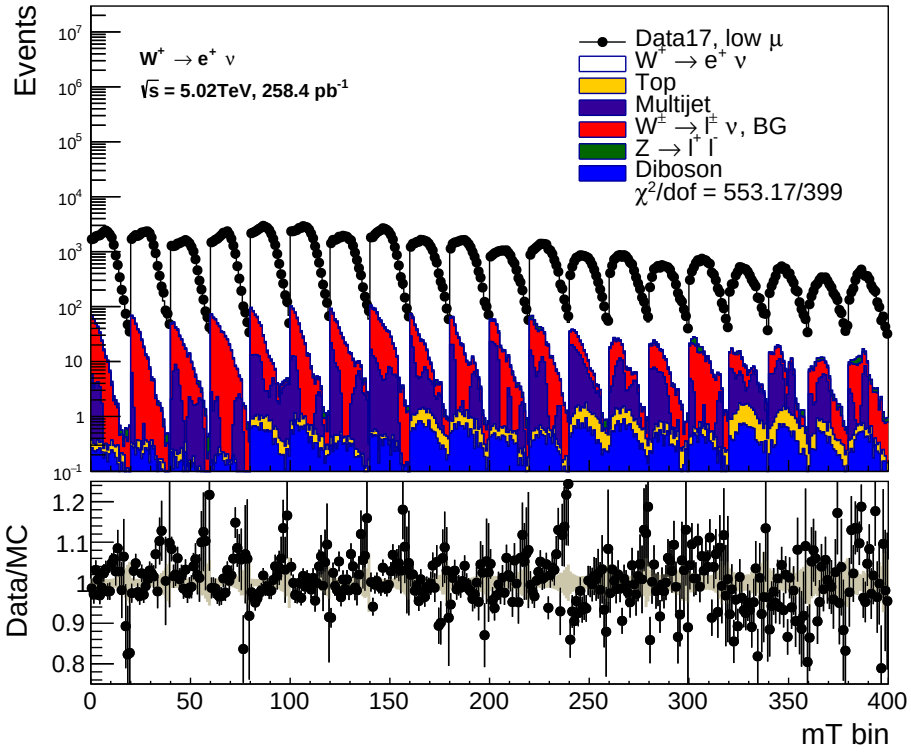

(b)

Figure 8.2 – The control plots of unrolled m_{T} spectra in 5 TeV electron channels.

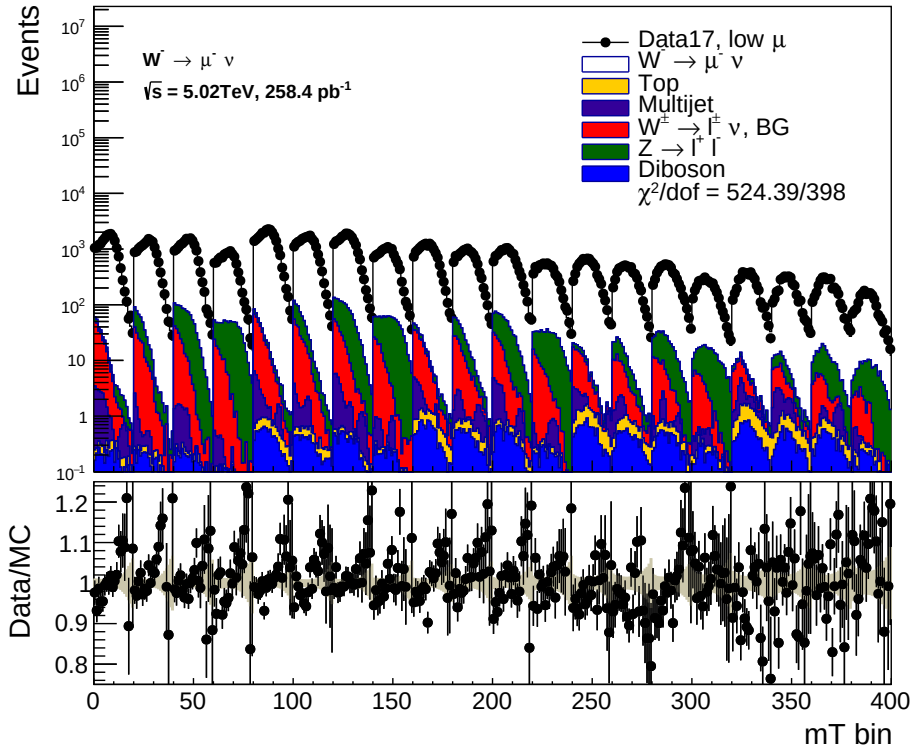

(a)

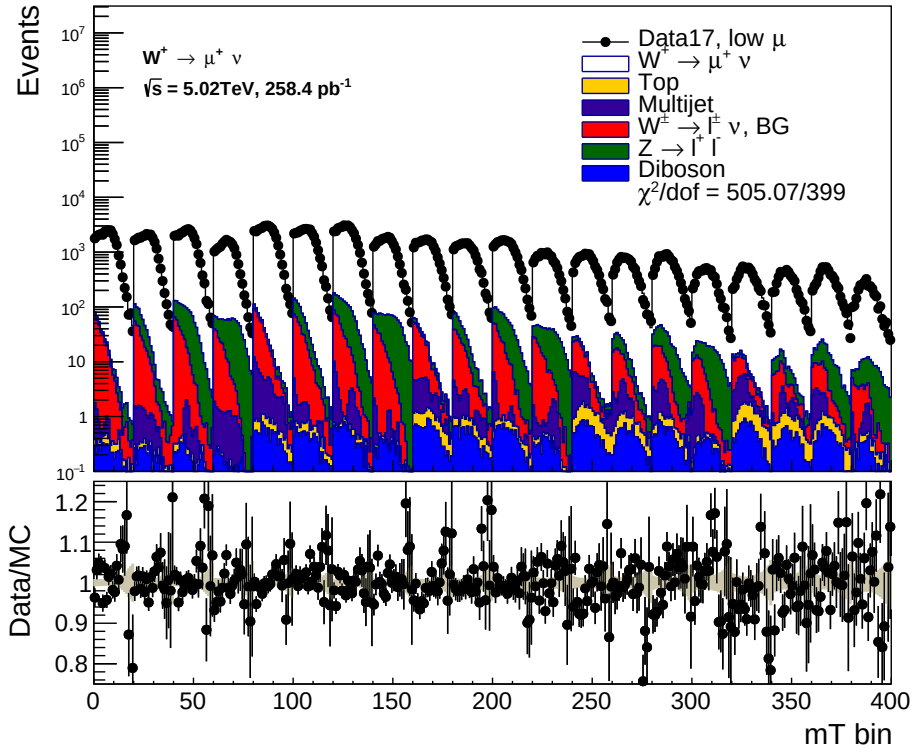

(b)

Figure 8.3 – The control plots of unrolled m_{T} spectra in 5 TeV muon channels.

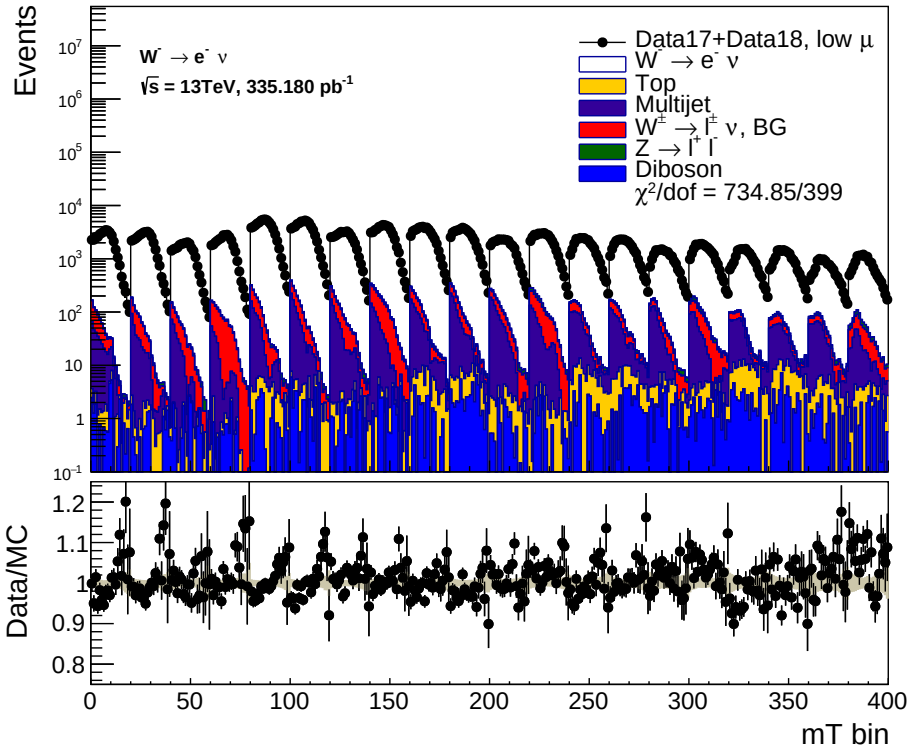

(a)

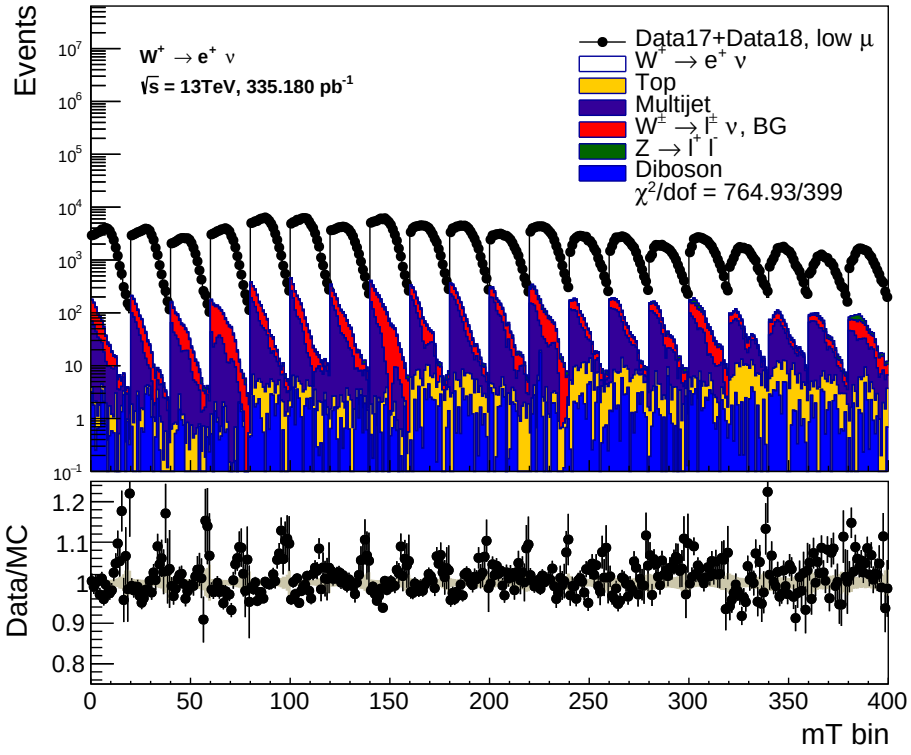

(b)

Figure 8.4 – The control plots of unrolled m_{T} spectra in 13 TeV electron channels.

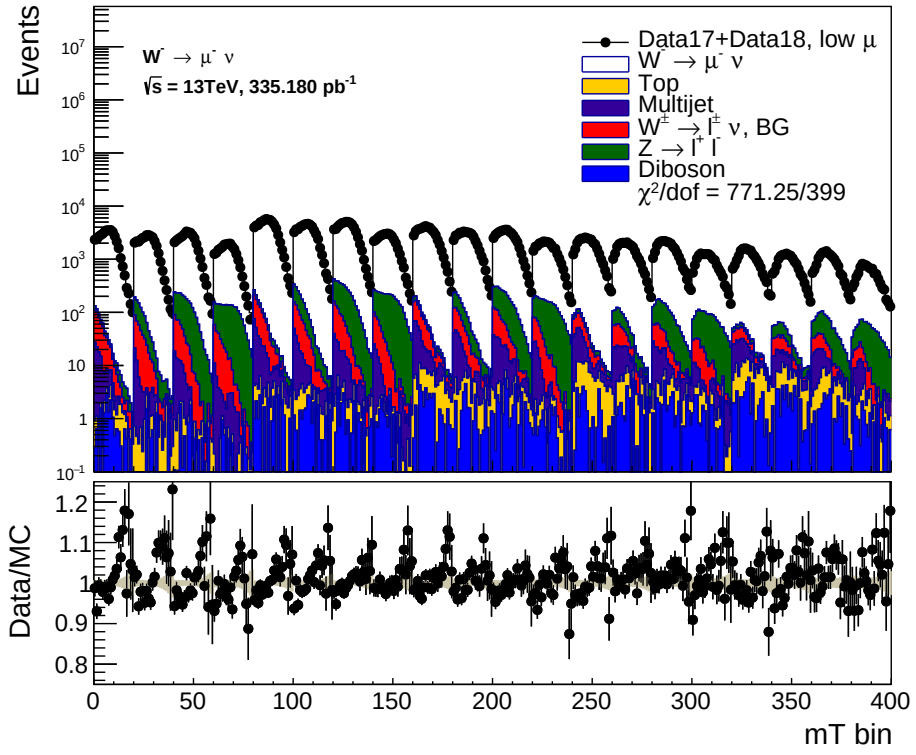

(a)

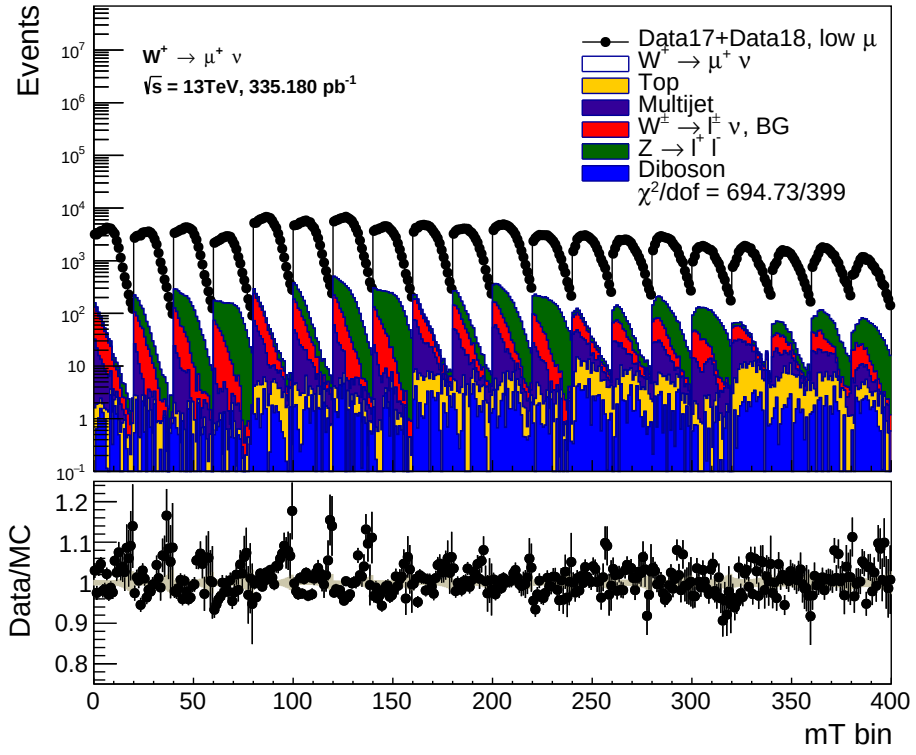

(b)

Figure 8.5 – The control plots of unrolled m_{T} spectra in 13 TeV muon channels.

D is a diagonal matrix filled with N_{bins} eigenvalues of C^{syst}. X_L is made of N_{bins} rows of eigenvectors. Denoting $Z = \Sigma\Gamma^{-1}$, the original NPs α_p are transformed to a new set of NPs β_q according to:

$$\beta_q = \sum_p z_q^p \alpha_p \tag{8.17}$$

It can be easily shown that neither the post-fit value of the POI nor the total uncertainty of POI is affected by this transformation. In numerical computations, when C^{syst} is not full rank, the eigenvalues beyond the rank are not exactly zero but tiny values fluctuating around zero. For this reason, the absolute values are taken for the eigenvalues, so as to avoid the square root of negative values. As a result, a set of N_{bins} error vectors is always returned after the decomposition no matter C^{syst} is full rank or not. The up and down for each of these error vectors can be symmetrized with respect to 0 and then added to the nominal distribution to construct new paired systematic variations.

When the number of bins is smaller than the number of effective input systematic sources, the above procedure is guaranteed to reduce the number of NPs. However, in a real W-boson mass measurement with combined channels and categorization, the number of bins can easily exceed the number of NPs, especially when one would like to perform the NP transformation within each type of systematics to preserve the basic physics meanings of the NPs, i.e. in groups of electron SF, electron calibration, hadronic recoil and so on. As introduced in [6], a further step of approximation can be brought here to mitigate this issue by sorting the importance of the error vectors of C^{syst} from the highest to the lowest and then imposing a truncation below a certain threshold. The importance of the error vectors is assessed by the ranking of the corresponding eigenvalues, following the steps below.

First, all eigenvalues of the covariance matrix C^{syst} (taking the covariance matrix in Figure 8.6(a) for instance) are sorted from the highest to the lowest. Then the sum of absolute values of the eigenvalues are computed and normalized to unity. The absolute values of the eigenvalues are scaled according to the normalization. After that, a running sum is performed to sum up the absolute value of the eigenvalues from the last one to the n-th one, as shown in Figure 8.6(b), meaning that the running sum is equal to unity when $n = 1$ and decreases monotonically when n goes up. When setting a truncation at 1% for the relative importance of the eigenvalues in this example, the NPs for electron reconstruction SF systematics can be reduced from the initial 272 to only 3. Consequently, the probability model is largely simplified without losing much information of the systematics.

Only the error vectors associated with the eigenvalues above the truncation will be calculated and propagated to the probability model as new systematic variations. That being said, those error vectors associated with the eigenvalues below the truncation should in principle not be ignored either, otherwise one would expect an underestimation of the total uncertainty from the fit due to less systematic effects being accounted for in the probability model. One way to ensure a conservative total uncertainty, or in other words, to approximately preserve the total covariance matrix, is to first neglect the bin-by-bin correlation of the error vectors of those eigenvalues below the truncation, then treat them as bin-by-bin uncorrelated uncertainties and add them in quadrature. After that, these bin-by-bin uncorrelated systematic uncertainties are denoted to be σ_i^{trunc} for the i-th bin, and will still be taken into account in the profile likelihood fit in a way similar to the treatment of MC statistical uncertainty

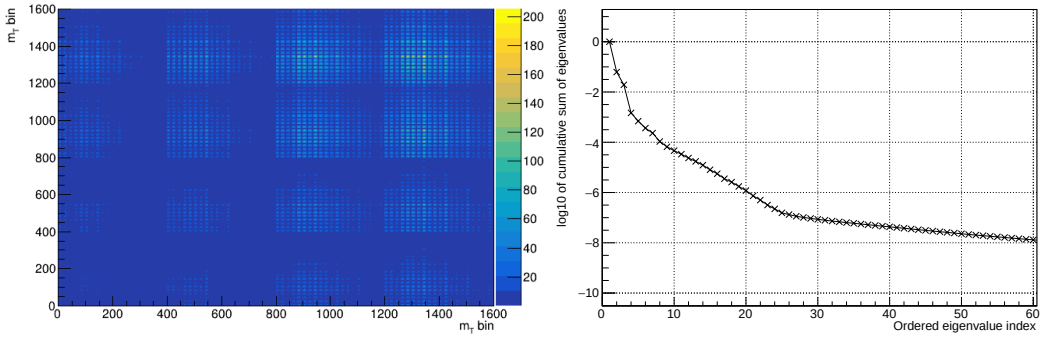

(a) (b)

Figure 8.6 – NP reduction based on covariance matrix. (a) The covariance matrix of electron reconstruction SF uncertainties on the m_{T} distribution. (b) The reserved running sum of eigenvalues of the covariance matrix.

(for instance, see Equation 8.24 for reference).

The above procedure of NP transformation can be justified for most experimental uncertainties because of their statistical nature. In contrast, all NPs accounting for theoretical uncertainties are kept unchanged, so as to avoid obscuring the physics meaning of the sources or mixing the possible non-Gaussian behaviour of some theory uncertainties. This strategy is expected to help the diagnostics of the fit and facilitate the interpretation of the result.

8.2.2 The handling of MC statistical uncertainty

Due to the finite number of recorded data events, fluctuations are expected in each bin of the observed kinematic distribution, bringing an uncertainty of statistical nature to the measurement when one extracts a physics quantity, such as m_W, from the kinematic distribution. Since the W-boson mass is inferred by comparing the data with the MC templates, a similar uncertainty originates from the limited number of the MC samples as well. The fluctuations in the prediction of each bin due to the limited number of MC samples result in the MC statistical uncertainty. Unlike in the χ^2 offset method, where the MC statistical uncertainty enters the total uncertainty following Equation 8.2, the MC statistical uncertainty in the profile likelihood fit needs to be handled by the Barlow-Beeston prescription [7], according to which one additional NP is assigned per analysis bin per sample to reflect the rate of statistical fluctuation. Once including these additional NPs into the probability model, the total uncertainty returned by the profile likelihood fit will correctly account for the effect of MC statistical uncertainty, as long as the difference of weights of MC events is relatively well under control. In practice, in order to reduce the total number of NPs in the probability model, a lighter version of this approach is implemented in HistFactory [3], which assigns one Barlow-Beeston NP to each analysis bin for all MC samples together. Following the Barlow-Beeston-Lite prescription, the statistical model for each bin is modified by a factor due to the presence of MC statistics:

$$Pois(n_i|v_i(\boldsymbol{\alpha}) + \gamma_i v_i^{MC}(\boldsymbol{\alpha}))Pois(m_i|\gamma_i\tau_i) \tag{8.18}$$

where $v_i(\boldsymbol{\alpha})$ stands for the MC predictions that do not need to include statistical uncertainty, and $v_i^{MC}(\boldsymbol{\alpha})$ are the MC predictions in which the statistical uncertainty has to be accounted for. The NP per bin, denoted as γ_i, corresponds to the true rate that may differ from the original prediction $v_i^{MC}(\boldsymbol{\alpha})$ within what is allowed by MC statistics. If the total MC statistical uncertainty is σ_i^{MC} for the i-th bin, then the relative statistical uncertainty becomes v_i^{MC}/σ_i^{MC}. Therefore, assuming a reasonable spread of the MC weights, the effective size of the MC samples can be written as $m_i = (v_i^{MC}/\sigma_i^{MC})^2$. The estimation of the MC bin content is deemed as an auxiliary measurement in this notation, so that the Poisson constraint term $Pois(m_i|\gamma_i\tau_i)$ is multiplied to the total likelihood, suggesting that m_i would fluctuate around $\gamma_i\tau_i$ when generating a new set of MC samples. While γ varies around unity in the fit, $\tau_i = (v_i^{MC}/\sigma_i^{MC})^2$ is treated to be a fixed constant as if it does not fluctuate when new MC samples are generated by pseudo-experiments. One advantage of Barlow-Beeston-Lite prescription is that the conditional maximum likelihood estimate $\hat{\hat{\gamma}}_i(\boldsymbol{\alpha})$ can be solved analytically as follows [3]:

$$\hat{\hat{\gamma}}_i(\boldsymbol{\alpha}) = \frac{-B + \sqrt{B^2 - 4AC}}{2A} \tag{8.19}$$

$$\begin{cases} A = v_i^{MC}(\boldsymbol{\alpha})^2 + \tau_i v_i^{MC}(\boldsymbol{\alpha}) \\ B = v_i(\boldsymbol{\alpha})\tau_i + v_i(\boldsymbol{\alpha})v_i^{MC}(\boldsymbol{\alpha}) - n_i v_i^{MC}(\boldsymbol{\alpha} - m_i v_i^{MC}(\boldsymbol{\alpha}) \\ C = -m_i v_i(\boldsymbol{\alpha}) \end{cases} \tag{8.20}$$

Despite the fact that the Barlow-Beeston-Lite approach is widely used in the analyses involving MC statistics, this method turns out to be CPU-wise demanding for the low pile-up W-boson mass analysis where the joint fit of all channels and all categories involves a few thousand analysis bins. However, neglecting completely the MC statistics in the fit will lead to an underestimated total uncertainty, which may affect the proper interpretation of the result of the measurement. As a preliminary attempt to speed up the fit, an effective approximation has been studied with the low pile-up m_W analysis which removes the Barlow-Beeston NPs. The approximation is valid as long as the size of the MC samples is at least a few times larger than that of the dataset. A similar method developed for the fit at the Gaussian limit is described in [8]. The formulation of this approximation, referred to as "data scaling" technique, will be illustrated in the paragraphs below.

Starting off without the presence of MC statistics, at the Gaussian limit of data statistics (more than a few tens of events in each bin), it is possible to describe the likelihood for each bin of the distribution by a Gaussian likelihood:

$$Pois(n_i|v_i) \approx Gaus(n_i|v_i, \sigma_i^{data}) \tag{8.21}$$

where σ_i^{data} is the data statistical uncertainty of the i-th bin. With the Gaussian likelihood, the MC statistics can be included in a straight-forward way:

$$Gaus(n_i|v_i, \sigma_i^{data}) \rightarrow Gaus(n_i|v_i, \sqrt{(\sigma_i^{data})^2 + (\sigma_i^{MC})^2}) \tag{8.22}$$

Due to the addition of MC statistics, the standard deviation enlarges, meaning the statistical power of the data diminishes accordingly, even though the observation stays at n_i. The Gaussian likelihood is capable of describing the mean and the standard deviation separately thanks to the two independent parameters in the function form.

In a Poisson likelihood, considering that the mean and the variance are described by the same single parameter, the only way to reflect the reduced statistical power is hence to scale down the mean and the observation of the Poisson by the same factor that catches the change in the variance:

$$Pois(n_i'|v_i') = Pois\left(n_i \cdot \frac{\left(\sigma_i^{data}\right)^2}{\left(\sigma_i^{data}\right)^2 + \left(\sigma_i^{MC}\right)^2} \middle| v_i \cdot \frac{\left(\sigma_i^{data}\right)^2}{\left(\sigma_i^{data}\right)^2 + \left(\sigma_i^{MC}\right)^2}\right) \tag{8.23}$$

Denoting the data scaling factor to be $s_i = \frac{\left(\sigma_i^{data}\right)^2}{\left(\sigma_i^{data}\right)^2 + \left(\sigma_i^{MC}\right)^2}$, the small bin-by-bin uncorrelated systematic uncertainties σ_i^{trunc} discussed in Section 8.2.1 can be treated in the same way as MC statistics and added back with an extended form of s_i:

$$s_i = \frac{\left(\sigma_i^{data}\right)^2}{\left(\sigma_i^{data}\right)^2 + \left(\sigma_i^{MC}\right)^2 + \left(\sigma_i^{trunc}\right)^2} \tag{8.24}$$

s_i is computed for each bin individually. The idea of the data scaling technique is consistent with the Barlow-Beeston-Lite prescription, which is to adjust the statistical power of the data by adding the effect of other sources of bin-by-bin uncorrelated uncertainties. It has to be pointed out that the MC statistical uncertainty is not parameterized in the formula of data scaling. As a result, the profile likelihood fit will gain significantly on the performance side. The approximation is anticipated to be applicable to the low pile-up m_W analysis, since the size of the signal MC samples is typically 5 to 10 times larger than the corresponding dataset. This approximate treatment of statistical uncertainty in the MC samples brings a marginal impact on the determination of the central value of m_W. A validation of this method, in terms of both the central value and the total uncertainty, has been performed with the following setup:

- Channel and kinematic distribution: 5 TeV $W^- \to e\nu$ channel, unrolled m_{T} distribution in categories of u_{T} and η_ℓ.
- Statistical uncertainties: data, signal MC, background MC and multijet.
- Systematic uncertainties: PDF, electron calibration, luminosity, background cross-section uncertainty, multijet shape and yield uncertainties.

When applying the data scaling, the NP reduction is only applied to the electron calibration systematics in the signal part of the probability model. The total uncertainty is retrieved from the nominal fit, where the pseudo data is the sum of nominal MC, nominal background and nominal multijet. In addition, 400 bootstrap toys of the pseudo data are generated in order to quantify the non-closure between the Barlow-Beeston-Lite prescription (BBL) and the data scaling: the discrepancy between the central values of the POI between the two methods for the 400 toys is presented in 8.7. As it turns out, the central values of the fits using data scaling technique slightly deviate from those of the fit using the BBL prescription, but well within the level of MC statistical uncertainty (around 10 MeV in the channel under study). Also, as summarized in Table 8.1, the total uncertainty of the fit with the data scaling is compatible and more conservative with respect to the Barlow-Beeston-Lite method in this exercise. Although the systematic variations and the luminosity calibration are not up-to-date in this study, the above conclusion will not be affected.

The final data scaling for each bin takes into account the statistical uncertainty in signal MC, in the background simulation, in the multijet estimation, as well as the

NP for systematics	MC statistics	Total uncertainty [MeV]
Full NP	No MC stats.	40.76
Full NP	BBL	42.63
NP reduction	No MC stats.	40.76
NP reduction	Data scaling	42.64

Table 8.1 – The status of the systematic uncertainties in the W-boson mass measurement. The MC statistics is taken into account by either the Barlow-Beeston-Lite prescription (BBL) or the data scaling.

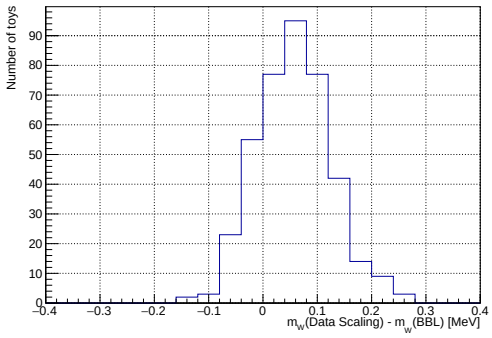

Figure 8.7 – The non-closure of the central value of the POI between data scaling and Barlow-Beeston-Lite prescription estimated from 400 bootstrap toys of the pseudo data. Even though there is a noticeable bias caused by the data scaling with respect to the Barlow-Beeston-Lite prescription, the bias itself is within the spread of the non-closure. On top of that, both the bias and the spread of non-closure are small with respect to the total uncertainty of 43 MeV.

small systematic uncertainties that are considered to be bin-by-bin uncorrelated. The level of the scaling is shown in Figures 8.8 and 8.9 for 5.02 and 13 TeV, respectively.

The factor of data scaling is smooth in the muon channels. However, due to the larger fraction of multijet background and the associated larger statistical uncertainty, the effect of data scaling is in general stronger in the electron channels. The noticeable spikes of the data scaling in the electron channels are also brought by the larger statistical uncertainty in the multijet estimation.

After a recent update of RooFit that significantly speeds up the fit, the CPU consumption of using the BBL prescription becomes affordable for the low pile-up m_W analysis. In order to avoid the compromise brought by the approximation of data scaling technique, the BBL prescription is eventually chosen to handle the MC statistical uncertainty in the profile likelihood fit. As an improvement introduced to this analysis, in m_i and τ_i of Equation 8.18, σ_i^{MC} is replaced by the quadratic sum of σ_i^{trunc} and σ_i^{MC} to keep the total uncertainty conservative. Even though it is not implemented in the low pile-up m_W analysis, the data scaling technique still remains highly interesting, since it is very likely to benefit to the future profile likelihood fit joining multiple m_W measurements, in which a huge total number of analysis bins is anticipated.

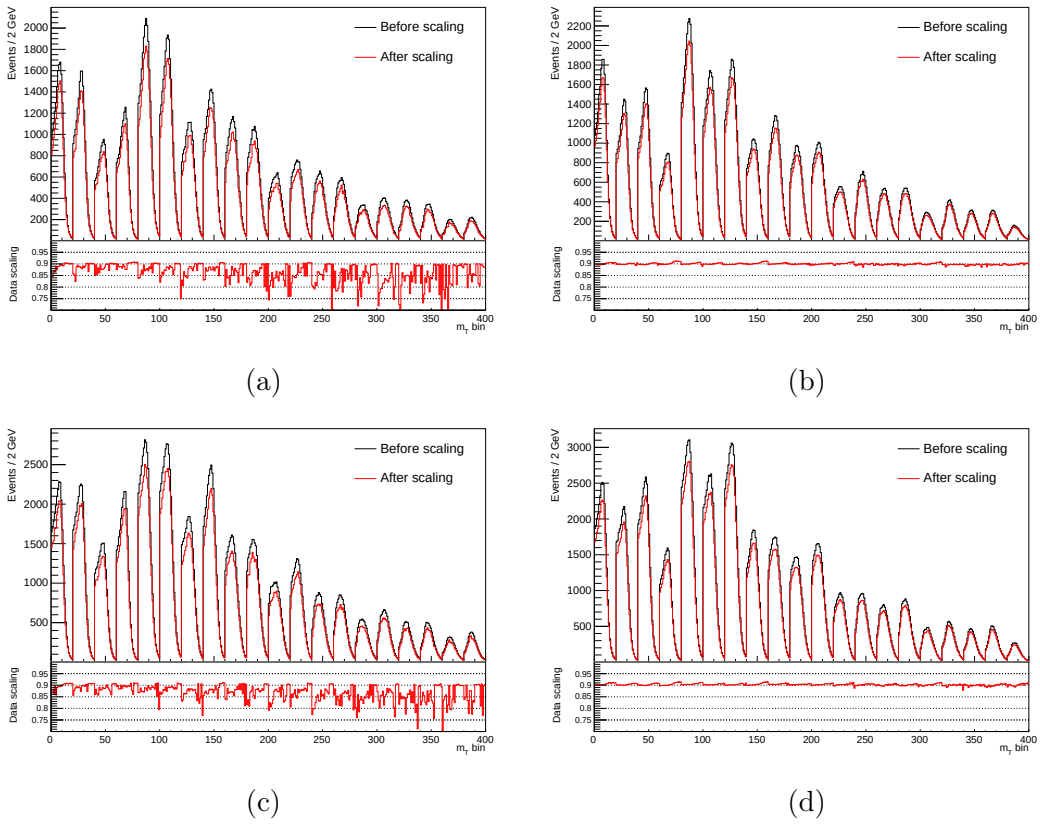

Figure 8.8 – The data scaling applied to the unrolled m_{T} spectra at 5 TeV. The distribution before the data scaling is pseudo data made of a sum of nominal signal MC, simulated background and multijet. (a) $W^- \to e\nu$ channel. (b) $W^- \to \mu\nu$ channel. (c) $W^+ \to e\nu$ channel. (d) $W^+ \to \mu\nu$ channel.

8.2.3 Combination of statistically correlated observables

Another limitation of the profile likelihood fit, compared to the χ^2 offset method, is the difficulty in combining the measurements from statistically correlated observables. While the results of the χ^2 offset method can be combined using the standard BLUE procedure [9][10], provided that the correlations between different observables are known, the Poisson terms in the profile likelihood fit make it impossible to introduce a simple correlation matrix to describe the statistical correlation between the bins of two kinematic distributions. Although one can always add one more dimension of the distribution to measure a new observable simultaneously, the events of the data in each measurement bin is drastically diluted when one more dimension is added to the probability model. Not only will there be a higher chance of finding an empty bin, but also the computation of the fit will become more time consuming with more bins. In order to mitigate or ultimately solve this drawback of the profile likelihood fit, several proposals have been worked out so far.

The first plan would be to fill a linear combination of the observables of interest and fit to the distribution of the new observable. For instance, the lepton p_{T} and m_{T} are statistically correlated in the W-boson mass analysis. Both of these two quantities have good sensitivity to the W-boson mass. Instead of doing the measurement using each observable separately and then combining the two results, a linear combination,

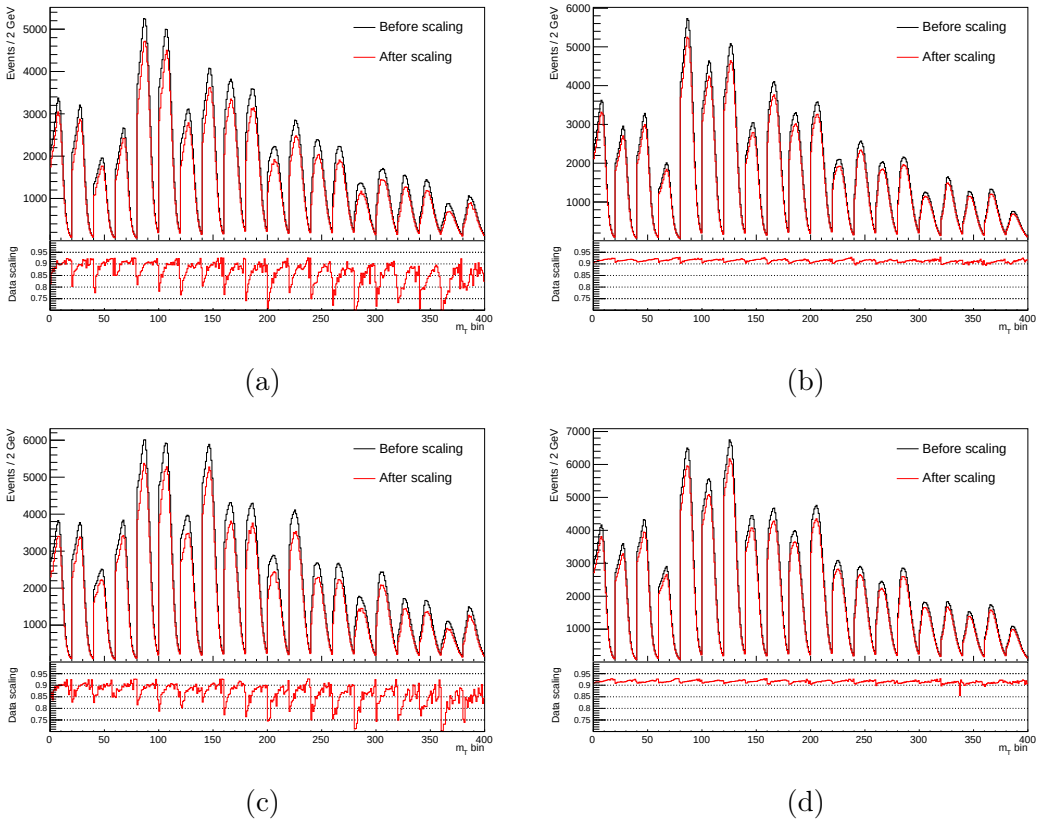

Figure 8.9 – The data scaling applied to the unrolled m_{T} spectra at 13 TeV. The distribution before the data scaling is pseudo data made of a sum of nominal signal MC, simulated background and multijet. (a) $W^- \to e\nu$ channel. (b) $W^- \to \mu\nu$ channel. (c) $W^+ \to e\nu$ channel. (d) $W^+ \to \mu\nu$ channel.

for example

$$Sm_{\mathrm{T}} = 2a \cdot p_{\mathrm{T}}^{\ell} + (1-a) \cdot m_{\mathrm{T}} \tag{8.25}$$

can be devised for each event in data and MC. The distribution of Sm_{T} is a valid input to the profile likelihood fit, since its bins are statistically uncorrelated, such that the information of both lepton p_{T} and m_{T} is used simultaneously with double counting. A factor of 2 is multiplied to p_{T} to make the scales of the two observables more compatible in the sum, as $m_{\mathrm{T}} \approx 2p_{\mathrm{T}}^{\ell}$ in the $u_{\mathrm{T}} <\approx 25\,\mathrm{GeV}$ region that is interesting for the W-boson mass analysis. The combination coefficient a, which resembles the combination weight in the BLUE method, cannot be known from any prior knowledge and has to be optimized using (pseudo) data to achieve the smallest total uncertainty. The flexibility of this proposal is that Equation 8.25 can be easily extended to include other observables such as the neutrino $E_{\mathrm{T}}^{\mathrm{miss}}$ to better constrain recoil calibration systematics. In case there is categorization in the fit, the combination coefficient a needs to be determined separately in each category. The determination of the combination coefficients is shown in Figure 8.10 for an illustration, where only the signal part of the probability model is fitted and only the data and MC statistical uncertainties are taken into account. The Sm_{T} is ultimately optimized against statistical uncertainty, recoil calibration systematics, lepton calibration and efficiency scale factor systematics, PDF uncertainty and the p_{T}^{W} modelling uncertainty. The optimization of the

coefficients is studied with an interval of 0.1. The corresponding result is summarized in Table 8.2. A joint Sm_{T} fit of all the 20 categories using the optimized combination coefficients yields an total uncertainty of 37.22 MeV. In comparison, the total uncertainty of the m_{T} fit is slightly worse: 37.84 MeV. A better performance of the Sm_{T} is anticipated, provided that the two observables in the combination share a moderate correlation but carry comparable BLUE weights.

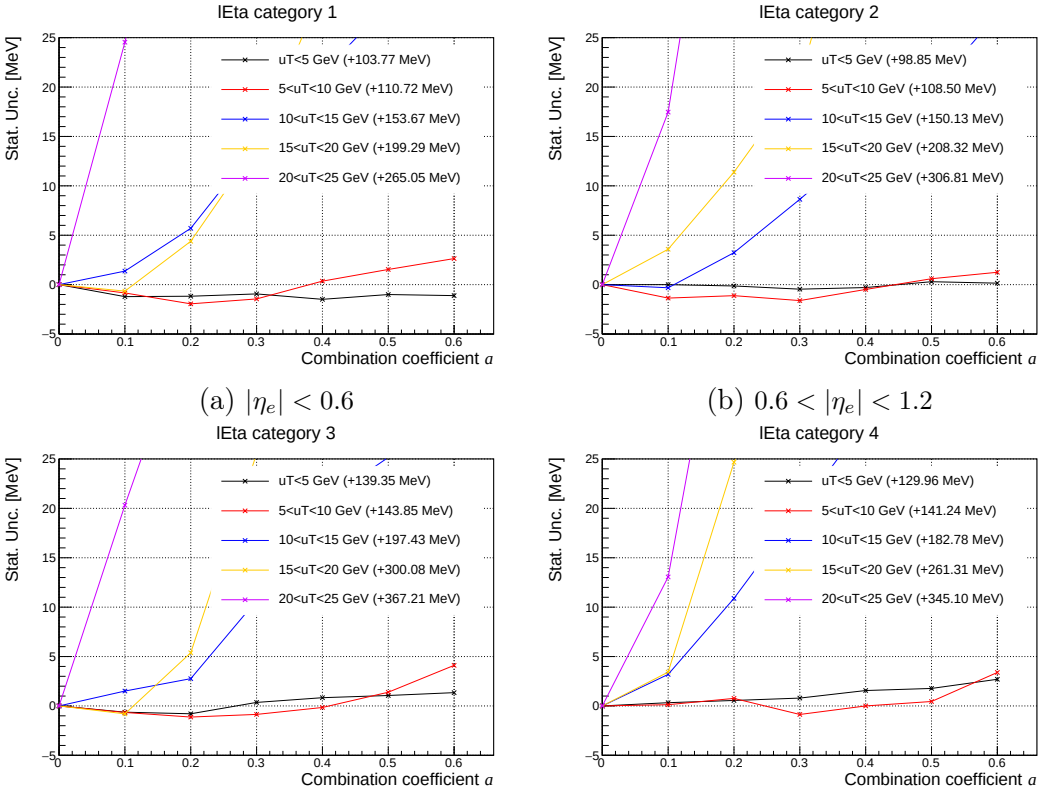

(a) $|\eta_e| < 0.6$ (b) $0.6 < |\eta_e| < 1.2$

(c) $1.2 < |\eta_e| < 1.8$ (d) $1.8 < |\eta_e| < 2.47$

Figure 8.10 – The optimization of combination coefficients for Sm_{T} in 5 TeV $W^- \to e\nu$ channel taking into account the data and MC statistical uncertainties. The minima of the uncertainty curves for each channel correspond to the preferred value of the combination coefficients.

Despite the elegance of the formula, the optimization of the combination coefficients against the total uncertainty is time consuming. Besides, due to the bin-to-bin correlation in the systematic variations, the optimization in separate categories including systematics may not lead to the optimal total uncertainty when all categories are combined in a joint fit. Finally, with the Run 2 low pile-up data, the improved recoil resolution greatly helps m_{T} gain statistical sensitivity to the W-boson mass. Particularly, in the region 15< u_{T} <25 GeV, m_{T} becomes way more sensitive to the W-boson mass than p_{T}^{ℓ} in comparison. The addition of p_{T}^{ℓ} is not expected to improve the result of m_{T} by a large degree, which justifies the setup of the profile likelihood fit focusing on only the m_{T} distribution at this stage of the analysis.

A possible alternative solution, as already implemented in the reanalysis of ATLAS measurement of the W-boson mass at 7 TeV [11], would be to simultaneously run bootstrap toys in m_{T} fit and p_{T}^{ℓ} fit, for both the data n_i and the global observables

$a(u_{\mathrm{T}}, \eta_e)$	$\lvert\eta_e\rvert < 0.6$	$0.6 < \lvert\eta_e\rvert < 1.2$	$1.2 < \lvert\eta_e\rvert < 1.8$	$1.8 < \lvert\eta_e\rvert < 2.47$
u_{T} <5 GeV	0.4	0.3	0.2	0
5<u_{T} <10 GeV	0.2	0.3	0.2	0.3
10<u_{T} <15 GeV	0	0.1	0	0
15<u_{T} <20 GeV	0.1	0	0.1	0
20<u_{T} <25 GeV	0	0	0	0

Table 8.2 – The optimal combination coefficients for Sm_{T} in 5 TeV $W^- \to e\nu$ channel.

a_p in Equation 8.8. The correlation revealed by the bootstrap toys can be used to combine the uncertainties of the measurement from multiple observables.

8.3 Review of uncertainties in the W-boson mass fit

The types of uncertainty sources entering the determination of the W-boson mass should include:

- Statistical uncertainty: bin-by-bin uncorrelated uncertainty stemming from data, signal MC, background MC and multijet estimation.
- Experimental uncertainty: electron SF, electron calibration, muon SF, muon calibration and recoil calibration.
- Background uncertainty: luminosity uncertainty, cross-section uncertainty of simulated background process, multijet yield and shape uncertainties.
- Uncertainty in electroweak corrections.
- QCD modelling uncertainty: fixed-order PDF uncertainty, spin-correlation and the p_{T}^W modelling uncertainty.

All the systematic variations are symmetrized with respect to the nominal in the probability model for the W-boson mass fit.

8.3.1 Experimental, background and luminosity uncertainties

All experimental uncertainties, as discussed in Sections 6.1 6.2 and 6.3, along with the background cross-section uncertainties and luminosity uncertainties reuse what has been applied to the p_{T}^W analysis.

The electron reconstruction SFs are extrapolated from the standard high pile-up SFs to the low pile-up regime and is applied to both the 5.02 and 13 TeV datasets. The electron identification SFs are measurement in-situ using Z samples, separately for 5.02 and 13 TeV data. The electron isolation and trigger efficiencies SF are measured in-situ using combined 5.02 and 13 TeV low pile-up datasets. The uncertainties of the electron SFs measurements include the statistical uncertainty due to the limited number of tag-and-probe pairs and the systematic uncertainties dominated by the photons and background control performance. The statistical uncertainies are uncorrelated in the SF bins, while the systematics are considered to be correlated. The electron energy scale and resolution corrections are determined from the Z events in the low pile-up datasets using the standard ATLAS procedures [12]. The systematic uncertainties related to the calorimeter modelling estimated at high pile-up conditions are not yet included in the low pile-up m_W analysis due their overly con-

servative variations in the available version at the time. After further investigations and validations, these uncertainty sources will be accounted for in the future.

The muon reconstruction SFs are extrapolated from the high pile-up results [13], while the trigger SFs, the isolation SFs and the TTVA SFs are meausred in-situ using the low pile-up data. The muon SF uncertainties consist of both the statistical uncertainty of the tag-and-probe method and the systematic uncertainties mainly attributed to the background subtraction and the variation of the selection criteria used in the tag-and-probe method [14]. The muon momentum scale and resolution are derived from the high pile-up data. The muon sagitta bias corrections are derived from the 2017 low pile-up datasets. The muon calibration will have to be further improved for the m_W measurement, since large uncertainties have been found in muon energy scale and muon sagitta bias.

The hadronic recoil calibration corrects for the mis-modelling of the underlying events, the direction of the recoil, as well as the response and the resolution the recoil. The recoil calibration uncertainties originate from the non-closure in the extrapolation of the calibration from Z events to W events, and from the statistical uncertainty in the response and resolution corrections.

A cross-section uncertainty of 10 % is assigned to the simulated top-quark related background processes and di-boson background, except for an uncertainty of 7 % on the $t\bar{t}$ process. The cross-section uncertainty of background contributed by the Z-boson, charge flip of the lepton detection and the W-boson decaying into a pair of tau and neutrino are conservatively estimated to be 5 %. The luminosity uncertainty, 1.0% for 5 and 0.92% for 13 TeV are determined from the luminosity calibration using a combination of the primary measurement with the LUCID-2 detector [15] and the complementary measurements with inner detector and calorimeters [16]. The multijet background is estimated using the data-driven method for the p_{T}^{W} analysis. However, small modifications are introduced to the determination of the yield and shape for both the central value and the associated uncertainties, in order to adapt to the different event selection as well as the categorization in the m_W analysis.

An additional selection u_{T} <25 GeV is applied to all four regions for the data-driven multijet estimation defined in Section 5.4. The extrapolation of the yield keeps the same methodology, based on p_{T}^{ℓ}, m_{T} and $E_{\mathrm{T}}^{\mathrm{miss}}$ spectra. For the moment, the multijet yield uncertainty is only given by the extrapolation uncertainty.

The linear extrapolation formula Equation 5.23 requires ample statistics in all anti-isolated slices. But in the W-boson mass measurement, the estimation of the multijet shape relies on the unrolled m_{T} spectrum in categories of u_{T} and η_{ℓ}. The 2D categorization causes low statistics in each anti-isolated slice of CR2 with an interval of 0.1, making the linear extrapolation formula no longer reliable. Therefore, the central value of the multijet shape in SR (0<isolation<0.1) is simply taken from the first anti-isolated slice in CR2 (0.1<isolation<0.2), while the shape variation is defined to be the overall shape in CR2 for 0.1<isolation<0.5. The histogram smoothing in ROOT based on the algorithm 353QH [17] is applied to both the central value and the shape variation. Any bins of the distribution below zero are set to zero manually afterwards. The statistical uncertainty is directly taken from the 0.1<isolation<0.2 slice in CR2 regardless of the smoothing or the manual modification of negative bin content. As an example, the multijet background on m_{T} for the W-boson mass fit in is shown in Figure 8.11 for the 13 TeV $W^{+} \to \mu\nu$ channel. The central value with the statistical uncertainty, the yield variations and the shape variations are all displayed

in the plot.

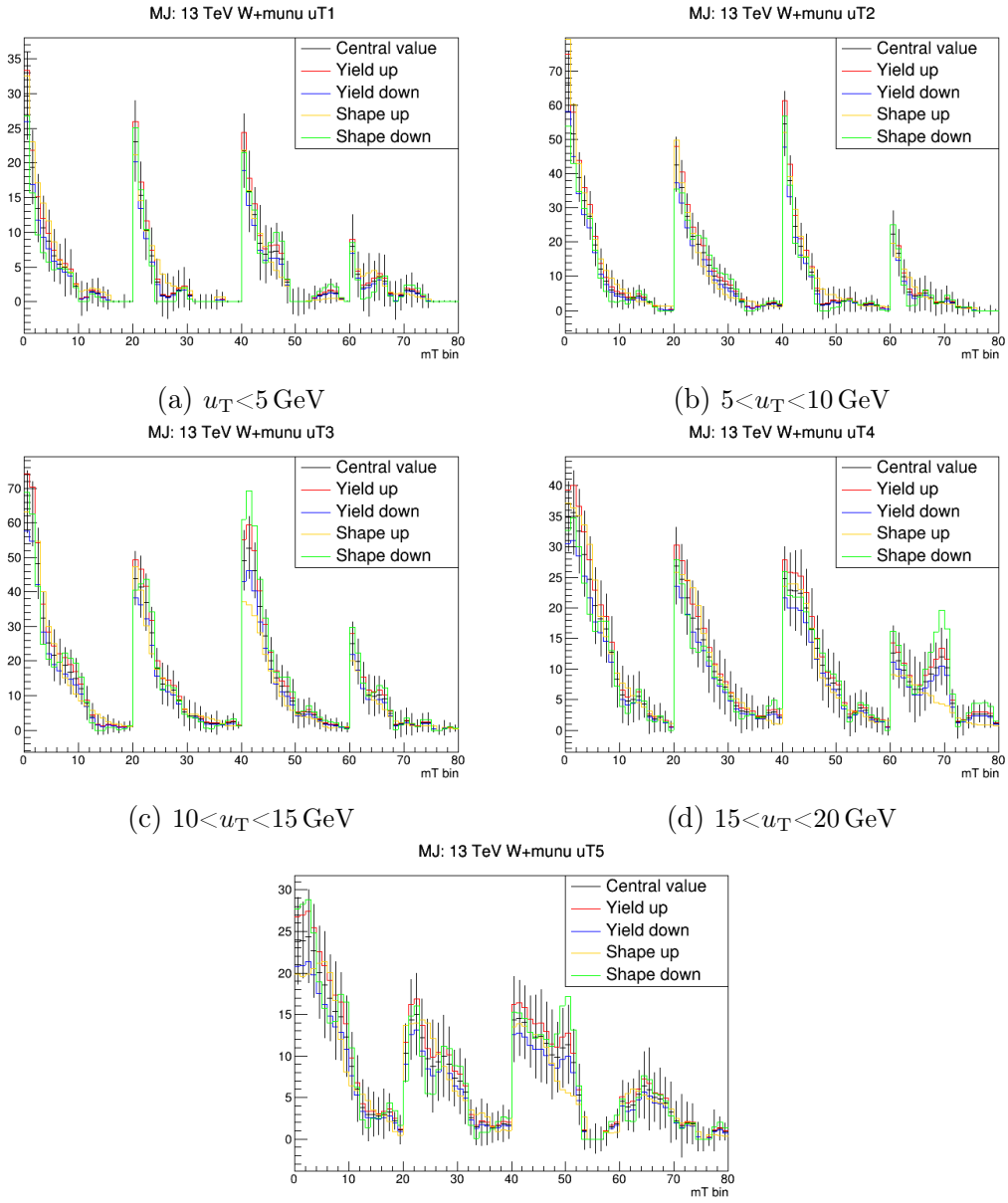

(a) u_{T}<5 GeV

(b) 5<u_{T}<10 GeV

(c) 10<u_{T}<15 GeV

(d) 15<u_{T}<20 GeV

(e) 20<u_{T}<25 GeV

Figure 8.11 – The data-driven multijet background of m_{T} spectra in 13 TeV $W^{+}\mu\nu$ channel. The data scaling described in Section 8.2.2 is not applied to the distributions. Every 20 bins in the unrolled m_{T} distribution correspond to a category of η_{ℓ}.

8.3.2 Propagation of the p_{T}^{W} uncertainty from the measurement

In the 7 TeV m_W measurement by ATLAS [5], the systematic uncertainty that stems from the p_{T}^{W} modelling is at the level of 6 MeV, including the uncertainty in parton shower tuning, the parton shower PDF uncertainty, the variations of the masses of the charm and bottom quarks, as well as the variations of the factorization

scale in the calculation of QCD ISR. In order to constrain the p_{T}^{W} uncertainty, the m_W measurement using low pile-up data will make use of the result of the direct p_{T}^{W} measurement. As a preliminary study of the m_W fit, one important goal is to estimate the level of uncertainty originating from the p_{T}^{W} in low pile-up data. This estimation can be achieved by propagating the unfolded level p_{T}^{W} uncertainty from the direct measurement reported in Section 7.5.1 to the probability model of the W-boson mass fit.

The central value of the underlying p_{T}^{W} distribution in the simulation is reweighted in p_{T}^{W} as described in Section 7.3. The uncertainty variations of the p_{T}^{W} distribution are derived from the total covariance matrix at unfolded level, also provided by the p_{T}^{W} measurement. The total covariance matrix at unfolded level for p_{T}^{W} <63 GeV (9 bins in each dimension) is shown in Figure 8.12 for the electron channels. An eigenvalue decomposition is performed on the covariance matrix to produce 9 pairs of error vectors of the p_{T}^{W}, with each pair symmetrized with respect to the central value of the measurement. Similar to the reweighting of the central value, the underlying p_{T}^{W} distribution in the simulation can also be reweighted to the up and down variations of the 9 pairs of error vectors, shown in the top rows of Figures 8.13 and 8.14. For the m_W measurement, all kinematic distributions of the signal process at the reconstructed level are produced with the underlying p_{T}^{W} reweighted to the central value of the measurement and to the 9 pairs of up and down variations. For example, the bottom rows of Figures 8.13 and 8.14 present the p_{T}^{W} variations on the m_{T} spectra. After that, the p_{T}^{W} variations of the reconstructed level distributions are injected to the probability model for template morphing, and 9 NPs are assigned to the p_{T}^{W} systematics per boson charge and per center-of-mass energy.

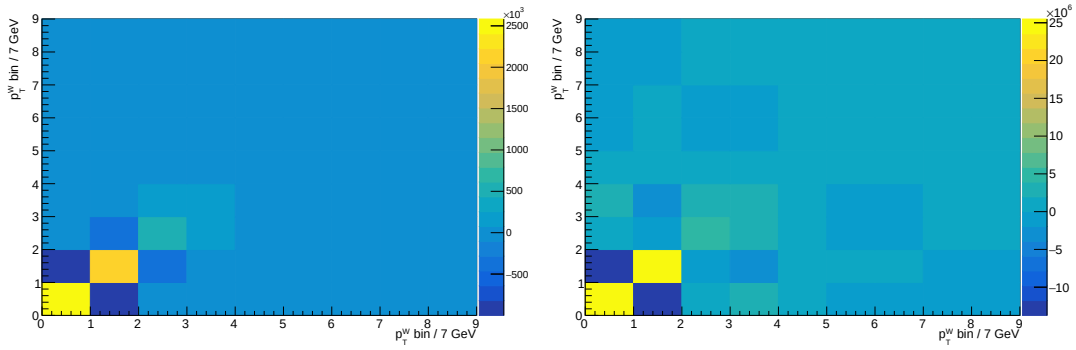

(a) (b)

Figure 8.12 – Examples of the total covariance matrix of the p_{T}^{W} at unfolded level. (a) 5 TeV $W^- \to e\nu$ channel. (b) 13 TeV $W^- \to e\nu$ channel.

Although the propagation of the p_{T}^{W} uncertainty described above provides a simplified treatment of the p_{T}^{W} modelling uncertainty in the low pile-up W-boson mass measurement, by no means it should become the final strategy for the p_{T}^{W} uncertainty in the analysis. First, the correlation between the boson p_{T} and rapidity are ignored in the 1D p_{T}^{W} reweighting. Second, the recoil calibration uncertainties are major sources of systematic uncertainty shared by the p_{T}^{W} analysis and the W-boson mass analysis. The correlation of recoil calibration uncertainties at unfolded level for the p_{T}^{W} analysis and at reconstructed level for the W-boson mass analysis is not properly accounted

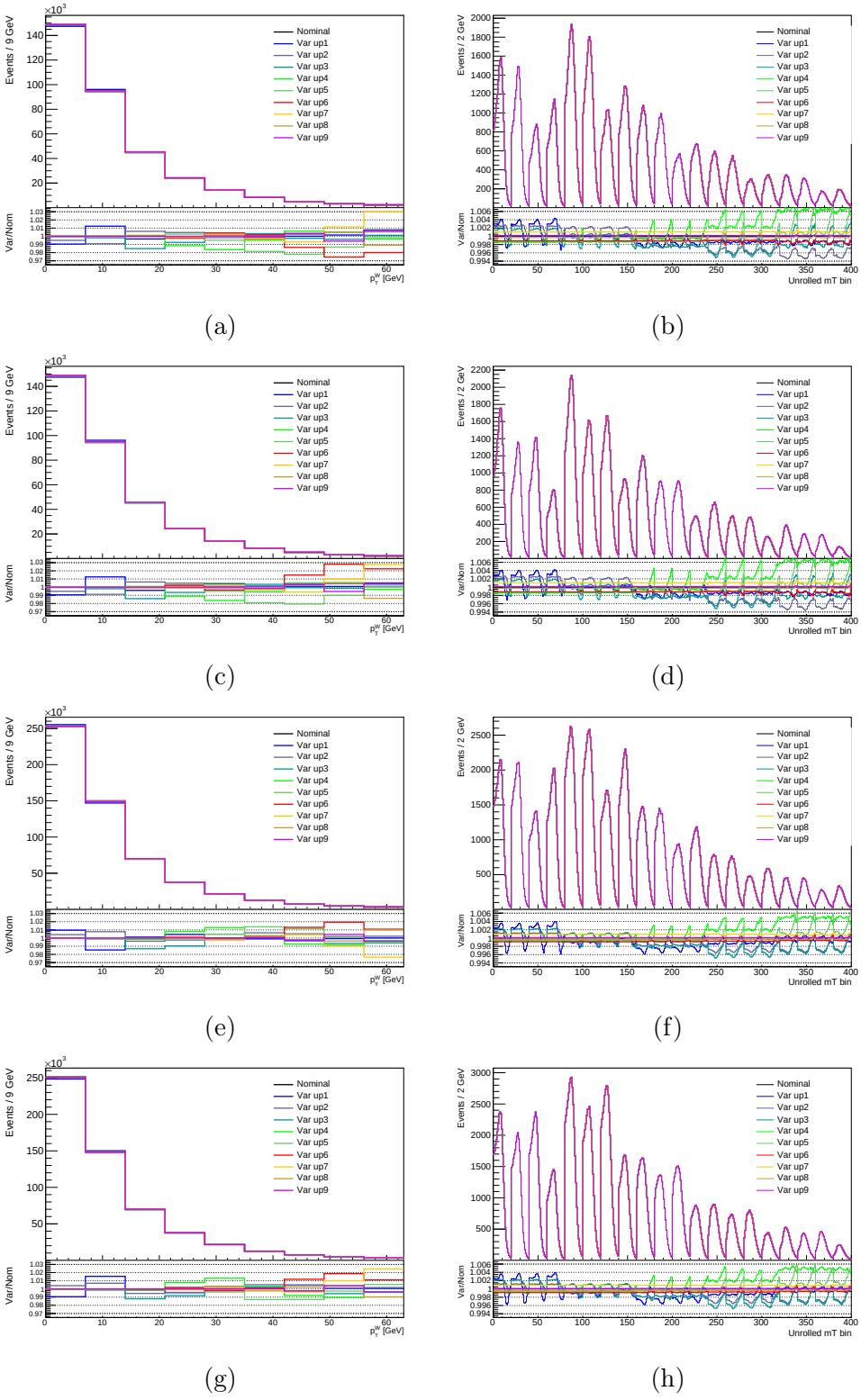

Figure 8.13 – Propagation of the p_{T}^{W} uncertainty from the direct measurement at 5 TeV to the W-boson mass fit. Orthogonal error vectors (left): at unfolded level. (right): on the reconstructed level m_{T} distributions. (a)(b) $W^- \to e\nu$. (c)(d) $W^- \to \mu\nu$. (e)(f) $W^+ \to e\nu$. (g)(h) $W^+ \to \mu\nu$.

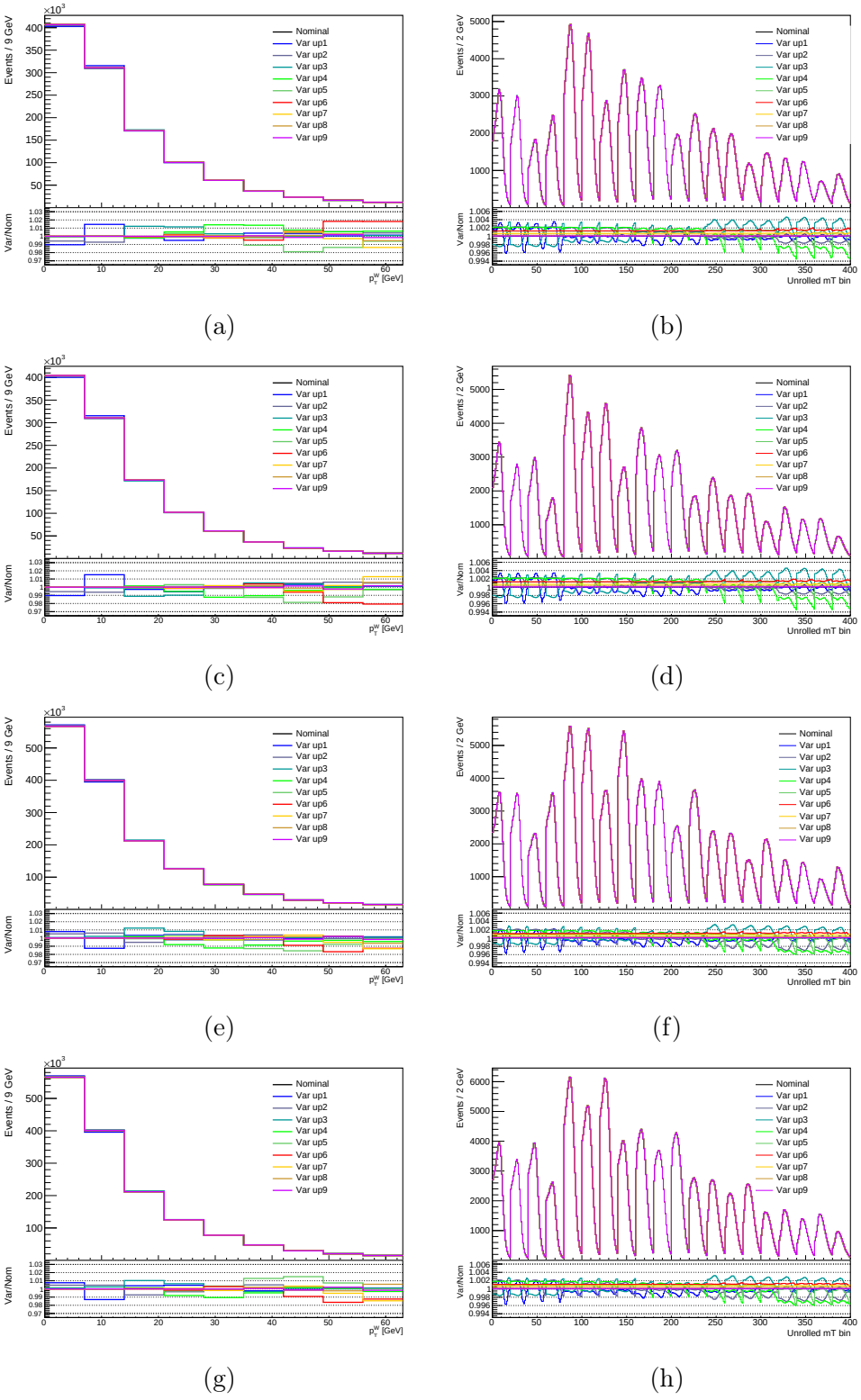

Figure 8.14 – Propagation of the p_{T}^{W} uncertainty from the direct measurement at 13 TeV to the W-boson mass fit. Orthogonal error vectors (left): at unfolded level. (right): on the reconstructed level m_{T} distributions. (a)(b) $W^- \to e\nu$. (c)(d) $W^- \to \mu\nu$. (e)(f) $W^+ \to e\nu$. (g)(h) $W^+ \to \mu\nu$.

for in the current method. A possible solution to making use of the results of the p_{T}^{W} measurement in a more appropriate way will be discussed in Section 8.5.

8.3.3 PDF and other modelling uncertainties

A major QCD modelling uncertainty for W-boson mass measurements in hadron colliders is the uncertainty in the fixed-order QCD calculation. The fixed-order QCD uncertainty is assessed with the help of global PDF sets. The central value of the default PDF set used in the generation of signal MC samples is CT10 [18], a NLO accuracy PDF set, even though the most up-to-date PDF uncertainties are available at NNLO accuracy and are considered for the W-boson mass measurement. To keep the PDF baseline matching the variations, a reconstructed level PDF reweighting is applied to the unrolled m_{T} spectrum to replace the baseline PDF by an NNLO prediction: CT18ANNLO [19], a global PDF set including the ATLAS 7 TeV data of W/Z rapidity distributions [20] in the fit. The PDF baseline reweighting procedure goes as the following:

- Generate the nominal signal MC distribution using CT10 and using CT18ANNLO with the help of an internal Powheg+Herwig7 [21] PDF reweighting.
- Calculate the reconstructed level ratio of CT18ANNLO/CT10 (p_{T}^{W}, y) 2D reweighting for the nominal signal MC distribution.
- Apply the CT18ANNLO/CT10 derived in the step above to all the entire signal part of the probability model, including: nominal MC, the W-boson mass templates, the systematic variations related to the signal apart from the PDF variations of CT18ANNLO.

The effect of this PDF baseline reweighting is shown in Figures 8.15 and 8.16.

For the moment, the uncertainty in the fixed-order QCD calculation is assessed using the 29 pairs of eigenvector sets of CT18ANNLO global PDF. As a more recent global PDF set, CT18ANNLO provides better precision than the CT10NNLO [22], CT14NNLO [23] and MMHT2014 [24] considered in the previous ATLAS m_W measurement at 7 TeV center-of-mass energy. The PDF uncertainty in the low pile-up m_W measurement is expected to be lower than the 9 MeV reported in the 7 TeV publication, thanks to the updated result of the global PDF analysis and the profile likelihood technique used in the statistical analysis.

Another source of QCD modelling uncertainty is the spin-correlation uncertainty. For the nominal signal process, the spin-correlation coefficients in the signal MC is reweighted from the Powheg prediction to the DYTURBO prediction using CT10 PDF at NNLO accuracy in a 2D mapping of spin-correlation coefficients in bins of the W-boson p_{T} and rapidity. Different from the estimation of spin-correlation uncertainty in the 7 TeV paper, where the uncertainties in the prediction of the W-boson angular coefficients are propagated from the experimental uncertainty of the Z-boson production measurement [25] while taking into account the non-closure between the measurement and the prediction of A_2 as a function of p_{T}^{Z}, for the low pile-up analysis a variation of spin-correlation coefficients will be produced by reweighting the Powheg prediction to DYTURBO prediction at NLO accuracy. However, whether or not the NLO vs NNLO difference of spin-correlation coefficients can be used as the systematic variation for the analysis needs validation in the future.

As for baseline electroweak corrections, the QED ISR is included in Pythia8 parton [26] shower, while the QED FSR is taken into account by interfacing the

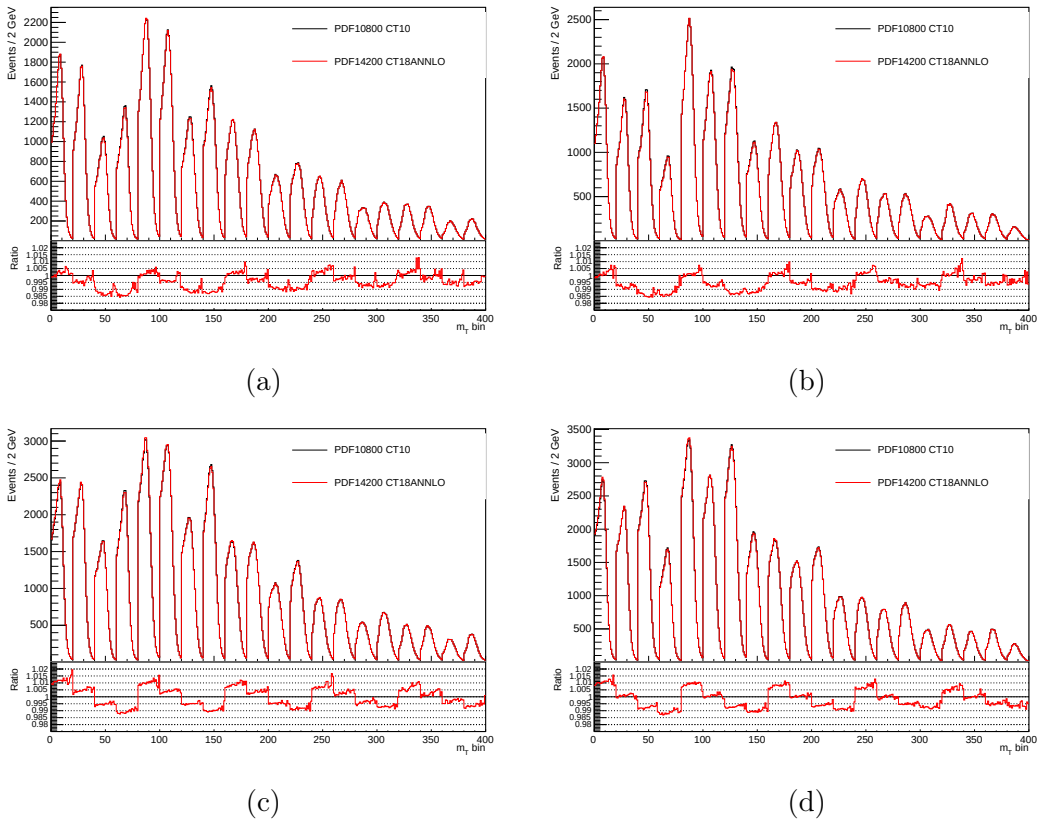

Figure 8.15 – The ratio of reconstructed level CT10ANNLO/CT10 reweighting on the unrolled m_{T} spectra at 5 TeV. (a) $W^- \to e\nu$ channel. (b) $W^- \to \mu\nu$ channel. (c) $W^+ \to e\nu$ channel. (d) $W^+ \to \mu\nu$ channel.

Powheg+Pythia8 [27]–[30] prediction to PHOTOS++ [31]. The electroweak uncertainty will be evaluated by Winhac [32] at reconstructed level. The uncertainty in QED FSR correction is obtained by comparing the default photon emission matrix elements of PHOTOS++ with the calculation of Yennie–Frautschi–Suura formalism available in Winhac. The other sources of electroweak uncertainty include the missing pure weak correction, the interference between QED ISR and QED FSR, as well as the effect of lepton pair production in the final state. As for an improvement in the low pile-up m_W analysis, the electroweak correction uncertainties will be folded to the reconstructed level to give a more conservative and realistic representation of the uncertainty with respect to the previous 7 TeV measurement.

8.4 Summary of preliminary results

Profile likelihood fits have been used to extract the W-boson mass from the low pile-up data. A blinding of m_W is applied to the fitting procedures. The report of preliminary results of the low pile-up m_W measurement focuses on the uncertainty of the measurement. The uncertainty decomposition for the profile likelihood fit is presented following the prescription of [33], and will be explained in details in the next chapter. In brief, the bin-by-by uncorrelated statistical uncertainties can be estimated by fluctuating the (pseudo) data to make bootstrap toys and by repeating

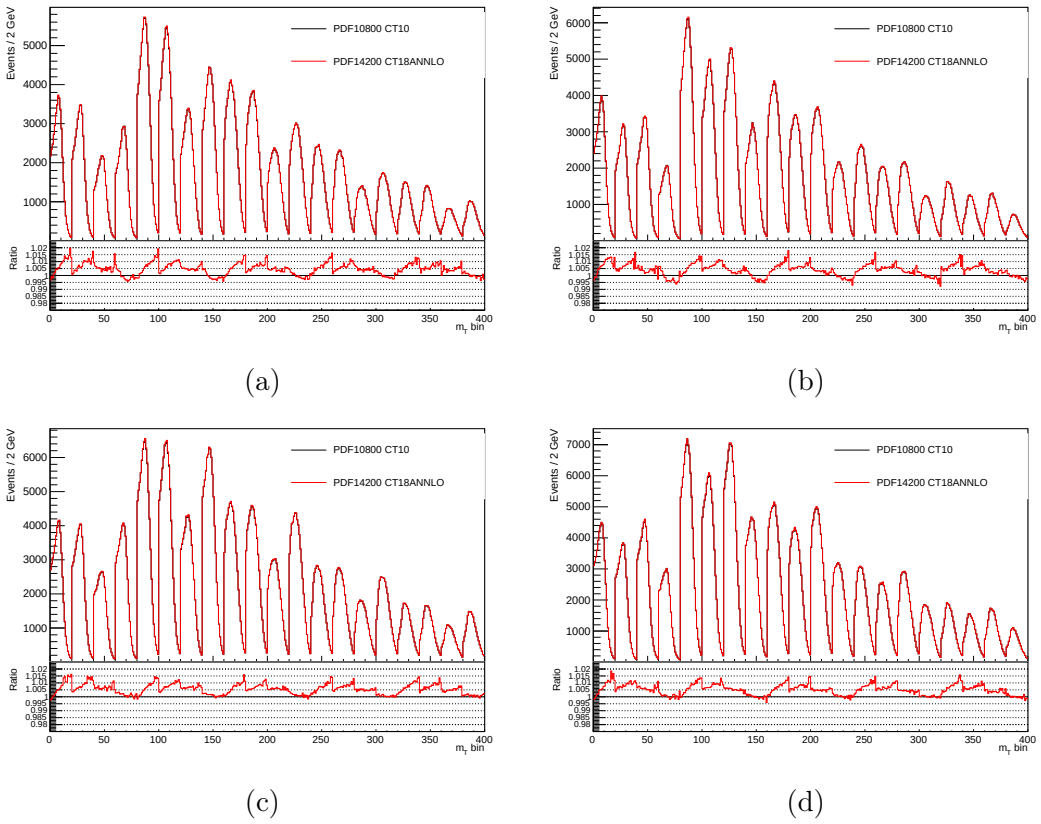

Figure 8.16 – The ratio of reconstructed level CT10ANNLO/CT10 reweighting on the unrolled m_{T} spectra at 13 TeV. (a) $W^- \to e\nu$ channel. (b) $W^- \to \mu\nu$ channel. (c) $W^+ \to e\nu$ channel. (d) $W^+ \to \mu\nu$ channel.

the fit to these toys using the full probability model. The spread of the toys gives the contribution from the statistical uncertainty. A source of systematic uncertainty that affects the kinematic distribution in a bin-by-bin correlated manner can be estimated by pulling the corresponding global observable from the central value to ± 1 standard deviation, then repeating the fit using the full probability model. The offset in the POI with respect to the nominal fit to the Asimov data corresponds to the contribution from this systematic source.

The current status of the systematic uncertainties considered in the measurement is summarized in Table 8.3.

Experimental systematics		Theoretical systematics	
Source	Status	Source	Status
Recoil calibration	Done	PDF uncertainties	CT18ANNLO
Lepton SF	Done	Spin-correlation coefficients	On-going
Lepton calibration	Done	EW corrections	On-going
Luminosity	Done	Background cross-sections	Done
Multijet systematics	Done	p_{T}^{W} modelling	Done

Table 8.3 – The status of the systematic uncertainties in the W-boson mass measurement.

8.4.1 Separate fit in individual channels

With the current scheme of categorization, each W-boson decay channel comprises 400 bins of (m_{T},u_{T},η_ℓ) distribution. The NP reduction is carried out at the level of all channels and categories. The details of the uncertainty break-down in each channel are presented in Tables 8.4, 8.5 and 8.6.

Channel	Total	Stat.	Syst.
5 TeV $W^- \to e\nu$	40.78	33.20	23.68
5 TeV $W^+ \to e\nu$	37.56	28.35	24.64
5 TeV $W^- \to \mu\nu$	60.37	50.41	33.21
5 TeV $W^+ \to \mu\nu$	60.67	49.34	35.31
13 TeV $W^- \to e\nu$	33.21	25.86	20.84
13 TeV $W^+ \to e\nu$	31.09	23.35	20.53
13 TeV $W^- \to \mu\nu$	59.05	46.61	36.25
13 TeV $W^+ \to \mu\nu$	59.61	46.51	37.29

Table 8.4 – The total uncertainty, statistical uncertainty and total systematic uncertainty of the fit in separate channels. Unit in [MeV]. The statistical uncertainty is the quadratic difference between the total uncertainty and the systematic uncertainty.

Channel	Lepton SF	Lepton Calib.	Recoil	Lumi.	MJ
5 TeV $W^- \to e\nu$	7.55	17.17	6.89	1.14	2.17
5 TeV $W^+ \to e\nu$	6.89	18.44	6.96	0.69	1.39
5 TeV $W^- \to \mu\nu$	11.19	27.35	5.37	1.46	1.98
5 TeV $W^+ \to \mu\nu$	11.84	29.16	5.96	0.79	1.44
13 TeV $W^- \to e\nu$	7.23	11.38	6.36	0.87	4.86
13 TeV $W^+ \to e\nu$	6.74	11.62	6.46	0.62	2.84
13 TeV $W^- \to \mu\nu$	8.38	31.03	5.24	1.44	4.16
13 TeV $W^+ \to \mu\nu$	8.59	32.36	5.40	0.98	2.80

Table 8.5 – The decomposition of the experimental uncertainty for the fit in separate channels. Unit in [MeV].

Even though the numbers of events are comparable between the electron and the muon channels in the data, the statistical uncertainties in the muon channels are much higher due to the large muon calibration systematic variations and the strong correlations between the POI and the NPs for muon calibration systematics.

8.4.2 Joint fit of all channels

The joint fit of eight channels in the low pile-up datasets involves a minimization of 3200 bins in total, with more than 500 NPs for systematics after the NP reduction. In order to estimate the contribution of the bin-by-bin uncorrelated uncertainties, 400 bootstrap toys of data are produced for data statistical uncertainty, along with another 400 bootstrap toys of the nominal prediction (the sum of signal MC samples, background MC samples and multijet) as pseudo data for MC statistical uncertainty.

Channel	MC background	PDF	p_{T}^{W}
5 TeV $W^- \to e\nu$	4.12	11.53	2.36
5 TeV $W^+ \to e\nu$	3.25	12.51	1.30
5 TeV $W^- \to \mu\nu$	4.99	12.66	3.11
5 TeV $W^+ \to \mu\nu$	4.27	14.01	1.86
13 TeV $W^- \to e\nu$	3.86	12.90	2.42
13 TeV $W^+ \to e\nu$	2.88	13.30	2.33
13 TeV $W^- \to \mu\nu$	5.35	14.07	2.72
13 TeV $W^+ \to \mu\nu$	3.21	14.53	2.35

Table 8.6 – The decomposition of the modelling uncertainty for the fit in separate channels. Unit in [MeV].

In this process, the pseudo data of the nominal prediction is fluctuated according to the power of MC statistics. The decomposition of the uncertainty is shown in Tables 8.7, 8.8 and 8.9.

Total	Stat.	Syst.
16.64	13.49 ± 0.75	9.97

Table 8.7 – The total uncertainty, statistical uncertainty and total systematic uncertainty of the joint fit. Unit in [MeV]. The error on the statistical uncertainty is caused by the limited number of bootstrap toys (Equation 9.3).

Elec. SF	Elec. Calib.	Muon SF	Muon Calib.	Recoil	Lumi.	MJ
2.20	6.38	2.42	2.33	2.52	0.57	0.76

Table 8.8 – The decomposition of the experimental uncertainty for the joint fit. Unit in [MeV].

The fixed-order perturbative QCD uncertainty estimated using the CT18ANNLO global PDF set is around 5 MeV. With the measurement of the p_{T}^{W} distributions, the p_{T}^{W} uncertainty is expected to be well under control in the W-boson mass fit using the m_{T} spectrum, and is around 2 MeV, much lower than that in the previous ATLAS 7 TeV measurement where large uncertainty is brought by the p_{T}^{Z} to p_{T}^{W} extrapolation. The leading experimental uncertainty in the low pile-up measurement is the electron calibration systematics. More investigations are needed to improve the lepton calibration for the W-boson mass measurement.

8.5 Prospects

So far, the preliminary fit for the low pile-up W-boson mass measurement has been successfully carried out. The total uncertainty of the fit to the data is about 17 MeV when the W-boson mass is extracted from the unrolled m_{T} distribution. Further optimization of the categorization in u_{T} and η_{ℓ} may help to bring down the

MC background	PDF	p_{T}^{W}
1.69	5.33	1.99

Table 8.9 – The decomposition of the modelling uncertainty for the joint fit. Unit in [MeV].

total uncertainty by a certain amount. Also, some studies related to statistics are on-going, which are expected to facilitate the combination of statistically correlated observables in the profile likelihood fit.

One possible solution to improve the electron calibration uncertainty, which currently contributes as high as 6 MeV to the total uncertainty, would be to extrapolate from the full Run 2 dataset to help reduce the uncertainty in electron energy scale and resolution. The sources of high pile-up systematics, such as the temperature effect and difference in the topo-cluster noise threshold, however, will need to be handled carefully during the extrapolation.

The application of the data-driven multijet estimation to the m_W measurement is still preliminary. More efforts are anticipated on the validation and the improvement of the method, including the optimization of the function form for the extrapolation of the yield, the smoothing of the multijet shape in the Signal Region and so on.

On the physics modelling side, Powheg EW [34][35] may become an alternative tool for the estimation of electroweak uncertainty. As for the QCD modelling, possible improvements in the PDF uncertainties can be brought by the measurements of W and Z differential cross sections. The effect of missing higher-order QCD corrections has to be accounted for in the future. The spread of the central value of the fit using different global PDF set needs to be studied as well, which involves the development of a flexible tool for the PDF reweighting. The propagation of the p_{T}^{W} uncertainty from the direct measurement is sufficient for preliminary studies. The only caveat is that in order to ensure a good description of the recoil in the data, the function of the p_{T}^{W} reweighting has to be re-derived each time when the reconstructed level PDF baseline reweighting is applied, which is not yet implemented at this stage. In the next phase, the result of the p_{T}^{W} measurement can be used for a parton shower tuning, so that the correlation between the p_{T}^{W} and the W rapidity will be appropriately modelled in the simulation.

The W-boson mass measurement using low pile-up data requires all the above aspects and methods to be properly understood and scrutinized. The preliminary study covers most of the above topics to some extent, revealing the great potential of low pile-up data for the precision determination of the W-boson mass. It has been shown that the low pile-up m_W measurement will achieve a comparable precision as to the existing 7 TeV results [5], with most systematic sources better under control. In particular, the improved u_{T} resolution in the low pile-up conditions enhances the statistical sensitivity of the m_{T} distribution to m_W and facilitates a direct p_{T}^{W} measurement instead of extrapolating p_{T}^{W} from p_{T}^{Z}, which has been found to effectively constrain the corresponding modelling uncertainty in the m_W measurement. Furthermore, the use of profile likelihood fit in the statistical analysis constrains all systematic sources using the power of data statistics.

References

[1] D. Bardin, A. Leike, T. Riemann, and M. Sachwitz, "Energy-dependent width effects in e+e–annihilation near the z-boson pole", *Physics Letters B*, vol. 206, no. 3, pp. 539–542, 1988, ISSN: 0370-2693. DOI: https://doi.org/10.1016/0370-2693(88)91627-9. [Online]. Available: https://www.sciencedirect.com/science/article/pii/0370269388916279 (cit. on p. 172).

[2] J. Smith, W. L. van Neerven, and J. A. M. Vermaseren, "Transverse mass and width of the W boson", *Phys. Rev. Lett.*, vol. 50, pp. 1738–1740, 22 May 1983. DOI: 10.1103/PhysRevLett.50.1738. [Online]. Available: https://link.aps.org/doi/10.1103/PhysRevLett.50.1738 (cit. on p. 172).

[3] K. Cranmer, G. Lewis, L. Moneta, A. Shibata, and W. Verkerke, "HistFactory: A tool for creating statistical models for use with RooFit and RooStats", New York U., New York, Tech. Rep., 2012. [Online]. Available: https://cds.cern.ch/record/1456844 (cit. on pp. 174, 176, 184, 185).

[4] W. Verkerke and D. P. Kirkby, "The RooFit toolkit for data modeling", in *Proceedings of the 13th International Conference for Computing in High-Energy and Nuclear Physics (CHEP03)*, [eConf C0303241, MOLT007], 2003. arXiv: physics/0306116. [Online]. Available: http://inspirehep.net/record/634021 (cit. on p. 176).

[5] The ATLAS Collaboration, "Measurement of the W-boson mass in pp collisions at $\sqrt{s} = 7\,\text{TeV}$ with the ATLAS detector", *The European Physical Journal C*, vol. 78, p. 110, 2018. DOI: 10.1140/epjc/s10052-017-5475-4 (cit. on pp. 177, 193, 202).

[6] E. Rizvi, A. Glazov, L. J. Armitage, *et al.*, "Measurement of the Drell-Yan triple-differential cross-section in pp collisions at $\sqrt{s} = 8$ TeV", CERN, Geneva, Tech. Rep., 2015. [Online]. Available: https://cds.cern.ch/record/2117171 (cit. on p. 183).

[7] R. Barlow and C. Beeston, "Fitting using finite monte carlo samples", *Computer Physics Communications*, vol. 77, no. 2, pp. 219–228, 1993, ISSN: 0010-4655. DOI: https://doi.org/10.1016/0010-4655(93)90005-W. [Online]. Available: https://www.sciencedirect.com/science/article/pii/001046559390005W (cit. on p. 184).

[8] M. K. Bugge, A. Ezhilov, V. Solovyev, *et al.*, "Search for new particles in the charged lepton plus missing transverse energy final state using pp collisions at $\sqrt{s} = 13$ TeV in the ATLAS detector", CERN, Geneva, Tech. Rep., 2016. [Online]. Available: https://cds.cern.ch/record/2217650 (cit. on p. 185).

[9] L. Lyons, D. Gibaut, and P. Clifford, "How to combine correlated estimates of a single physical quantity", *Nuclear Instruments and Methods in Physics Research Section A: Accelerators, Spectrometers, Detectors and Associated Equipment*, vol. 270, no. 1, pp. 110–117, 1988, ISSN: 0168-9002. DOI: https://doi.org/10.1016/0168-9002(88)90018-6. [Online]. Available: https://www.sciencedirect.com/science/article/pii/0168900288900186 (cit. on p. 188).

[10] A. Valassi, "Combining correlated measurements of several different physical quantities", *Nuclear Instruments and Methods in Physics Research Section A: Accelerators, Spectrometers, Detectors and Associated Equipment*, vol. 500, no. 1, pp. 391–405, 2003, NIMA Vol 500, ISSN: 0168-9002. DOI: https://doi.org/10.1016/S0168-9002(03)00329-2. [Online]. Available: https://www.sciencedirect.com/science/article/pii/S0168900203003292 (cit. on p. 188).

[11] A. Collaboration, "Improved W boson Mass Measurement using 7 TeV Proton-Proton Collisions with the ATLAS Detector", CERN, Geneva, Tech. Rep., 2023. [Online]. Available: https://cds.cern.ch/record/2852059 (cit. on p. 190).

[12] "Electron and photon energy calibration with the ATLAS detector using data collected in 2015 at $\sqrt{s} = 13$ TeV", CERN, Geneva, Tech. Rep., 2016. [Online]. Available: https://cds.cern.ch/record/2203514 (cit. on p. 191).

[13] A. Collaboration, *Studies of the muon momentum calibration and performance of the atlas detector with pp collisions at $\sqrt{s}$=13 tev*, 2022. arXiv: 2212.07338 [hep-ex]. [Online]. Available: https://doi.org/10.48550/arXiv.2212.07338 (cit. on p. 192).

[14] N. M. Koehler, J. J. Junggeburth, F. Sforza, *et al.*, "Muon Efficiency Measurements on the Full Run 2 dataset", CERN, Geneva, Tech. Rep., 2019. [Online]. Available: https://cds.cern.ch/record/2665704 (cit. on p. 192).

[15] G. Avoni, M. Bruschi, G. Cabras, *et al.*, "The new lucid-2 detector for luminosity measurement and monitoring in atlas", *Journal of Instrumentation*, vol. 13, no. 07, P07017, Jul. 2018. DOI: 10.1088/1748-0221/13/07/P07017. [Online]. Available: https://dx.doi.org/10.1088/1748-0221/13/07/P07017 (cit. on p. 192).

[16] "Luminosity determination in *pp* collisions at $\sqrt{s} = 13$ TeV using the ATLAS detector at the LHC", Dec. 2022. arXiv: 2212.09379 [hep-ex] (cit. on p. 192).

[17] *Proceedings of the 1974 CERN School of Computing: Godøysund, Norway 11 - 24 Aug 1974. 3rd CERN School of Computing*, CERN, Geneva: CERN, 1974. DOI: 10.5170/CERN-1974-023. [Online]. Available: https://cds.cern.ch/record/186223 (cit. on p. 192).

[18] H.-L. Lai, M. Guzzi, J. Huston, *et al.*, "New parton distributions for collider physics", *Phys. Rev. D*, vol. 82, p. 074 024, 7 Oct. 2010. DOI: 10.1103/PhysRevD.82.074024. [Online]. Available: https://link.aps.org/doi/10.1103/PhysRevD.82.074024 (cit. on p. 197).

[19] T.-J. Hou, K. Xie, J. Gao, *et al.*, *Progress in the cteq-tea nnlo global qcd analysis*, 2019. arXiv: 1908.11394 [hep-ph] (cit. on p. 197).

[20] The ATLAS Collaboration, "Precision measurement and interpretation of inclusive W^+, W^- and Z/γ^* production cross sections with the atlas detector", *The European Physical Journal C*, vol. 77, no. 367, 6 1993, ISSN: 1434-6052. DOI: https://10.1140/epjc/s10052-017-4911-9. [Online]. Available: https://doi.org/10.1140/epjc/s10052-017-4911-9 (cit. on p. 197).

[21] J. Bellm *et al.*, "Herwig 7.0/Herwig++ 3.0 release note", *Eur. Phys. J. C*, vol. 76, no. 4, p. 196, 2016. DOI: 10.1140/epjc/s10052-016-4018-8. arXiv: 1512.01178 [hep-ph] (cit. on p. 197).

[22] J. Gao, M. Guzzi, J. Huston, *et al.*, "CT10 next-to-next-to-leading order global analysis of QCD", *Phys. Rev. D*, vol. 89, no. 3, p. 033 009, 2014. DOI: 10.1103/PhysRevD.89.033009. arXiv: 1302.6246 [hep-ph] (cit. on p. 197).

[23] S. Dulat, T.-J. Hou, J. Gao, *et al.*, "New parton distribution functions from a global analysis of quantum chromodynamics", *Phys. Rev. D*, vol. 93, p. 033 006, 3 Feb. 2016. DOI: 10.1103/PhysRevD.93.033006. [Online]. Available: https://link.aps.org/doi/10.1103/PhysRevD.93.033006 (cit. on p. 197).

[24] L. A. Harland-Lang, A. D. Martin, P. Motylinski, and R. S. Thorne, "Parton distributions in the lhc era: mmht 2014 pdfs", *The European Physical Journal C*, vol. 75, p. 204, 5 May 2015. DOI: 10.1140/epjc/s10052-015-3397-6. [Online]. Available: https://doi.org/10.1140/epjc/s10052-015-3397-6 (cit. on p. 197).

[25] The ATLAS Collaboration, "Measurement of the angular coefficients in z-boson events using electron and muon pairs from data taken at $\sqrt{s} = 8$tev with the atlas detector", *Journal of High Energy Physics*, vol. 2016, p. 159, 8 Aug. 2016. DOI: 10.1007/JHEP08(2016)159. [Online]. Available: https://doi.org/10.1007/JHEP08(2016)159 (cit. on p. 197).

[26] T. Sjöstrand, S. Mrenna, and P. Skands, "A brief introduction to pythia 8.1", *Computer Physics Communications*, vol. 178, no. 11, pp. 852–867, 2008, ISSN: 0010-4655. DOI: https://doi.org/10.1016/j.cpc.2008.01.036. [Online]. Available: https://www.sciencedirect.com/science/article/pii/S0010465508000441 (cit. on p. 197).

[27] P. Nason, "A new method for combining nlo qcd with shower monte carlo algorithms", *Journal of High Energy Physics*, vol. 2004, no. 11, p. 040, Dec. 2004. DOI: 10.1088/1126-6708/2004/11/040. [Online]. Available: https://dx.doi.org/10.1088/1126-6708/2004/11/040 (cit. on p. 198).

[28] S. Frixione, P. Nason, and C. Oleari, "Matching nlo qcd computations with parton shower simulations: the powheg method", *Journal of High Energy Physics*, vol. 2007, no. 11, p. 070, Nov. 2007. DOI: 10.1088/1126-6708/2007/11/070. [Online]. Available: https://dx.doi.org/10.1088/1126-6708/2007/11/070 (cit. on p. 198).

[29] S. Alioli, P. Nason, C. Oleari, and E. Re, "Nlo vector-boson production matched with shower in powheg", *Journal of High Energy Physics*, vol. 2008, no. 07, p. 060, Jul. 2008. DOI: 10.1088/1126-6708/2008/07/060. [Online]. Available: https://dx.doi.org/10.1088/1126-6708/2008/07/060 (cit. on p. 198).

[30] S. Alioli, P. Nason, C. Oleari, and E. Re, "A general framework for implementing nlo calculations in shower monte carlo programs: the powheg box", *Journal of High Energy Physics*, vol. 2010, p. 43, 6 Jul. 2010. DOI: 10.1007/JHEP06(2010)043. [Online]. Available: https://doi.org/10.1007/JHEP06(2010)043 (cit. on p. 198).

[31] Golonka, P. and Was, Z., "Photos monte carlo: a precision tool for qed corrections in z and w decays", *The European Physical Journal C - Particles and Fields*, vol. 45, pp. 97–107, 1 2006. DOI: https://doi.org/10.1140/epjc/s2005-02396-4. [Online]. Available: https://doi.org/10.1140/epjc/s2005-02396-4 (cit. on p. 198).

[32] W. Płaczek, S. Jadach, and M. W. Krasny, "Drell-Yan processes with WINHAC", *Acta Phys. Polon. B*, vol. 44, no. 11, pp. 2171–2178, 2013. DOI: 10.5506/APhysPolB.44.2171. arXiv: 1310.5994 [hep-ph] (cit. on p. 198).

[33] A. Pinto, Z. Wu, F. Balli, *et al.*, *Uncertainty components in profile likelihood fits*, 2023. arXiv: 2307.04007 [physics.data-an] (cit. on p. 198).

[34] L. Barzè, G. Montagna, P. Nason, O. Nicrosini, and F. Piccinini, "Implementation of electroweak corrections in the powheg box: single w production", *Journal of High Energy Physics*, vol. 2012, p. 37, 4 Apr. 2012. DOI: 10.1007/JHEP04(2012)037. [Online]. Available: https://doi.org/10.1007/JHEP04(2012)037 (cit. on p. 202).

[35] C. M. Carloni Calame, M. Chiesa, H. Martinez, *et al.*, "Precision measurement of the W-boson mass: theoretical contributions and uncertainties", *Phys. Rev. D*, vol. 96, p. 093 005, 9 Nov. 2017. DOI: 10.1103/PhysRevD.96.093005. [Online]. Available: https://link.aps.org/doi/10.1103/PhysRevD.96.093005 (cit. on p. 202).

Chapter 9

Uncertainty components in profile likelihood fit

Contents

9.1 Uncertainty decomposition for profile likelihood fit

9.1.1 Measurement and uncertainty decomposition

In order to facilitate physics interpretation of the result, the measurements of physics quantities are often reported not only the quoting total uncertainty, but also including the breakdown into components with reasonable physics meanings, such as statistical uncertainty and one or multiple sources of systematic uncertainty.

In this study, the statistical uncertainty is defined by its frequentist interpretation, that is the standard deviation of a statistical estimator when the exact same experiment is repeated with the same systematics on independent data samples of the identical expected size. However, depending on the design and the technical details of the statistical analysis, the decomposition of the total uncertainty can be carried out in different ways based on the choice of test statistic used for the measurement.

In the simplest case, the statistical analysis compares the measurement of a quantity or distribution to a model that is parameterized by physical constants to be determined. The auxiliary parameters of systematic effects are fixed to their best estimates in the model. The measured central values of the physics constants are derived from the maximum of the likelihood, while the curvature of the likelihood contour near the maximum reflects the lower bound of statistical uncertainty of the measurement according to the Cramér–Rao bound. The systematic uncertainties relevant to the measurement are assessed by repeating the procedure using varied models for which auxiliary parameters are changed within their uncertainty. Each of these variations represents a source of uncertainty. And the resulting uncertainties are often uncorrelated by construction, such that the total uncertainty is the quadratic sum of statistical uncertainty and all the components of systematic uncertainties. An example of the measurement using this analysis strategy is the ATLAS 7 TeV m_W measurement [1].

An improved method of statistical analysis involves parameterizing the model with both the physical constants and the sources of systematic uncertainty [2][3]. The best values of the physical constants and the uncertainty parameters are determined simultaneously. The maximum of the likelihood in this model therefore corresponds to the global optimum for all fit parameters, while the curvature of the likelihood contour represents the total uncertainty, or in other words, the combined fluctuations of the data and all sources of uncertainties. The current practice for breaking down the statistical and systematic uncertainties in these fits is referred to as impact method [4]–

[6], following which the contribution of a given source of systematics comes from quadratic difference between the total uncertainty of the fit including or excluding this source in the model. The statistical uncertainty in the impact method is, on the other hand, determined by the uncertainty of the fit excluding the presence of all systematics in the model. Although the impacts quantify the inflation in the total uncertainty when a new source of systematic is added to a measurement, by no means they are supposed to be interpreted as the contribution of the systematic sources to the total uncertainty of a complete measurement. The supporting reasons are that the quadratic sum of statistical uncertainty and all the impacts do not reproduce the total uncertainty, and that the impacts do not obey the usual uncertainty decomposition formulas even if the uncertainties are genuinely Gaussian, as it has been pointed out in [7]. The solution to a coherent uncertainty decomposition will be provided in Section 9.1.2.

In the sections below, the measurements and the predictions in a model will be denoted as $\vec{m}$ and $\vec{t}$, labelled by indices i. The predictions are functions of the parameters of interest (POIs) θ and nuisance parameters (NPs) for systematics $\vec{\alpha}$ labelled r. The sources of uncertainty are denoted as $\vec{a}$, corresponding to $\vec{\alpha}$.

9.1.2 Uncertainty decomposition from shifted observables

Once the form of the probability model is given for a measurement, post-fit central value of a POI is solely dependent on the global observable and the (pseudo) data in the input, such that:

$$\hat{\theta} = \hat{\theta}(\vec{m}, \vec{a}) \tag{9.1}$$

In the most common cases, for instance, the extraction of a physical constant from a reconstructed level kinematic distribution, the measurements and global observables are uncorrelated at source level. If so, regardless of the distribution of the uncertainty distributions in the probability model, the post-fit uncertainty of the POI can be expressed via a linear error propagation:

$$\Delta\theta = \sqrt{\sum_i \left(\frac{\partial\hat{\theta}}{\partial m_i}\Delta m_i\right)^2 + \sum_r \left(\frac{\partial\hat{\theta}}{\partial a_r}\Delta a_r\right)^2} \tag{9.2}$$

where Δm_i and Δa_r are the standard deviations of m_i and a_r, respectively. The first sum under the square root originates from the fluctuations of the data, while the second term sums up the contributions from all the systematic sources. Following the spirit of this formula, the contribution of a given source of uncertainty can be estimated by shifting the corresponding measurement (for data statistics) or global observable (for systematics) by one standard deviation in the expression of the likelihood, then repeating the fit with everything else remaining the same in the probability model. The difference between the post-fit value of $\hat{\theta}$ before and after shifting the measurement or global observable is the corresponding uncertainty. This prescription allows a coherent uncertainty decomposition, since the quadratic sum of all uncertainty sources adds up to the total uncertainty, and the contribution of each uncertainty source is uniquely determined.

Instead of shifting measurements or global observables by one standard deviation, an equivalent procedure of uncertainty decomposition based on Equation 9.2 would be to fluctuate all the bins m_i together according to the statistical uncertainty in

each bin, or to fluctuate the a_r's in interest according to their distributions given by the auxiliary measurements. This procedure generates bootstrap toys of the data or those of the global observables. The spread of the bootstrap toys of m_i gives the data statistical uncertainty. Similarly, the spread of the bootstrap toys of a_r corresponds to the systematic uncertainty arising from the sources of which the global observables are fluctuated. The bootstrap error ($Error_{BS}$) in the involved uncertainty components (σ_{BS}) due to limited number of bootstrap toys (N_{BS}) is estimated by

$$Error_{BS} \approx \frac{\sigma_{BS}}{\sqrt{2N_{BS}}} \tag{9.3}$$

In particular, the bootstrap equivalence of the shifted observable approach can be more convenient when the number of measurements or global observables are way more than the number of toys needed to achieve the desired numerical precision.

9.2 Illustrative example: m_W fit on pseudo data

In order to validate the method of uncertainty decomposition discussed in Section 9.1.2, a numerical exercise featuring m_W measurement is provided in this section. The statistical analysis of the measurement is a shape analysis that uses profile likelihood fit, where the fit to the distribution is parameterized by a POI and several NPs accounting for the effect of systematics. While the effect of varying the hypothetical value of m_W is parameterized by the POI in the profile likelihood fit, three representative sources of systematic uncertainty of a m_W measurement encountered in hadron colliders [8]–[11] are parameterized by the corresponding NPs: the lepton momentum scale uncertainty, the hadronic recoil resolution uncertainty and the p_{T}^W modelling uncertainty. The mass of W-boson can be extracted from either p_{T}^{ℓ} or m_{T} distributions. However, the sensitivity to certain types of systematics is very different depending on the choice of the kinematic spectrum.

Since the measurement of m_W is a typical shape analysis, the conclusions drawn from this example can be in principle generalized to all kinds of shape analysis.

9.2.1 MC samples

The signal process being simulated is the charge-current Drell-Yan process [12] $pp \to W^- \to \mu^-\nu$ at $\sqrt{s}$ =13 TeV. The samples are generated using Madgraph+Pythia8 [13][14], of which the details of the generation is listed in Table 9.1. No background process is considered in this exercise.

The m_W templates are produced with Breit-Wigner reweighting [15] of the nominal signal MC. The systematic variation of p_{T}^W modelling is implemented by first using a linear reweighting as a function of the p_{T}^W: $w(p_{\mathrm{T}}^W) = 0.96 + 8 \times 10^{-4} \times p_{\mathrm{T}}^W$[GeV] before the event selection, then taking the shape effect on the underlying p_{T}^W distribution. The reweighting is fixed at 1.04 for p_{T}^W >100 GeV. At reconstructed level, the p_{T} of the bare muon is smeared by 2 % following a Gaussian distribution. A source of systematic uncertainty in the muon momentum scale is considered. This variation changes the muon momentum scale by 0.5 per-mille. For simplicity, the muon reconstruction and identification is considered to be 100 % efficient. The hadronic recoil $\vec{u}_{\mathrm{T}}$ is taken to be the opposite of $\vec{p}_{\mathrm{T}}^W$ smeared by a constant 6 GeV in both directions of the transverse plane. The variation in the recoil resolution uncertainty is made by changing the

Event Generator	
$pp \to W^- \to \mu^- \nu_\mu$ at $\sqrt{s}$=13 [TeV]	
Integrated luminosity	76.42 [pb^{-1}]
Number of events	10,000,000
Matrix elements	Madgraph at LO
Input m_W	80.419 [GeV]
Input Γ_W	2.0476 [GeV]
Parton shower & QED FSR	Pythia8
MC sample weight	0.05

Table 9.1 – Madgraph+Pythia8 event generation for MC samples. Events with an off-shell boson are excluded in the event generation at parton level, leading to a total cross-section of 6543 pb.

recoil resolutions by 5 per-mille in both directions. The recoil resolution uncertainty is taken as the second source of experimental systematics.

The bare muon is considered to be the muon at reconstructed level. The neutrino missing energy $\vec{E}_{\mathrm{T}}^{\mathrm{miss}}$ is calculated vectorially from the reconstructed hadronic recoil and the reconstructed muon. The m_{T} spectrum is calculated from the reconstructed level muon p_{T} and $\vec{E}_{\mathrm{T}}^{\mathrm{miss}}$. As listed in Table 9.2, the event selection is chosen to be as close as possible to the design of a realistic m_W measurement at hadron colliders. The cut-flow efficiency for these signal events is around 29 %.

The reconstructed level muon p_{T} and m_{T} distributions are shown in Figure 9.1. All m_W templates and systematic variations are normalized to the integral of the nominal signal MC in the fit range. The distortion on the spectra brought by the lepton energy scale variation resembles the effect of changing the hypothetical value of m_W. The muon p_{T} distribution is sensitive to the p_{T}^W modelling uncertainty but almost unaffected by the recoil resolution variation. In contrast, the m_{T} distribution is insensitive to p_{T}^W variation by construction, but more sensitive to the recoil resolution uncertainty, since the hadronic recoil enters the computation of m_{T}.

Event selection	
η_ℓ selection	[-2.5, 2.5]
p_{T}^ℓ selection	>25 [GeV]
$E_{\mathrm{T}}^{\mathrm{miss}}$ selection	>25 [GeV]
m_{T} selection	>50 [GeV]
u_{T} selection	<25 [GeV]

Table 9.2 – Event selection for the Madgraph+Pythia8 samples.

9.2.2 Validation of uncertainty decomposition

The profile likelihood fit is performed using HistFactory [16] and RooFit [17], the same framework for the statistical analysis used in the low pile-up m_W measurement. The output of the fit returns both the post-fit central values and the post-fit uncertainties of all fit parameters. Each uncertainty component of the profile likelihood fit is obtained by first repeating the fit to the bootstrap toys of the pseudo data for

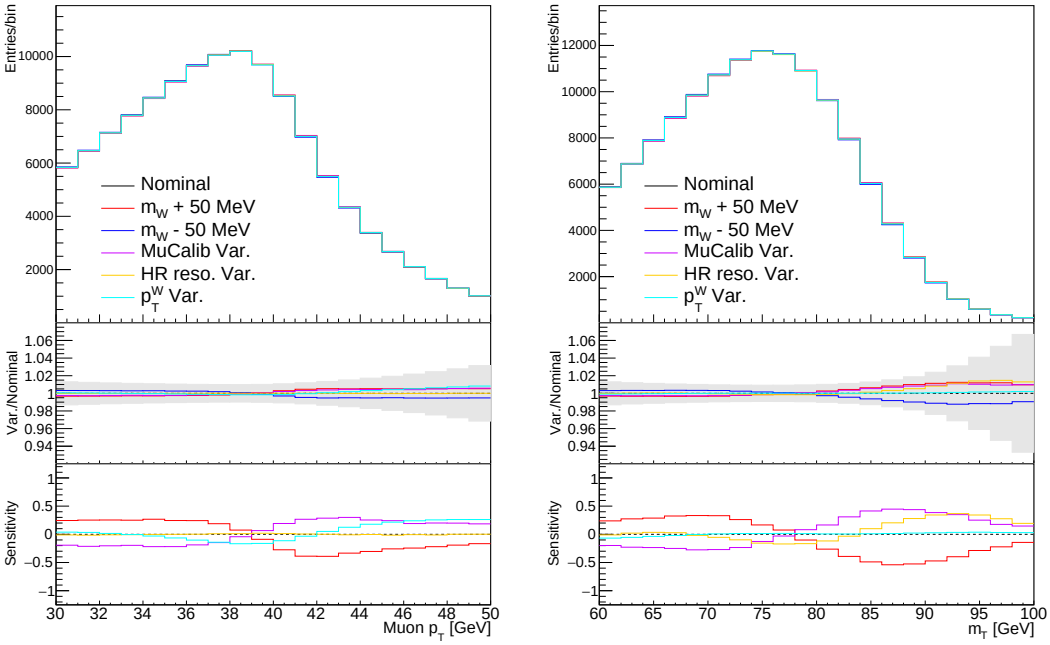

(a) p_{T}^{ℓ}. (b) m_{T}.

Figure 9.1 – Reconstructed muon p_{T} and m_{T} distributions of the Madgraph + Pythia8 samples. The integrated luminosity is 76.42 pb^{-1}. (top): Kinematic spectra. (middle): The variation to nominal ratio with statistical uncertainty indicated by the error band. (bottom): Sensitivity (the difference between variation and nominal, divided by statistical uncertainty) of m_W templates (unit: [50 GeV]$^{-1}$) and systematic variations.

statistical uncertainty, or those of the global observables for systematics, then calculating the spread of the offsets in the POI. Changing the relative luminosity of the samples corresponds to a change of data statistics, for which the effect is emulated by repeating the fit with an overall luminosity scale factor multiplied to all reconstructed distributions. By using the luminosity scale factor, it doesn't require to generate more samples to match an increased relative luminosity. The setup of these validation fits are listed in Table 9.3.

Probability model	Full model	Stat. only
NPs	Lepton momentum scale Recoil resolution p_{T}^{W} systematics	—
Luminosity scale factor	0.1, 0.4, 0.7, 1.0, 2.0, 5.0, 10.0	
Fit range	$30<p_{\mathrm{T}}^{\ell}<50$ [GeV] $60<m_{\mathrm{T}}<100$ [GeV]	

Table 9.3 – Configuration of the m_W fits. The luminosity scale factor of 1.0 corresponds to 76.42 [pb^{-1}].

The responses of uncertainty components towards relative luminosity are presented in Figures 9.2 and 9.3, with error bars computed using Equation 9.3. The quadratic sum of all uncertainty components reproduces the total uncertainty returned by the

profile likelihood fit. As one would expect, more statistics reduces both total uncertainty and statistical uncertainty of the fit. However, increasing the statistical power does not help the fit effectively constrain the muon energy scale uncertainty, mainly because it is difficult to disentangle the effect of varying muon energy scale and that of changing the assumed value of m_W. The contribution of recoil resolution systematics is low for a fit based on muon p_{T} distribution regardless of the statistics, while the p_{T}^W behaves similarly for a fit based on the m_{T} spectrum. The uncertainty decomposition also reveals that with more data, certain sources of systematics can be effectively constrained by the profile likelihood fit, for instance the p_{T}^W uncertainty in the muon p_{T} fit in this exercise, or the recoil resolution uncertainty in the m_{T} fit. Tables 9.4 and 9.5 present the uncertainty decomposition using impact approach and the shifted observable approach at two different values of the luminosity scale factor. In the shifted observable approach, the quadratic sum of the statistical uncertainty and the systematic uncertainty reproduces the total uncertainty within the tolerance of numerical errors. The statistical uncertainty estimated by the impact approach decreases by the square root of the increase in luminosity scale factor ($\sqrt{10}$), while the statistical uncertainty given by the shifted observable approach decreases slower than that rate.

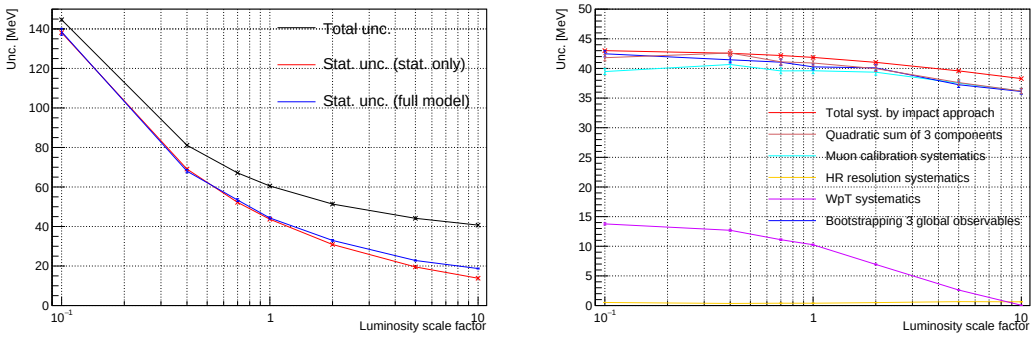

(a) Total and statistical uncertainties.

(b) Systematic uncertainties.

Figure 9.2 – Uncertainty decomposition for the profile likelihood fit based on muon p_{T} spectrum. For the total systematic uncertainty, the result of bootstrapping three global observables simultaneously is compatible with the quadratic sum of bootstrapping the three components individually.

Muon p_{T} fit			
Measurement	σ_{stat}	σ_{syst}	σ_{tot}
1.0 lumi. impact	43.68	41.86	60.50
1.0 lumi. shifted obs.	43.96 ± 0.55	40.99 ± 1.02	60.50
10.0 lumi. impact	13.81	38.29	40.70
10.0 lumi. shifted obs.	18.76 ± 0.23	36.19 ± 0.45	40.70

Table 9.4 – The uncertainty break-down for the muon p_{T} fit at two different values of the luminosity scale factor, using the impact approach and the shifted observable approach for profile likelihood fit (unit in [MeV]). The errors arise from the limited number of bootstrap toys. The baseline luminosity is 76.42 [pb^{-1}].

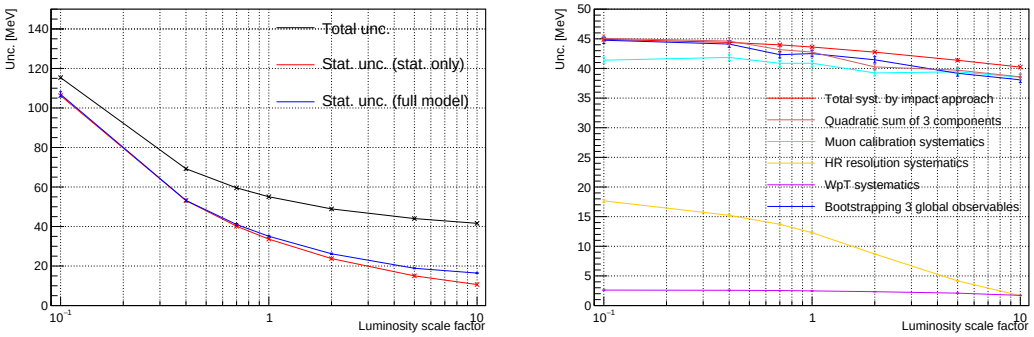

(a) Total and statistical uncertainties.

(b) Systematic uncertainties.

Figure 9.3 – Uncertainty decomposition for the profile likelihood fit based on m_{T} spectrum. For the total systematic uncertainty, the result of bootstrapping three global observables simultaneously is compatible with the quadratic sum of bootstrapping the three components individually.

m_{T} fit			
Measurement	σ_{stat}	σ_{syst}	σ_{tot}
1.0 lumi. impact	33.60	43.62	55.06
1.0 lumi. shifted obs.	34.41 ± 0.43	39.14 ± 0.98	55.06
10.0 lumi. impact	10.63	40.23	41.61
10.0 lumi. shifted obs.	15.73 ± 0.20	38.59 ± 0.48	41.61

Table 9.5 – The uncertainty break-down for the m_{T} fit at two different values of the luminosity scale factor, using the impact approach and the shifted observable approach for profile likelihood fit (unit in [MeV]). The errors arise from the limited number of bootstrap toys. The baseline luminosity is 76.42 [pb^{-1}].

The dependence of post-fit uncertainties of the NPs on the relative luminosity is shown in Figure 9.4. The responses of NPs are consistent with those of the corresponding source of systematic uncertainty in Figures 9.2 and 9.3.

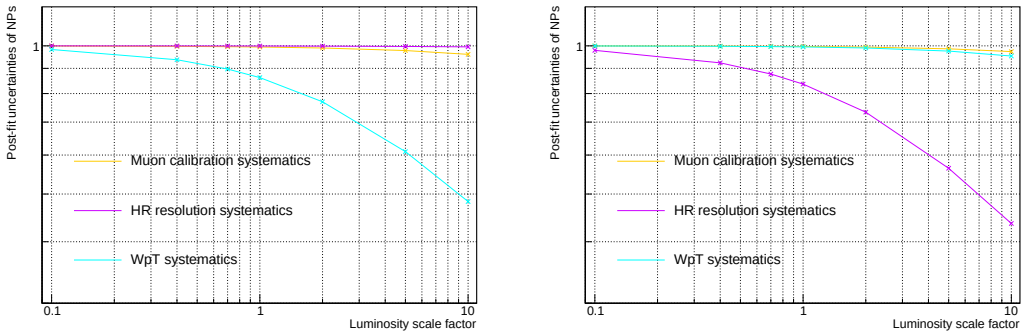

(a) Muon p_{T} fit. (b) m_{T} fit.

Figure 9.4 – Post-fit uncertainties of the NPs at different values of the luminosity scale factor.

References

[1] The ATLAS Collaboration, "Measurement of the W-boson mass in pp collisions at $\sqrt{s} = 7\,\text{TeV}$ with the ATLAS detector", *The European Physical Journal C*, vol. 78, p. 110, 2018. DOI: 10.1140/epjc/s10052-017-5475-4 (cit. on p. 208).

[2] W. A. Rolke, A. M. Lopez, and J. Conrad, "Limits and confidence intervals in the presence of nuisance parameters", *Nucl. Instrum. Meth. A*, vol. 551, L. Lyons and M. Karagoz, Eds., pp. 493–503, 2005. DOI: 10.1016/j.nima.2005.05.068. arXiv: physics/0403059 (cit. on p. 208).

[3] S. Schael *et al.*, "Electroweak Measurements in Electron-Positron Collisions at W-Boson-Pair Energies at LEP", *Phys. Rept.*, vol. 532, pp. 119–244, 2013. DOI: 10.1016/j.physrep.2013.07.004. arXiv: 1302.3415 [hep-ex] (cit. on p. 208).

[4] R. Barlow, R. Cahn, G. Cowan, *et al.*, "Recommended Statistical Procedures for BABAR", BABAR Analysis Document 318, 2002. [Online]. Available: https://babar.heprc.uvic.ca/BFROOT/www/Statistics/Report/report.pdf (cit. on p. 208).

[5] R. A. Fisher, "XV.—The Correlation between Relatives on the Supposition of Mendelian Inheritance.", *Earth and Environmental Science Transactions of The Royal Society of Edinburgh*, vol. 52, no. 2, pp. 399–433, 1919. DOI: 10.1017/S0080456800012163 (cit. on p. 208).

[6] R. A. Fisher, "Studies in crop variation. I. An examination of the yield of dressed grain from Broadbalk", *The Journal of Agricultural Science*, vol. 11, no. 2, pp. 107–135, 1921. DOI: 10.1017/S0021859600003750 (cit. on p. 208).

[7] A. Pinto, Z. Wu, F. Balli, *et al.*, *Uncertainty components in profile likelihood fits*, 2023. arXiv: 2307.04007 [physics.data-an] (cit. on p. 209).

[8] V. M. Abazov *et al.*, "Measurement of the W Boson Mass with the D0 Detector", *Phys. Rev. Lett.*, vol. 108, p. 151 804, 2012. DOI: 10.1103/PhysRevLett.108.151804. arXiv: 1203.0293 [hep-ex] (cit. on p. 210).

[9] M. Aaboud *et al.*, "Measurement of the W-boson mass in pp collisions at $\sqrt{s} = 7$ TeV with the ATLAS detector", *Eur. Phys. J. C*, vol. 78, no. 2, p. 110, 2018, [Erratum: Eur.Phys.J.C 78, 898 (2018)]. DOI: 10.1140/epjc/s10052-017-5475-4. arXiv: 1701.07240 [hep-ex] (cit. on p. 210).

[10] R. Aaij *et al.*, "Measurement of the W boson mass", *JHEP*, vol. 01, p. 036, 2022. DOI: 10.1007/JHEP01(2022)036. arXiv: 2109.01113 [hep-ex] (cit. on p. 210).

[11] T. Aaltonen *et al.*, "High-precision measurement of the W boson mass with the CDF II detector", *Science*, vol. 376, no. 6589, pp. 170–176, 2022. DOI: 10.1126/science.abk1781 (cit. on p. 210).

[12] S. D. Drell and T.-M. Yan, "Massive lepton-pair production in hadron-hadron collisions at high energies", *Phys. Rev. Lett.*, vol. 25, pp. 316–320, 5 Aug. 1970. DOI: 10.1103/PhysRevLett.25.316. [Online]. Available: https://link.aps.org/doi/10.1103/PhysRevLett.25.316 (cit. on p. 210).

[13] J. Alwall, R. Frederix, S. Frixione, *et al.*, "The automated computation of tree-level and next-to-leading order differential cross sections, and their matching to parton shower simulations", *JHEP*, vol. 07, p. 079, 2014. DOI: 10.1007/JHEP07(2014)079. arXiv: 1405.0301 [hep-ph] (cit. on p. 210).

[14] T. Sjostrand, S. Mrenna, and P. Z. Skands, "A Brief Introduction to PYTHIA 8.1", *Comput. Phys. Commun.*, vol. 178, pp. 852–867, 2008. DOI: 10.1016/j.cpc.2008.01.036. arXiv: 0710.3820 [hep-ph] (cit. on p. 210).

[15] D. Bardin, A. Leike, T. Riemann, and M. Sachwitz, "Energy-dependent width effects in e+e–annihilation near the z-boson pole", *Physics Letters B*, vol. 206, no. 3, pp. 539–542, 1988, ISSN: 0370-2693. DOI: https://doi.org/10.1016/0370-2693(88)91627-9. [Online]. Available: https://www.sciencedirect.com/science/article/pii/0370269388916279 (cit. on p. 210).

[16] K. Cranmer, G. Lewis, L. Moneta, A. Shibata, and W. Verkerke, "HistFactory: A tool for creating statistical models for use with RooFit and RooStats", New York U., New York, Tech. Rep., 2012. [Online]. Available: https://cds.cern.ch/record/1456844 (cit. on p. 211).

[17] W. Verkerke and D. P. Kirkby, "The RooFit toolkit for data modeling", in *Proceedings of the 13th International Conference for Computing in High-Energy and Nuclear Physics (CHEP03)*, [eConf C0303241, MOLT007], 2003. arXiv: physics/0306116. [Online]. Available: http://inspirehep.net/record/634021 (cit. on p. 211).

Chapter 10

Conclusion

This thesis presents the work on the production and the qualification of NSW Micromegas for the ATLAS Phase-I upgrade, as well as the measurements of the W-boson properties at 5.02 and 13 TeV center-of-mass energies using low pile-up data recorded by ATLAS.

The increasing luminosity of LHC during Run 3 demands improved rate capability of detectors on the inner end-caps of the ATLAS muon system. The old inner end-caps of the muon spectrometer have been replaced by the NSWs during the Phase-I upgrade. The NSWs comprise two complementary detector technologies to combine the fast trigger capability given by the sTGC, and the tracking capabilities obtained with the Micromegas. Micromegas, one of the main micro-pattern gaseous detectors, are capable of sustaining a high flux rate of $15\,\mathrm{kHz\,cm^{-2}}$ while keeping a high tracking precision of 100 µm per detecting layer, thanks to the micro-mesh technology and the separation of the conversion region and the amplification region. All the LM1 Micromegas modules are produced and qualified at Saclay. With the setup of the cosmic bench at Saclay, particularly in the presence of the three layers of 2D external trackers, the performance of the LM1 Micromegas modules are examined with a high granularity in terms of efficiency and gain. The 2D maps of efficiency and gain are produced per detecting layer for each LM1 Micromegas module. The efficiency loss due to the structure of interconnection in the module has also been estimated. An improved mixture of working gas for the NSW Micromegas was initially proposed by Saclay and tested on the cosmic bench. With the improved working gas compared to the default choice used on the cosmic bench characterization for most of the time, the NSW Micromegas benefits from attaining the same gain in a lower high voltage, therefore suppressing the high voltage instabilities and the loss of efficiency. Comprehensive follow-up studies have been carried out at CERN in parallel to and after the production of the NSW modules, proving the feasibility of this improved working gas mixture for the NSW Micromegas in Run 3. So far, no significant aging effect has been observed with the improved gas mixture. All Micromegas modules have been delivered and mounted on the NSWs. With the NSW commissioned and operational, ATLAS will retain the performance of muon reconstruction at higher instantaneous luminosity during the Run 3 data taking.

The measurements of the W-boson properties benefit from the low pile-up data taking conditions in specialized datasets, thanks to which the resolution of the hadronic recoil is largely improved with respect to the higher pile-up datasets. The thesis covers the description of the Run 2 low pile-up datasets, as well as an introduction to the

dedicated detector calibration for the low pile-up datasets. The multijet background contamination in the W event selection is estimated by a data-driven method, with improvements in the determination of the yield: A shape correction to the multijet templates in the control region, and the compensation for a bias introduced by the reconstruction of the hadronic recoil. The measurement of the p_{T}^{W} spectrum is mostly driven by the need for a precise determination of the W-boson mass, which allows to perform stringent tests of the Standard Model. The low pile-up p_{T}^{W} measurement adopts the Iteration Bayesian Unfolding to infer the underlying p_{T}^{W} distribution from the reconstructed level hadronic recoil spectrum. A data-driven boson-p_{T} correction is implemented in the analysis to correct for the large mis-modelling of the boson-p_{T} distribution in the default simulation. Bias uncertainties associated with the boson-p_{T} correction are assessed, and are taken into account in the optimization of the regularization parameters for the unfolding. The unfolded p_{T}^{W} spectra in the electron channels and in the muon channels are combined and compared with various theoretical predictions. Several discrepancies between the measurement and the predictions suggest the needs for an improved QCD modelling in the predictions.

The low pile-up m_W measurement benefits from the calibration work of the p_{T}^{W} measurement. A profile likelihood fit has been set up for the extraction of m_W from the reconstructed level kinematic distributions. The effects of systematic uncertainties are parameterized in the probability model of the fit. Even though the final strategy for the boson-p_{T} modelling has not yet been decided, the results of the low pile-up p_{T}^{W} measurement are tentatively propagated to the m_W measurement as a preliminary study, revealing an effective constraint on the modelling of p_{T}^{W} distribution. Efforts are also spent on the improvement of the statistical analysis, including the reduction of the number of nuisance parameter in the probability model using a standard procedure for experimental systematics, as well as the study of a preliminary data scaling technique for MC statistical uncertainty. The possibilities of combining the results from the profile likelihood fit using statistically correlated observables are briefly discussed. In addition, a coherent uncertainty decomposition for the profile likelihood fit has been introduced for the first time, and applied to the preliminary study of low pile-up m_W measurement. The formulation and the validation of the uncertainty decomposition approach are summarized in a stand-alone chapter.

As an on-going analysis, the low pile-up m_W measurement requires not only further improvement in the detector calibration, but also in the theoretical modelling of the W-boson production and decay, as well as the estimation of relevant uncertainties. The low pile-up m_W measurement is expected to demonstrate the power of the profile likelihood fit in terms of constraining the theoretical uncertainties, and provide new results complementary to the previous ATLAS measurement using the 7 TeV dataset. The low pile-up m_W measurement will improve the world average of direct m_W measurements and test the consistency of the SM. In the meantime, the low pile-up data has shown its great potential for precision electroweak measurements in ATLAS. In particular, the improved detector resolution with the low pile-up conditions enhances the statistical sensitivity of the measurement and helps better constrain p_{T}^{W} modelling uncertainties.